

Relation between composition, structure and morphology in C-S-H

Elena Tajuelo Rodriguez

Submitted in accordance with the requirements for the degree of
Doctor of Philosophy

The University of Leeds

School of Civil Engineering

February 2015

The candidate confirms that the work submitted is her own and that appropriate credit has been given where reference has been made to the work of others.

This copy has been supplied on the understanding that it is copyright material and that no quotation from the thesis may be published without proper acknowledgement.

Acknowledgements

First of all I would like to thank the TRANSCEND recruiting committee for having offered me the opportunity to participate in this collaboration. I would also like to thank my supervisor Prof. Ian G. Richardson for accepting my supervision and having allowed me to do my research with freedom.

My cosupervisor Dr. Leon Black and Prof. Karen L. Scrivener deserve a special mention for believing in me when I did not even believe in myself. I am deeply grateful to Leon for the emails out of hours, thorough checking of documents and all the suggestions to improve my experiments during the first year.

Thanks to my parents, my brother, his girlfriend Ana and my aunt Pili, for being a great supportive and loving family during the ups and downs of this journey!

I would like to express my gratitude to my group colleagues Rachel, Qiu, Mien, Robin, Sharlly, Shanshan, Mark, James, Julia, Josh and Sam, and our visitors Elina and Marçal, for their company, help and chats in the corridors during all these years. I am immensely grateful to Les and Becky for their technical support. This thesis would have remained a dream had it not been for you!

Thanks to my office mates throughout these years: Carl, Amir, Dongming, Miller, Marco, Laura, Azael, Ann and Andrew. You were great company and offered unmeasurable support for technical and non-technical issues!

I would like to thank Prof. Andre Nonat and his entire research group at the University of Bourgogne in Dijon. I especially owe my gratitude to Gilles and Jeremy. My 4 months in Dijon were very enjoyable thanks to you all. I am deeply grateful to Andre, for having taught me how to focus on the problems of today and not to worry about tomorrow, for his constant good mood, and for his help in the lab when the lime solutions went out of control.

I cannot find words to express my gratitude to Prof. Jorgen Skibsted and his entire research group at the University of Aarhus. I am indebted to Jorgen for his dedication, his patience and the priority given to my experiments during my visits. Thanks to Anne-Birgitte, Nicklas, Wolfgang, Erika, Zhuo-Dai, Kasper, Nishant and Zhenguo. You were really like a family to me!

It was a pleasure to work with the entire LMC group at EPFL, especially with Arnaud, John, Amelie, Berta, Mathieu and Emmanuelle. You were enormously helpful!

I would like to acknowledge Dr. Barbara Lothenbach and Dr. Emilie L'Hopital for making me a part of the C-A-S-H family!

I owe my deepest gratitude to Emiliano Fratini at CSGI, for all the hours spent next to a neutron source keeping his sense of humour and the transfer of knowledge about SANS applied to cements.

It was a pleasure to work with Dr. Daniela Merz and Prof. Krassimir Garbev at KIT. I would like to thank both of them for all their help regarding the TG-FTIR experiments and valuable discussions.

Thanks to Mike and John at LEMAS for all their technical support with TEM!

I would like to express my greatest gratitude to my TRANSCEND colleagues Arnaud, Agata, Monika, Merlin, Noemi, Vadim, Serge-Henri, Mohamed, Wu-Min, Saeed, Mahsa, Luis, Zhidong, Xiaomeng and Pierre-Vincent for all the shared moments during meetings, courses, discussions, road and skiing trips. You were exceptional company and a great source of support and fun! Thanks Noemi for all the shared hotel evenings, Merlin and Luis for listening and offering great moral support, and Arnaud for sharing music, road hours and being a sweet host. I truly thank all Nanocem members who enriched our meetings and courses. Among them, Dr. Jeff Chen deserves special thanks for providing material and very useful documents.

I am grateful to Nabil, Ria, Doreen, Rupert, Andrea and Cornelia. You all know there is a unique reason to thank you, and it is called Music.

Thanks to my friends that I left back in Spain: Cristina, Rocio, Bea, Ariana, Ana and Jose. The power of your words and the magnitude of your support were strengthened by the distance!

I wish to thank Andrea, Ignacio, David and Raman, my friends in Leeds, for all the stress-relief lunches, coffee breaks and games evenings. You were a motivation to keep going. Special thanks to David for helping in the last hours before the thesis submission!

And finally I would like to acknowledge the European Commission since the research leading to these results has received funding from the European Union Seventh Framework Programme (FP7 / 2007-2013) under *grant agreement* 264448.

I want to dedicate this thesis to my parents *Antonia and Pedro*, and my brother *Javier*.

This thesis is also dedicated to the memory of my grandfather *Anastasio*, who used to laugh at my usual greeting on the phone: What's up grandpa?

Abstract

The aim of this study was to determine if there is a relationship between the morphology of C-S-H (calcium silicate hydrates) with its chemical composition and structure or the morphological change is kinetically driven. The morphology of C-S-H, the binding phase of cement, has been an open subject of debate for decades. C-S-H morphology affects the shape of the capillary pores, as the capillary porosity is defined by the outer product C-S-H. Thus, the morphology of C-S-H partially determines transport properties and the durability of cementitious materials. This underlines the importance of understanding it to model the degradation and predict the service life of such materials. The Op C-S-H (outer product) exhibits different morphologies from fibrillar to sheet-like foils in different cementitious systems. It is not clear whether the change in morphology is determined by the structure and chemical composition or it is kinetically driven [1]. Finding suitable synthetic analogues of materials formed under normal conditions remains a challenge. However, synthetic analogues are ideal systems for the aim of this project. Their fabrication is controlled under synthesis parameters which can affect the morphology and can be tailored. Therefore synthetic C-S-H, with Ca/Si ratios between 0.75 to ~1.7 (covering part of the range that commercial cements exhibit) were proposed as model systems to be compared with real cementitious systems in this study. TEM and NMR were the main techniques to analyze the morphology, chemical composition and structure of the samples. Other techniques such as STA, XRD, XRF, TG-FTIR-DSC and SEM were used to get complementary information.

The results obtained indicate that C-S-H morphology of samples fabricated via silica-lime reactions with bulk Ca/Si ratios from 0.75 to 1.5, and C-A-S-H samples with Ca/Si=1 and Al/Si=0-0.05 is foil-like. The morphology of C-S-H in samples hydrated via the controlled hydration of C_3S at fixed lime concentrations was found to be dependent on the lime concentration in solution; being foil-like for lime concentrations from 12 to 20mmol/l (Ca/Si ratios from ~1.25 to ~1.4), a mixture of foils and fibrils for 22mmol/l (Ca/Si ratio of ~1.58) and fibrillar for concentrations ≥ 25 mmol/l (Ca/Si ratios of ~1.60-1.65). For each lime concentration, the morphology was found to be independent of the growth rate, being the same for the acceleration period (fast growth) and the deceleration period (slow growth). This implies the morphology is composition dependent and not kinetically driven. However, a link between the silicate structure of C-S-H and its morphology was also found. Samples fabricated via the controlled hydration of C_3S , with an ultrasound gun, at lime concentrations of 27-29mmol/l, were found to have higher percentages of Q^2 silicate species and more flattened surfaces, than samples fabricated at the same lime concentrations but with the use of C-S-H seeds (Xseed). This agrees with the fact that flattened surfaces could accommodate longer silicate chains while surfaces with more features would accommodate more Q^1 end-chains.

Table of contents

1	Introduction	1
1.1	Project framework.....	1
1.2	Project objectives.....	3
1.2.1	Objectives.....	3
2	Literature review	4
2.1	Portland cement.....	4
2.1.1	Tricalcium silicate.....	4
2.1.2	Dicalcium silicate.....	5
2.1.3	Tricalcium aluminate.....	5
2.1.4	Calcium aluminoferrite.....	5
2.1.5	Hydration reactions and hydration products.....	6
2.1.6	Microstructure development during the hydration of Portland cement.....	8
2.2	Most common supplementary cementitious materials.....	10
2.3	Minerals and synthetic phases related to C-S-H.....	10
2.3.1	Tobermorite 14Å.....	11
2.3.2	Jennite.....	12
2.3.3	C-S-H (I).....	13
2.3.4	C-S-H (II).....	13
2.3.5	Wollastonite.....	14
2.4	Atomic and molecular models for C-S-H.....	15
2.4.1	Taylor model.....	16
2.4.2	Richardson and Groves' model.....	16
2.4.3	Richardson's model structures for C-(A)-S-H(I).....	19
2.4.4	Pellenq's molecular model.....	23
2.5	Mesostructure models for C-S-H.....	24
2.5.1	Powers (layer model).....	24
2.5.2	Feldman and Sereda (layer model).....	24
2.5.3	Jennings (colloid model).....	25
2.5.4	Growth model of sheets in 3D confinements.....	27
2.6	Morphology, chemical composition and structure of C-S-H.....	28
2.7	The use of SANS to study C-S-H.....	31
2.8	Synthesis routes to produce C-S-H.....	34
2.8.1	A solution method.....	34
2.8.2	Hydrothermal treatment.....	34

2.8.3	Mechanochemical method	35
2.8.4	Double decomposition	36
2.8.5	Leaching of C ₃ S paste and recalcification	36
2.8.6	Hydration of C ₃ S at constant lime concentration	37
2.9	Synthesis methods to produce C-A-S-H.....	40
3	Characterization techniques	41
3.1	STA.....	41
3.2	XRD.....	43
3.3	XRF	44
3.4	TEM and EDX.....	44
3.5	SEM.....	46
3.6	NMR.....	47
4	Experimental details	51
4.1	Sample description	51
4.2	Fresh mechanochemically synthesized C-S-H: Synthesis details.....	52
4.2.1	Test samples.....	52
4.2.2	Optimized synthesis route for the mechanochemical samples.....	56
4.3	Synthesis details for the CaO-SiO ₂ C-S-H series	57
4.4	Hydration of C ₃ S at constant lime concentration: Method and device.....	57
4.4.1	Hydration of C ₃ S at constant lime concentration: Kinetics C-S-H series	60
4.4.2	Hydration of C ₃ S at constant lime concentration: Ultrasound C-S-H series.....	61
4.4.3	Hydration of C ₃ S at constant lime concentration: Xseed C-S-H series	62
4.5	Synthesis details for the C-A-S-H series	62
4.6	STA.....	63
4.7	TA-FTIR.....	63
4.8	XRD.....	64
4.9	TEM.....	64
4.9.1	Wollastonite reference sample details for TEM-EDX	65
4.10	XRF	67
4.11	SEM.....	67
4.12	²⁹ Si DP MAS NMR	68
5	Results and discussion	70
5.1	C ₃ S paste.....	70
5.2	7-year old mechanochemically synthesized C-S-H.....	76
5.3	Fresh mechanochemically synthesized C-S-H	80

5.4	CaO-SiO ₂ C-S-H series	95
5.5	Hydration of C ₃ S at constant lime concentration: Kinetics C-S-H series	107
5.6	Hydration of C ₃ S at constant lime concentration: Ultrasound C-S-H series.....	126
5.7	Hydration of C ₃ S at constant lime concentration: Xseed C-S-H series	135
5.8	Comparison of morphology and chemical structure of C-S-H samples of the ultrasound and Xseed series	144
5.9	Comparison of MCL vs. Ca/Si and Ca/Si vs. [CaO] with reported data.....	145
5.10	C-A-S-H series.....	148
6	Conclusions and further work	154
	References.....	158

List of tables

Table 3.1. NMR shifts for silicon in cement pastes [3].	48
Table 4.1. Composition and properties of the nanosilica (Elkem) used for the mechanochemical synthesis of C-S-H.	53
Table 4.2. Experimental details of the test C-S-H samples prepared by the mechanochemical method.	53
Table 4.3. Synthesis details for the C-S-H samples fabricated by C ₃ S hydration at fixed [CaO] for the kinetics series. The hydration times and added volumes of water are indicated for both the short series (hydration stopped at the acceleration period) and the long series (hydration stopped at the deceleration period). All the samples were synthesized at 25°C and at w/s=50. 4g of C ₃ S were used for lime concentrations up to 20mmol/l and 3g of C ₃ S for higher lime concentrations.	61
Table 4.4. Synthesis details of the C-S-H samples fabricated adding the ultrasound gun to the reactor in which the lime concentration was fixed. The w/s was 50 and the temperature was 25°C. 4g of C ₃ S were used for each sample.	61
Table 4.5. Synthesis details of the C-S-H samples fabricated at constant lime concentration adding Xseed to the solution. The initial w/s was 100 and the temperature was 20°C.	62
Table 5.1. Comparison between mean Ca/Si ratios of synthetic C-S-H samples obtained by three different methods: EDX from TEM (with the standard deviations), XPS [132] and TG [122].	77
Table 5.2. Percentages of the silicate species and MCL for the mechanochemical series. The results have been calculated from the deconvolution of the NMR spectra shown in Figure 5.11.	81
Table 5.3. Temperature transformation of C-S-H into β-wollastonite and β-wollastonite into α-wollastonite of the mechanochemical series of C-S-H samples.	85
Table 5.4. Quantification of the CO ₂ and H ₂ O content and total loss mass percentage of the mechanochemical C-S-H series obtained from FTIR, total loss percentage obtained from TG, and real Ca/Si recalculated taking into account the traces of carbonates and portlandite.	87
Table 5.5. Ca/Si of the mechanochemical samples obtained by TEM-EDX (with standard deviations), XRF and TG.	89
Table 5.6. Calculated values for the parameters of the T/J view point of Richardson and Groves' model for the mechanochemical C-S-H samples.	93
Table 5.7. Basal spacing in Å for the C-S-H mechanochemical samples and the CaO-SiO ₂ C-S-H samples.	96
Table 5.8. Percentages of the silicate species and MCL for the C-S-H samples fabricated in Dijon by the silica-lime reaction. The results have been calculated from the deconvolution of the NMR spectra shown in Figure 5.25. (The error is not given for the first sample because it results bigger than the measurement, given the atypical low percentage of Q ¹).	99

Table 5.9. Mean Ca/Si values (with the standard deviations) obtained by TEM-EDX for the C-S-H samples in the CaO-SiO ₂ series.	99
Table 5.10. Calculated values for the parameters of the T/J view point of Richardson and Groves' model for the mechanochemical C-S-H samples.	105
Table 5.11. Percentages of the silicate species, MCL and DR (degree of reaction) for the C-S-H samples fabricated via the controlled hydration of C ₃ S in the short series (Hydration time I). The results have been calculated from the deconvolution of the NMR spectra shown in Figure 5.36. ...	111
Table 5.12. Percentages of the silicate species, MCL and DR, for the C-S-H samples fabricated via the controlled hydration of C ₃ S in the long series (Hydration time II). The results have been calculated from the deconvolution of the NMR spectra shown in Figure 5.37.	111
Table 5.13. Summary of the calculated Ca/Si (with the standard deviations) from TEM-EDX for the C-S-H present in the C ₃ S samples hydrated at fixed lime concentrations (left column) in the long series (Hydration time II). The number of EDX point analyses used to calculate the average Ca/Si is indicated in the right column.	117
Table 5.14. Degree of reaction of the C-S-H samples synthesized by the controlled hydration of C ₃ S at fixed lime concentrations indicated in the left column given by the results in the left graph of Figure 5.43, marked with * and the right graph in Figure 5.43, marked with **. The degree of reaction given by ²⁹ Si NMR is also listed in the last column for comparison.	118
Table 5.15. Calculated values for the parameters of the T/J view point of Richardson and Groves' model for the C-S-H samples fabricated via the controlled hydration of C ₃ S at Hydration times II.	124
Table 5.16. Percentages of the silicate species, mean silicate chain length and degree of reaction of the C-S-H samples prepared by controlled hydration of C ₃ S with the use of an ultrasound gun. The results are obtained from the deconvolutions of the ²⁹ Si NMR spectra shown in Figure 5.53.	127
Table 5.17. Mean Ca/Si values (with the standard deviations) of C-S-H fabricated via the controlled hydration of C ₃ S with the use of an ultrasound gun.	130
Table 5.18. Calculated values for the parameters of the T/J view point of Richardson and Groves' model for the C-S-H samples fabricated via the controlled hydration of C ₃ S with the use of an ultrasound gun.	133
Table 5.19. Percentage of the silicate connectivities calculated from the deconvolutions in Figure 5.60, mean silicate chain length and the degree of reaction of the C-S-H samples synthesized via the controlled hydration of C ₃ S with the use of Xseed.	137
Table 5.20. Mean Ca/Si values (with standard deviations) of C-S-H fabricated via the controlled hydration of C ₃ S with the use of Xseed.	139
Table 5.21. Calculated values for the parameters of the T/J view point of Richardson and Groves' model for the C-S-H samples fabricated via the controlled hydration of C ₃ S with the use of Xseed.	142

Table 5.22. Fraction of vacant bridging tetrahedra $f_{v_{BT}}$, fraction of vacant tetrahedral sites v , and the corresponding MCL and Ca/Si ratios for minimum ($i=0$), intermediate ($i=1$) and maximum ($i=2$) degrees of protonation in a tobermorite-like chain..... 146

Table 5.23. Al/Si, Ca/Si and Ca/(Si+Al) ratios from TEM-EDX of the series of C-A-S-H samples 148

Table 5.24. Calculated values for the parameters of the T/J view point of Richardson and Groves' model for the C-A-S-H samples. 152

List of figures

Figure 1.1. Schematic of the relations between the projects in TRANSCEND collaboration indicating the topic, category, and type of host. The corresponding project to this PhD thesis is marked with a star (LB and MD stand for Lattice Boltzmann and Molecular Dynamics).	2
Figure 2.1. Rate of heat evolution for the hydration of Portland cement at 20°C [3].	8
Figure 2.2. Microstructural development for a cement grain [22].	9
Figure 2.3. Tobermorite structure along [010] with silicate tetrahedra in dark grey, Ca polyhedra in light grey and W4 sites as dark dots (left). Atomic structure in the interlayer space along [001] with sites Ca2 octahedra in dark grey, bridging silicate tetrahedra from the chains above and below the interlayer space in light grey and water sites (W4) as dark dots (right) [25].	12
Figure 2.4. Crystal structure of jennite along [010] (left) and [100] (right) showing some of the Ca and Si sites [26].	13
Figure 2.5. Structure of wollastonite 1T a), and parawollastonite 2M b) along the c-axis. Different wollastonite polytypes depending on the stacking sequence of (100) slabs [30]. The unit cell is marked with thicker lines c). Stacking sequences of a two layer pseudowollastonite d) and a four layer pseudowollastonite e). (Figures taken from ref. [29]).	15
Figure 2.6. Al/Ca atom ratio vs. Si/Ca atom ratio of TEM points in Op C-S-H in a hardened white PC/20% metakaolin blend (●) described by the T/CH view point, and a hydrated synthetic slag glass (×) described by the T/J view point, both activated in 5M KOH solution. Taken from ref. [1].	18
Figure 2.7. Ca/Si ratio frequency histogram of TEM analyses of C-S-H in a hardened PC paste hydrated for 2 years vs. the reciprocal mean chain length. Modified from ref.[1]. The relations of Ca/Si ratio and reciprocal mean chain length for tobermorite (T) and jennite (J), with different levels of protonation in Richardson and Groves' model, are indicated on the right. The C-S-H in this case is based on jennite dimers and pentamers.	18
Figure 2.8. Compilation of literature data of layer spacing vs. Ca/Si ratio of C-S-H taken from ref. [36], with the middle trend line representing the model structures for C-(A)-S-H.	20
Figure 2.9. MCL (mean chain length) vs. Ca/Si (left plot); data are from ref. [38, 39, 46-49], $(Ca/Si)_{max}$ vs. experimental Ca/Si (middle plot); data are from ref. [38, 39, 46-49] and SOF_{BT} (site occupancy factor for bridging tetrahedra) vs. Ca/Si (right plot); data are from ref. [38, 39, 46-51]. The dotted lines are defined by Eq. 2.14 and Eq. 2.15 (left and middle) and Eq. 2.16 (right). The bold symbols (right) represent the model structures for C-(A)-S-H. The dashed lines are equivalent to the tobermorite lines in Figure 2.7 with $w/n=0, 1$ and 2 from left to right in the middle and right plots. The dashed line in the left plot is the one for $i=0$. The three graphs are taken from ref. [36].	22
Figure 2.10. Molecular model of C-S-H. The blue and white spheres represent water molecules. The green and grey spheres represent interlayer and intra-layer calcium ions and the yellow and red bars represent silicon and oxygen in silicate tetrahedra. Taken from ref. [52].	23
Figure 2.11. Powers model of C-S-H with interconnected fibrous particles. C: Capillary pore [55].	24

Figure 2.12. Representation of Feldman and Sereda model for C-S-H. A: Intercrystallite bond, B: Tobermorite sheet, C: Entrance to a gel pore, X: Interlayer water, O: Physically adsorbed water [3].	25
Figure 2.13. Schematic of Jennings colloidal model with LD C-S-H as circles and HD C-S-H as rectangles with the variation of the surface area measured by N ₂ for different configurations [57].	26
Figure 2.14. Schematic of the assembly of the globules in CM-II model showing small and large gel pores (SGP and LGP) (left). Enlargement of one globule in a saturated state with a monolayer of water on the surface and water filling the interlayer and interglobule pores at 11% RH (right) [58].	26
Figure 2.15. Different cross-sections of the structures generated using a sheet growth algorithm. The first row represents the starting growth at different configurations and the second row represents the final structures for the same configurations. The different configurations correspond to $p_p/p_i=10^4$ (a and b), $p_p/p_i=1$ c) and d), $p_p/p_i=10^{-4}$ e) and f) and $p_p/p_i=10^3$ with a tilting angle of 11° and a probability for tilting of 0.2.....	27
Figure 2.16. a) TEM micrograph showing fibrillar Op C-S-H in a 70% white PC-30% class F fly ash activated in water [65]. b) TEM micrograph showing foil-like Op C-S-H in a 10% OPC-90% GGBS blend [66]. c) TEM micrograph showing foil-like and fibrillar Op C-S-H in the same blend as a) [65].	29
Figure 2.17. Surface area and heat evolved with hydration time for an OPC paste hydrated at 30°C and w/s=0.4. Taken from ref.[71].	32
Figure 2.18. Diagram of the calcium silicate hydrate phases stable at hydrothermal conditions. The x axis represents Ca/Si and the y axis temperature. C-S-H (G) and C-S-H (F) stand for Gyrolite an Faujasite gel respectively. Pt, Rh, Af, 11T, H and X stand for Portlandite, Reinhardbraunsite, Afwillite, 11Å tobermorite, Hillebrandite and Xonotlite. Taken from ref. [89].	35
Figure 2.19. Relationship between Ca/Si and weight loss after leaching of a C ₃ S paste in NH ₄ NO ₃ [18].	36
Figure 2.20. Ca/Si ratio of C-S-H prepared by the full hydration of C ₃ S at constant lime concentration [49].	38
Figure 2.21. Typical metastable equilibrium curve for Ca/Si ratios of C-S-H vs. the lime concentration in solution. Taken from ref. [4].	38
Figure 2.22. Structural units used by Haas to build solubility equilibria of C-S-H. Taken from ref. [93].	39
Figure 2.23. Simulation of the stoichiometric evolution of C-S-H with the lime concentration in solution at equilibrium built with the three structural units in Figure 2.22. Taken from ref. [94].	39
Figure 3.1. Typical TG curve for a cementitious material (Derivative shown in blue) [98].	42
Figure 3.2. Schematic representation of Bragg's law in real space.	43

Figure 3.3. Schematic representation of the emission of characteristic X-rays due to e-beam excitation of an atom [103].	46
Figure 4.1. STA results of the test C-S-H samples fabricated mechanochemically listed in Table 4.2.	55
Figure 4.2. ²⁹ Si MAS NMR results of test samples 3 and 4 (left), showing Q ¹ and Q ² intensity coming from C-S-H and Q ⁴ intensity coming from unreacted silica. TEM micrograph of sample 4 (right) showing a C-S-H particle (top) and an unreacted silica particle surrounded by C-S-H (bottom).	56
Figure 4.3. Drying set up used for the mechanochemical C-S-H samples showing the entries and exits for N ₂ and cooling water for the condenser.	57
Figure 4.4. Device used to synthesize C-S-H via the controlled hydration of C ₃ S implemented by A. Nonat.	58
Figure 4.5. Graph showing the controlled hydration of 3g of C ₃ S at ~ [CaO]=22mmol/l (9.9 mS/cm at 25°C). The controlled conductivity is shown in black. It can be noticed that from a mean conductivity value, the variations were not higher than ± 0.1 mS/cm. The hydration curve expressed as the addition of water vs. time is shown in blue.	59
Figure 4.6. XRD pattern of the wollastonite sample used as TEM-EDX reference together with a reference pattern of pseudowollastonite taken from ref.[129].	66
Figure 4.7. TEM micrographs of the wollastonite reference sample dispersed in ethanol (left) and acetone (right).	66
Figure 5.1. TG, DTG and DTA data of a 5-year old C ₃ S paste with w/s=0.5.	70
Figure 5.2. XRD pattern of a 5-year old C ₃ S paste with w/s=0.5. Peaks are labeled as P for portlandite and C for C-S-H.	71
Figure 5.3. Upper image: Backscattered electron image from the 5-year old C ₃ S paste with w/s=0.5. Three different phases are identified: C ₃ S (white), CH (light grey) and C-S-H (dark grey). Porosity is displayed as black, Central image: Central area of upper image at higher magnification, Lower image: Backscattered electron image from the C ₃ S paste with the white features in the center corresponding to belite traces. (All images taken by M. S. Chen).	72
Figure 5.4. Upper image: TEM micrograph showing globular dense Ip C-S-H and fibrillar Op C-S-H of a 5-year old C ₃ S paste with w/s=0.5. Central image and lower images: TEM micrographs showing fibrillar Op C-S-H in the same paste (marked with white arrows).	73
Figure 5.5. Deconvolution of the ²⁹ Si MAS NMR spectrum of a 5-year old C ₃ S paste with w/s=0.5. From top to bottom: Residue, experimental spectrum and fitted spectrum showing the individual peaks.	74
Figure 5.6. TG, DTG and DTA of C-S-H sample with target Ca/Si=0.66 (Upper graphs), and target Ca/Si=0.75 (Lower graphs).	77

Figure 5.7. TG, DTG and DTA of C-S-H sample with target Ca/Si=1 (Upper graphs), and target Ca/Si=1.5 (Lower graphs).	78
Figure 5.8. TEM micrographs showing the fine crumpled foil-like morphology of mechanochemically synthesized C-S-H with target Ca/Si=0.66 (Upper image), Ca/Si=0.75 (Central image) and Ca/Si=1 (Lower image).	79
Figure 5.9. XRD patterns of the series of mechanochemical samples fabricated with CaO and Aerosil. The Ca/Si ratios are indicated above the patterns.	80
Figure 5.10. ²⁹ Si MAS NMR spectra of the mechanochemical C-S-H samples.....	81
Figure 5.11. Deconvolutions of the ²⁹ Si MAS NMR spectra of the mechanochemical samples showing the individual frequencies (green), the simulated spectra as a sum of the individual frequencies (blue) and the experimental spectra (black).	82
Figure 5.12. Percentage of the silicate species Q ¹ , Q ² and Q ³ obtained from NMR vs. the experimental Ca/Si (TEM-EDX) in the mechanochemical C-S-H.....	83
Figure 5.13. Mean silicate chain length vs. Ca/Si (TEM-EDX) in the mechanochemical series.	84
Figure 5.14. TG results from the mechanochemical series of C-S-H samples.	84
Figure 5.15. DSC data from the mechanochemical C-S-H samples. The curves have been vertically shifted for clarity.	85
Figure 5.16. Transformation temperature of C-S-H into wollastonite from Mitsuda [87] , Bornefeld [134], Suzuki [125] and the mechanochemical samples from this study.	86
Figure 5.17. Graphs showing TG (black), DSC (green) and the FTIR traces of H ₂ O (blue) and CO ₂ (red) for the mechanochemical series of C-S-H. The FTIR traces have been normalized by sample weight. The vertical scales for the FTIR traces have been chosen arbitrary for clarity, and are not shown in the graphs. For comparison of intensities of the FTIR traces between samples, see Figure 5.18.	88
Figure 5.18. Water and CO ₂ FTIR traces of the mechanochemical samples recorded while performing TG and DSC.	89
Figure 5.19. TEM micrographs of the mechanochemically synthesized C-S-H. The Ca/Si of the sample is indicated in each micrograph.....	90
Figure 5.20. Histograms of the Ca/Si obtained with TEM-EDX of the C-S-H mechanochemical samples.	91
Figure 5.21. Ca/Si vs. reciprocal mean chain length of the mechanochemical C-S-H samples. The length of the bars is limited by the minimum and maximum Ca/Si obtained by TEM-EDX and the mean value is marked with a cross. The structural units for tobermorite and jennite with minimum (w=0), intermediate (w=1) and maximum (w=2) degree of protonation are also marked. The vertical dashed lines represent the (3n-1) structural units: dimer (2), pentamer (5), octamer (8)... ..	92

Figure 5.22. XRD patterns of the CaO-SiO ₂ C-S-H series with a reference pattern for calcite, portlandite, aragonite and vaterite.....	95
Figure 5.23. Basal spacing against Ca/Si ratio (TEM-EDX) for the C-S-H mechanochemical and the CaO-SiO ₂ C-S-H series. Data from Matsuyama and Young [42] was fitted to configure the lower trend line. Data from Richardson's model structures for C-(A)-S-H(I) [36] configure the middle trend line. Data from Grudemo [42] and Cong and Kirkpatrick [39] configure the upper trend line. Symbols marked with points or crosses belong to the same data groups as the identical unfilled symbols. They are both not used to fit the upper trend line and the crosses indicate the presence of CH.....	96
Figure 5.24. ²⁹ Si MAS NMR spectra of the CaO-SiO ₂ C-S-H samples (Dijon).	98
Figure 5.25. Deconvolutions of the ²⁹ Si MAS NMR spectra of the CaO-SiO ₂ C-S-H samples showing the individual frequencies (green), the simulated spectra as a sum of the individual frequencies (blue) and the experimental spectra (black).....	100
Figure 5.26. Percentage of the silicate species Q ¹ , Q ² and Q ³ obtained from NMR vs. the Ca/Si (TEM-EDX) in the CaO-SiO ₂ C-S-H series.	101
Figure 5.27. Mean silicate chain length vs. Ca/Si (TEM-EDX) in the CaO-SiO ₂ C-S-H series.....	101
Figure 5.28. TEM micrographs of the CaO-SiO ₂ C-S-H series. The Ca/Si of the sample is indicated in each micrograph.....	102
Figure 5.29. Histograms of the Ca/Si obtained with TEM-EDX of the C-S-H CaO-SiO ₂ samples.	103
Figure 5.30. Ca/Si vs. reciprocal mean chain length of the CaO-SiO ₂ C-S-H samples. The length of the bars is limited by the minimum and maximum Ca/Si obtained by TEM-EDX and the mean value is marked with a cross. The structural units for tobermorite and jennite with minimum (w=0), intermediate (w=1) and maximum (w=2) degree of protonation are also marked. The vertical dashed lines represent the (3n-1) structural units: dimer (2), pentamer (5), octamer (8).....	104
Figure 5.31. Hydration curves (Added water vs. hydration time) of C ₃ S at fixed lime concentration, from [CaO]=12mmol/l (burgundy curve) to [CaO]=27mmol/l (pink curve), corresponding to hydration times II in Table 4.3.....	107
Figure 5.32. XRD patterns of the C ₃ S hydrated samples at fixed lime concentrations of 12, 15, 17 and 20mmol/l with the hydration stopped at the acceleration period (hydration time I in Table 4.3). The pattern of the anhydrous C ₃ S is shown for comparison, as well as a reference for CH.....	108
Figure 5.33. XRD patterns of the C ₃ S hydrated samples at fixed lime concentrations of 12, 15, 17 and 20mmol/l with the hydration stopped at the deceleration period (hydration time II in Table 4.3). The pattern of the anhydrous C ₃ S is shown for comparison, as well as a reference for CH.....	108
Figure 5.34. XRD patterns of the C ₃ S hydrated samples at fixed lime concentrations of 22, 25 and 27 mmol/l with the hydration stopped at the acceleration period (hydration time I in Table 4.3). The pattern of the anhydrous C ₃ S is shown for comparison, as well as a reference for CH.....	109

- Figure 5.35.** XRD patterns of the C_3S hydrated samples at fixed lime concentrations of 22, 25 and 27mmol/l with the hydration stopped at the deceleration period (hydration time II in Table 4.3). The pattern of the anhydrous C_3S is shown for comparison, as well as a reference for CH. The enlarged area in the figure shows the increase in intensity at $\sim 2\theta=32^\circ$ due to the formation of C-S-H in the pattern for $[CaO]=27\text{mmol/l}$ compared to the pattern of anhydrous C_3S 109
- Figure 5.36.** ^{29}Si NMR spectra of the C_3S hydrated samples that belong to the short series (Hydration time I). The fixed lime concentration in solution is indicated over each spectrum. 110
- Figure 5.37.** ^{29}Si NMR spectra of the C_3S hydrated samples that belong to the long series (Hydration time II). The fixed lime concentration in solution is indicated over each spectrum. 110
- Figure 5.38.** ^{29}Si NMR experimental spectra (black), simulated spectra (blue), and individual frequencies (green), of the C_3S samples hydrated for hydration times I and II at fixed lime concentrations of 12, 15, 17 and 20mmol/l. 112
- Figure 5.39.** ^{29}Si NMR experimental spectra (black), simulated spectra (blue), and individual frequencies (green), of the C_3S samples hydrated for hydration times I and II at fixed lime concentrations of 22, 25 and 27mmol/l. 113
- Figure 5.40.** TEM micrographs of C_3S samples hydrated at $[CaO]=12\text{mmol/l}$ for 170 min (left) and 240 min (right), showing foil-like C-S-H. 114
- Figure 5.41.** TEM micrographs of C_3S samples hydrated at $[CaO]=15\text{mmol/l}$ for 260 min and 1161 min (upper left and right respectively), at $[CaO]=17\text{mmol/l}$ hydrated for 255 min and 1011 min (middle left and right respectively), and $[CaO]=20\text{mmol/l}$ hydrated for 375 min and 1398 min (lower left and right respectively) showing foil-like C-S-H. 115
- Figure 5.42.** TEM micrographs of C_3S samples hydrated at $[CaO]=22\text{mmol/l}$ for 401 min and 1048 min (upper left and right respectively), showing a mixture of foil-like and fibrillar C-S-H, at $[CaO]=25\text{mmol/l}$ for 492 min and 835 min (middle left and right respectively) and $[CaO]=27\text{mmol/l}$ for 600 min and 840 min (lower left and right respectively), showing fibrillar C-S-H. 116
- Figure 5.43.** Degree of hydration (%) vs. hydration time for the C-S-H samples fabricated via the controlled hydration of C_3S at fixed lime concentration up to the deceleration period (Hydration times II in Table 4.3). The degree of hydration was calculated using Eq. 4.5 taking the experimental Ca/Si ratios from TEM-EDX in Table 5.13 (Left) and expected Ca/Si ratios at equilibrium in Table 5.14 (Right). 118
- Figure 5.44.** SEM micrographs of the sample hydrated at $[CaO]=12\text{mmol/l}$ for 240 min (Hydration time II). The surface of the samples appears to be crumpled foil-like presenting hollow features (Images taken by Emmanuel Boehm-Courjault at EPFL). 119
- Figure 5.45.** SEM micrographs of the samples hydrated at $[CaO]=27\text{mmol/l}$ for 600 min (Upper micrographs) and 840 min (lower micrographs), showing fibrillar C-S-H. The development of the fibrils with hydration time is appreciated, since the lower micrographs show longer fibrils (Images taken by Emmanuelle Boehm-Courjault at EPFL). 119
- Figure 5.46.** SEM and TEM micrographs of the C_3S samples hydrated at $[CaO]=12\text{mmol/l}$ for 240 min (Hydration time II) showing foil-like C-S-H (upper images) and at $[CaO]=27\text{mmol/l}$ for 600 min (Hydration time II) showing fibrillar C-S-H (lower images). 120

Figure 5.47. Histograms of the Ca/Si obtained by TEM-EDX for the samples hydrated at [CaO]=12 and 15mmol/l at Hydration times II.	120
Figure 5.48. Histograms of the Ca/Si obtained with TEM-EDX of the samples hydrated at [CaO]=17, 20, 22, 25 and 27 mmol/l for Hydration times II.	121
Figure 5.49. Ca/Si (obtained by TEM-EDX) vs. reciprocal mean chain length (obtained by NMR) of the C-S-H series fabricated via the controlled hydration of C ₃ S at Hydration times II. The length of the bars is limited by the minimum and maximum Ca/Si and the mean value is marked with a cross. The values indicated with squares are those given by Haas model [93] (Ca/Si ** in Table 5.14). The structural units for tobermorite and jennite with minimum (w=0), intermediate (w=1) and maximum (w=2) degree of protonation are also marked. The pentamer is marked over the top axis. The dimer is out of the scale of the plot and would be situated at reciprocal mean chain length 0.5.	122
Figure 5.50. Selected area electron diffraction patterns of the C-S-H samples hydrated at: a) [CaO]=15mmol/l, c) and d) [CaO]=25mmol/l. The halos in the patterns shown in a) and b) are consistent with C-S-H, while the reflections seen in pattern c) are characteristic of microcrystalline CH.	123
Figure 5.51. XRD patterns of C-S-H samples fabricated by the controlled hydration of C ₃ S at lime concentrations of 27, 28 and 29mmol/l with the use of an ultrasound gun. The pattern of anhydrous C ₃ S and a reference for portlandite are also included.	126
Figure 5.52. ²⁹ Si MAS NMR spectra of the C-S-H samples synthesized via the controlled hydration of C ₃ S with the use of an ultrasound gun at fixed lime concentrations of 27, 28 and 29mmol/l.	127
Figure 5.53. Deconvolutions of the ²⁹ Si MAS NMR spectra of the C-S-H samples fabricated via the controlled hydration of C ₃ S with an ultrasound gun at fixed lime concentrations of 27mmol/l (upper left), 28mmol/l (upper right) and 29mmol/l (low). The individual frequencies are shown in green, the simulated spectra in blue and the experimental spectra in black.	128
Figure 5.54. TEM micrographs of the C-S-H samples synthesized via the controlled hydration of C ₃ S with the use of an ultrasound gun at fixed lime concentrations of 27mmol/l (Upper images with a SAED pattern), 28mmol/l (middle images) and 29mmol/l (lower images). The enlargement in the upper right corner shows a fibrillar area of the sample hydrated at 27mmol/l.	129
Figure 5.55. SEM micrographs of the C-S-H sample fabricated via the controlled hydration of C ₃ S with an ultrasound gun at lime concentration of 27mmol/l. The left image shows a considerably flattened surface, however, an area with sticky features is shown on the right image (Micrographs taken by Emmanuelle Boehm-Courjault at EPFL).	130
Figure 5.56. Histograms of the Ca/Si obtained with TEM-EDX of the samples hydrated at [CaO]=27, 28 and 29mmol/l with the use of an ultrasound gun.	131
Figure 5.57. Ca/Si (obtained by TEM-EDX) vs. reciprocal mean chain length (obtained by NMR) of the C-S-H series fabricated via the controlled hydration of C ₃ S with the use of an ultrasound gun. The length of the bars is limited by the minimum and maximum Ca/Si and the mean value is marked with a cross. The structural units for tobermorite and jennite with minimum (w=0), intermediate (w=1) and maximum (w=2) degree of protonation are also marked. The vertical dashed lines represent the (3n-1) structural units: dimer (2), pentamer (5), octamer (8).	132

Figure 5.58. XRD patterns of C-S-H samples fabricated by the controlled hydration of C_3S at lime concentrations of 27, 28 and 29mmol/l with the use of C-S-H platelets (X-seed). The pattern of anhydrous C_3S and a reference for portlandite are also included. 135

Figure 5.59. ^{29}Si MAS NMR spectra of the C-S-H samples synthesized via the controlled hydration of C_3S with the use of C-S-H platelets (Xseed) at fixed lime concentrations of 27, 28 and 29mmol/l. 136

Figure 5.60. Deconvolutions of the ^{29}Si MAS NMR spectra of the C-S-H samples fabricated via the controlled hydration of C_3S with C-S-H platelets (Xseed) at fixed lime concentrations of 27mmol/l (upper left), 28mmol/l (upper right) and 29mmol/l (low). The individual frequencies are shown in green, the simulated spectra in blue and the experimental spectra in black. 136

Figure 5.61. TEM micrographs of the C-S-H samples synthesized via the controlled hydration of C_3S with C-S-H platelets (Xseed) at fixed lime concentrations of 27mmol/l (Upper images with a SAED pattern), 28mmol/l (middle images) and 29mmol/l (lower images). The enlargements in the upper/lower right corners show a mixed foil-fibrillar area of the sample hydrated at $[CaO]=27mmol/l$ and a fibrillar area of the sample hydrated at $[CaO]=29mmol/l$ 138

Figure 5.62. SEM micrographs of the C-S-H sample fabricated via the controlled hydration of C_3S with Xseed at $[CaO]=27mmol/l$. The left image shows a flowery surface. Some sticky fibrillar elements are seen on the right image (Micrographs taken by Emmanuelle Boehm-Courjault at EPFL). 139

Figure 5.63. Histograms of the Ca/Si obtained with TEM-EDX of the samples hydrated at $[CaO]=27, 28$ and 29mmol/l with the use of an ultrasound gun. 140

Figure 5.64. Ca/Si (obtained by TEM-EDX) vs. reciprocal mean chain length (obtained by NMR) of the C-S-H series fabricated via the controlled hydration of C_3S with the use of Xseed. The length of the bars is limited by the minimum and maximum Ca/Si and the mean value is marked with a cross. The structural units for tobermorite and jennite with minimum ($w=0$), intermediate ($w=1$) and maximum ($w=2$) degree of protonation are also marked. The vertical dashed lines represent the $(3n-1)$ structural units: dimer (2), pentamer (5), octamer (8)... 141

Figure 5.65. Graph showing the ratio of silicate connectivities Q^2/Q^1 vs. the degree of reaction for the C-S-H samples synthesized via the controlled hydration of C_3S with the use of an ultrasound gun (circles) and Xseed (squares). 144

Figure 5.66. MCL vs. Ca/Si for all the C-S-H series of samples. Reported data is marked with black filled symbols and it is taken from ref. [39, 46, 93]. The dotted line represents the constraint for Richardson's C-(A)-S-H(I) model structures [36] and the dashed lines are equivalent to the tobermorite lines with minimum, intermediate and maximum degree of protonation from Richardson and Groves' model [1]. The inset shows the same plot with the y axis expanded to MCL=150. 145

Figure 5.67. Ca/Si ratio vs. lime concentration in solution for the kinetics, ultrasound and Xseed C-S-H series (predicted Ca/Si ratios calculated with the thermodynamic model by Haas [93] for the kinetics series, and Ca/Si ratios obtained with TEM-EDX for the ultrasound and Xseed series). Other reported data by Haas [93], Nonat and Lecoq [49] and Taylor [4] are also plotted. 147

Figure 5.68. TEM micrographs of the C-A-S-H series. The Al/Si of the sample is indicated in each micrograph. 149

Figure 5.69. Histograms of the Ca/(Si+Al) obtained with TEM-EDX of the C-A-S-H samples....150

Figure 5.70. Ca/(Si+Al) (obtained by TEM-EDX) vs. reciprocal mean chain length (taken from ref.[140]) of the C-A-S-H series. The length of the bars is limited by the minimum and maximum Ca/(Si+Al) and the mean value is marked with a cross. The structural units for tobermorite and jennite with minimum (w=0), intermediate (w=1) and maximum (w=2) degree of protonation are also marked. The vertical dashed lines represent the (3n-1) structural units: dimer (2), pentamer (5), octamer (8).....151

List of abbreviations

AFm: Monosulfoaluminate

AFt: Trisulfoaluminate

BO: Bridging oxygen

C-A-S-H: Aluminum substituted calcium silicate hydrate

CH: Calcium hydroxide or porlandite

CP NMR: Cross polarization nuclear magnetic resonance

C-S-H: Calcium silicate hydrate

DP MAS NMR: Direct pulse magic angle spinning nuclear magnetic resonance

DSC: Differential scanning calorimetry

DTA: Differential thermal analysis

EDX: Energy dispersive X-ray analysis

EXAFS: Extended X-ray absorption fine structure

FTIR: Fourier transform infrared spectroscopy

GGBFS: Ground granulated blast furnace slag

HRTEM: High resolution transmission electron microscopy

Ip C-S-H: Inner product C-S-H

MCL: Mean silicate chainlength

NBO: Non-bridging oxygen

Op C-S-H: Outer product C-S-H

PE-HD: High density polyethylene

PTFE: Polytetrafluoroethylene

RH: Relative humidity

SAED: Selected area electron diffraction

SANS: Small angle neutron scattering

SEM: Scanning electron microscopy

STA: Simultaneous thermal analysis

TEM: Transmission electron microscopy

TGA: Thermogravimetry analysis

TMS: Tetramethylsilane

w/s: water to solid ratio

XRD: X-ray diffraction

XRF: X-ray fluorescence

Cement chemistry terminology

A: Al_2O_3

C: CaO

F: Fe_2O_3

H: H_2O

S: SiO_2

1 Introduction

1.1 Project framework

Cement and concrete are materials widely used specially in the building sector today. The main reason behind the massive use of these materials is their low cost with respect to others such as steel or wood. Intrinsically, they are low energy and low CO₂ materials, however, the large volumes used, make cement production to account for ~5% of the global CO₂ emissions. A possible solution to decrease the CO₂ emissions is recycling, but this measure will be more costly than the production itself. Therefore, other measures need to be implemented [2].

CO₂ is released by two different means in the cement production process. Approximately 40% of the emissions come from the fuel and 60% come from the dissociation of limestone. The production process is highly optimized, so few improvements are to be made in terms of fuel. This leads to the conclusion that if CO₂ emissions have to be reduced, the amount of limestone has to be reduced too. The cement industry has been replacing part of the limestone with by-products of other industries (supplementary cementitious materials), changing thus the chemistry of cement. This change affects the hydration reactions, microstructure, performance and service life of the final product [2]. The use of supplementary materials needs to be supported by the understanding of its consequences, especially in terms of durability. It is essential to know how long the new materials will last to ensure that infrastructure remains operable for its design life. As most of the degradation processes of cement and concrete are related to water, water transport has to be understood if new materials are to last.

Describing the water transport in cement is the context in which this PhD project is conceived. It is part of a European research collaboration called TRANSCEND (Understanding transport for concrete which is eco-friendly, innovative and durable). It is carried out within Nanocem, a consortium of academic and industrial partners that share an interest in cementitious materials. The collaboration is based on a bottom-up approach, from understanding the water dynamics at an atomic level to a structural level. It consists of fifteen PhDs divided into 3 categories: experimental, modelling and validation. A brief introduction to the topics of all the projects, relations between them, categories and hosts, is illustrated in Figure 1.1. These 3 categories are intimately related, since the data that experiments provide will be used to build models that have to be further validated. In particular, this project deals with the morphology of C-S-H, which is of interest to simulate the water dynamics within its layer structure in a nm scale. C-S-H also defines the capillary porosity; an interconnected pore network that affects properties such as strength, permeability to water and the rate at which ions and gases diffuse in it. Besides, C-S-H

represents a high volume percentage of a final cement paste (~50-65%), thus the understanding of its structure, morphology and properties is crucial to gain some insight into the overall behavior of cement.

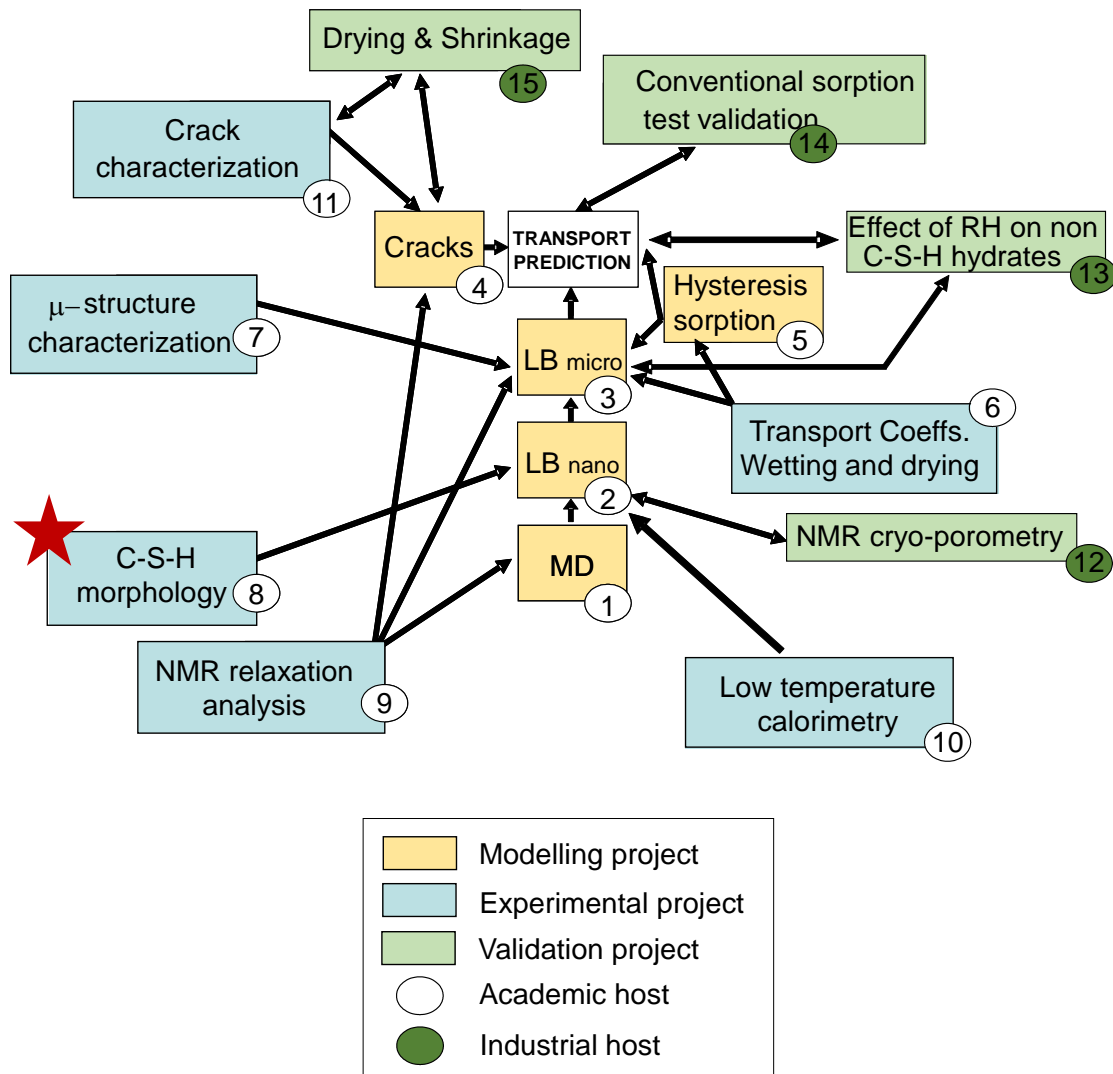


Figure 1.1. Schematic of the relations between the projects in TRANSCEND collaboration indicating the topic, category, and type of host. The corresponding project to this PhD thesis is marked with a star (LB and MD stand for Lattice Boltzmann and Molecular Dynamics).

1.2 Project objectives

1.2.1 Objectives

- Synthesize C-S-H with a wide range of chemical compositions to cover most of the Ca/Si range of C-S-H in commercial cements ($0.66 < \text{Ca/Si} < 2$).
- Determine the morphology of C-S-H with a wide range of chemical compositions and forming at different rates for a fixed composition.
- Establish a link between the chemical composition, structure and morphology in C-S-H or state whether the change in morphology is only kinetically driven.
- Determine the synthesis route that approximates better the synthesized material to real cementitious systems.

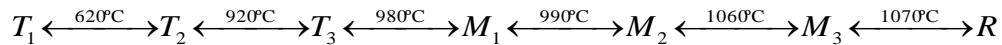
2 Literature review

2.1 Portland cement

Cement is a material that becomes rigid and develops compressive strength, properties known as setting and hardening, when hydration reactions with water take place [3]. It is produced by heating a mixture of limestone (85% CaCO_3) and SiO_2 with traces of Al_2O_3 and Fe_2O_3 up to 1400°C [2]. In the heating process CaCO_3 decarbonates to form CaO , and then, at higher temperatures undergoes clinkering reactions to form principally 4 hydraulic phases. The typical elemental composition of the final powder, which is called clinker, is of ~ 67% CaO (C), 22% SiO_2 (S), 5% Al_2O_3 (A), 3% Fe_2O_3 (F) and 3% of other components. A small percentage of calcium sulfate (usually gypsum) is added to the clinker and the mixture is ground to form cement. Cement contains 4 main hydraulic phases: C_3S or alite (Ca_3SiO_5), C_2S or belite (Ca_2SiO_4), C_3A ($\text{Ca}_3\text{Al}_2\text{O}_6$) and C_4AF ($\text{Ca}_2(\text{Al}, \text{Fe})\text{O}_5$) [4].

2.1.1 Tricalcium silicate

C_3S presents the following phase transitions at the stated temperatures:

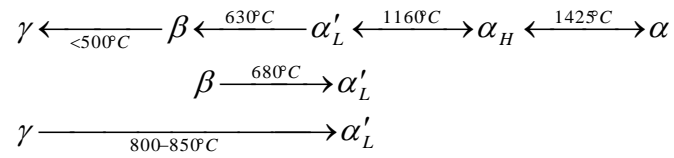


where T, M and R are triclinic, monoclinic and rhombohedral phases respectively. The existence of all the phases except M_3 , was evidenced by DTA and XRD [5]. M_3 was discovered by heating crystals while changes in twinning were observed by microscopy [6]. The different phases are equally hydraulic, which means that they develop similar strength when stored under water after setting.

Tricalcium silicate is stable within the temperature range of $1250\text{-}1800^\circ\text{C}$. The high temperature forms can be stabilized at room temperature by adding impurities (foreign ions) from the raw materials used in cement manufacture, and it is this impure C_3S which is known as alite. Alite is normally monoclinic, being M_1 or M_3 . The most common foreign ions that alite contains in commercial clinkers are Mg^{2+} , Al^{3+} , Fe^{3+} , K^+ , Na^+ and SO_3 [3].

2.1.2 Dicalcium silicate

C_2S undergoes the following phase transitions:



The different phases are not equally hydraulic, and γ in particular is much less hydraulic than β [7]. The phase found in clinkers is normally βC_2S , which is stabilized at room temperature with substituent ions and is then called belite. The ions found in solid solution are mainly Al^{3+} , Fe^{3+} , Mg^{2+} , K^+ , SO_4^{2-} and PO_4^{3-} . The presence of alkalis, such as K^+ , stabilizes βC_2S with respect to γC_2S after the clinkering process during cooling. If the phase transition from β to γ occurs, the clinker disintegrates due to the volume changes and the result of the transition will also affect the quality of the product, since γC_2S is almost non-hydraulic [3]. It is also important that phosphate ions are present in low quantities, below 0.3%, since their presence inhibits the formation of C_3S during clinkering because they form a solid solution with C_2S [8].

2.1.3 Tricalcium aluminate

C_3A does not undergo phase transitions and is cubic when pure. It reacts strongly with water but the strength of the product is low. It can also contain substituent ions such as Fe^{3+} , Mg^{2+} , Na^+ , K^+ and Si^{4+} . The solid solution of alkalis changes the structure, and among them, the solution with Na^+ ions is the most common. This solution reacts less strongly with water. Ca^{2+} is substituted by Na^+ and a second Na^+ is placed in the center of a kinked ring defined by six-membered AlO_4 tetrahedra [3]. The change in symmetry with the solution of different quantities of Na_2O was studied and the results showed that the structure changes from cubic to orthorhombic and monoclinic while increasing the percentage of Na_2O [9].

2.1.4 Calcium aluminoferrite

C_4AF is only one of the particular compositions of ferrite that is found in clinkers. In fact, the ferrite phase in clinkers can be any in the solid solution series $Ca_2(Al_xFe_{1-x})_2O_5$ where $x < 0.7$, since this is the limit for normal pressures [3, 4]. The end member C_2F ($x=0$) is stable at ambient conditions while the end member C_2A ($x=1$) only at high pressures [10]. C_2F is orthorhombic with Ca^{2+} ions packed between layers of FeO_6 octahedra and FeO_4 tetrahedra. For values of $x < 0.33$ Fe^{3+} is substituted by Al^{3+} in tetrahedral sites. For higher values of x the substitution starts taking place in octahedral sites too. Some foreign ions can also be found in this phase, the most common being

Mg²⁺, Si⁴⁺ and Ti⁴⁺. Increasing A/F ratio enhances the reactivity of calcium aluminoferrite with water, which is moderate in general. Its hydraulicity is low. Both reactivity and hydraulicity can be enhanced by sintering the compound at lower temperatures than those used for clinkering [3].

2.1.5 Hydration reactions and hydration products

The reaction of tricalcium silicate with water yields two hydration products:



The products are an almost amorphous calcium silicate hydrate phase and calcium hydroxide, also known as portlandite [3]. This phase has the form of hexagonal crystals if growing under ideal conditions and has been found to be present as finely dispersed microcrystals in Portland cement pastes of low water to solid ratio [11], or large imperfect crystals in C₃S pastes [12].

The calcium silicate hydrate phase is named C-S-H, where the hyphens imply that its chemical composition can vary. The examination of thinned sections of C₃S pastes with TEM has shown the Ca/Si ratio of C-S-H in these particular pastes has a mean value of ~1.7-1.8 but varies over the nanometer scale from 1.2 to 2.1 [13].

Upon hydration, the quantity of silicate species changes in C-S-H. The isolated silicate tetrahedra in C₃S are transformed to disilicate ions and a higher degree of polymerization appears with time. Polymerization occurs in chains rather than sheets or 3D networks. After six months the dimer content reaches a maximum of ~60% and then decreases to ~50% after one year, reaching 40% after two or three decades of hydration. Meanwhile the content of polymeric species rises from 30% to 50% from the first year to 30 years of hydration [14]. The mean silicate chain length (MCL) of C-S-H in C₃S pastes increases from 2 to 4 during the 5 first years of hydration [15, 16], and reaches a value of 5 after 2-3 decades of hydration [17]. Aged concrete specimens also show an MCL of 5 after 4-9 decades of hydration [18].

The reaction of dicalcium silicate with water yields also C-S-H and CH:



The proportion of produced CH is about a fifth of the amount produced in the hydration of tricalcium silicate. The rate of hydration of β-C₂S is much lower than for tricalcium silicate.

Comparing rates of hydration of different dicalcium silicate polymorphs has shown that the rate of hydration of γ -C₂S is much lower than that for the rest of the polymorphs. This is attributed to the fact that the oxygen atoms are arranged in a regular octahedral manner around Ca²⁺ ions in this phase, while for the rest of the polymorphs the arrangement of oxygen atoms is irregular [3]. The rate of hydration does not affect the C-S-H composition, which is the same composition that results from hydrating C₃S.

During the hydration of tricalcium aluminate, several crystalline hydration products are formed with different Ca/Al ratios. They are metastable with respect to C₃AH₆ and transformed to it at temperatures over 30°C [3]. However, if lime is present, the transformation from C₄AH₁₃ to C₃AH₆ is inhibited and the hydration is slower. The reaction is anyway sufficient so that flash set is induced if gypsum is not added to regulate setting. When the hydration of tricalcium aluminate occurs in the presence of calcium sulfate or gypsum, the hydration product that is formed is the mineral called ettringite which is a calcium sulfoaluminate hydrate:



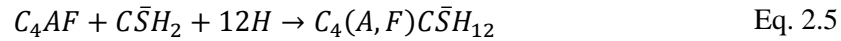
Fe³⁺ can substitute Al³⁺ in ettringite giving rise to phases that are known as AFt, where A and F indicate that Al³⁺ and Fe³⁺ are interchangeable and t indicates a trisulfoaluminate phase. When sulfate ions are not enough to complete the hydration of C₃A, then ettringite reacts with the remaining C₃A and water to form an AFm phase, where m indicates a monosulfoaluminate phase:



The hydration of calcium aluminate in presence of calcium sulphate to form ettringite is evidenced to be a two-stage process. The examination of such a paste has shown that after 10 min of hydration a film of amorphous material is found to be at the surface of C₃A and rods of ettringite are seen 1µm separated from the surface [19]. The formation of ettringite and amorphous material was also evidenced by following the hydration with synchrotron radiation energy-dispersive diffraction [20].

The hydration of the calcium aluminoferrite phase Ca₂(Al_xFe_{1-x})₂O₅ gives similar products as the hydration of tricalcium aluminate, however Fe³⁺ substitutes part of the Al³⁺. The reactivity is higher when the index x increases. Cubic hydrogarnets and C₄(A,F)H₁₃ are formed in the presence of lime.

The hydration reactions for this phase with and without gypsum are:



2.1.6 Microstructure development during the hydration of Portland cement

As the hydration reactions are exothermic, heat is evolved during cement hydration. Monitoring the rate of heat evolution has shown that there are mainly three stages in Portland cement hydration that correspond to three peaks (I, II and III in Figure 2.1), that are associated with the microstructure development [21]:

- From 0 to 3 hours: Cement is fluid and workable. A large amount of heat is evolved when mixing and decreases dramatically after ~3 hours. This is known as the induction or dormant period. The hydration of free calcium oxide takes place up to 2 hours.
- From 3 to 24 hours: The main peak in the rate of heat evolution appears during this period in which cement starts setting. Approximately 30% of the hydration occurs at this stage. The period before the top of peak II is reached is known as the acceleration period, and coincides with the fast hydration of tricalcium silicate. The remaining part of the curve corresponds to the deceleration period.
- From 24 hours onward: During this period there is another peak in the rate of heat evolution, but not as intense as in the previous stage, due to the formation of AFm.

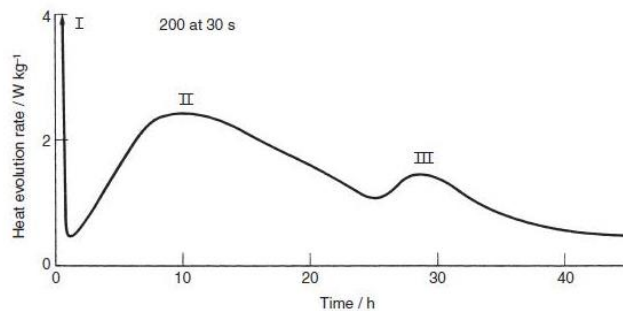


Figure 2.1. Rate of heat evolution for the hydration of Portland cement at 20°C [3].

The first symptom of the development of microstructure during cement hydration is the formation of a gelatinous product on the surface of cement grains after mixing. This product contains alumina and silica, and calcium and sulfate to a lesser extent. After 10 min of hydration

rods of AFt are formed outside the gelatinous layer. At 3 hours C-S-H can be seen on fracture surfaces [21].

During the second period of hydration C-S-H and CH grow fast. This C-S-H is known as Op C-S-H (Outer product) and grows on the AFt network, separated from the cement grains, in spaces originally filled with water. This growth of C-S-H is responsible for setting, bonding the paste together after 3 or 4 hours of hydration. After 12 hours of hydration, CH grows in hexagonal crystals in space that was occupied by water. After 16 hours, AFt grows again in long rods on the C-S-H layer. At the end of the second peak in the rate of heat evolution, after one day of hydration, grains smaller than 5 μm have reacted completely [21].

During the third hydration period, the shell of hydration products gets thicker and its permeability decreases. This causes C-S-H to start growing on the surface of the grains as Ip C-S-H (Inner product). This growth decreases the distance between the hydration shell and the grains. This distance can actually disappear completely after 7 days of hydration. From 1 to 3 days of hydration, hexagonal AFm plates form on the shells by the reaction of C_3A and AFt. With prolonged hydration during several days and years, Ip C-S-H continues growing filling the space the cement grain occupied. Even after years of hydration, the ferrite phase remains unreacted [21].

A schematic picture representing the development of the microstructure while a cement grain hydrates is shown in Figure 2.2. Belite is not taken into account since its reaction is slower than the one for alite and even after 14 months the hydration is only local.

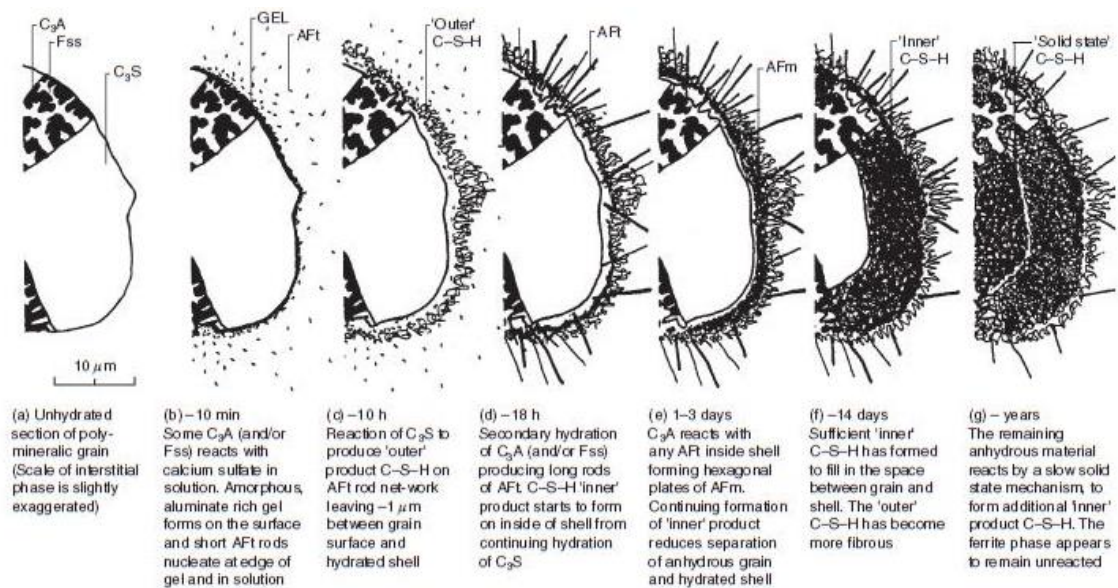


Figure 2.2. Microstructural development for a cement grain [22].

2.2 Most common supplementary cementitious materials

Supplementary cementitious materials are used in cement manufacture nowadays to reduce the CO₂ emissions and also for technical reasons, to improve certain properties of cement and concrete. Their use changes the kinetics of the hydration reaction and also the microstructure and nanostructure of the final product [2]. They also have an impact on the Ca/Si ratio of C-S-H, that is reduced with respect to OPC. Four of the most used supplementary materials are GGBFS (ground granulated blast furnace slag), fly ash, silica fume and metakaolin.

GGBFS is an industrial and glassy by-product that is generated from molten slag during the production of iron which is used to make steel. Its major components are CaO and SiO₂ and also smaller percentages of Al₂O₃, Fe₂O₃ and MgO [2].

Fly ash is also an industrial by-product formed during the combustion of ground or powdered coal in coal-fired electric power generating plants. The fly ashes are spherical glassy particles that can be hollow or contain other small spheres. They are silicate glasses that contain silica, alumina, iron and calcium, and other minor components such as sulfur, magnesium, sodium, potassium and carbon. Crystalline compounds are found in small amounts, but only the amorphous compounds are reactive. Their composition can vary depending on their origin. For instance Class F is typically a low calcium fly ash that contains ~52% silica, ~23% alumina, 11% ferrite, %5 CaO and the rest in minor components, while Class C is a typically high calcium fly ash that contains ~35% silica, 18% alumina, 6% ferrite, ~21% CaO and the rest in minor components [2].

Silica fume is a by-product of the production of silicon metals and ferrosilicon alloys which forms as ultra fine non-crystalline silica in electric-arc furnaces. Its composition is of at least 85% SiO₂. It is used in applications where a high degree of impermeability is required as well as high-strength concrete [2, 23].

Metakaolin is a special type of calcined clay. It is produced by low-temperature calcination of kaolin clay and it is used when low permeability or high strength are required. It is used as an additive (in low quantities such as 10% in mass), rather than as a replacement of cement [23].

2.3 Minerals and synthetic phases related to C-S-H

In the system of calcium silicate hydrates, there are several minerals such as gyrolite, xonotlite, tobermorite 9Å, clinotobermorite, tobermorite 11Å, tobermorite 14 Å and jennite. The comparison of XRD patterns of C-S-H formed in cement pastes with those of the natural minerals

tobermorite and jennite has shown that C-S-H has some structural features related to them. C-S-H in pastes gives XRD peaks at ~0.3 nm and ~0.18 nm, which coincide with important distances in the Ca-O layer of tobermorite, jennite and also CH. Synthetic imperfect forms of tobermorite and jennite formed in aqueous suspensions, called respectively C-S-H (I) and C-S-H (II) are also related to C-S-H [4]. Thomas et al. [24] have shown recently that C-S-H has a much higher atomic packing density than both tobermorite and jennite. This may be due to its defective atomic structure and to nanosolid effects linked to its nanoparticulate morphology. Upon dehydration C-S-H transforms into the calcium silicate called wollastonite.

2.3.1 Tobermorite 14Å

The crystal chemical formula of tobermorite is $\text{Ca}_5\text{Si}_6\text{O}_{16}(\text{OH})_2 \cdot 7\text{H}_2\text{O}$ from which its Ca/Si ratio is 0.83. It consists of a central Ca-O layer with attached silicate dreierketten chains on both sides. The space in between the layers contains water molecules and Ca. In tobermorite there are three different sites for Ca, three sites for Si, eight sites for O, five sites for water and a site for OH; for occupancy and atomic coordinates of the sites see ref. [25]. The main layers are formed by two types of calcium polyhedra. The first one is bonded to four oxygen atoms and an OH group and the second one is bonded to four oxygen atoms and a water molecule. The silicate chains are formed by a repeated pattern of two silicate paired tetrahedra in which Si is bonded to four oxygens of which two are shared with the central CaO_2 layer, and a bridging silicate tetrahedra in which Si is bonded to three oxygen atoms and an OH group (paired and bridging tetrahedra indicated in Figure 2.3). In the interlayer there is one site for Ca which is bonded to oxygen atoms and water molecules that form an octahedron around it. This is illustrated in Figure 2.3, which shows two oxygens (sites O5 in ref. [25]) that are shared with bridging tetrahedra. There is a water site (W4 in ref. [25]) very close to this site of Ca, which means that these two sites cannot be occupied at the same time, thus the atomic arrangement in the interlayer has to be of alternate Ca octahedron and water molecules occupying W4 sites [25]. Apart from the mentioned bonds, there is also a hydrogen bonding system involving all water sites and several oxygen sites.

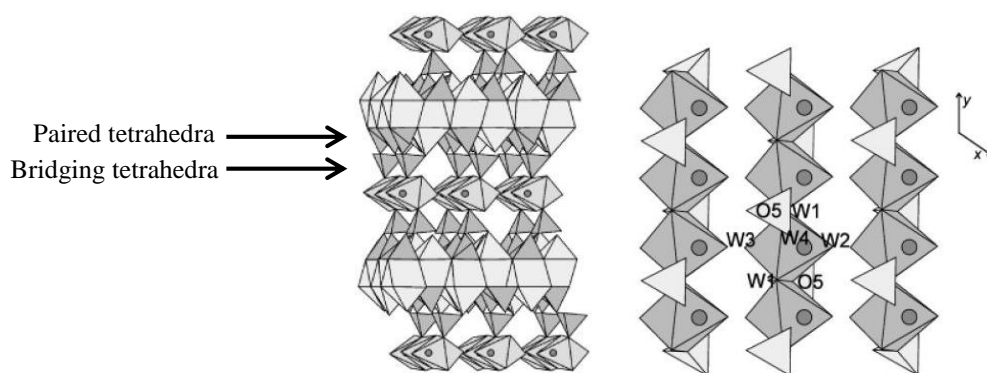


Figure 2.3. Tobermorite structure along [010] with silicate tetrahedra in dark grey, Ca polyhedra in light grey and W4 sites as dark dots (left). Atomic structure in the interlayer space along [001] with sites Ca2 octahedra in dark grey, bridging silicate tetrahedra from the chains above and below the interlayer space in light grey and water sites (W4) as dark dots (right) [25].

2.3.2 Jennite

The crystal chemical formula of jennite is $\text{Ca}_9\text{Si}_6\text{O}_{18}(\text{OH})_6 \cdot 8\text{H}_2\text{O}$ from which its Ca/Si is 1.5. The structure consists of ribbons of two calcium octahedra which share edges and are linked by vertices to other ribbons forming a zigzag chain. On both sides of the zigzag chain there are dreierketten silicate chains. The main layers formed by calcium octahedra and silicate tetrahedra are linked by additional calcium octahedra on inversion centers (Figure 2.4) [26].

In jennite there are five different sites for Ca, three sites for Si, 14 sites for O and two for water. The interpretation of the bond valences and a proposed net of hydrogen bonds have revealed that three of the oxygen sites are in fact OH groups and two of the oxygen sites correspond to water molecules. The Ca atoms are bonded to different number of oxygen atoms, hydroxyl groups and water molecules and are part of two different kinds of ribbons. Two of the Ca sites that are bonded to four oxygens and two hydroxyl groups are part of ribbons where all the vertices are shared with other octahedra (Ca) or tetrahedra (Si). Another Ca site that is bonded to three oxygens, two OH groups, and a water molecule is part of the other kind of ribbons, as well as a Ca site which is bonded to two oxygen atoms and four water molecules. This last type of ribbon has free apical positions on both sides of the zigzag which correspond to water molecules. All the silicate tetrahedra have oxygen sites in their vertices. There is also a hydrogen bonding system that involves all the water sites, all the OH groups and some of the oxygen sites [26].

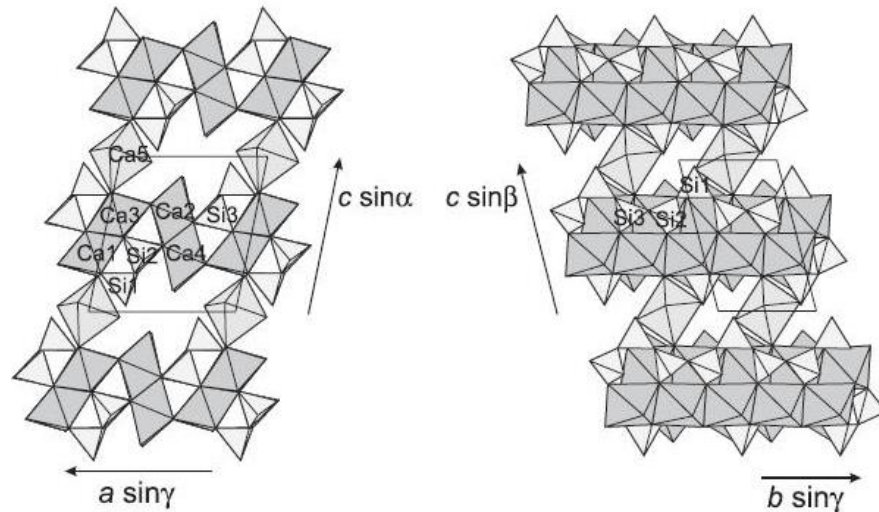


Figure 2.4. Crystal structure of jennite along [010] (left) and [100] (right) showing some of the Ca and Si sites [26].

The main structural differences between jennite and tobermorite is that the main CaO_2 layer in jennite is more corrugated and there are no Si-OH bonds in jennite.

2.3.3 C-S-H (I)

According to Taylor, C-S-H (I) can be obtained by the reaction of tricalcium silicate with water, by mixing silica gel and CH in water solution or by the double decomposition of calcium nitrate and sodium silicate when the Ca/Si ratios range from 0.66 to 1.5 [4]. However, the product is more crystalline using the first method, due to a probably slower formation of the hydrate or a different reaction mechanism. XRD patterns of samples with Ca/Si below 1.65, prepared by these three methods, give similar results, only differing in the longest observed spacing, which is 10 Å for the first method and 11.5 Å for the other two [27]. They all show hk0 reflections of 1.4 nm tobermorite and sometimes a basal reflection, which suggests they are ordered in two dimensions and slightly ordered in a third one. The basal reflection corresponds to the longest observed spacing, which varies upon changes on Ca/Si, decreasing with increasing Ca/Si. The structure is then explained in terms of well ordered layers with an irregular distance between them. The morphology of C-S-H (I) is crumpled foil-like [4].

2.3.4 C-S-H (II)

Taylor studied different C-S-H samples prepared by the three methods mentioned in section 2.3.3 and found that products resulting from the hydration of tricalcium silicate with Ca/Si ratios ~ 1.9 showed different structural features than C-S-H (I), as per XRD results. He first named

those products as C-S-H (II) [27]. This phase can also be formed by the hydration of β -C₂S. The XRD patterns of C-S-H (II) show similarities with jennite and the morphology is fibrillar [28].

2.3.5 Wollastonite

Wollastonite is a calcium silicate natural mineral, but can be obtained by the dehydration of C-S-H above 800°C. Its chemical formula is CaSiO₃ and it presents two polymorphs at low pressure: wollastonite and pseudowollastonite. They have drastically different silicate structures, since wollastonite has a single-silicate chain, while pseudowollastonite has a structure with rings of three Si₃O₉ groups. Seryotkin et al. [29] presented some polytypes of these polymorphs that can be seen in Figure 2.5. The simplest one is Wollastonite 1T, which has a single silicate chain. Other wollastonite polytypes (2M, 3T, 4T and 4M) exist as the result of different stacking sequences of the unit cell, as can be appreciated in Figure 2.5 c). Hemni et al. [30] discovered the 3T, 4T, 4M and 5T polytypes. Pseudowollastonite can also exhibit different polytypes with stacks of two or four layers, see Figure 2.5 d) and e). Mazzucato and Gualtieri studied the formation of 1T and 2M wollastonite by heating a mixture of lime and silica in the temperature range of 700-1000°C [31]. They observed that wollastonite 1T does not transform directly into wollastonite 2M, but transforms into an intermediate disordered phase called 1Td. They did not account for the formation of pseudowollastonite at higher temperatures.

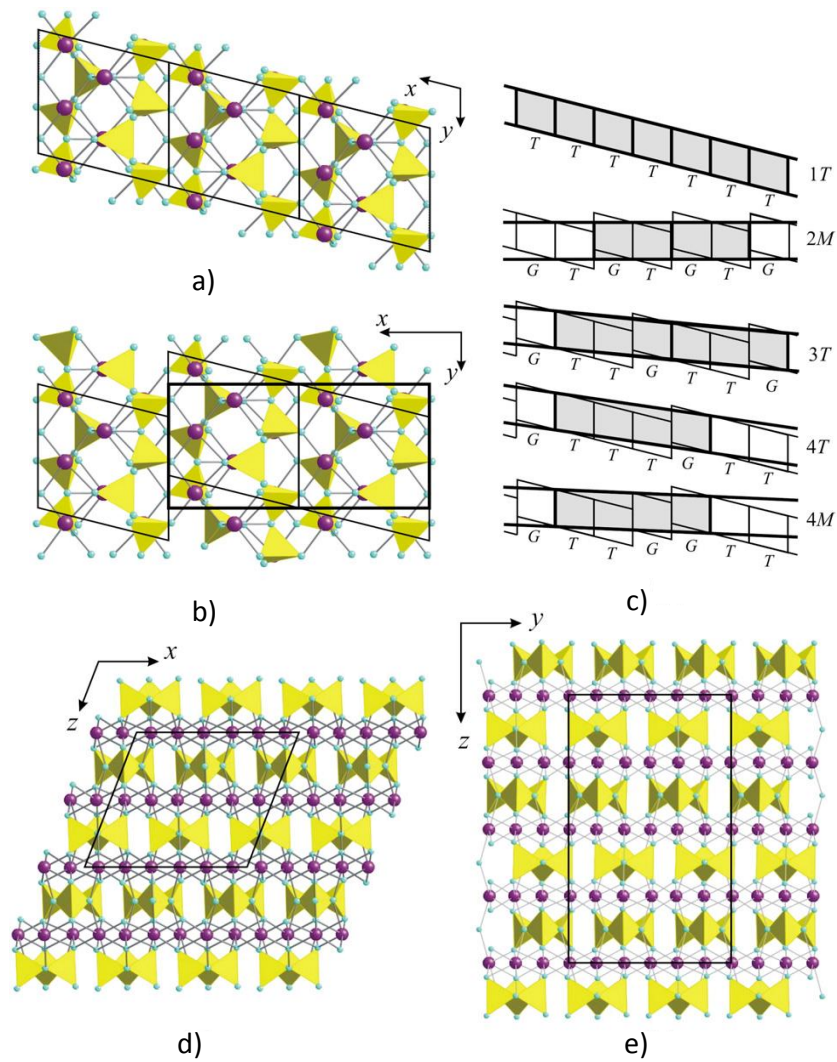


Figure 2.5. Structure of wollastonite 1T a), and parawollastonite 2M b) along the c -axis. Different wollastonite polytypes depending on the stacking sequence of (100) slabs [30]. The unit cell is marked with thicker lines c). Stacking sequences of a two layer pseudowollastonite d) and a four layer pseudowollastonite e). (Figures taken from ref. [29])

2.4 Atomic and molecular models for C-S-H

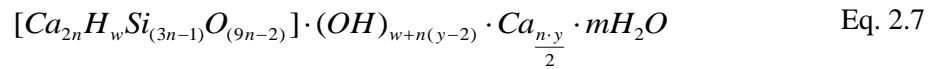
A number of models aim at providing structural chemical formulae for C-S-H phases, based predominantly on Ca/Si ratio. Some of them will be discussed in this section. Models based on the combinations of tobermorite and jennite and the combination of tobermorite and CH can explain the variation of Ca/Si and other structural features that C-S-H exhibits. Tobermorite and jennite have Ca/Si ratios of 0.83 and 1.5 respectively, while in commercial cement pastes the Ca/Si ratio of C-S-H varies from 0.77 to 2.3 [32]. Therefore combinations of structural units of both minerals and other phases are needed to cover all the compositional range for C-S-H. A molecular model based on Ca/Si ratio and density of C-S-H in Portland cement will also be introduced.

2.4.1 Taylor model

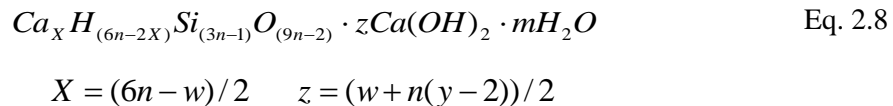
Taylor proposed a model to explain C-S-H that is based on the combination of imperfect layers of jennite and a smaller proportion of imperfect layers of tobermorite. The minimum and maximum values for Ca/Si in this model are 0.83 and 2.25 respectively. The imperfections of the layers lie on the elimination of some of the silicate tetrahedra, especially in the tobermorite ones. Eliminating all the bridging tetrahedra in both minerals leaves pure dimeric structures which would have a Ca/Si ratio of 1.25 in the case of tobermorite and 2.25 in the case of jennite. Taylor proposed the material formed at an early stage of hydration to be a mixture of tobermorite and jennite dimers to explain the dimeric silicate structure found in early age products. As pentameric jennite has a Ca/Si ratio of 1.8, he then proposed that aged material would then be formed of a majority of jennite layers with longer silicate chains. His model is also consistent with electron diffraction patterns of C-S-H which reveal that this material can be compatible with tobermorite or jennite-like structures or a combination of both [33].

2.4.2 Richardson and Groves' model

Richardson and Groves proposed a model to describe C-S-H in terms of two different combinations: T/J (tobermorite/jennite) and T/CH (tobermorite/calcium hydroxide) [34]. This model is more flexible than Taylor's model since the minimum and maximum values for Ca/Si ratios are 0.67 and 2.5 respectively. The main difference between the two viewpoints lies on the position of Ca²⁺ ions that are not part of the main layers neither charge balancing. These Ca²⁺ ions are within CH layers, between the silicate layers of tobermorite-like structure on the T/CH viewpoint, while they are part of the main jennite-like layers, as Si-O-Ca-OH, on the T/J viewpoint [1]. The structural chemical formula for the T/J viewpoint is:



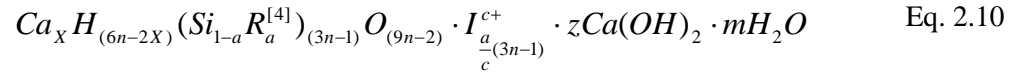
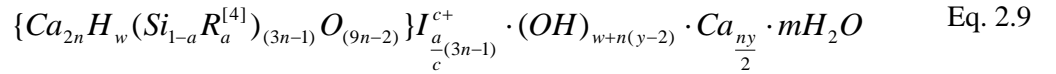
Where w is the number of silanol groups, w/n is the degree of the protonation of the silicate chain and n is an integer (1,2,3...), so that the silicate tetrahedra are arranged in dimers, pentamers, octamers, etc. The T/CH viewpoint is expressed as the following formula rearranging the terms in the T/J formula and changing the indexes as indicated below:



This model is very flexible and the values of the indexes can be obtained experimentally. The silicate mean chain length $(3n-1)$ can be obtained by ^{29}Si NMR and thus the value of n ; the Ca/Si ratio, which is related to n and y , can be measured directly with EDX on a TEM, so that knowing the value of n , y can be determined. The degree of protonation, w , can have a range of values which is limited by restrictions to maintain the layer structure and neutrality:

$$\begin{aligned} 0 \leq y \leq 2 &\rightarrow n(2-y) \leq w \leq 2n \\ 2 \leq y \leq 4 &\rightarrow 0 \leq w \leq 2n \\ 4 \leq y \leq 6 &\rightarrow 0 \leq w \leq n(6-y) \end{aligned}$$

As in most cements C-S-H has substitution ions, the model was extended to include the incorporation of trace elements (trivalent cations such as Al^{3+}) [35]. The T/J and T/CH viewpoints with incorporation of other elements are:



Where $R_a^{[4]}$ is a trivalent cation in tetrahedral coordination and I^{c+} is a monovalent alkali cation or Ca^{2+} needed for charge balance. The parameters in the formula can also be obtained experimentally in a similar way than for the case without trace elements. Knowing the mean chain length from ^{29}Si NMR gives the value of n . The index a can be obtained with the R/Si ratio ($a/(1-a)$) measured directly with EDX in TEM. Measuring the Ca/Si ratio gives the value of y , but two cases are to be considered taking into account if the charge is balanced entirely by monovalent alkali cations or by Ca^{2+} . The restrictions for the degree of protonation are the same that for the case without trace elements [1].

An example of the applicability of the model to two different pastes is illustrated in Figure 2.6. Plotting the Al/Ca ratio vs. the Si/Ca ratio can help to identify which of the view points (T/CH or T/J) is more suitable to describe a paste, if in the same plot the different structural units: CH, tobermorite and jennite dimers, pentamers and octamers with different protonation and ionic substitution levels are marked. Another plot that is useful to decide the combination of structural units that is suitable is the Ca/(Si+Al) or Ca/Si distribution against the reciprocal mean chain length (Figure 2.7). The lines for the different structural units must also be represented in the plot, so that placing the ratio distribution over the experimental reciprocal mean chain length gives a straight

line that lies in between different structural units that may be combined within the C-S-H structure in the paste.

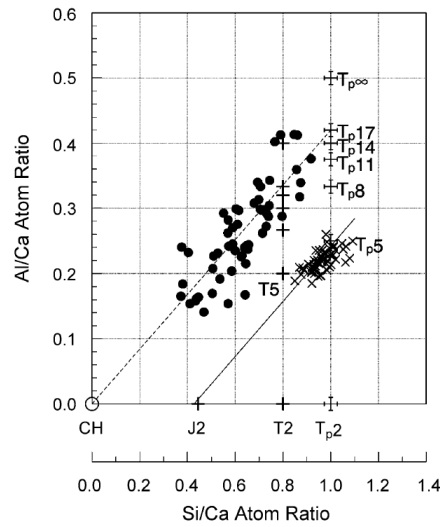


Figure 2.6. Al/Ca atom ratio vs. Si/Ca atom ratio of TEM points in Op C-S-H in a hardened white PC/20% metakaolin blend (●) described by the T/CH view point, and a hydrated synthetic slag glass (×) described by the T/J view point, both activated in 5M KOH solution. Taken from ref. [1].

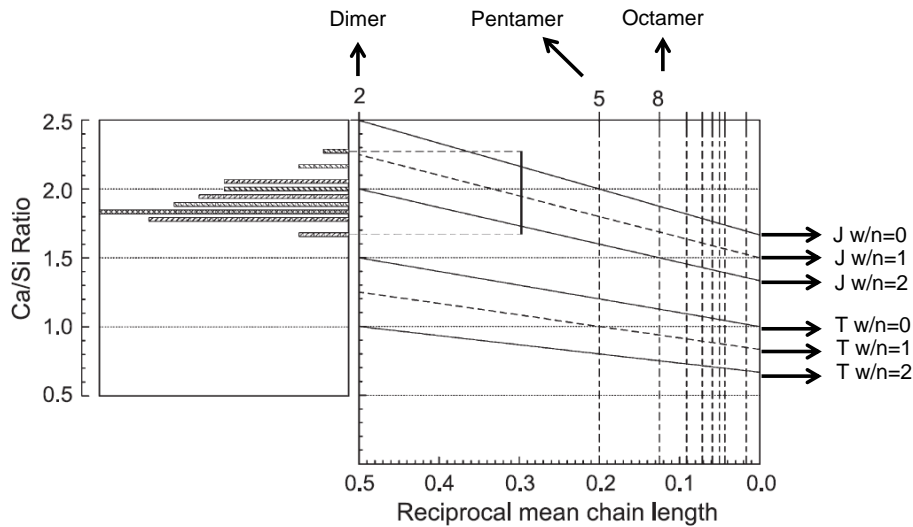


Figure 2.7. Ca/Si ratio frequency histogram of TEM analyses of C-S-H in a hardened PC paste hydrated for 2 years vs. the reciprocal mean chain length. Modified from ref.[1]. The relations of Ca/Si ratio and reciprocal mean chain length for tobermorite (T) and jennite (J), with different levels of protonation in Richardson and Groves’ model, are indicated on the right. The C-S-H in this case is based on jennite dimers and pentamers.

This model, being the most flexible to provide chemical structural formulae in a broad range of Ca/Si ratios, is the one chosen in this study to obtain structural representations of synthetic C-S-H phases.

2.4.3 Richardson's model structures for C-(A)-S-H(I)

Richardson has recently derived model structures for C-(A)-S-H(I) based on clinotobermorite [36]. Orthotobermorite presents an orthorhombic subcell while clinotobermorite presents a monoclinic subcell. Orthotobermorite was always used as a model for C-S-H, but Richardson has found the construction of a plausible silicate dimer in terms of crystal-chemical reasoning was only possible starting from a clinotobermorite structure. The structures are derived from single-chain tobermorite and present no interlayer calcium ions when the chains are infinite and one interlayer calcium ion for each silicate tetrahedra that is missing. For $\text{Ca/Si} > 1.4$ the structures include an inter-mixed Ca-rich phase. The structure chosen to represent the hypothetical dimer presents ribbons of Ca-O octahedra which are very similar to those present in CH. This similarity could explain the intergrowth of CH layers with the dimeric structures and justify the T/CH view point in Richardson and Groves' model.

The model structures were built so that they present Ca-O distances and coordination numbers that are within the limits of known data for crystalline calcium silicate hydrates and other related phases. They are in agreement with the trends of experimental data such as the linear decrease of the basal spacing with increasing Ca/Si ratio, the change of the basal spacing with water content, the increase of $\text{H}_2\text{O/Si}$ with Ca/Si ratio, the existence of dimeric silicate anions at low Ca/Si ratios, the substitution of Al^{3+} for Si^{4+} , the decrease in the site occupancy factor for bridging tetrahedra with increasing Ca/Si ratio and the significant features of XRD patterns.

The agreement of the model with experimental data of the basal spacing vs. Ca/Si is illustrated in Figure 2.8. The bold symbols with the center trend line represent the model structures for an undecamer, a pentamer, a trimer and a dimer and the other two trend lines are taken from various authors [37-45]. The interpretation of these data combined with $\text{H}_2\text{O/Si}$ vs. Ca/Si (See Figure 2 in ref. [36]) suggests that the difference in basal spacing from the lower trend line and the upper trend line is due to the loss of one water molecule per silicon atom. Data for $\text{Ca/Si} < 0.66$ that are placed outside the lower trend line are due to intermixture of C-S-H and silica, while data for $\text{Ca/Si} > 1.25$ with a basal spacing of about 11.75, that are placed outside the upper trend line are due to intermixture of C-S-H and CH. Therefore, data for C-S-H that lies within both trend lines can be due to a different level of drying or due to intermixture of C-S-H with CH.

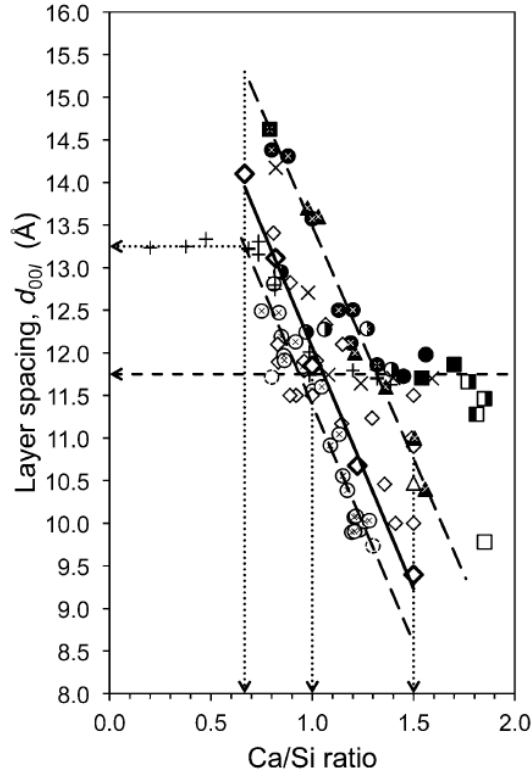
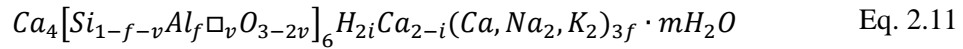


Figure 2.8. Compilation of literature data of layer spacing vs. Ca/Si ratio of C-S-H taken from ref. [36], with the middle trend line representing the model structures for C-(A)-S-H.

The model was derived from a general expression of a single-chain tobermorite:



Where f is the fraction of tetrahedral sites occupied by Al, v is the fraction of vacant tetrahedral sites (represented by a square), and i can take values from 0 to 2 depending on the negative charge balanced entirely by protons Ca ($i=2$), equally by Ca and protons ($i=1$) or entirely by protons ($i=0$). There are 4 main layer Ca atoms for every 6 tetrahedral sites. The aluminosilicate part of the structure is in square brackets, and the interlayer extra ions in rounded brackets. According to this equation, the Ca/Si ratio is:

$$\frac{Ca}{Si} = \frac{6 - i}{6(1 - v)} \quad \text{Eq. 2.12}$$

The maximum Ca/Si ratio is obtained when the negative charge is entirely balanced by Ca (i=0):

$$\left(\frac{Ca}{Si}\right)_{max} = \frac{1}{(1-v)} \quad \text{Eq. 2.13}$$

And the MCL can be expressed as:

$$MCL = \frac{1-v}{v} \quad \text{Eq. 2.14}$$

Thanks to a compilation of MCL vs. Ca/Si data and plotting the $(Ca/Si)_{max}$ vs. the experimental Ca/Si ratio (Figure 2.9), Richardson obtained a constraint for the Ca/Si ratio expressed in terms of the vacant tetrahedral sites in order to develop his model structures:

$$\frac{Ca}{Si} = \frac{\frac{2}{3} + v}{1-v} \quad \text{Eq. 2.15}$$

This last equation can be equally expressed in terms of the percentages of Q^1 and Q^2 species and the site occupancy factor for bridging tetrahedra (SOF_{BT}):

$$\frac{Ca}{Si} = \frac{(3 - SOF_{BT})}{(2 + SOF_{BT})} = \frac{\frac{3}{2}Q^1 + \frac{2}{3}Q^2}{Q^1 + Q^2} \quad \text{Eq. 2.16}$$

The compilation of MCL vs. Ca/Si is shown in Figure 2.9 (left). The dashed line represents the tobermorite line for minimum degree of protonation (i=0 or w/n=0 in Richardson and Groves' model) in Figure 2.7. This represents the maximum Ca/Si ratio that is possible without Ca-OH groups in the structure (Eq. 2.13), thus Ca-OH must exist to the right of the line. Most of the data are placed along the dotted line, which represents the model structures by Eq. 2.15. An equivalent plot is shown in Figure 2.9 (right), where the model structures are marked with bold symbols over the dotted line, which represents Eq. 2.16. The dashed lines are the equivalent to the tobermorite lines in Figure 2.7 with maximum to minimum degree of protonation from left to right. Maximum degree of protonation implies the negative charge entirely balanced by protons in Si-OH groups, intermediate protonation implies the negative charge balanced equally by protons in Si-OH groups

and Ca, and minimum degree of protonation implies the negative charge balanced entirely by Ca. The data marked with squares belong to samples with CH. The middle plot shows $(Ca/Si)_{max}$ vs. experimental Ca/Si. The dotted diagonal follows Eq. 2.15.

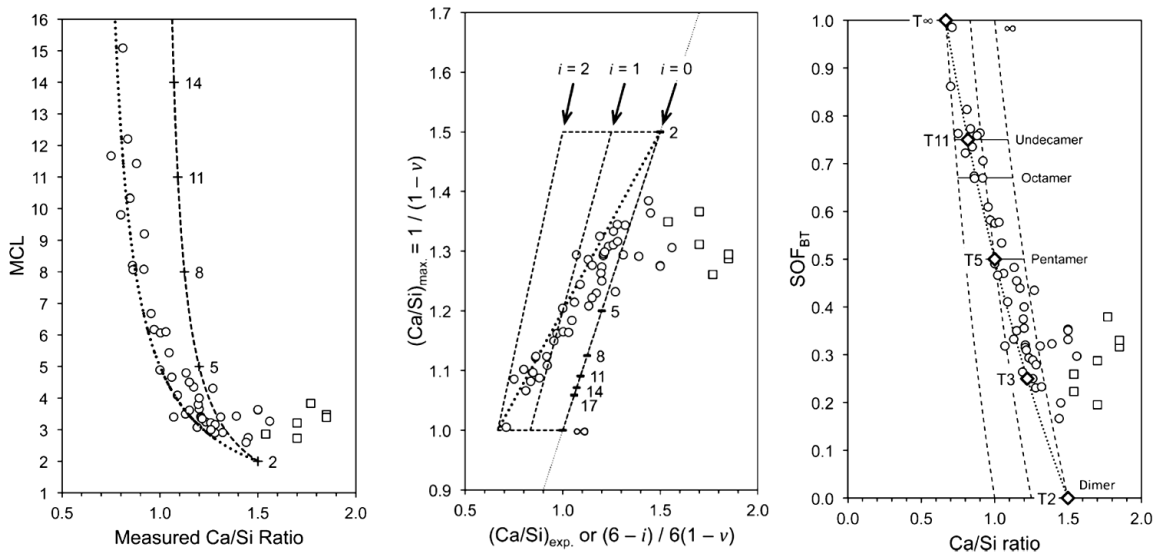


Figure 2.9. MCL (mean chain length) vs. Ca/Si (left plot); data are from ref. [38, 39, 46-49], $(Ca/Si)_{max}$ vs. experimental Ca/Si (middle plot); data are from ref. [38, 39, 46-49] and SOF_{BT} (site occupancy factor for bridging tetrahedra) vs. Ca/Si (right plot); data are from ref. [38, 39, 46-51]. The dotted lines are defined by Eq. 2.14 and Eq. 2.15 (left and middle) and Eq. 2.16 (right). The bold symbols (right) represent the model structures for C-(A)-S-H. The dashed lines are equivalent to the tobermorite lines in Figure 2.7 with $w/n=0, 1$ and 2 from left to right in the middle and right plots. The dashed line in the left plot is the one for $i=0$. The three graphs are taken from ref. [36].

2.4.4 Pellenq's molecular model

Pellenq et al. [52] molecular model is claimed to be a bottom up approach to describe the structure of C-S-H from its Ca/Si ratio and its density. It is based on the deformation of a monoclinic periodic computational cell of tobermorite with initial Ca/Si ratio of 1. Several SiO₂ groups are removed from the cell to obtain a distribution of silicate species according to NMR results and reach a Ca/Si of 1.65. The cell is then allowed to relax, what causes the interlayer distance to increase from 11Å to 11.3Å. Monte Carlo simulations of water adsorption are then performed. This step increases the density to 2.56g/cm³; a value that is close to the experimental value of 2.6g/cm³ given by neutron scattering [53]. The composition of C-S-H given by the final model is (CaO)_{1.65}(SiO₂)(H₂O)_{1.75}. The final model is illustrated in Figure 2.10.

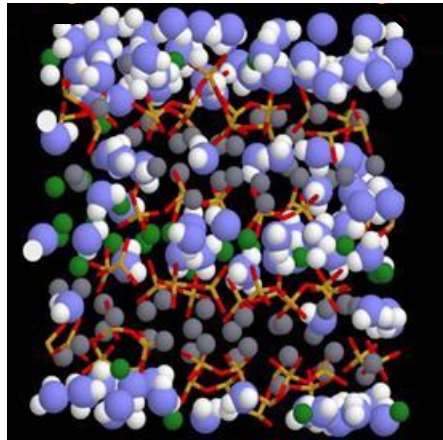


Figure 2.10. Molecular model of C-S-H. The blue and white spheres represent water molecules. The green and grey spheres represent interlayer and intra-layer calcium ions and the yellow and red bars represent silicon and oxygen in silicate tetrahedra. Taken from ref. [52].

The final cell was used to generate simulated EXAFS, XRD, infrared and nanoindentation data. Despite their simulated data being in agreement with experimental data of C-S-H, their model has been criticized due to the unrealistic structure that it creates in terms of crystal chemical and geometrical reasons. Richardson has stated that some of the Ca-O distances they derive are shorter or longer than the minimum and maximum known distances for crystalline calcium silicate hydrates and criticized the unrealistic generation of calcium atoms in five, four and threefold coordination; when the natural coordination of calcium atoms in many calcium silicates is six or sevenfold [54].

2.5 Mesostructure models for C-S-H

Other models for C-S-H aim at describing the phase in an intermediate scale (~50-100 nm). They describe what is known as the mesostructure; i.e. arrangement of building blocks of C-S-H to define pores of different sizes. Although a bit aside from this group, a model that simulates the growth of C-S-H in spherical confinements is also discussed in this section. The outcomes of this model are directly linked to the ways in which C-S-H can grow to give result to a known fibrous morphology, and they are comparable with morphological studies that are central to this thesis.

2.5.1 Powers (layer model)

Powers conceived C-S-H as a gel formed by fibrous particles with straight edges and with gel pores inside. The particles were arranged forming a cross-linked network defining capillary pores, which were placed on the originally water-filled space. The capillary pores could be connected by channels, or gel pores if the structure was denser [55].

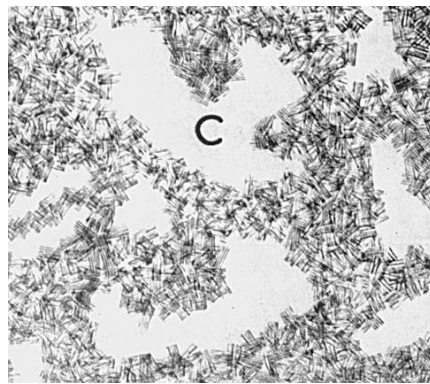


Figure 2.11. Powers model of C-S-H with interconnected fibrous particles. C: Capillary pore [55].

2.5.2 Feldman and Sereda (layer model)

Feldman and Sereda presented a model for C-S-H that could explain the hysteresis behavior of the deformation, weight and Young modulus of cement paste with RH during water sorption and desorption. They found that up to 50% RH the Young modulus remained almost constant upon sorption, increasing significantly until 100% RH. Upon desorption the Young modulus remained constant until very low RH, when it decreased drastically. The changes in weight also followed a similar trend, while the deformation upon sorption increased almost at a constant rate from 0% to 100% RH. These results lead to propose a layered structure of tobermorite thin layers with interlayer water allocated between them. During sorption, the water molecules enter from the edges of a layer expanding it, with no increase of the Young modulus until the middle part is filled. During desorption, the water starts being lost from the edges, but the Young modulus does

not decrease until the water is lost from the middle part. This happens when the RH is very low explaining thus the hysteresis behaviour of this property [56].

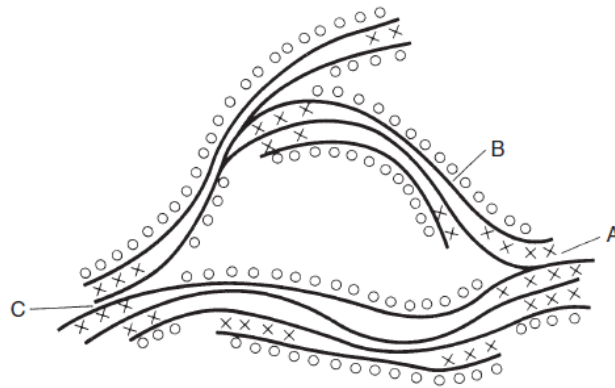


Figure 2.12. Representation of Feldman and Sereda model for C-S-H. A: Intercrystallite bond, B: Tobermorite sheet, C: Entrance to a gel pore, X: Interlayer water, O: Physically adsorbed water [3].

The assemblage of the units which they proposed was a conclusion of their measurements of Young modulus versus porosity of cement pastes prepared by different methods. These results showed no difference upon preparation method, which was not reported to be so for materials that develop strength due to the intergrowth of crystals. Thus the assemblage of the units of C-S-H was thought to be due to Van der Waals bonds between sheets [56].

2.5.3 Jennings (colloid model)

Jennings model was developed taking into account the colloid nature of C-S-H in a scale of 1 to 100 nm in order to give a quantitative mechanistic explanation of deformation. Two densities of C-S-H are considered in this model to understand the values of surface area and pore volume given by N_2 sorption. Jennings considered that water sorption gave the value of the total porosity of the samples, since it was roughly a constant regardless of the preparation method or water to solid ratio. However, N_2 sorption yielded different pore volumes depending on preparation, drying method and other variables. Thus the difference between the pore volumes measured by water and N_2 gives the volume of pores which are not accessible to N_2 , which should be related to the surface area of the sample. It should be expectable that the surface area decreases with higher inaccessible volume to N_2 , i.e. when the pores between the layers and the capillary pores are not too open. However, available data in the literature show the complete opposite trend. To explain this, Jennings postulated the existence of two different densities of C-S-H; low density (LD) and high density (HD). LD particles have an accessible surface to N_2 but their interior is mainly inaccessible to N_2 , while HD particles have a surface which is not accessible to N_2 , but an interior which is.

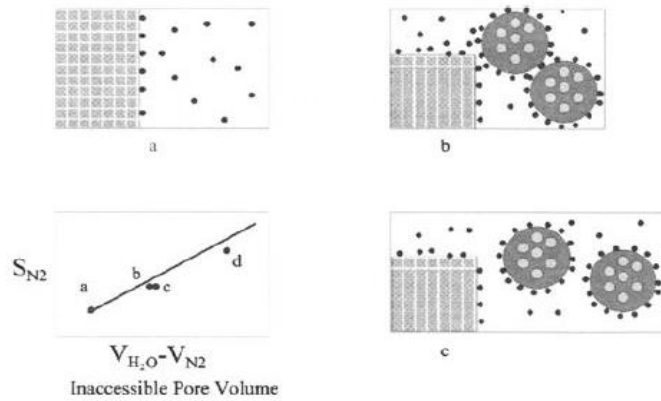


Figure 2.13. Schematic of Jennings colloidal model with LD C-S-H as circles and HD C-S-H as rectangles with the variation of the surface area measured by N_2 for different configurations [57].

Thus increasing the amount of LD particles in a paste leads to an increase in both surface area and inaccessible pore volume for N_2 . The model postulates a bimodal density in which only LD C-S-H contributes to the surface area measured by N_2 . C-S-H particles must have a size of at least a unit cell and form spherical globules which aggregate into LD structures [57].

This model was refined in the so-called CM-II model [58] in which all the pore and interlayer spaces are defined to explain the hysteresis of water sorption and desorption isotherms. C-S-H is assumed to be an assembly of non-spherical globules with a 5 nm cross section. This assembly leaves pores between the globules that are small gel pores (SGP) of dimensions from 1 to 3 nm and large gel pores (LGP) from 3 to 12 nm (Figure 2.14). The globules also have interlayer spaces and intraglobule spaces (IGP) (Figure 2.14). The hysteresis at low pressures on the isotherms is due to interlayer water that leaves the globules below 11% RH and does not enter the structure again until high RH.

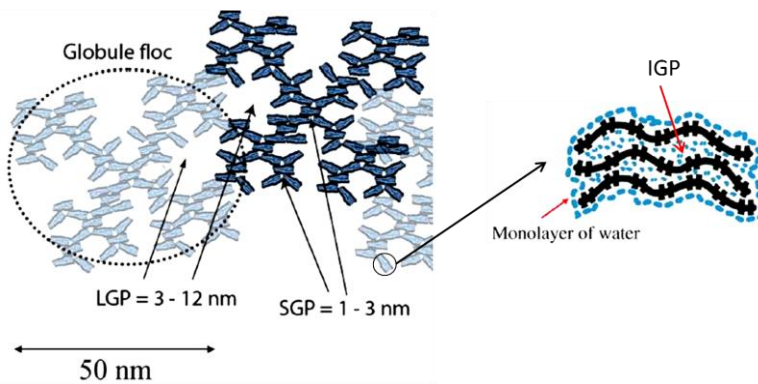


Figure 2.14. Schematic of the assembly of the globules in CM-II model showing small and large gel pores (SGP and LGP) (left). Enlargement of one globule in a saturated state with a monolayer of water on the surface and water filling the interlayer and interglobule pores at 11% RH (right) [58].

2.5.4 Growth model of sheets in 3D confinements

Etzold et al. [59] have recently reported a growing algorithm to simulate the growth of outer product C-S-H during cement hydration. The model treats C-S-H as a quasi-continuous sheet structure and simulates its growth in spherical space confinements of 100 nm radius between cement grains. Growth starts from a number of seeds or nucleation sites represented by triangles with side length of 1.5 nm and height of 0.65 nm so that they represent a single tobermorite 14\AA layer with a calcium oxide central layer and pairing silicate tetrahedra on top and bottom. Growth can occur in two different modes: plane growth and layering growth. During plane growth another triangle is added at the edge of the existing structure and during layering growth a triangle is added in a different layer over the existing one at 1.4 nm of distance. Layering can also be affected by certain tilting angle when the next layer does not grow parallel to the previous one. Different cross sections of the spherical confinement were generated exploring different relationships between the probabilities of plane growth (p_p) and layer growth (p_l). These configurations are shown in Figure 2.15. When the probability of layering growth is dominating (a, b) cases in Figure 2.15), the space starts being filled by loose sheet structures that densify. When both probabilities for plane growth and layering growth are equal (cases c) and d)), the space fills radially. When layering dominates over plane growth (e) and f) cases), the space is filled with needle-like features. When tilting is incorporated in a case with dominating plane growth (cases g) and h)), the resulting structure is less dense and more disordered. C-S-H has been proven to densify with hydration time by NMR [60], hence a dominating planar growth is in agreement with the densification of C-S-H. Moreover, the structures generated in cases b) and h) present similarities with TEM micrographs of outer product C-S-H in real cementitious systems (See Figure 2.16). The tilting chosen in cases g) and h) was needed to fit volume fractions derived from NMR [60].

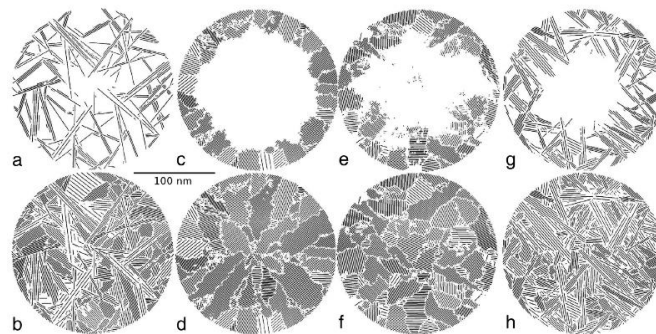


Figure 2.15. Different cross-sections of the structures generated using a sheet growth algorithm. The first row represents the starting growth at different configurations and the second row represents the final structures for the same configurations. The different configurations correspond to $p_p/p_l=10^4$ (a and b), $p_p/p_l=1$ (c) and d), $p_p/p_l=10^{-4}$ (e) and f) and $p_p/p_l=10^3$ with a tilting angle of 11° and a probability for tilting of 0.2.

2.6 Morphology, chemical composition and structure of C-S-H

The morphology of C-S-H has been a subject of debate for decades and has been studied in many different systems; varying from synthetic samples, C_3S pastes with and without admixtures, and cementitious systems with supplementary cementitious materials hydrated in different solutions. The application of Richardson and Groves' model to different pastes has meant the first more general attempt to establish a link between the morphology, the chemical composition and the chemical structure of C-S-H.

In the 1950's Grudemo [42] was the first to study C-S-H morphology by TEM and reported a change from foils to fibrils while increasing the Ca/Si. Kalousek and Prebus [61] reported the existence of three different products according to their Ca/Si ratios. Samples with $0.8 < \text{Ca/Si} < 1$ consisted of flat platy crystals. Crinkled foils were found when $0.8 < \text{Ca/Si} < 1.33$ in samples synthesized via silica-lime reactions, while fibrils appeared in systems with $1.5 < \text{Ca/Si} < 2$ formed by the reaction of CH and silica. Nonetheless, some of their high Ca/Si products were not homogeneous, and were possibly a mixture of a fibrous lime rich phase and a lower Ca/Si phase. Changes in C-S-H morphology on hydrating C_3S pastes at different hydration times were also studied with TEM by Collepardi and Marchese [62]. They found that the initial growing product was foil-like (at 4 hours of hydration) and was transforming into fibrils while increasing the hydration time (1 day and 100 days of hydration). When calcium chloride was added to the solution, this morphological change did not occur. This suggested that Cl^- ions could have been introduced in the structure to maintain the foil-like morphology. Following their publication, Berger et al. [63] extended their studies analysing C-S-H morphology in hydrated C_3S pastes including various different admixtures. They classified the resulting morphologies in two types: fibrillar and foil-like. Jennings et al. [64] elaborated a classification on C-S-H morphologies based on following the hydration of C_3S during the distinct stages upon heat evolution. They named Type E the product that appears during the induction period, which consists in flakes or thin sheets. The gelatinous product that grows during the acceleration period was named Type O. This product could develop into fibrils (Type 1), when the space availability was greater than $1\mu\text{m}$ or interlocked crumpled foils (Type 3) in confined space. They designated the dense inner product as 'late' product Type 4 and one last category as Type 1', which consists in tapered fibrils that develop from Type O if adjacent particles are pulled apart. The distinction between Type 1 (Fibrils) and Type 3 (interlocked crumpled foils) was questioned by Groves et al. [12], who preferred to call these two types as outer fibrillar product, since Type 3 shows some internal lamellar structure and it seems unlikely to have been formed by rolling foils, and seems to be fairly similar to Type 1. They suggested the different fibrillar products were a consequence of different growing aspect ratios due to space constraints.

In fully reacted Portland cement, C-S-H is accepted to have a Ca/Si ratio of ~ 1.7 and a fibrillar morphology. With the use of supplementary cementitious materials, the systems in which C-S-H forms vary widely, therefore its composition can also be very different ranging from Ca/Si of ~ 0.7 to ~ 2.3 [32]. The C-S-H morphologies found in these systems are fibrillar, foil-like or a mixture of both (See Figure 2.16).

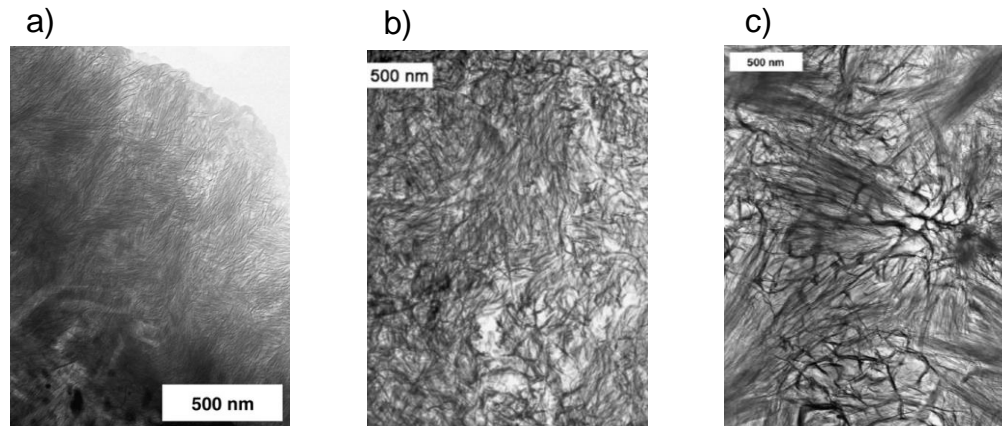


Figure 2.16. a) TEM micrograph showing fibrillar Op C-S-H in a 70% white PC-30% class F fly ash activated in water [65]. b) TEM micrograph showing foil-like Op C-S-H in a 10% OPC-90% GGBS blend [66]. c) TEM micrograph showing foil-like and fibrillar Op C-S-H in the same blend as a) [65].

To establish a relationship between the morphology, chemical composition and structure of C-S-H, a chemical structural model is needed. The most complete model up to date is Richardson and Groves [34]. Its flexibility implies it can be used for a wide variety of systems. Using the model with parallel morphological and ^{29}Si MAS NMR studies can serve to couple changes in morphology with changes in chemical composition and structure. Richardson reported the applicability of his model to different systems: hardened pastes of tricalcium silicate, β -dicalcium silicate, Portland cement and blends of Portland cement with ground granulated blast furnace slag, metakaolin and silica fume [1]. The results for water activated OPC-slag blends showed there was a change in C-S-H morphology from foils to fibrils as the Ca/Si increases, or the content of slag decreases. The application of Richardson and Groves' model to these blends indicated that a paste with 90% slag [67] (foil-like with $\text{Ca/Si}=1.26\pm 0.05$) was described only by using tobermorite like units, while a paste with 50% slag (fibrillar with $\text{Ca/Si}=1.56\pm 0.17$) was described by the T/J point of view. Different alkali hydroxide activated blended systems contained foil like Op C-S-H that could be accounted for the T/CH point of view or even explained by only tobermorite units. Data from Op C-S-H from a 5M KOH activated synthetic slag paste was well described by tobermorite pentameric units, a 5M KOH activated PC (Portland cement) -20% metakaolin blend was accounted for the T/CH point of view, a 5M KOH neat PC-50% slag was also accounted for the T/CH point of view

and the same blend changing the content of slag to 90% could be explained with tobermorite dimers and pentamers. By comparing the results on these pastes Richardson concluded that foil-like morphology can be associated to tobermorite units, while fibrillar to jennite ones. However, an open question about how growth kinetics may affect the C-S-H morphology was also raised: Is the morphology of C-S-H dependent on its chemical composition and structure or on the growth kinetics of each specific system? Richardson stated that it is possible that the rate at which chemical complexes are transferred from solution to the growing C-S-H particles depends on the chemistry of the systems, i.e., their activators (water or KOH), and can therefore determine the way C-S-H grows in one or two dimensions and in a more ordered or disordered manner [1].

Further work applying Richardson and Groves' model to pastes has shown contradictory results. Taylor et al. [66] reported that a neat PC paste that had fibrillar Op C-S-H could be explained by both T/CH and T/J points of view, but the data were more consistent with the T/CH model. This then questions the relationship of jennite units with fibrillar morphology. Moreover, a blended system with C-S-H that exhibited mainly foil-like morphology, but contained also areas with fibrils, was entirely explained by tobermorite units. If the chemical analysis was done only in regions with foils, the results agree with Richardson's conclusions, but if data was taken from points including both morphologies, the analysis would then contradict previous hypothesis, since the presence of fibrils was supposed to be associated with jennite units. Girão et al. [65] examined water activated and alkali hydroxide activated blends of white Portland cement with 30% fly ash. They found that the alkali activated blend had foil-like C-S-H and was well described by only tobermorite units, which seems to follow the trend found by Richardson for alkali activated pastes. The water activated blend showed a mixture of foil and fibrillar Op C-S-H and foil-like Ip C-S-H, and data from both Op and Ip C-S-H needed the presence of jennite or CH in the model, which is in agreement with Richardson's conclusions. The results of this last blend would have been more meaningful to prove that jennite may be responsible for fibrillar morphology, if regions with only fibrils and only foils had been analyzed separately, and data had been used as two separate inputs for the model.

With respect to the silicate anion structure, there are three types of silicate species which are normally found in C-S-H: chain-end groups or Q^1 (two silicate tetrahedra that share an oxygen atom), middle-chain groups or Q^2 (three silicate tetrahedra; the central one sharing an oxygen atom with each of the other two) and chain branching sites or Q^3 (four silicate tetrahedra; the central one sharing an oxygen atom with the other three). The examination of synthetic C-S-H has shown that samples with low Ca/Si ratios are dominated by Q^2 sites (longer silicate chains), while samples with higher Ca/Si are dominated by Q^1 sites (mainly dimeric silicate chains). The value of the Ca/Si ratio

at which Q^1 starts dominating the structures seems to depend on the nature of the samples (synthesis routes) and is in a range from 1 to 1.3 [39, 46, 48, 68].

2.7 The use of SANS to study C-S-H

SANS has been used in cement science from the 1980's, since it is very useful to probe the structure of colloids, and C-S-H can be considered of colloid nature. Allen et al. [69] used SANS to follow the specific surface area increase in OPC with hydration time. They concluded that the scattering signal was related to the hydration periods (induction and acceleration). The signal they found during the induction period was not varying and only originated from the scattering with the surfaces of the cement grains. After the induction period, they found increasing scattering associated with structures of ~5nm that were identified as C-S-H globules. To obtain the surface area values of C-S-H from a scattering curve of cement, it is necessary to employ an accurate value of the scattering contrast between C-S-H and water. Thomas et al. [70] obtained a defined value of this scattering contrast making use of SANS results from OPC at different saturation conditions with an exchange of H₂O by D₂O (heavy water), and obtained a value of $6.78 \cdot 10^{28} \text{ m}^{-4}$. This value was consistent with a C-S-H composition of C_{1.7}SH_{2.1} and a density of 2.18 g/cm³, values that included the interlayer water in the solid structure of C-S-H, but not the gel water. The composition of C-S-H was refined to C_{1.7}SH_{1.8} with a density of 2.6 g/cm³ by Allen et al. [53] combining SANS and SAXS (Small angle x-ray scattering). Thomas et al. [71] also showed that two different C-S-H morphologies with different surface areas grow during the hydration process. They monitored the surface area evolution of OPC by SANS and found out that the surface area was increasing rapidly in the first 24h of hydration and leveling off afterwards for the next 2 days (See Figure 2.17). Doing the same experiments with heavy water, that reduces the degree of hydration around 3 times [72], they found an increase in the surface area during 3 days of hydration. Their results are consistent with the growth of outer product C-S-H with high surface area and low density, which grows in the spaces originally filled with water, followed by the growth of inner product C-S-H with low surface area and high density due to the limitations in space availability. They also showed that the surface area increases with w/s ratio and that this increase was proportional to the volume fraction of water. These observations are also supported by other reported results of surface area coming from different techniques such as gas sorption, NMR and SAXS that Thomas et al. reviewed [73].

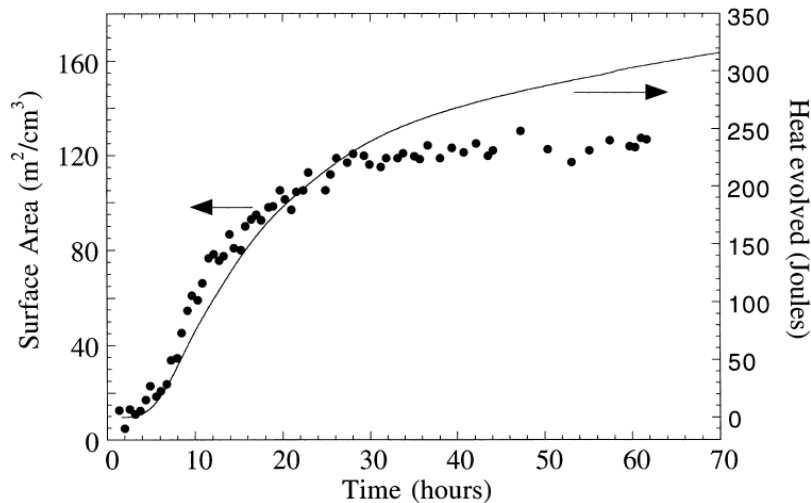


Figure 2.17. Surface area and heat evolved with hydration time for an OPC paste hydrated at 30°C and w/s=0.4. Taken from ref.[71].

SANS has also been used to study how degradation means and reaction accelerators/decelerators affect C-S-H structure. Allen [74] used SANS to prove that sulfate attack breaks down outer product C-S-H, while irradiation damage seems to affect inner product C-S-H. Thomas et al. [75] found that the surface area increases upon decalcification of cement and C₃S pastes with ammonium nitrate. Their results supported the idea of a growth of low density C-S-H with high surface area and a high density C-S-H with lower surface area that is measured by SANS before leaching. Allen and Thomas [76] studied the influence of CaCl₂ and sucrose in OPC hydration. They found that CaCl₂, which is an accelerator, increases the amount of outer product C-S-H; while sucrose, which is a decelerator, had no major influences on growing C-S-H. SANS can also serve to study changes in the development of C-S-H with the addition of supplementary cementitious materials. Allen and Livingston [77] studied blends of silica fume and OPC with SANS and concluded that the increase in the overall surface area that they found in blended systems with respect to OPC systems was due to the reaction of silica fume with OPC to form more outer product C-S-H.

The theory of fractal structures can be applied to scattering curves. The scattering intensity is fitted as a power law of Q (scattering vector) in which the exponent is linked to a fractal dimension that can be identified with a mass or volume fractal or a surface fractal. The fractal dimensions can indicate a density of the systems they represent, and can therefore be linked to the morphology. The fractal nature of pores in rocks was shown by Sen et al. [78] fitting SANS data. Häussler et al. [79] fitted scattering curves of C₃S that was stored at 100% RH for 24h at w/s=0.4, 0.52 and 0.6. They found a surface fractal (from C₃S) at w/s=0.4 and volume fractals (from C-S-H)

at the other two w/s. The fractal dimension of the volume fractal associated to C-S-H was decreasing with increasing w/s, indicating a structure that was more loosely packed. The results were compared with SEM studies of the same samples. The comparison showed that the sample was almost non-hydrated at the lower w/s. The hydration products were of different morphologies for the other two w/s, exhibiting a more open hydration shell at higher w/s. The same authors followed with similar studies of carbonation on C₃S samples [80]. They applied a model in which the scattering curve was fitted to a combination of a mass and a surface fractal obtaining information about the packing density of the carbonation products and the roughness of their surfaces. The same authors and Häussler and Tritthart also showed by SANS how carbonation increases with w/s [79, 81], finding an increase of the scattering in the Q range attributed to carbonation products. Thomas et al. [82] used SANS to study the changes on C-S-H structure upon drying and resaturation in young and mature cement pastes using a fractal model. Their results pointed out that the structural changes in C-S-H that occur upon drying are less significant in mature pastes, therefore they are more likely to retain structural features in C-S-H than young pastes.

Fratini et al. [83] combined Ultra-SANS with SANS to study the influence of superplasticizers (additives mainly used to improve the flow in concrete technology) in the hydration process of C₃S. Fitting the scattering curves with a model that takes into account the radius of the unreacted particles, they found that the use of superplasticizers reduces the size of the unreacted C₃S grains after one day, when compared with hydrated C₃S without superplasticizers. Thus the superplasticizer acted as an accelerator during the first day.

Chiang et al. [84] have recently developed a model to fit SANS data according to Jennings CM-II model. The parameters that describe the C-S-H globule geometry were estimated for synthetic C-S-H with different water contents. In the model, the globule is considered a multilamellar object with thickness t and radius R . Depending on the relation between R and t , the globule can adopt different geometries and become a disk-like, spheroidal or rod-like object. It exhibits an internal layered structure with alternated water layers of thickness L_1 , and calcium silicate layers of thickness L_2 , which are repeated n times. The interlayer spacing L is thus the sum of L_1 and L_2 . This model has been applied to C-S-H with Ca/Si 1.65 and water contents of 10%, 17% and 30% resulting in disk-like globules. Considering that L_2 is constant (as the Ca/Si is the same for all the samples) and has a value of 3.5 Å, the estimated water layer thickness increases upon water content from 5.51 Å to 7.86 Å. The average number of layers is 4.53, 4.73 and 10.86 as the water content increases. However, while the drier samples are dominated by globules with the average number of layers, the sample with 30% water content is dominated by globules with 2

layers. This leaves the description of the microstructure of this sample as a distribution of globules of different sizes, which may be a result of a high water to solid ratio used for the synthesis. These results suggest that upon drying, the globules decompose or collapse into a more uniform globule size. The same model was generalized by Chiang et al. [85] to be applied both to SANS and SAXS data to study the influence of superplasticizers on the structural parameters of C-S-H. They found that superplasticizers increase the average number of layers in C-S-H globules and that the volume fractal dimension was decreasing with respect to pure C-S-H, indicating more loosely packed structures. This was in agreement with SEM studies of the samples, which showed that the growth of C-S-H fibrils was suppressed by the use of the superplasticizers, since foil-like C-S-H was observed.

2.8 Synthesis routes to produce C-S-H

There are several routes to synthesize calcium silicate hydrates. They involve the reaction of either CH or CaO with silica in solution, the reaction of an alkali silicate with a Ca-salt (double decomposition), or the hydration of C₃S under certain conditions, sometimes combined with decalcification and recalcification processes.

2.8.1 A solution method

Cong and Kirkpatrick synthesized C-S-H with Ca/Si from 0.75 to 1.5 by dissolution and mixing [86]. Silica gel was dissolved in 5ml of 1M KOH solution and mixed with 10 ml of 1M CaCl₂ solution. The Ca/Si was controlled by varying the amount of dissolved silica. The reaction time was 15 min at room temperature. After reaction the samples were filtered and vacuum dried at room temperature. All the process was done under an N₂ flow to prevent the samples from getting carbonated. Some of the samples contained also CH.

2.8.2 Hydrothermal treatment

The hydrothermal synthesis consists in crystallizing C-S-H by a reaction performed in a high temperature solution at high vapour pressure. Mitsuda et al. [87] synthesized C-S-H by the reaction of CaO and silicic acid at saturated steam pressures. They stirred suspensions of initial Ca/Si ratios of 3, 2.5 and 2 at temperatures of 120, 150, 180 and 210°C obtaining C-S-H products of final Ca/Si ratios from 1.59 to 1.75. Depending on the temperature and Ca/Si ratios, several calcium silicate hydrate phases can exist under hydrothermal conditions. Shaw et al. [88] presented a driagram of the existence of these different phases from which Z-phase is a metastable crystalline phase. A more complete diagram by K. Garbev is shown in Figure 2.18 [89].

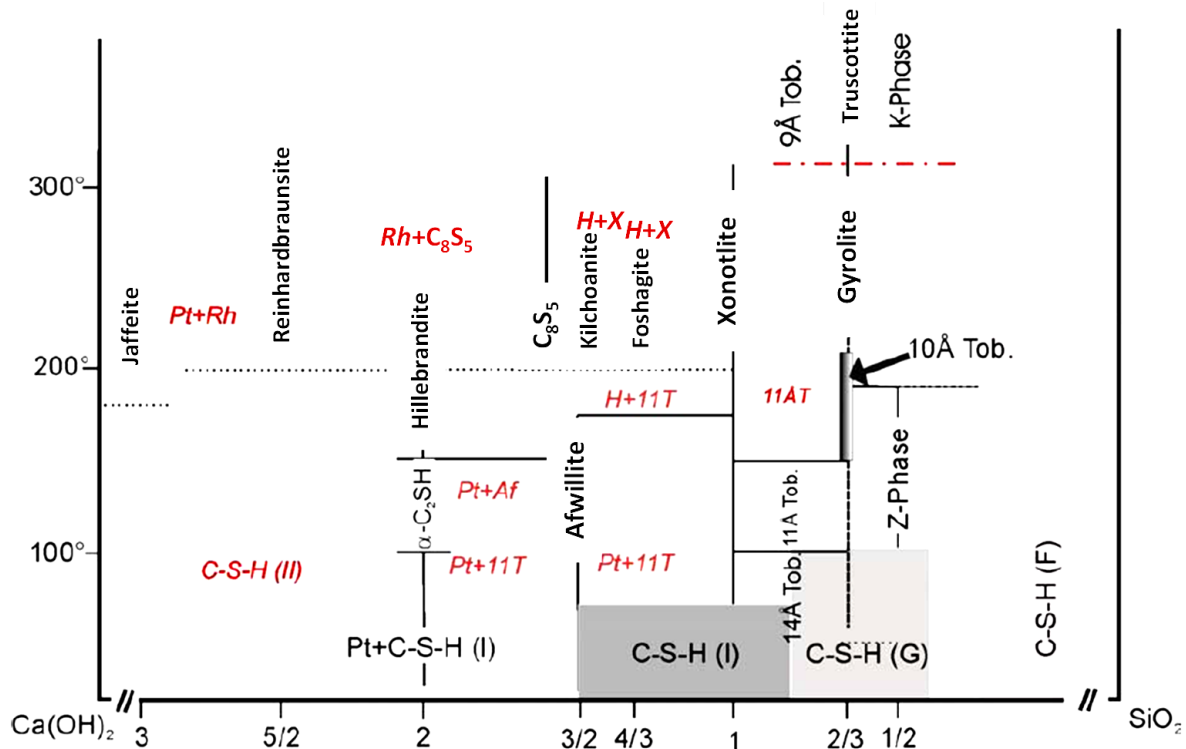


Figure 2.18. Diagram of the calcium silicate hydrate phases stable at hydrothermal conditions. The x axis represents Ca/Si and the y axis temperature. C-S-H (G) and C-S-H (F) stand for Gyrolite and Faujasite gel respectively. Pt, Rh, Af, 11T, H and X stand for Portlandite, Reinhardbraunsite, Afwillite, 11Å tobermorite, Hillebrandite and Xonotlite. Taken from ref. [89].

2.8.3 Mechanochemical method

Saito et al. used the mechanochemical route to produce afwillite $\text{Ca}_3(\text{SiO}_3(\text{OH}))_2 \cdot 2\text{H}_2\text{O}$ and tobermorite $\text{Ca}_5\text{Si}_6\text{O}_{16}(\text{OH})_2 \cdot 7\text{H}_2\text{O}$ [90]. A mixture of calcium hydroxide and silica gel with different contents of distilled water was ground at room temperature in a planetary ball mill in a pot of 45 cm^3 with seven steel balls of 15 mm diameter. After 15 min of grinding, the mill was stopped to prevent overheating. Afwillite was obtained when water/(water + mixture) was $\sim 0.23\text{--}0.30$ and $\text{Ca}(\text{OH})_2/\text{SiO}_2$ molar ratio was 1.5 and the grinding process was performed for 90 min or 120 min. Tobermorite was obtained when water weight rate was 0.8, $\text{Ca}/\text{Si}=1$ and the grinding time was 3 hours. Garbev et al. followed the same route. Changing the raw materials to CaO and Aerosil, they synthesized C-S-H (I) with different Ca/Si ratios [40]. The stoichiometric mixtures were milled for 36 hours with on-off cycles of 20 min and 10 min. All the preparation was done in an N_2 atmosphere to avoid carbonation. The slurries were then dried under N_2 during 120 h at 60°C . It was found that samples with $0.5 \leq \text{Ca}/\text{Si} \leq 1.2$ contained only C-S-H, while samples with $\text{Ca}/\text{Si} \leq 0.4$ contained also unreacted amorphous silica gel and samples with $\text{Ca}/\text{Si} > 1.2$ contained also CH. Thus, this method is suitable to fabricate single-phase C-S-H with $0.5 \leq \text{Ca}/\text{Si} \leq 1.2$.

2.8.4 Double decomposition

Another synthesis route to produce C-S-H is the so-called double decomposition. Chen et al. prepared synthetic C-S-H using this method mixing solutions of sodium silicate $\text{Na}_2\text{SiO}_3 \cdot 5\text{H}_2\text{O}$ and calcium nitrate $\text{Ca}(\text{NO}_3)_2 \cdot 4\text{H}_2\text{O}$. The mixture was stirred for 1 hour in a sealed container filled with N_2 . The precipitated material was washed with 2 l of a 20 mM CH solution. The equilibration of the samples was done in three different ways. The first one was simply in water or a CH solution obtaining Ca/Si from 0.92 to 1.48. Other samples were leached in ammonium nitrate and equilibrated in CH solution to final Ca/Si from 1.35 to 1.45 or leached in water and equilibrated in a CH solution to final Ca/Si from 1.26 to 1.28 [46].

2.8.5 Leaching of C_3S paste and recalcification

Chen et al. also synthesized a series of C-S-H with Ca/Si ratios from 0.62 to 1.4 by leaching a C_3S hydrated paste in an ammonium nitrate solution and equilibrating the solids in water [46]. The conditions of the preparation were as follows: C_3S was hydrated with deionized water with $w/s=0.5$, casted and demolded after 3 days. Then it was stored in a saturated CH solution in sealed containers for 8 months. Discs of 0.8 mm thickness of the samples were stirred in a solution of 6M NH_4NO_3 until the sample reached a desired weight loss that was predetermined to give certain Ca/Si ratio. The relationship between the weight loss and the Ca/Si ratio is illustrated in Figure 2.19. It is linear with two different slopes. Up to Ca/Si ratio 1.4, the weight loss is due to the replacement of CH with water, which is completely removed up to this point. For higher Ca/Si the decalcification of C-S-H starts taking place [18]. After removing the samples from the solution, they were immersed in deionized water to remove NH_4NO_3 and equilibrated in water.

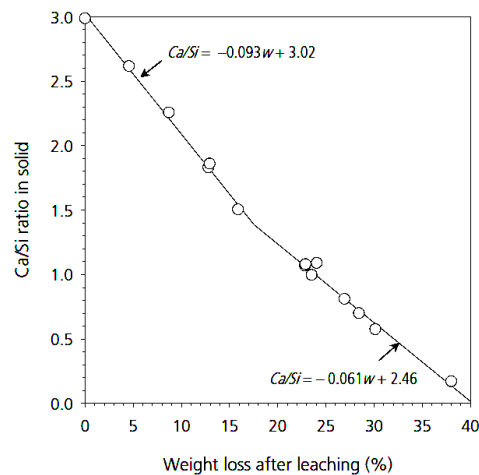


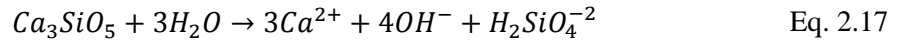
Figure 2.19. Relationship between Ca/Si and weight loss after leaching of a C_3S paste in NH_4NO_3 [18].

Chen et al. synthesized C-S-H with higher Ca/Si by a similar method to that explained previously, but equilibrating samples that were decalcified in ammonium nitrate until they reached Ca/Si=1.09 and recalculating them in a CH solution. The Ca/Si of this series ranged from 1.08 to 1.87 [46].

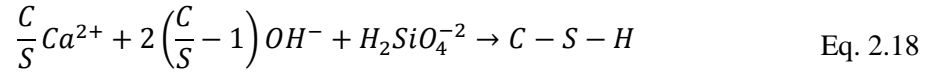
2.8.6 Hydration of C₃S at constant lime concentration

Another synthesis route that offers flexibility in the final Ca/Si ratio is the hydration of C₃S at constant lime concentration, which was implemented by Nonat and Lecoq [49].

The dissolution of tricalcium silicate in water gives the following species [91]:



As the solution starts becoming supersaturated with respect to C-S-H, its nucleation proceeds [91]:



Since all the calcium in the dissolution is not consumed by the precipitation of C-S-H, the solution starts getting saturated with respect to portlandite that also precipitates [91]:



To maintain the lime concentration constant in the solution, the (3-Ca/Si) mol of Ca(OH)₂ have to be removed. This is done by sucking up a volume (3- Ca/Si)/C₀ (C₀ is the lime concentration to be kept constant) from the solution by an air pump through a filter and replacing it by the same volume of pure water. [91]. Measuring the electrical conductivity, which is proportional to the CH concentration, the lime concentration is monitored. To enhance the complete hydration of C₃S grains, the solution can be under strong ultrasonication. This prevents C-S-H from growing and nucleating on the surface of the grains, but does not remove it from the surface completely. After complete hydration (less than 48 hours), the samples were filtered, washed with acetone and ether and dried under vacuum. Maintaining the lime concentration from 6mmol/l to 30 mmol/l, C-S-H can be synthesized by this method with Ca/Si ratios from 1.2 to 2.

The Ca/Si versus the lime concentration is illustrated in Figure 2.20. There is an abrupt change in Ca/Si ratio at ~22mmol/l of lime concentration, which coincides with the lime saturation value for the precipitation of portlandite. This was already noted by Steinour [92].

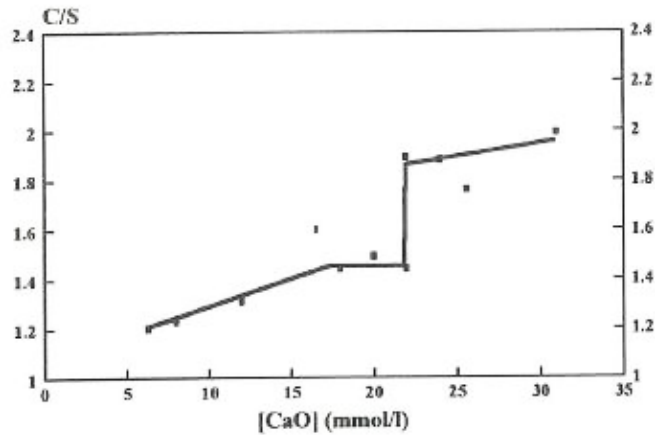


Figure 2.20. Ca/Si ratio of C-S-H prepared by the full hydration of C_3S at constant lime concentration [49].

Taylor chose the curve in Figure 2.21 [4] as the typical to represent the variation in Ca/Si of C-S-H with lime concentration in solution at equilibrium. This curve presents a step at Ca/Si 1.1. Grutzeck et al. [48] obtained a similar curve for the Ca/Si versus Ph and concluded the step was due to a change from a tobermorite based structure to a jennite type one.

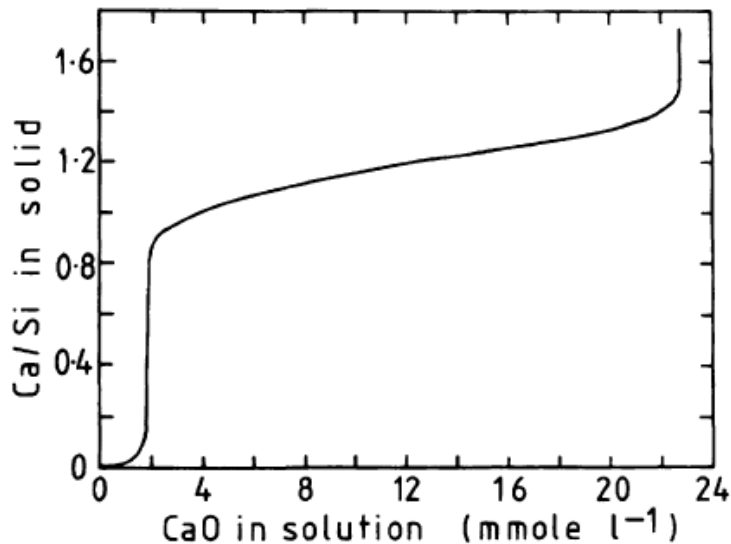


Figure 2.21. Typical metastable equilibrium curve for Ca/Si ratios of C-S-H vs. the lime concentration in solution. Taken from ref. [4].

A recent thermodynamic model developed by Haas and Nonat [93] defends the existence of three curves for Ca/Si vs. [CaO], that correspond to the solid-solution equilibrium of C-S-H defined by three different structural units. The structural units are shown in Figure 2.22 and correspond to α , β and γ -C-S-H with increasing Ca/Si ratios, according to Nonat's structural model of C-S-H [49]. For Ca/Si ratios between 0.75 and 1, the chosen structural unit is a pentamer with Ca/Si=0.8, for Ca/Si ratios between 1 and 1.5 the structural unit is a dimer of Ca/Si=1, and for Ca/Si>1.5 the structural unit is a hypothetical double dimer with Ca/Si=1.5 with two protons substituted by Ca-OH⁺ groups. The curves that the model generated for solubility equilibrium are shown in Figure 2.23 together with experimental data.

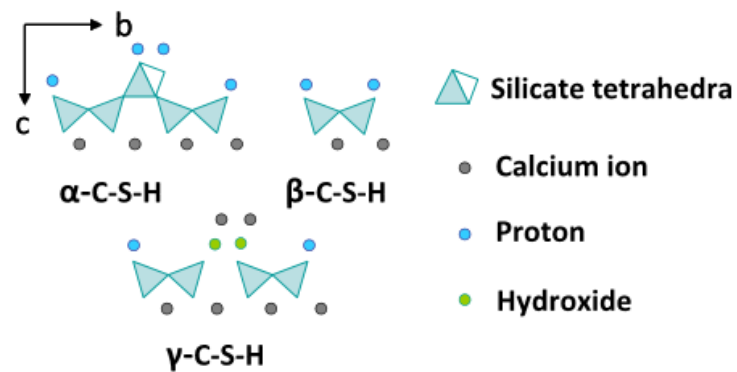


Figure 2.22. Structural units used by Haas to build solubility equilibria of C-S-H. Taken from ref. [93].

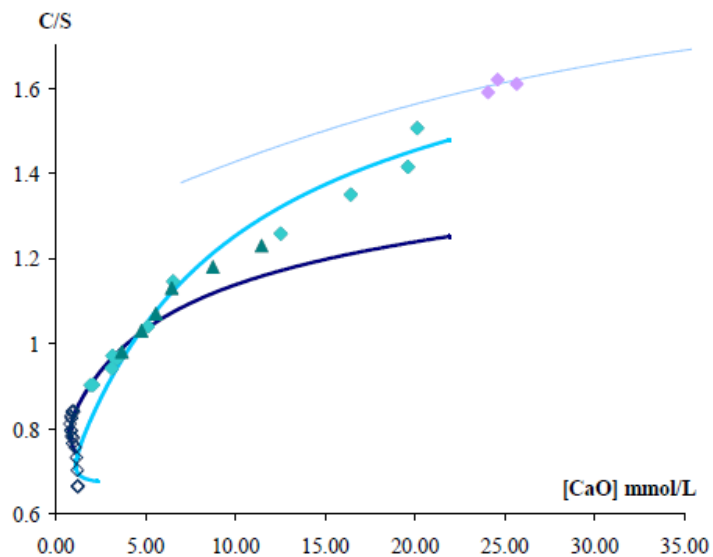


Figure 2.23. Simulation of the stoichiometric evolution of C-S-H with the lime concentration in solution at equilibrium built with the three structural units in Figure 2.22. Taken from ref. [94].

2.9 Synthesis methods to produce C-A-S-H

Aluminium substituted C-S-H, called C-A-S-H, can be fabricated mechanochemically adding $\text{Al}(\text{OH})_3$ to the mixture of CaO and SiO_2 . Black et al. synthesized aluminium substituted tobermorite by this method. They obtained nanocrystalline material after milling the mixture for 32 hours and heat it in an autoclave to make it crystallize into tobermorite [95].

Another method of fabricating C-A-S-H is adding already synthesized C-S-H into a calcium aluminate solution. Pardal et al. used this route to produce C-A-S-H starting with C-S-H with Ca/Si ratios of 0.66, 0.95 and 1.42. C-S-H was added to a calcium aluminate solution obtained by hydrating $\text{Ca}_3\text{Al}_2\text{O}_6$ in a diluted suspension. They obtained single-phase samples for the lower two Ca/Si ratios. The Ca/(Si+Al) ratio of the final products was very close to the initial Ca/Si ratio. The Al/Si ratios of the samples depended on the aluminate concentration in the equilibrium solution and ranged from 0.1 to ~0.3, being almost constant at a value of 0.18 for the C-A-S-H samples synthesized from the 0.66 C-S-H samples [96].

3 Characterization techniques

A general description of all the experimental techniques used in this study is presented in this chapter. All the sections include a short explanation on the working principles of the techniques, a short review of their use in cement science and the motivation to use them in this study of C-S-H.

3.1 STA

The changes that a substance undergoes under thermal treatment are monitored as a function of temperature in thermal analysis. STA combines two types of analysis: TG (Thermogravimetry) and DTA (Differential thermal analysis). TG analysis consists in recording the weight loss as a function of the temperature while a sample is being heated at a constant rate in a crucible. DTA monitors the difference in temperatures of the sample of interest (s) and a reference sample (r) $\Delta T = T_s - T_r$, while both of them are heated at the same rate. Thus in DTA, exothermic and endothermic processes are shown as peaks and valleys with respect to the base line respectively [97]. STA can serve to identify the phases present in a sample and to quantify them.

TG applied to cement pastes in which hydration has not been stopped can serve to estimate the w/s ratio by knowing the percentage of residue left in the crucible r_s :

$$\frac{w}{s} = \frac{100 - r_s}{r_s} \quad \text{Eq. 3.1}$$

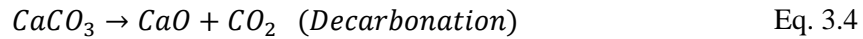
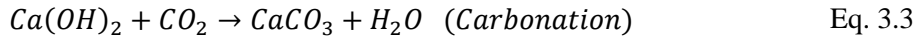
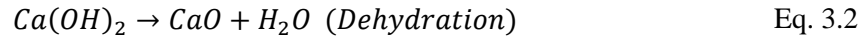
DTA peaks are characteristic of the phases that are present in the sample and in the particular case of pastes of calcium silicates, the peaks that are found are the following:

- Below 200°C : Endothermal peak that represents the dehydration of C-S-H
- 450°C-550°C: Endothermal peak that is associated to the dehydration of CH
- 600°C-780°C: Decarbonation of calcium carbonates

Other peaks corresponding to crystal transformations, such as the formation of wollastonite may appear at higher temperatures. In the case of cement samples, peaks related to gypsum and ettringite are also detected in DTA curves as endothermal effects at 150°C-200°C and 110°C-125°C respectively [97].

The amount of calcium hydroxide in a sample can easily be calculated from a TG curve taking into account the reactions in which CH is involved and considering all the carbonates are due

to the carbonation of CH. The reactions for a general case in which calcium carbonate is present in the sample are the following:



To obtain the amount of CH, the weight losses for the dehydration (w_{deh}) and decarbonation (w_{dec}) have to be calculated.

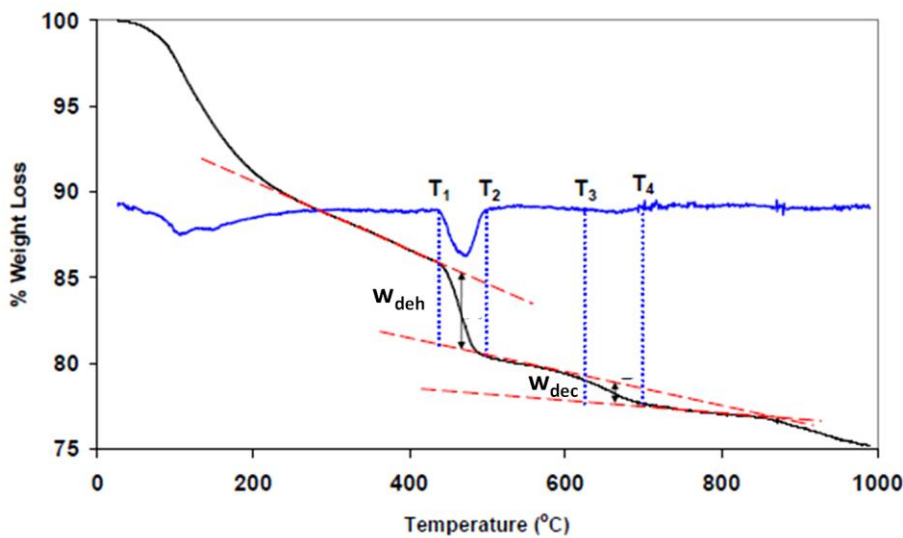


Figure 3.1. Typical TG curve for a cementitious material (Derivative shown in blue) [98].

The onset and the end of these weight losses can be estimated thanks to the inflexion points of the derivative of the TG curve. Once these points are identified, two tangent lines are drawn in the TG curve. The inflexion points are then joined by a line in which a middle point is considered. A vertical line passing through the middle point is drawn until touching the tangents. The vertical length of this line is then measured as a percentage in weight loss, see Figure 3.1.

Taking into account that from the dehydration of CH, 74 g of CH yield 18 g of water and from the carbonation and decarbonation reactions, 74 g of CH yield 100 g $CaCO_3$, that upon heating release 44 g of CO_2 , the amount of CH in the sample is:

$$CH = \frac{74}{18} w_{deh} + \frac{74}{44} w_{dec} \quad \text{Eq. 3.5}$$

The standard way of expressing the amount of CH is as ignited weight, dividing the amount of calculated CH by the percentage of residue left in the crucible.

3.2 XRD

X-rays are used to study long range order in crystalline materials. They are a suitable tool to get information of materials such as lattice constants, structure and orientation, because their wavelength is in the order of several ångströms which is the range order of lattice constants. They can also be used for identification and quantitative determination of phases in a compound material. In cement science XRD is used to identify the crystalline phases present in a sample, since their individual diffraction patterns are unique, and to quantify them separating their contributions by Rietveld refinement. This method was introduced by Hugo Rietveld for neutron scattering and was later adapted to XRD [99]. An x-ray photon can interact with an atom in different ways being scattered, diffracted, reflected or absorbed. For diffraction to occur, the x-rays that are reflected from different atoms in different planes have to be in phase. This is expressed as the diffraction condition which is known as Bragg's law:

$$n\lambda = 2d\sin\theta \quad \text{Eq. 3.6}$$

Where n is an integer called the order of diffraction, λ is the x-ray wavelength, d is the interplanar spacing and θ is the incident angle measured from the reflecting plane, see Figure 3.2.

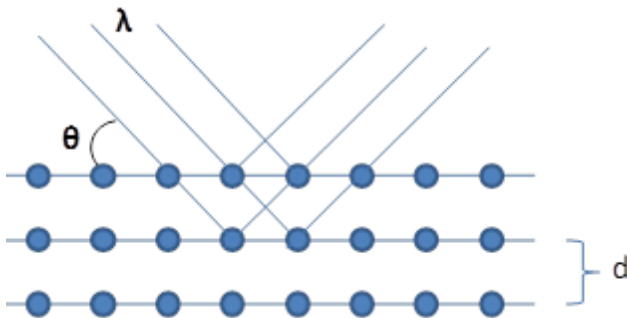


Figure 3.2. Schematic representation of Bragg's law in real space.

In the specific case of a cubic cell, the interplanar distance for a set of (hkl) planes is related to the lattice constant a by the following expression:

$$d = \frac{a}{\sqrt{h^2 + k^2 + l^2}} \quad \text{Eq. 3.7}$$

By varying the incident angle, the Bragg's law is satisfied by different interplanar spacings in polycrystalline materials. Plotting the intensities of the diffracted beam versus 2θ gives characteristic patterns of a sample. The comparison of these patterns with a data base can then serve to identify the phases present in a sample and their degree of crystallinity. This is possible because peaks are sharper when they belong to well defined crystals and broad when the strain and/or the crystallite size are not uniform, which implies the existence of more amorphous phases [100]. Comparing the XRD patterns of C-S-H phases in real systems, synthetic preparations and natural occurring C-S-H phases such as tobermorite or jennite, has shown that C-S-H in real systems is more amorphous than synthetic preparations, which also present less long range order than natural minerals.

3.3 XRF

X-ray fluorescence is used in cement science to estimate the oxide bulk content of samples. In the particular case of C-S-H, it can serve to give a rough estimation of the Ca/Si ratio by knowing the CaO and SiO₂ contents. The technique consists in irradiating a sample with high energy X-rays. The sample absorbs the incident X-rays and this causes the ejection of electrons from the low energy levels creating holes. These holes are then filled due to electronic transitions from higher levels. During the transitions, characteristic X-rays of the elements are emitted and detected to identify the elements present in the sample [101, 102].

3.4 TEM and EDX

TEM is a very useful technique to analyze the morphology of C-S-H in the scale of hundreds of nanometers. The chemical analysis performed by EDX in a TEM can serve to characterize and quantify the chemical species present in C-S-H, since it is possible to focus the beam on areas free of admixture with other phases. C-S-H can be intermixed with other phases in a very fine scale. The analysis of single phase areas can be difficult with other techniques such as SEM, because the x-ray generation volume in this technique is much bigger than the intermixture volumes of hydration products. It is important that for EDX in TEM the analysis is done in very thin areas, because if the analysis is done in a thick area, some of the X-rays that are emitted from the material can also be adsorbed modifying the results [103].

TEM is based on the transmission of an electron beam through a sample. The electron beam is generated by a thermionic gun or a field emission gun and interacts with optical elements and the sample to form an image. The optical elements are two condenser lenses that are placed under the gun, an objective lens, an intermediate lens, a projector lens, and several apertures. The

electron beam is first focused by the two condenser lenses on the sample, which is located at the objective plane of the objective lens. The transmitted and diffracted beams form an image on the image plane of the objective lens. This image is magnified and projected into a fluorescent screen or a CCD-camera by the intermediate and projector lenses. The kind of information that can be extracted using a TEM depends on the focal point of the system. If the focal point is no longer the image plane of the objective lens but the back focal plane, diffraction patterns are obtained instead of images. They are representations of the reciprocal space of a specific area of the sample. The geometry of the diffraction patterns is related to the microstructure and can serve to identify crystalline or amorphous phases [104]. Spot-like patterns are characteristic of partly crystalline materials and can be indexed, while amorphous materials yield patterns with halos [105]. The identification of the patterns is done following the expression $d \cdot r = \lambda \cdot L$, where d is a planar distance in the sample, r is the radius of the diffraction ring and $\lambda \cdot L$ is a constant formed by the product of the wavelength of the electrons λ and the distance from the diffraction object to the screen L .

Three types of images can be taken in TEM, so-called bright field, dark field and high resolution images. In the bright field mode an aperture is inserted in the back focal plane of the objective lens to block the diffracted beams. This results in a contrast image where the areas of the sample that diffract more appear dark while the areas of the sample where the electron beam is more transmitted straight through appear bright. In the dark field mode the aperture is placed so that the transmitted beam is blocked. Thus the contrast is reversed with respect to bright field mode. In HRTEM (High Resolution transmission electron microscopy) the aperture is removed and the image is formed by a contribution of both transmitted and diffracted beams. The images then may have atomic resolution and thus enable to study the crystallographic structure at atomic scale [104]. TEM bright field images have been widely used to characterize the morphology of C-S-H and examine its admixture with other phases in cement pastes. For taking images of C-S-H, it is particularly important not to exceed the magnification up to $\times 20000$, because serious beam damage can be induced in the sample, which can affect the interpretation of images and the chemical data. Hydrated cements have low melting temperatures and low thermal conductivity which can lead to thermal damage. They can also suffer from irradiation damage due to electron bombardment causing mass loss [103]. Thus HRTEM images have low applicability to cementitious systems.

The chemical analysis in TEM is done with EDX. When a specimen is irradiated by a beam of electrons, the interaction of these electrons with the atoms in the specimen can yield two types of X-ray radiation. When the electron is inelastically scattered, the loss of its kinetic energy is translated into the emission of continuum or background radiation. If the electron knocks out an electron from the inner shells of an atom in the specimen, another electron from an outer shell can

fill the vacancy. The energy difference between the shells is emitted as a characteristic X-ray, which is unique for every element, and thus serves to identify chemical species in a sample. Depending on the shells where the vacancy is and the electron that fills the vacancy comes from, different types of characteristic X-rays are emitted, being $K\alpha$, $K\beta$, $L\alpha$, $L\beta$... (see Figure 3.3).

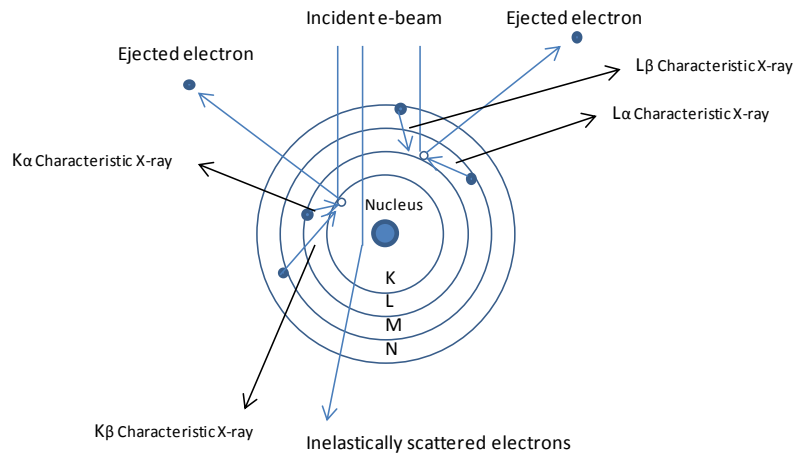


Figure 3.3. Schematic representation of the emission of characteristic X-rays due to e-beam excitation of an atom [103].

3.5 SEM

An SEM is based on the interaction of an e-beam with a sample. The beam emitted by a gun is focused on the sample by a lens system with typical probe sizes from 30 to 60 Å. SEM can provide information about topography, morphology, elemental composition and electronic properties of the material. The excitation in a sample goes from 0,5 to 3µm from its surface and results in ejection of electrons and photons, which can be collected, detected and evaluated. The different signals come from:

- Backscattered electrons: They are electrons that belong to the excitation electron beam and are ejected after suffering several collisions in all the excitation volume of the sample. Their energy ranges from 50eV to the energy of the excitation beam and they are originated in an area of the sample located at 1-2µm from the surface. They give information about composition (average atomic number), crystallography and topography.
- Secondary electrons: They are ejected after inelastic collisions with electrons of the excitation beam or backscattered electrons. Their energy is < 50eV. They come from the surface of the sample (50-100Å), thus providing topographic information.

- Auger electrons: The excitation beam can create vacancies in the core shells of the specimen atoms. If electrons from outer shells occupy these vacancies, but part of the energy is transmitted in a radiationless process to another electron, this electron can leave the atom and is called auger electron. These kind of emitted electrons have constant kinetic energy between 10 and 2000 eV. They can be created in all the excitation volume, but as their mean free path is on the order of only a few atomic layers, only the auger electrons created in the topmost layers (10 Å) contribute to auger peaks, while the rest to the secondary electron background. They are then suitable for surface elemental analysis.
- Characteristic X-rays: The emission of X-rays is due to the kind of interactions already described in section 3.4 for TEM. They are originated at 2-5 μm from the surface of the sample. They can provide quantitative and qualitative information about sample composition and elemental distribution.
- Visible light (cathodoluminescence): It provides information about the optical and electronic properties, as for example the band gap in semiconductor materials.

From all these signals, backscattered electrons and secondary electrons are used for imaging and have been widely employed for cementitious materials. Backscattered images from flat polished surfaces have mostly been used to quantify the phases and the porosity present in a sample by assigning a grey level to each phase and pores and quantifying the areas that correspond to each of them. The contrast and brightness have to be set up so that all the required information is present in a grey-scale histogram. Analysis of a number of images is required to obtain significant data, since each image may correspond to a small area of the sample which may not be so representative. Secondary electron images are mainly used to characterize the morphology on fracture surfaces [103]. These images can be very useful to detect crystals of portlandite and calcite, which can be difficult to appreciate in a TEM.

The elemental analysis with EDX in SEM is of limited application in the case of the study of C-S-H in cementitious systems. This is due to the fact that the interaction volume in the sample for SEM is bigger than the volumes where C-S-H is present free of admixture with other phases. Thus normally the Ca/Si ratios obtained by this technique are not representative of the phase, but of a mixture of phases. This can be checked by plotting Al/Ca ratios versus Si/Ca and observing if the data follow the typical trends of other phases.

3.6 NMR

NMR is based in the splitting, under the influence of an external strong magnetic field, of the degenerate energy levels of nuclei that have non-zero nuclear spin such as ²⁹Si, ²⁷Al, ¹⁷O or ¹H.

If the sample is simultaneously exposed to a radiofrequency pulse, transitions between the energy levels can be observed as resonant absorption of photons. The frequencies at which absorption occurs are called chemical shifts and depend on the chemical environment of the nuclei, thus NMR serves to characterize the local chemical environment of certain atomic species in a sample. To make results from different spectrometers comparable and eliminate effects of the strength of the magnetic field, the chemical shifts (differences in resonance frequency of the sample and a reference) are recorded in ppm as the ratio of a shift in Hz to a resonant frequency in MHz. The anisotropic environment of atoms in solids results in a considerable peak broadening in an NMR spectrum [3]. This fact limited its application only to liquids until it was discovered that spinning the sample at an angle $54^{\circ} 74'$ to the magnetic field, the so called magic angle, served to resolve the spectrum [106]. Long range order is not required to obtain NMR data, which makes this technique particularly useful to study C-S-H, since it is nanocrystalline.

^{29}Si DP MAS NMR (Direct pulse magic angle spinning nuclear magnetic resonance) is used to gain information about the silicate anion structure in C-S-H. The silicate species can be quantified by the deconvolution of the spectrum, since the intensity of the spectrum is directly proportional to their concentration due to the fact that the NMR spectrum is a sum of all the signals of each Si nuclei. The chemical shifts of the silicate species depend on the condensation of the silicon-oxygen tetrahedra. In the particular case of cementitious materials, the different silicate species give typical chemical shifts in the ranges specified in Table 3.1.

Table 3.1. NMR shifts for silicon in cement pastes [3].

Type of silicate	Designation	Chemical shift (ppm)
Monomers	Q^0	-66 to -74
Dimers	Q^1	-75 to -82
Middle chain groups	Q^2	-85 to -89
Chain branching sites	Q^3	-95 to -100
Three dimensional network	Q^4	-103 to -115

Monomers (single silicate tetrahedra) are present in alite and belite, although several authors have observed hydrated monomers, denoted $Q^0(\text{H})$, in the early stage hydration of tricalcium silicate pastes [47, 107, 108]. C-S-H generally presents Q^1 and Q^2 groups indicating that it has single linear chains. Q^1 can be isolated dimers or end-chain groups and Q^2 can be bridging sites (at ~ 82 ppm) or middle-chain groups (at ~ 85 ppm). When Al substitutes Si in a bridging site, the Q^2 for the adjacent Si tetrahedra is denominated $Q^2(1\text{Al})$ and it is located at ~ 82 ppm [109,

110]. The polymerization of C-S-H gel to yield Q^3 and Q^4 sites (five silicate tetrahedra; the central one sharing an oxygen atom with each of the other four) can happen in old pastes and partly carbonated ones [111]. The quantitative analysis of the DP spectrum can give additional information apart from the percentage of the silicate species, such as the mean alumino-silicate chain length, the degree of hydration and the Al/Si ratio.

A different technique, ^{29}Si - ^1H CP NMR (Cross polarization), can be used to study the hydrated phases. In the cross polarization mode the resonance condition for ^{29}Si occurs due to the transfer of energy from ^1H , thus the technique detects Si atoms in proximity to H atoms, i.e. hydrated phases. Tong et al. [112] compared DP and CP spectrums of hydrated $\beta\text{C}_2\text{S}$ and showed that the CP spectrum lacked the anhydrous peak typical of Q^0 sites at -71.3 ppm, which is attributed to $\beta\text{C}_2\text{S}$. Bellmann et al. [108] used ^{29}Si - ^1H CP NMR to show the existence of an intermediate hydration phase with hydrated silicate monomers during the induction period of the hydration of C_3S . Other more complicated experiments in two dimensions, such as ^{29}Si - ^{29}Si homonuclear double quantum correlation or ^1H - ^{29}Si heteronuclear experiments, have been applied to C-S-H to establish the connectivity between the different silicate Q species [50]. The conclusions of these studies by Brunet et al. pointed out a constant increase in the mean silicate chain-length with decreasing Ca/Si ratio. They claimed the increase in the formation of Q^1 isolated dimers while increasing the Ca/Si. This contradicts Cong and Kirkpatrick's observations [113] that agreed with a bimodal distribution of chain length. For samples with $\text{Ca/Si} > 1$, they suggested the coexistence of dimers and relatively long silicate chains and attributed the increase in Ca/Si ratio to the formation of dimers maintaining the mean chain length constant.

NMR offers other possibilities to investigate the chemical environments of other elements. ^{27}Al MAS NMR can be used to identify whether Al is substituting Si in tetrahedral or octahedral coordination [114]. ^{17}O MAS NMR results have shown the existence of at least six environments for oxygen in C-S-H: Two NBO (non-bridging oxygens bonded to a Si atom), BO (bridging oxygens bonded to two Si atoms), Ca-OH, Si-OH and H_2O . The results also point a dependence of the chemical shifts of NBO and BO with the Ca/Si ratio, becoming more positive (more deshielded) with increasing Ca/Si ratio [115]. ^1H NMR can be used not only to investigate the chemical environment of H, but also to follow the cement hydration and identify different water states [116] (solid or mobile water) and to describe the pore-size distribution in hydrating cements [117]. This has been possible using the fast diffusion model of relaxation [118], that was first applied to cements by Halperin et al. [119]. This model relates the surface/volume fraction of a water filled pore with characteristic NMR relaxation times. This technique, combined with XRD, has recently been applied to white cement pastes in order to follow the density of C-S-H as a function of w/s

ratio and degree of hydration [60]. The results show five distinct populations of water: bound water in CH and ettringite, interlayer C-S-H water, C-S-H gel pore water, water in nanoscale interhydrate spaces and free water or water in large capillary pores. Quantifying these populations at different w/s ratios and degrees of hydration, has shown that until 1 day of hydration, C-S-H interlayers and gel pores are formed while water in capillary pores is being consumed. From that point onwards, the amount of C-S-H gel pores seem to be constant, while interlayers keep growing in expense of the consumption of free water. The same experimental procedure has enabled the measurement of the first pore-type resolved desorption isotherm of cement paste, showing the location of water in different pores as a function of the relative humidity [120]. ^{13}C MAS NMR has recently been applied to cement pastes and synthetic C-S-H phases to study the degree of carbonation and how it affects the silicate anion structure. The results reveal that carbonation induces decalcification, which is slower in the case of high Ca/Si ratios. The process converts Q^1 silicate species into Q^2 , that finally transform into Q^3 and Q^4 when all the silicate chain structure has decomposed [121].

4 Experimental details

4.1 Sample description

The following types of samples have been analyzed:

- A 5 year-old C_3S paste with $w/s=0.5$, which was stored in a sealed mould in a water bath at $25^\circ C$ (Kindly provided by Q. Li).
- 7 year-old mechanochemically synthesized C-S-H with Ca/Si ratios of 0.66, 0.75, 1 and 1.5, fabricated by Garbev et al. following the route described in section 2.8.3 [40].
- Fresh mechanochemically synthesized C-S-H with Ca/Si=0.75, 0.83, 1, 1.25, 1.33 and 1.5. The raw materials and optimization of the fabrication method are specified in section 4.2.2.
- A C-S-H series with Ca/Si= 0.75, 0.8, 1, 1.27, 1.35 and 1.42 synthesized via CaO-SiO₂ reactions under continuous stirring (Kindly provided by A. Nonat). The synthesis method is described in section 4.3.
- A C-S-H batch fabricated hydrating C_3S at constant lime concentrations from 12 to 27mmol/l and $w/s=50$, in which the hydration was stopped at the acceleration period and deceleration period for each lime concentration to address how the reaction kinetics affect C-S-H morphology. The synthesis details are described in section 4.4.1.
- A C-S-H series fabricated via the controlled hydration of C_3S at lime concentrations of 27, 28 and 29mmol/l with $w/s=50$ using an ultrasound gun to promote faster hydration and obtain purer C-S-H. The synthesis details are described in section 4.4.2.
- A C-S-H series fabricated via the controlled hydration of C_3S at lime concentrations of 27, 28 and 29mmol/l (without the control of w/s) using 1ml of Xseed solution to aid the reaction and obtain purer C-S-H. The synthesis details are described in section 4.4.3.
- A C-A-S-H series with Ca/Si=1 and Al/Si=0, 0.001, 0.002, 0.003, 0.004 and 0.005. The synthesis details are described in section 4.5.

Since C-S-H in real cementitious systems grows primarily from the hydration of C_3S , the C_3S paste has been chosen as a standard cementitious system comparable with OPC. The fact that it was a 5 years old paste, implies it was expected to be fully reacted, so that most of its volume was C-S-H, being thus an ideal system to study this phase. The 7 year old mechanochemical C-S-H series was chosen because studies including synchrotron X-ray diffraction [40], XRD and TG [122], XPS [123] and Raman spectroscopy [68, 124] had been published on these samples, but their morphology was never studied by TEM. TG revealed some of the samples in this group were carbonated, probably due to improper storage. That is why a new series of fresh C-S-H samples was fabricated by a similar method. Another series fabricated with the same reactants (CaO-SiO₂) via a

softer route, was studied to be compared with the mechanochemical series. This comparison was done with the aim to assess how changes in the synthesis route can affect the morphology of the final product. The limiting Ca/Si ratio of samples fabricated via silica-lime reactions is accepted to be 1.5. To obtain C-S-H with higher Ca/Si ratios C_3S is normally involved. The hydration of C_3S at constant lime concentration is a very versatile method to produce C-S-H with a wide range of Ca/Si from 1.2 to 2. This is the main reason why the batch fabricated via this method was chosen. Moreover this synthesis route allows the study of both fast and slow growth regimes of C-S-H, and therefore, it is useful to study the role of kinetics in the formation of C-S-H. Another two other batches of samples fabricated via the controlled hydration of C_3S with accelerators (ultrasound gun and Xseed) were chosen due to their higher degree of reaction compared to the previous series; hence higher content of C-S-H and less content of C_3S . The synthesis of these samples was performed at high lime concentrations in order to obtain purer C-S-H with $Ca/Si > 1.5$. Finally a C-A-S-H series was chosen because it is common that Al^{3+} substitutes Si^{4+} in the silicate chain of C-S-H that forms in OPC pastes and in OPC blends with supplementary cementitious materials. The chosen Al/Si ratios represent either C-A-S-H in OPC pastes or very early hydration stages in blends with no alkali content. The Al/Si ratios of C-A-S-H depend on the hydration time, activators and blends. For metakaolin blends the Al/Si can vary from 0.06 to 0.28 from 1 to 28 days of hydration in water, and from 0.27 to 0.34 from 1 to 28 days of hydration in a KOH solution (alkalis are also incorporated in C-S-H in this case) [110]. OPC old pastes (20 years old) present an Al/Si ratio of 0.09 and a 20 years old blend with 90% GGBFS has an Al/Si of 0.18 [66].

4.2 Fresh mechanochemically synthesized C-S-H: Synthesis details

The synthesis details for the mechanochemical route were optimized in terms of the raw materials used, milling time and the drying process, to ensure single phase samples were formed when possible and all the materials had reacted.

4.2.1 Test samples

Several tests were run using CaO freshly obtained from roasting $CaCO_3$ at $900^\circ C$ for 3 hours in an oven and nanosilica (Elkem), that was also roasted at the same conditions than the $CaCO_3$. The details of the nanosilica as specified by the supplier are given in Table 4.1. They show the nanosilica contained several impurities that correspond to $\sim 3.7\%$ in mass.

After being roasted, the materials were transported to a glovebox in a desiccator with a little container full of liquid N_2 to avoid carbonation. An N_2 cylinder was connected to the glovebox, which was then pumped and filled with N_2 for three consecutive times to provide an N_2

atmosphere to avoid carbonation. The materials were mixed with deionized water or freshly boiled CO₂-free deionized water with w/s=8. The mixture was placed in a miller pot of 14 cm diameter and 13 cm height with 10 balls of 2 cm diameter. The lid of the pot was tightened and sealed with parafilm to make it air and CO₂ tight.

Table 4.1. Composition and properties of the nanosilica (Elkem) used for the mechanochemical synthesis of C-S-H.

Property	Units	Value
SiO ₂	%	96.29
Free Silicon	%	0.04
CaO	%	0.2
Free CaO	%	<1
SO ₃	%	0.17
Na ₂ O	%	0.28
K ₂ O	%	0.93
Na ₂ O-equiv	%	0.89
Cl	%	0.04
Loss on Ignition @ 950°C	%	0.75
Specific Surface area (BET)	m ² /g	20.48
Pozzolanic index	%	120.32

The mixtures were milled in a Glen Creston laboratory ball mill for several hours with cycles of 25 min on and 5 min off to prevent overheating. After milling, the samples were dried by different routes to identify the best one to avoid carbonation. The fabrication details of the samples are given in Table 4.2.

Table 4.2. Experimental details of the test C-S-H samples prepared by the mechanochemical method.

Sample	Ca/Si	Mill time (h)	Filtered	Drying time (h)	Drying T (°C)
1*	0.66	29	No	120	70
2	0.66	59	No	5	40
3	1.00	58	Yes	24	60
4	1.25	66	Yes	72	60

The sample marked with * was made with unboiled deionized water, the rest of the samples were made with freshly boiled deionized water that was at ~50 °C before mixing.

The different drying procedures for the samples listed in Table 4.2 were as follows:

- Sample 1: The drying process consisted in placing the sample inside a beaker on a sand bath placed on a hot plate in a glovebox under an N₂ atmosphere (Flushing N₂ once an hour during the first 8 hours).
- Sample 2: The sample was dried directly in a Petri dish on the hot plate in a glovebox under an N₂ atmosphere (Flushing N₂ once an hour).
- Samples 3 and 4: The drying process consisted in filtering the sample in a Büchner funnel to remove the excess water. Then the sample was placed in a beaker inside a reaction vessel under a constant flow of N₂ of 20cm³/min. The vessel was placed over a temperature control hot plate. A water condenser was also attached to the vessel to condense the water vapour that comes from the sample. Water being cooled down by a chiller was continuously running along the condenser. The condenser was kept open to release the N₂ from the vessel. The whole set up was placed inside a glovebox. The atmosphere was controlled in the glovebox while introducing and taking the sample out by pumping the air out and filling it with N₂ for 3 consecutive times.

The samples were analyzed with STA to verify the level of reaction of the raw materials and the carbonation of the final products. The results are shown in Figure 4.1. For simplicity, the axis of the DTG has been removed. The results from sample 1 show that there are three phases in the sample: C-S-H (weight loss until 200°C), CH (weight loss at ~400°C) and calcium carbonates (weight loss at ~600°C). The presence of CH in the sample suggests that the milling time (23h 20min, counted as when the roller is on) is not enough to enable a complete reaction. Approximately the same total milling time (24 h) was used by Garbev et al. [40], but they used Aerosil, which is potentially more reactive than Nanosilica. This points out that a longer milling time is required to fabricate single phase C-S-H with Nanosilica. The presence of CH can have also been caused by the evaporation of the water during drying, since this increases the concentration of CaO in solution and CH may precipitate if the saturation concentration is reached. The presence of carbonates in the sample is due to the contact with CO₂, which can happen either in the pot of the roller mill, during the drying process or as a consequence of the used of non-boiled water. Since the pot was tightly sealed, it is very unlikely that carbonation occurs during milling.

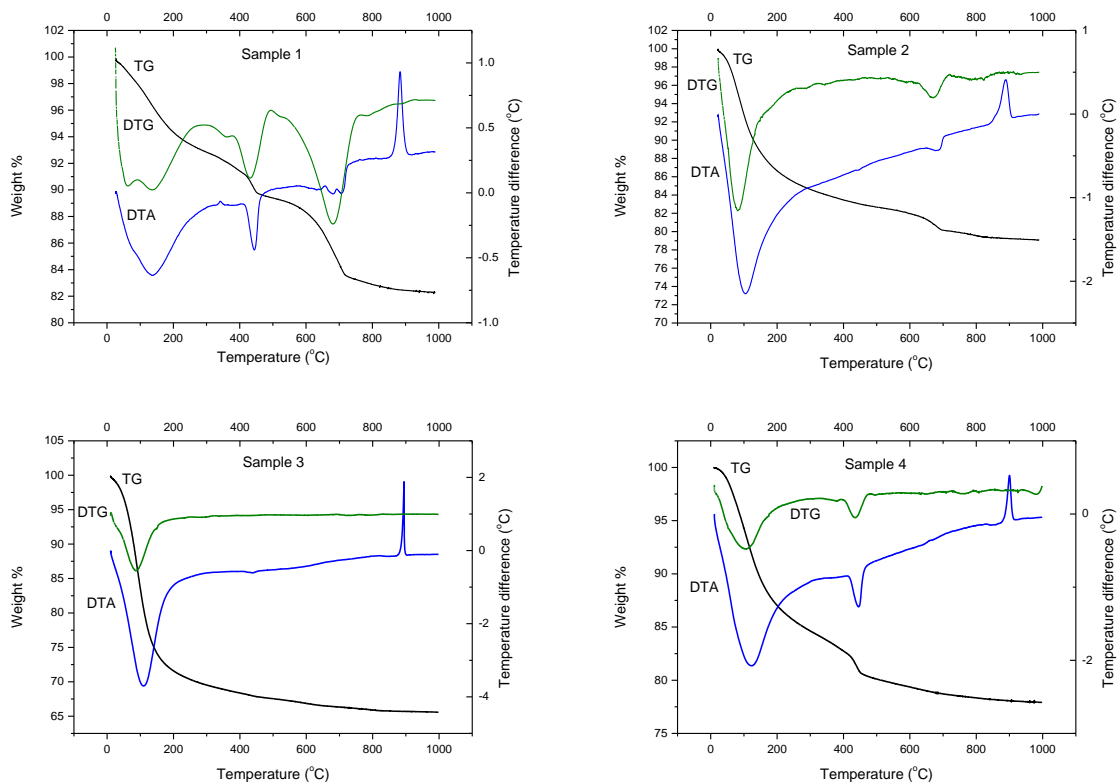


Figure 4.1. STA results of the test C-S-H samples fabricated mechanochemically listed in Table 4.2.

The lack of flushing N_2 overnight probably raised the concentration of CO_2 in the glovebox. The DTA curve shows an exothermic peak at $\sim 900^\circ C$ that is attributed to the formation of the compound wollastonite ($CaSiO_3$) [125]. The results for sample 2, which was milled longer than sample 1, show that the longer milling time helps not to form CH. There are still some carbonates present in the sample, but the level of carbonation is much less than for the previous sample, which indicates the introduction of N_2 in the glovebox more often prevents the carbonation. A drying set up with a continuous flow of N_2 directed to the sample (described below Table 4.2) was implemented and tested with samples 3 and 4. The STA results show that carbonation is minimized with this set up. CH is still present in the sample with $Ca/Si=1.25$, but this is in agreement with previous results reported for similar samples by Garbev et al. [122]. Samples 3 and 4 were also examined with TEM and ^{29}Si NMR. The results are shown in Figure 4.2. The presence of Q^4 silicate groups in the samples is an indication of remaining unreacted silica, which implies that the desired Ca/Si is not reached. TEM results also support NMR results, since it is possible to see darker silica particles surrounded by C-S-H foils. The measure to improve the synthesis method was to replace nanosilica for Aerosil 200. The optimized final synthesis details for this route are specified in the next section.

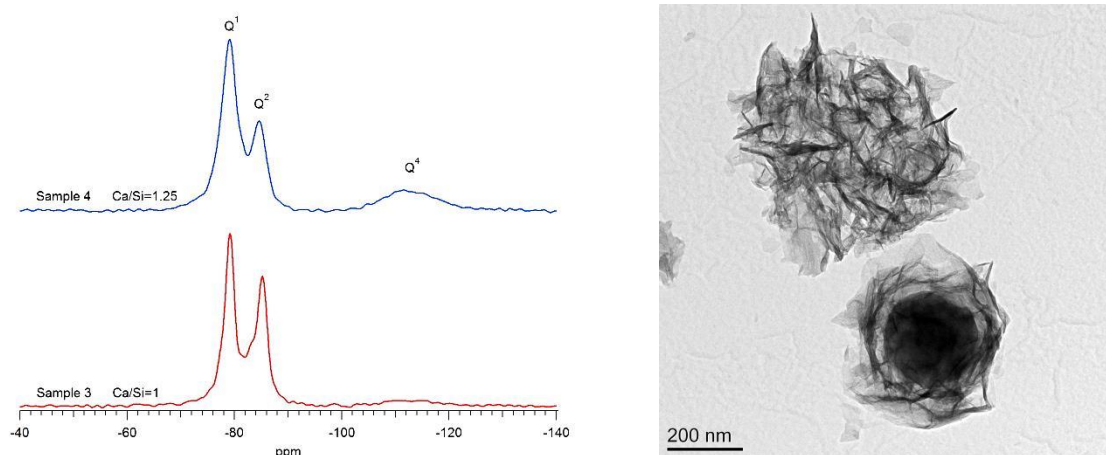


Figure 4.2. ^{29}Si MAS NMR results of test samples 3 and 4 (left), showing Q^1 and Q^2 intensity coming from C-S-H and Q^4 intensity coming from unreacted silica. TEM micrograph of sample 4 (right) showing a C-S-H particle (top) and an unreacted silica particle surrounded by C-S-H (bottom).

4.2.2 Optimized synthesis route for the mechanochemical samples

The mechanochemical C-S-H samples were prepared following similar steps to Garbev et al. [40] mixing 5g of Aerosil 200 (SiO_2) with CaO (obtained from roasting CaCO_3 for 3 hours at 900°C) with Ca/Si=0.75, 0.83, 1, 1.25, 1.33 and 1.5. The powders were mixed inside a glovebox. CaO was transported from the oven to the glovebox in a desiccator with a small container of liquid N_2 to prevent carbonation. The powders were poured in a pot inside a glovebox under an N_2 atmosphere, with freshly boiled deionized water at w/s=8. The pot had 14 cm of diameter and 13 cm height and it was provided with 10 balls of 2 cm diameter. The pot lid was tightened and sealed with parafilm. The mixtures were milled in a roller mill using 20 min intervals, pausing for 10 min between milling to prevent overheating. The total residence time was 36 hours (24 hours of milling). After milling, the pot was opened inside the glovebox under an N_2 atmosphere and the slurries were rinsed with ethanol and filtered in a Büchner funnel. When most of the extra water was removed, the remaining paste was introduced in a beaker. The beaker was introduced in a closed reaction vessel with an N_2 entry and exit. A water condenser, being cooled down by flowing water coming from a water chiller, was connected to the vessel. The vessel was placed over a temperature control hot plate. The samples were then dried for 3 days at 60°C with a constant N_2 flux of $20 \text{ cm}^3/\text{min}$. A lamp was placed next to the lid of the vessel to heat it and prevent the condensed water drops to fall down back to the sample. After drying, the samples were stored in sealed containers before analysis. A picture of the set up is shown in Figure 4.3.

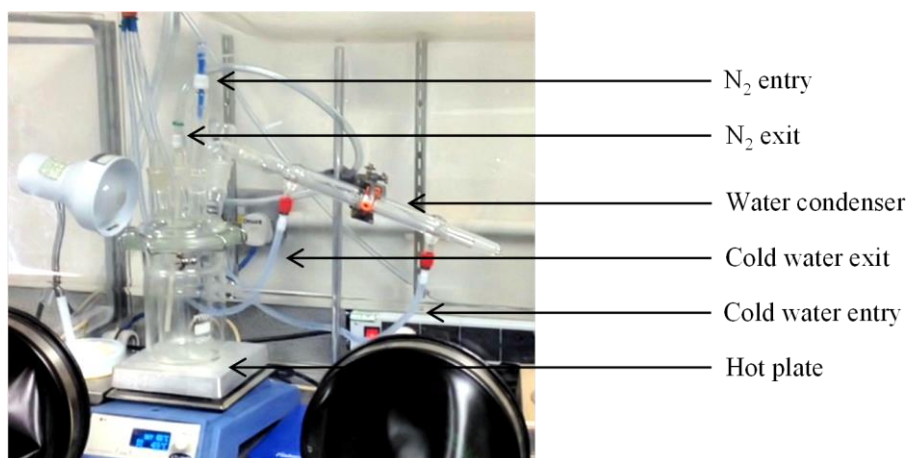


Figure 4.3. Drying set up used for the mechanochemical C-S-H samples showing the entries and exits for N₂ and cooling water for the condenser.

4.3 Synthesis details for the CaO-SiO₂ C-S-H series

The C-S-H samples of the CaO-SiO₂ series (kindly provided by A. Nonat and synthesized by J. Haas at the University of Bourgogne in Dijon) were synthesized mixing Aerosil 200 with CaO with Ca/Si=0.75, 0.8, 1, 1.27, 1.35 and 1.42. The powders were mixed with deionized water at w/s=50. The mixtures were sealed in plastic containers and continuously stirred for 4 weeks at 25°C. The slurries were then filtered and rinsed with a mix of 50%-50% ethanol and water and with pure ethanol afterwards in a Büchner funnel. The remaining powders were dried under vacuum for a day. The dried samples were stored in sealed containers before analysis.

4.4 Hydration of C₃S at constant lime concentration: Method and device

All the experiments concerning the hydration of C₃S under controlled conditions were performed at the ICB (Laboratoire Interdisciplinaire Carnot de Bourgogne) at the University of Bourgogne in Dijon. A way of varying the Ca/Si ratio of C-S-H formed by the hydration of C₃S consists in fixing the lime concentration in the solution. This was proved by A. Nonat and X. Lecoq [49], who synthesized C-S-H with Ca/Si from 1.2 to 2.2 by varying the lime concentration in solution from 6mmol/l to 30mmol/l (See section 2.8.6). By fixing the lime concentration in solution, the amount of Ca that is available to react and form C-S-H is also fixed, resulting thus in increasing Ca/Si while the lime concentration increases. C₃S from Lafarge Centre of Recherche with a mean particle size of 3µm was used. The hydration was started with a solution at the desired lime concentration for each experiment. All the solutions were prepared with deionized water. The solution was prepared either by filtering an undersaturated lime solution, for concentrations up to 20 mmol/l, or by filtering a supersaturated lime solution resulting from C₃S hydration for concentrations > 20mmol/l. The hydration was done in a temperature controlled reactor under

continuous stirring. The lime concentration was monitored via the conductivity of the solution with an electrode. The concentration of silicate ions was assumed to be negligible in solution (See Fig.3 in section I-2-2 in ref. [126]). Thus the conductivity in solution is proportional to the dissolved lime and the concentration of calcium ions. The relationship between the conductivity and $[Ca^{2+}]$ in solution was taken from J. Haas calibration [94], which follows this expression at 25°C:

$$y = 0.45x \quad \text{Eq. 4.1}$$

Where y is the conductivity in mS/cm and x is $[Ca^{2+}]$ in mmol/l. The slope for different working temperatures was calculated assuming a linear dependence, knowing the calibration done by S. Garrault [127] gave a slope of 0.38 for $T=21^\circ C$.

When the conductivity rises due to the release of ions because of C_3S dissolution, deionized water is added to the reactor from a reservoir. Simultaneously, a pump sucks the same volume of the solution, through a filter placed in the reactor, to maintain the w/s ratio constant. When the addition and removal of water are not operating, N_2 is being flushed into the solution through the filter, to minimize carbonation and prevent the blockage of the filter by the formation of a solid layer on its surface. The schematic of the device is shown in Figure 4.4.

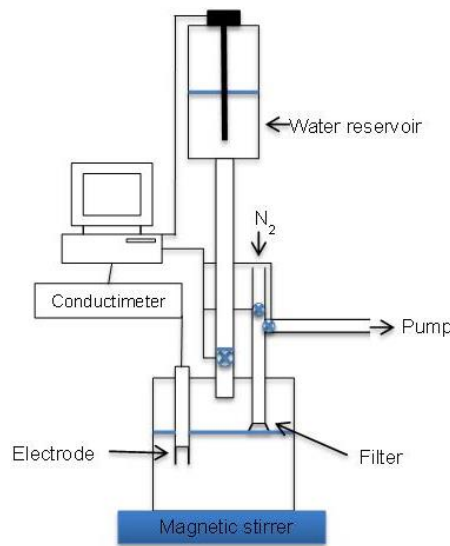


Figure 4.4. Device used to synthesize C-S-H via the controlled hydration of C_3S implemented by A. Nonat.

Both the conductivity and the volume of added water are recorded as a function of time (Figure 4.5). The hydration curve, expressed as added water vs. time, shows there are three regions

in the process. When hydration starts there is a period in which the addition of water to maintain the lime concentration constant is very slow, followed by an acceleration period in which water needs to be added into the system at a faster rate. After the acceleration period, there is a final stage in which the water addition is rather slow until the hydration curve reaches a plateau. Therefore the growth kinetics of C-S-H changes during hydration. This hydration curve can be transformed into a different hydration curve expressing the degree of reaction as a function of time.

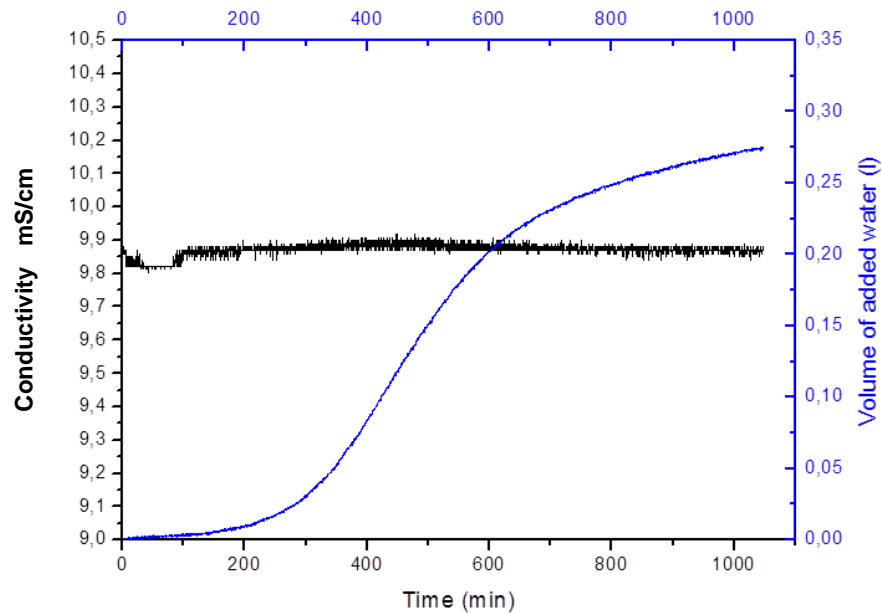


Figure 4.5. Graph showing the controlled hydration of 3g of C_3S at $\sim [CaO]=22\text{mmol/l}$ (9.9 mS/cm at 25°C). The controlled conductivity is shown in black. It can be noticed that from a mean conductivity value, the variations were not higher than $\pm 0.1\text{ mS/cm}$. The hydration curve expressed as the addition of water vs. time is shown in blue.

Under constant volume of the solution and fixed lime concentration, the degree of hydration can be calculated in terms of the C/S ratio of the C-S-H, the volume of added water and the fixed lime concentration [127]. When a mole of C_3S dissolves it gives the chemical species specified in Eq. 2.17. The precipitation of one mole of C-S-H consumes C/S moles of calcium according to Eq. 2.18. To maintain the calcium concentration constant in the solution, the moles of calcium that have not been consumed in the precipitation of C-S-H have to be removed.

The removed calcium moles are $3-C/S$ for every mol of C_3S that has been dissolved. Then for a number n of removed moles of calcium ions, the dissolved moles of C_3S (a) are:

$$a = \frac{n}{3 - \frac{C}{S}} \quad \text{Eq. 4.2}$$

The degree of hydration α can be calculated as the ratio between a and the initial moles of C_3S , n_0 :

$$\alpha = \frac{a}{n_0} = \frac{n}{n_0 \left(3 - \frac{C}{S}\right)} \quad \text{Eq. 4.3}$$

Since the volume of the solution that is removed is equal to the added volume of water, then the removed moles of calcium ions can be calculated as the product of the volume of added water and the fixed calcium concentration:

$$n = V_{H_2O} [Ca^{2+}] \quad \text{Eq. 4.4}$$

The degree of hydration can thus be expressed as:

$$\alpha = \frac{V_{H_2O} [Ca^{2+}]}{n_0 \left(3 - \frac{C}{S}\right)} \quad \text{Eq. 4.5}$$

4.4.1 Hydration of C_3S at constant lime concentration: Kinetics C-S-H series

To investigate if the hydration kinetics and the $[CaO]$ in solution has an effect on the morphology of the formed C-S-H, a series of samples was fabricated at different lime concentrations, stopping the hydration before the inflexion point in the hydration curve (at the acceleration period); samples named as short series, and after the inflexion point when the addition of water is much slower; samples named as long series. The synthesis details of these samples can be found in Table 4.3. The hydration was stopped by filtering the solution in a Büchner funnel and rinsing with a mix of 50%-50% ethanol-water and pure ethanol afterwards. The samples were subsequently dried in vacuum for a day and stored in sealed containers before analysis.

Table 4.3. Synthesis details for the C-S-H samples fabricated by C_3S hydration at fixed [CaO] for the kinetics series. The hydration times and added volumes of water are indicated for both the short series (hydration stopped at the acceleration period) and the long series (hydration stopped at the deceleration period). All the samples were synthesized at 25°C and at w/s=50. 4g of C_3S were used for lime concentrations up to 20mmol/l and 3g of C_3S for higher lime concentrations.

[CaO]	Hydration time I (min)	Added water (l)	Hydration time II (min)	Added water (l)
12	170	0.31	240	0.41
15	260	0.22	1161	0.59
17	255	0.13	1011	0.48
20	375	0.23	1398	0.49
22	401	0.06	1048	0.28
25	492	0.09	835	0.28
27	600	0.14	840	0.29

4.4.2 Hydration of C_3S at constant lime concentration: Ultrasound C-S-H series

A series of three samples was synthesized at high lime concentrations. Apart from controlling the [CaO], an ultrasound gun was inserted in the solution and used at 250W and regular pulses, being on for 1s and off for the subsequent 3s. The gun was used with the aim of promoting higher degree of hydration and obtaining purer C-S-H samples. The pulses break the layer of C-S-H that forms in the surface of C_3S grains and disperse C-S-H particles in the solution that act as nucleation sites. This prevents the formation of a layer of C-S-H on the C_3S grain that would slow down the dissolution process but does not remove the layer completely. The parameters of the synthesis can be found in Table 4.4. The samples were filtered and dried the same way as the batch from the previous section.

Table 4.4. Synthesis details of the C-S-H samples fabricated adding the ultrasound gun to the reactor in which the lime concentration was fixed. The w/s was 50 and the temperature was 25°C. 4g of C_3S were used for each sample.

[CaO]	Hydration time (min)	Added water (l)
27	1010	-
28	1417	-
29	1458	1.24

4.4.3 Hydration of C₃S at constant lime concentration: Xseed C-S-H series

The addition of an external agent (C-S-H seeds) was also tested to promote higher degree of hydration and fabricate purer C-S-H samples at high lime concentration. A commercial solution of C-S-H seeds produced by the Xseed technology by BASF was added to the solution. In this case the sucking function of the device was switched off and the addition of water was only used to control the conductivity. 1ml of the Xseed solution was added to the reactor. The Xseed solution contains nanoplatelets of C-S-H, synthesized from sodium metasilicate. The seeds act as nucleation sites and their presence prevents the formation of a C-S-H layer on the C₃S grain, which would slow down the dissolution of C₃S. A non-negligible amount of Na is present in the product; therefore a filtration process was used to remove it. The product, already filtered, was kindly supplied by J. Haas. The filtration process consists on placing it in a sealed dialysis membrane inside a lime saturated bath. The bath is placed in an orbital table for 3 days. The concentration of sodium in the solution is monitored and the solution is changed several times until this concentration is negligible [94]. The synthesis details for these samples are shown in Table 4.5. The samples were filtered and dried the same way as the batches in the two previous sections.

Table 4.5. Synthesis details of the C-S-H samples fabricated at constant lime concentration adding Xseed to the solution. The initial w/s was 100 and the temperature was 20°C.

[CaO]	Hydration time (min)	Added water (l)
27	1587	0.64
28	2182	0.61
29	1430	0.57

4.5 Synthesis details for the C-A-S-H series

The samples were synthesized and kindly provided by E. L'Hôpital at Empa, (Dübendorf, Switzerland). Proportions of CaO, SiO₂ (Aerosil 200) and CaAl₂O₄ (CA) were mixed to obtain C-A-S-H with Ca/Si=1 and Al/Si=0.01, 0.02, 0.03, 0.04 and 0.05. CaO was obtained by roasting calcium carbonate at 1000°C for 12 hours. CA was obtained reacting CaCO₃ and Al₂O₃. The homogenized powder mixture was heated for 1 hour at 800°C, 4 hours at 1000°C and 8 hours at 1400°C and cooled down at 600°C/h. The solid was ground to a Blaine surface area of 3790 cm²/g. The reactions were made at a w/s ratio of 45 to obtain homogeneous samples. The reactants were added simultaneously to the water. The synthesis was done for 182 days in 100 ml PE-HD sealed containers placed on a horizontal shaker at 100 rpm at 20°C. The solids were filtered and then rinsed with 50%-50% ethanol-water and pure ethanol afterwards. The samples were freeze-dried for

7 days. They were stored in desiccators under an N₂ atmosphere and with a CaCl₂ solution (~30% RH) and NaOH as a CO₂ trap. The handling and synthesis of the samples were performed in a glovebox under an N₂ atmosphere to avoid carbonation.

4.6 STA

For the C₃S paste, disks of approximately 2 mm thickness freshly cut in an Isomet low speed saw were crushed in a mortar. In the case of the synthetic C-S-H, the samples were crushed in an N₂ atmosphere inside a glovebox and carried in sealed containers to the STA equipment to minimize carbonation. The fine powders were analysed with a Stanton Redcroft STA 1000 (U.K.), which monitored the weight loss of 15-18 mg of sample while the temperature was increased from 20°C to 1000°C with a rate of 20°C/min. An N₂ flow of 58ml/min was used during the analysis. The derivative of the thermogravimetry curve with respect to the temperature is also included in the results and has been calculated using the software OriginPro 8.1 and smoothed iteratively with the Savitzky-Golay method with 300 points of window and polynomial order 5. The units of this curve are weight % / °C and the axis has been removed for simplicity in all plots.

4.7 TA-FTIR

For coupled TA-FTIR experiments, a thermo balance Jupiter 449-F3 (Netzsch, Selb), equipped with a DSC sample carrier, was coupled by a heated transfer line to a Bruker Tensor 27 FTIR Spectrometer with a TA-FTIR unity for simultaneous online gas measurements. The transfer line had a length of 100 cm and a PTFE inlet. The TA-FTIR unit with an FTIR cell had an optical path length of 123 mm, and KBr and ZnSe-windows. Both the transfer line and the FTIR cell were heated to 200°C. 10-30 mg of each sample were placed in a Pt/Rh crucible. The experiments were performed with a heating rate of 10 K/min. Nitrogen was used as a purge gas with a flow of 70 ml/min, including 20 ml of balance protective gas. The FTIR resolution was 4cm⁻¹ with a scan rate of 32. The spectra were recorded every 15s. In order to avoid the weight loss of the sample while measuring the FTIR baseline, the baseline was taken before the samples were introduced in the system. Therefore, residual atmospheric water and CO₂ were detected in the first few minutes of the experiments. This signal of residual atmospheric gases was removed for the quantification of the spectra. The evaluation of the spectra was done by Daniela Merz at KIT, with Bruker OPUS software and Netzsch Proteus software. The quantification method was based on the simultaneous control of the purge gas flow after an external calibration [128]. The calibration for CO₂ was done with a certified test gas of CO₂ in N₂ (certified by Basi, Rastatt), measured in the FTIR cell under identical conditions to the experimental setting. The calibration of H₂O was done by thermal degradation of 20 samples of calcium oxalate monohydrate. All absorption response curves in the

used concentration ranges can be described by linear fitting. Lambert-Beer's Law is valid in these concentration ranges.

4.8 XRD

Two disks of 2mm thickness of the C₃S paste were finely ground in a mortar. The powder was back-packed in a sample holder to ensure a uniform surface, in level with the holder, to be exposed to the X-rays. The pattern was taken under continuous spinning of the sample in a Panalytical X'Pert Pro diffractometer with a Cu K_α source operated at 40 kV and 40 mA. A 10 mm mask and a 10 mm antiscatter slit were used. The minimum and maximum values for 2θ were set at 4° and 80° respectively. The step size was 0.0083556° and the time per step 125.095 s, yielding a total time of nearly 3h for the scan. The synthetic C-S-H samples were scanned using a step size of 0.033° and a time per step of 95 s, yielding a total time of ~30 min for the scan. The patterns were compared with reference patterns downloaded from the Chemical Database Service to identify the phases present in the sample when required.

4.9 TEM

For the C₃S paste, disks of 1-2mm of thickness were cut with an Isomet low speed saw and dried in a desiccator being continuously pumped overnight. The sample preparation was done following the steps described in ref. [103]. The slices were polished on one side with 1200 grit silicon carbon paper and glued to a glass slide. The polishing was then continued until black ink could be read through the sample (~30 μm thickness). Silicon carbon paper of 800 grit was used to get a finer and smooth surface of the sample. The glass slide was immersed in acetone until the sample was removed from its surface when all the glue had dissolved. Then the sample was placed between two copper grids using epoxy resin. The centre of the sample was checked under the optical microscope to make sure that holes, other damages or resin were not present, since the rest of the preparation and the data can be affected by their presence. The sample was then ion milled in a Fischione Model 1010 Low angle ion milling and polishing system equipped with a cryo-cooling stage to avoid thermal damage. The process was continued until a small hole was found in the center of the sample, which was taken out of the chamber after warming up to room temperature to prevent it from thermal cracking. The last step of the sample preparation involved coating it with a carbon layer of ~ 20 nm in an Agar turbo carbon coater to prevent charging effects under the microscope. The sample was then stored in a vacuum desiccator until examination to avoid carbonation.

For the synthetic C-S-H, the samples were crushed in a mortar under an N₂ atmosphere in a glovebox. Then a small amount of the fine powder was introduced into a glass container with a spatula. Methanol or ethanol was poured into the glass container and the solution was placed in an ultrasonic bath for ~1 min. A drop of the middle of the solution was deposited with a pipette over a 200 mesh copper grid with a carbon film, which was then taken to the microscope immediately.

A Philips CM200 FEGTEM microscope operated at 200kV was used to analyze the C₃S sample and the old mechanochemical samples. Bright field images were taken at magnifications between 26-19.5kx. For each sample, between 20 and 40 EDX points were taken thanks to an Oxford UTW EDX detector (U.K.) and Oxford ISIS software. The analysis was done preferably in amorphous areas which corresponded to C-S-H, checked to be free of intermixing with other phases inserting a SAED aperture to confirm that the diffraction pattern consisted only of halos or rings but was free of diffraction spots. The EDX points were taken at 19.5kx magnification and spot size 6, with a real time of 50s and a beam diameter of ~ 200 nm.

A FEI Tecnai TF20 FEGTEM was used to examine the rest of the synthetic C-S-H samples. Bright field images were taken at magnifications of 10-19kx operating at 200kV and spotsize 3. Typically 20 EDX points were taken per sample with an Oxford Instruments HAADF detector and Inca 350 EDX software. The magnification was 17kx, the spotsize 8, the beam diameter ~200 nm and a live time of 50s. A thickness of 200 nm and a density of 2.8 g/cm³ were used for the quantification of the spectra. When the results were deviated from the expected Ca/Si ratios, the data were corrected with a multiplying factor provided by the EDX analysis of a wollastonite reference sample. The details of the analysis of this reference sample are provided in the following section. Selected area electron diffraction patterns were taken with a SAED aperture of 200 nm diameter at spotsize 3.

4.9.1 Wollastonite reference sample details for TEM-EDX

A synthetic wollastonite (CaSiO₃) sample was kindly provided by K. Garbev to be used as a reference for TEM-EDX. The sample was studied with XRD and TEM. The XRD pattern is shown in Figure 4.6 together with a reference pattern from pseudowollastonite taken from ref. [129]. The sample pattern is very similar to the reference one, thus confirming the purity of the sample. For TEM the sample was dispersed in ethanol, isopropanol and acetone and deposited over a 200 mesh copper grid with a carbon film. Bright field images show that the sample appears as flatty needle-like crystals of few hundreds of nanometers in width. EDX points for the three samples prepared with different solvents were taken at magnification of 17kx and spotsize 8. A thickness of 200 nm and a density of 2.8 g/cm³ were used for the quantification. A mean Ca/Si=

0.79 ± 0.02 was obtained. Since the Ca/Si of wollastonite must be 1, a correction factor of 1.27 is needed. This factor was used to correct all Ca/Si data that were acquired with the FEI Tecnai FEGTEM for the synthetic C-S-H samples.

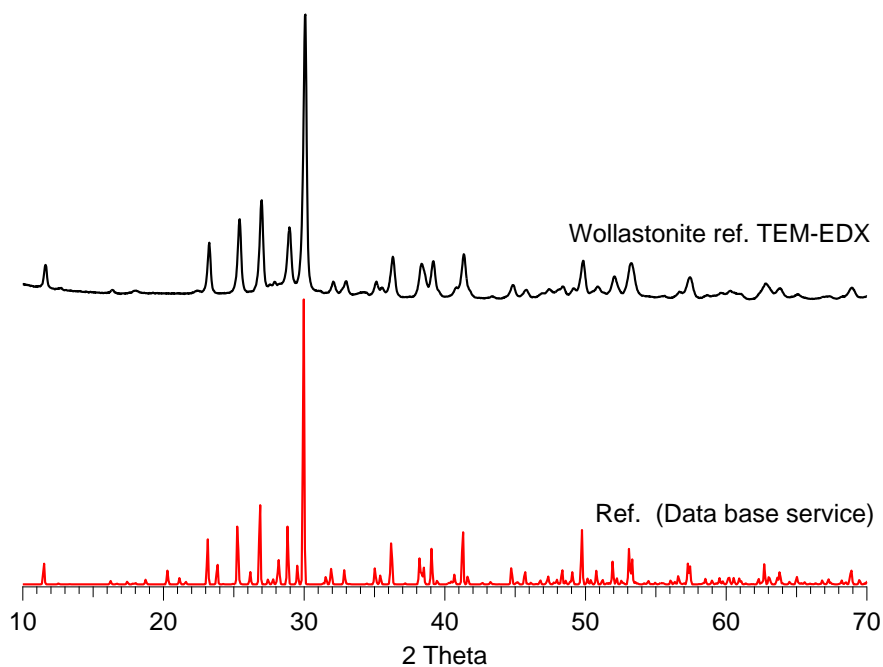


Figure 4.6. XRD pattern of the wollastonite sample used as TEM-EDX reference together with a reference pattern of pseudowollastonite taken from ref.[129].

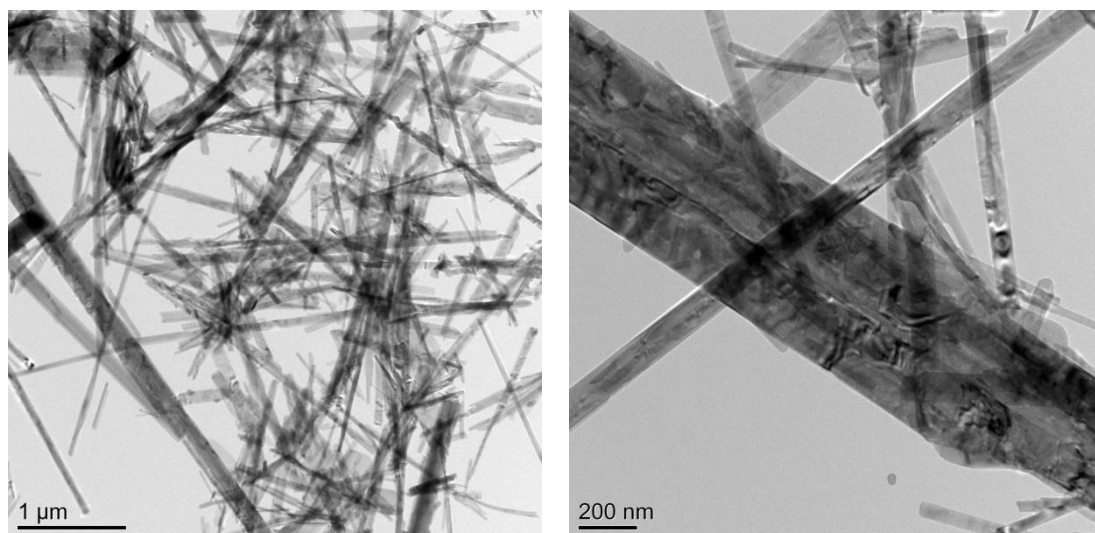


Figure 4.7. TEM micrographs of the wollastonite reference sample dispersed in ethanol (left) and acetone (right).

4.10 XRF

1 g of the ground fresh mechanochemically synthesized C-S-H samples was used to prepare fused beads using 10g of lithium tetraborate ($\text{Li}_2\text{B}_4\text{O}_7$) as the flux. The XRF measurements were done on the wide range oxide program on a Panalytical wavelength dispersive spectrometer, model PW2440.

4.11 SEM

Disks of 2mm thickness of the C_3S paste were placed in moulds and resin-impregnated under vacuum with Struers Epofix resin. After setting, the samples were demoulded and cut on the opposite side of the disks to get a flat surface parallel to the side of the disks. The samples were then polished on the disks sides on a Struers RotoPol-35 with a PdM-force-20 unit. SiC papers of 600, 1200 and 2400 microns were used until the surface was smooth, then 6, 3, 1 and $\frac{1}{4}$ micron diamond paste cloths were used with DP-stick lubricant. When the sample surface was smooth and free of scratches, the polishing process was considered to be finished. The sample was coated, to avoid charging effects under the microscope, with 15nm of C in an EMScope TB500 vacuum coater. Before observation, the sample was placed over a sample holder with a C sticker and painted with C paint on the sides to provide a contact with the holder.

The studies of the C_3S sample were done on an EVO MA15 operated at an acceleration voltage of 20kV. Backscattered images were taken at magnifications between 1000 and 2000, spot size 500 and working distance of 8 or 10mm. EDX was performed with a working distance of 8mm on different areas with different grey levels to identify their chemical composition and thus the phases present in the sample. The counting time was set to 40s.

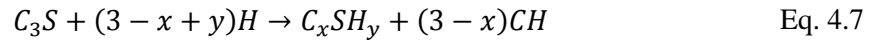
The surface of some of the synthetic C-S-H samples fabricated via the controlled hydration of C_3S was studied with a high resolution SEM. The samples were dispersed on carbon sticks and then coated with a carbon layer of about 15 nm with a 208 Carbon Cressington carbon coater. An XL-30 SFEG FEI HR-SEM, equipped with an Oxford Si(Li) EDX detector, was used for imaging. UHR mode (ultra high resolution mode), with an accelerating voltage of 2.5kV, spot size 3, working distance of ~2.5 mm and magnification of 15kx were used.

4.12 ²⁹Si DP MAS NMR

Freshly crushed and finely ground disks of the C₃S paste were packed in a 6 mm diameter zirconia rotor with a Teflon cap. The NMR spectrum was recorded in a Varian Infinity Plus 300 spectrometer equipped with Chemagnetics style MAS probes referenced with respect to belite (-71.3 ppm). The equipment was operated at 59.56 MHz for ²⁹Si and at a magnetic field of 7.0 T. The spinning speed at the magic angle was set to 6 KHz. The pulse delay was 30s, the pulse width was 5μs and the acquisition time was set at 6.83ms. The total number of scans was 7000. The resulting spectrum was then iteratively fitted using the software Igor Pro 5.0 with special macros written by Brough (1993) and further developed by Love and Brough. After the peaks are fitted, the program integrates the area below them to obtain the percentage of the silicate species in the sample: Q⁰, Q¹, Q², Q²(1Al) (Q² with one Si substituted by Al), etc. With this data, the percentage of reaction is given by the program as the percentage of the hydrated species. The mean chain length (MCL) is also calculated as [130]:

$$MCL = \frac{2 \left[\%Q^1 + \%Q^2 + \frac{3}{2} Q^2(1Al) + \%Q^3 \right]}{\%Q^1} \quad \text{Eq. 4.6}$$

The Ca/Si ratio of the paste was also estimated using the hydration reaction [3]:



Applying mass balance to the equation and knowing the w/s ratio, the % of hydration DR from NMR, the % of CH as ignited weight from STA, and the molar masses of C₃S (a) and CH (b), the Ca/Si, x, is:

$$x = 3 - \frac{\left(a + \frac{w}{s}a\right) \cdot DR\% \cdot CH_{iw} \cdot 10^{-4}}{b} \quad \text{Eq. 4.8}$$

All the synthetic C-S-H samples were analyzed in a Varian Direct-Drive VNMRS-600 spectrometer (14.09 T), equipped with a homebuilt CP/MAS probe for 7 mm o.d. zirconia rotors. The spectra were acquired at 119.137 MHz, employing a spinning speed of 6.0 kHz, a 90s relaxation, and were referenced to TMS using belite as an external reference. The spectra were deconvoluted and iteratively fitted using the Vnmrj software. Each frequency chosen to deconvolute the spectra was defined by position in ppm, height (intensity), line width and shape. The shape was

a mixture of a Gaussian and a Lorentzian distribution, being 1 if only Gaussian and 0 if only Lorentzian. The aim of the deconvolutions was to obtain the total integrals for Q^0 , Q^1 and Q^2 , rather than evaluating individual sites of each connectivity, such as Q^{2b} and Q^{2p} . Therefore the frequencies chosen to deconvolve the spectra do not have a direct structural meaning, but were chosen to give the best fit for the total contribution of each connectivity. If structural information needs to be derived from the spectra, the deconvolution process is much more complex, since the chosen frequencies should maintain their line widths and shapes in all the samples. These parameters were relaxed in the deconvolutions, resulting in variations between samples. Since the total integral for the connectivities was the essential information taken from the deconvolutions, if there was a significant overlap between the tails of frequencies of different connectivities, the shape of the frequencies was relaxed to minimize this overlap. The percentages of the silicate species that resulted from the deconvolutions were used to calculate the mean silicate chain lengths (MCL) in all cases (Eq. 4.6) and the degree of reaction (DR) for the samples fabricated via the controlled hydration of C_3S . The estimated error in the quantification was ± 2 for the silicate connectivities and the quadratic propagation of errors was used to calculate the error in the MCL and the degree of reaction (DR). The DR was calculated according to:

$$DR = 100 \cdot \frac{\%Q^1 + \%Q^2}{\%Q^0 + \%Q^1 + \%Q^2} = \%Q^1 + \%Q^2 \quad \text{Eq. 4.9}$$

5 Results and discussion

5.1 C₃S paste

The thermal analysis data of the C₃S paste is shown in Figure 5.1. The solid residue r_s , after heating the sample to 1000°C, was 73.26 %. The w/s ratio was calculated using the following expression, which is a modification of Eq. 3.1:

$$\frac{w}{s} = \frac{100}{r_s} - 1 \quad \text{Eq. 5.1}$$

The w/s ratio is 0.365 and expressed with its error is $(3650 \pm 2) \cdot 10^{-4}$. (Taking $\Delta r_s = 10^{-2}$ weight %, which is the precision that is given by the software that calculates r_s and assuming quadratic propagation of errors). As the original w/s ratio was 0.5, this result suggests some of the water has been lost during the hydration process. This may be due to evaporation if the mould was not well sealed while curing.

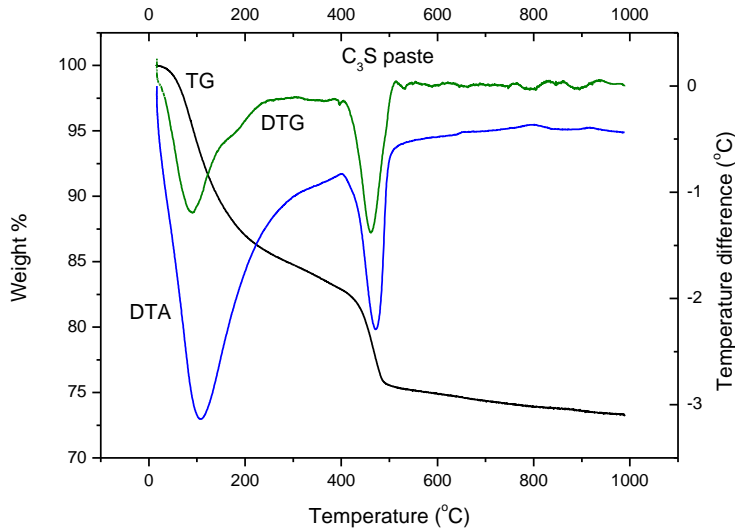


Figure 5.1. TG, DTG and DTA data of a 5-year old C₃S paste with w/s=0.5.

The % CH is calculated taking the weight loss from 404°C to 513°C using the following expression in which $y \cdot s$ is w_{deh} in Eq. 3.5:

$$\%CH = \frac{74}{18} \cdot y \cdot s = \frac{74}{18} \cdot w_{deh} \quad \text{Eq. 5.2}$$

Decarbonation has not been taken into account because the DTG is roughly constant in the region from 600°C to 780°C. The variable y is the length (in cm) of the arrow that marks the weight loss as in Figure 3.1, that in this case was 3.1cm, and s is a scale factor that indicates how much weight % corresponds to each length unit, which in this particular case was 30/16 weight %/cm. Considering the scale factor has no error, and $\Delta y = 10^{-1}$ cm, the amount of CH is then 23.89 ± 0.77 weight %. This expressed as ignited weight is 32.6 ± 1.1 weight %, calculated as follows:

$$\%CH_{iw} = \frac{\%CH}{r_s} \cdot 100 \quad \text{Eq. 5.3}$$

The XRD pattern of the sample is shown in Figure 5.2. The peaks belong to portlandite and C-S-H, suggesting that the hydration of the sample is complete with no alite remaining. However, alite can be present as very small crystals that may not be detected by X-rays. This is in fact confirmed by the examination of the sample on the SEM, which shows that it contains bright regions in backscattered images (Figure 5.3) that are identified as alite and belite as per EDX results. The presence of belite in the sample agrees with previous results of the same pastes when they were younger. Both XRD and ^{29}Si DP MAS NMR results showed the presence of belite when the samples were hydrated for 8 hours [131].

TEM micrographs of the sample are shown in Figure 5.4. The morphology of the Op C-S-H is fibrillar. The mean Ca/Si ratio and its standard deviation calculated from 30 EDX data points taken from the Ip C-S-H region in Figure 5.4 are 1.79 ± 0.06 , which is consistent with the nature of the paste.

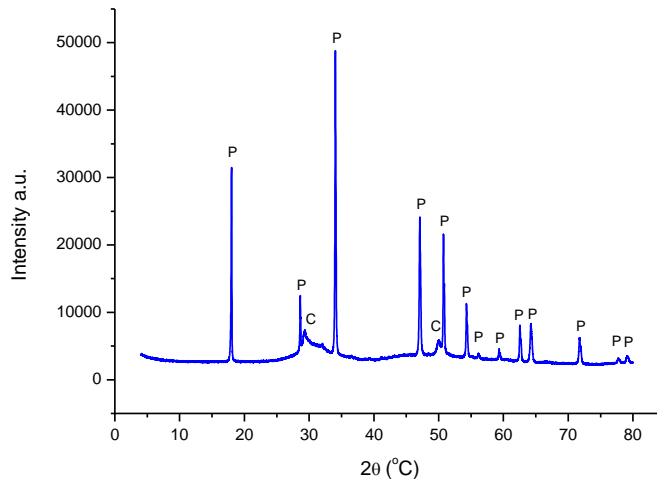


Figure 5.2. XRD pattern of a 5-year old C_3S paste with $w/s=0.5$. Peaks are labeled as P for portlandite and C for C-S-H.

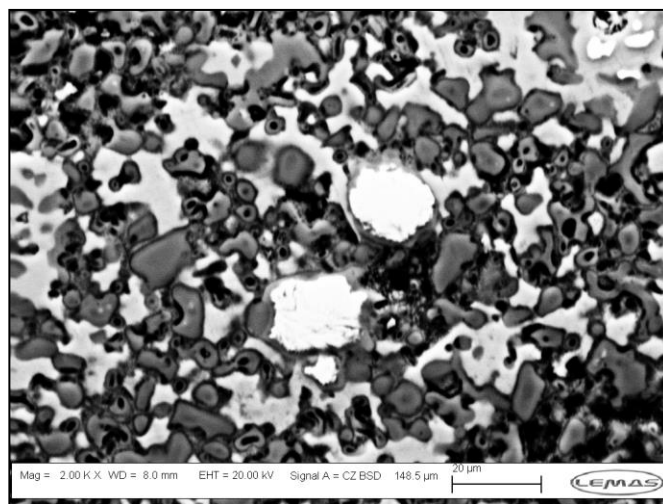
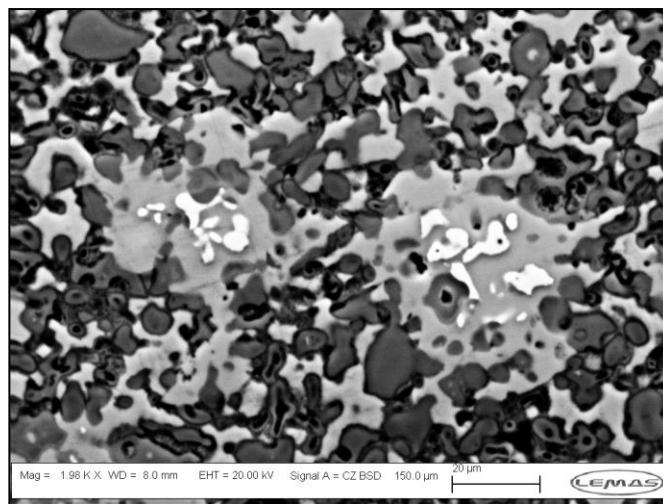
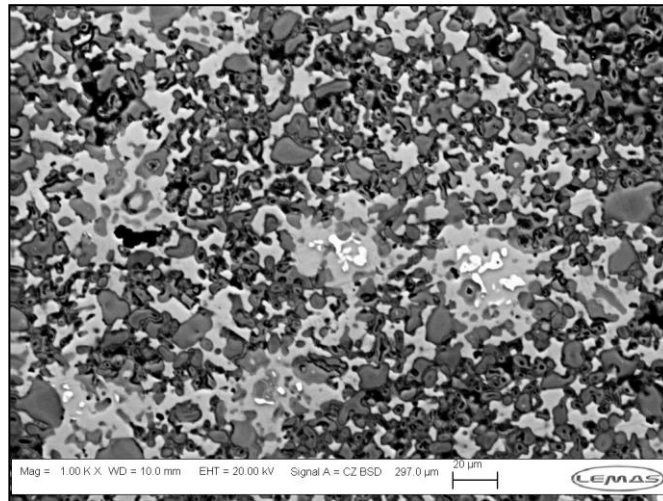


Figure 5.3. Upper image: Backscattered electron image from the 5-year old C_3S paste with $w/s=0.5$. Three different phases are identified: C_3S (white), CH (light grey) and C-S-H (dark grey). Porosity is displayed as black, Central image: Central area of upper image at higher magnification, Lower image: Backscattered electron image from the C_3S paste with the white features in the center corresponding to belite traces. (All images taken by M. S. Chen).

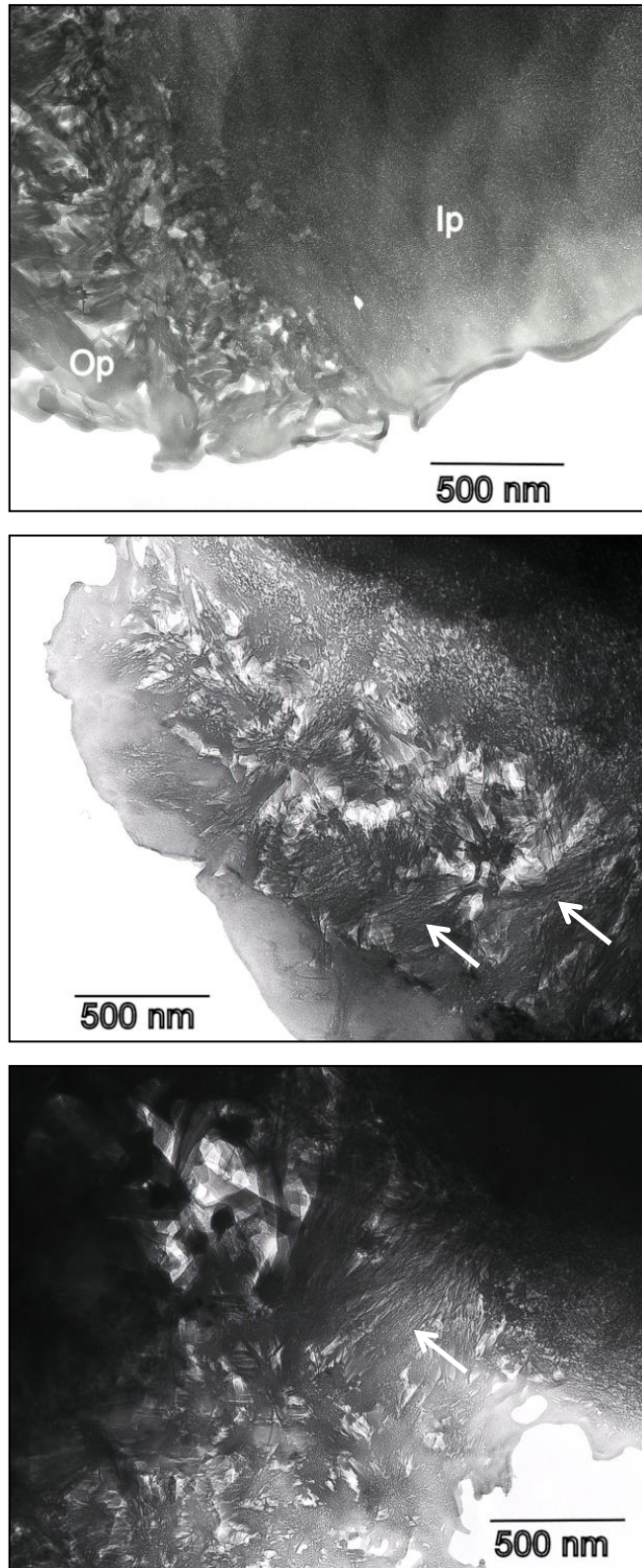


Figure 5.4. Upper image: TEM micrograph showing globular dense Ip C-S-H and fibrillar Op C-S-H of a 5-year old C₃S paste with w/s=0.5. Central image and lower images: TEM micrographs showing fibrillar Op C-S-H in the same paste (marked with white arrows).

The ^{29}Si DP MAS NMR spectrum of the C_3S paste is shown in Figure 5.5. The spectrum was fitted taking into account the main two peaks at ~ 79 ppm and ~ 85 ppm, that belong to Q^1 and Q^2 silicate species, a contribution from Q^{2b} at ~ 82 ppm and the humps at ~ 71 ppm and ~ 73 ppm that belong to Q^0 (from traces of belite and C_3S). The deconvolution of the spectrum provides a quantification of the species yielding 4.1% for Q^0 , 48.3% for Q^1 , 8.5% for Q^{2b} and 39.0% for Q^2 (The precision of the program ± 0.1 is taken as an error for all the individual %). The calculated MCL is 3.967 ± 0.007 and the percentage of reaction is $95.8\% \pm 0.2$, leaving 4.1% of anhydrous material. This agrees with the fact that small amounts of alite and belite were detected in the SEM images. The mean chain length is reasonable for the age of the paste, since C-S-H in C_3S pastes get a MCL between 2 and 4 up to ~ 5 years of hydration [15, 16]. The amount of dimers and middle chain groups also agrees with the age of the sample; the values are consistent with the ones commented in section 2.1.5 taken from ref. [14].

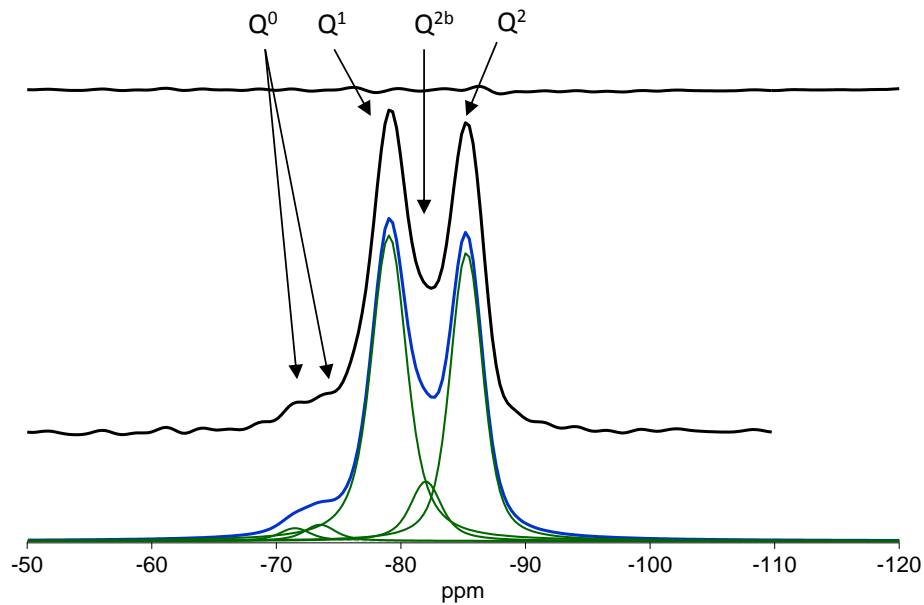
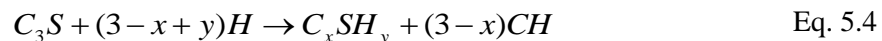


Figure 5.5. Deconvolution of the ^{29}Si MAS NMR spectrum of a 5-year old C_3S paste with $w/s=0.5$. From top to bottom: Residue, experimental spectrum and fitted spectrum showing the individual peaks.

The Ca/Si ratio of C-S-H, x , can be estimated using the following hydration reaction [3]:



Applying mass balance to the equation and knowing the w/s ratio, the % of hydration, the % of CH as ignited weight and the molar masses of C_3S (a) and CH (b), the Ca/Si, x, was calculated with Eq. 4.8. Taking 1Mol of C_3S reacting with water at a w/s ratio of 0.36 and a final content of CH of 32.6% (as indicated by STA results), the Ca/Si ratio of C-S-H is estimated to be 1.69 ± 0.04 (The error was calculated considering quadratic propagation of errors). This experimental value of the Ca/Si is lower than the one given by EDX with TEM which was 1.79 ± 0.06 . With the error, the maximum value given for the Ca/Si by STA and NMR will be 1.73 and the minimum value given by EDX taking into account the error is 1.73, therefore there is not a remarkable difference between the results.

5.2 7-year old mechanochemically synthesized C-S-H

Samples with Ca/Si ratios of 0.66, 0.75, 1 and 1.5 were analyzed by STA and TEM. The STA results with the DTG are shown with histograms of the calculated Ca/Si ratios from the EDX data in Figure 5.6 and Figure 5.7. STA results show that all samples contain C-S-H (dehydration as weight loss under 200°C). All samples except the one with Ca/Si=1 show carbonation (decarbonation as weight loss between 600°C and 780°C), with the sample with target Ca/Si=0.75 being the most carbonated. The sample with Ca/Si=1.5 also shows the presence of CH (dehydration as weight loss between 420°C and 550°C). For more detailed TG analysis of the same samples when they were fresh see ref. [122]. The EDX histograms show that samples with Ca/Si ratios of 0.66 and 1 are very homogeneous since the data are not very dispersed. However samples with Ca/Si of 0.75 and 1.5 are heterogeneous in composition. This is due to the presence of carbonates in sample with target Ca/Si=0.75. The presence of Ca/Si > 1.2 in the histogram for this sample in Figure 5.6, indicates that intermixing occurred, since the published Raman spectra of this samples showed no dimeric silicate content for this sample [68], and dimeric species are associated with Ca/Si > 1.2. The presence of CH in sample with target Ca/Si=1.5 may have also caused a dispersion in the data, since it was difficult to find areas free of diffraction spots. For the latter sample, the high data dispersion may also be due to the difficulties in finding very thin areas on which to perform EDX. The mean Ca/Si ratios calculated from EDX are shown in Table 5.1 and compared with reported values obtained by different techniques. The mean Ca/Si ratios calculated from EDX are all similar to the target ones and those reported by XPS, except for the sample with target Ca/Si=0.75, due to its high heterogeneity and degree of carbonation. However, for the sample with target Ca/Si=1.5, the reported value of 1.29 [122] is more realistic since the presence of CH must reduce the Ca/Si with respect to the target value. Again the mean Ca/Si of 1.48 calculated from EDX data for this sample, can be overestimated due to problems in finding thin areas for analysis and due to admixture with other phases in a possible very fine scale, since some of the EDX was performed in areas that were giving spot-like diffraction patterns. From the micrographs shown in Figure 5.8, it can be concluded that the morphology of the samples is foil-like regardless of the Ca/Si ratio. These samples are reported to resemble C-S-H (I), which is similar to tobermorite. Tobermorite is associated with foil-like morphology; thus the results are consistent with Richardson's assumption that associated tobermorite to foils.

From the results, it is evident that the carbonation of these samples affects the Ca/Si ratio since C-S-H decalcifies upon carbonation. Raman studies of the samples when they were fresh revealed Raman bands associated with carbonated species after minutes of exposure to air [68]. When the samples were stored for a longer period (up to 6 months) in a covered, but not closed, desiccator, samples with $\text{Ca/Si} > 1$ were especially sensitive to carbonation and silicate polymerization increased [124]. This indicates the importance of storing these samples properly, to preserve the C-S-H structure.

Table 5.1. Comparison between mean Ca/Si ratios of synthetic C-S-H samples obtained by three different methods: EDX from TEM (with the standard deviations), XPS [132] and TG [122].

Target Ca/Si	# EDX points	Ca/Si (EDX)	Ca/Si (XPS)	Ca/Si (TG)
0.66	28	0.65 ± 0.02	0.68	-
0.75	32	0.83 ± 0.29	0.74	-
1	40	1.05 ± 0.03	1.04	-
1.5	20	1.48 ± 0.14	1.48	1.29

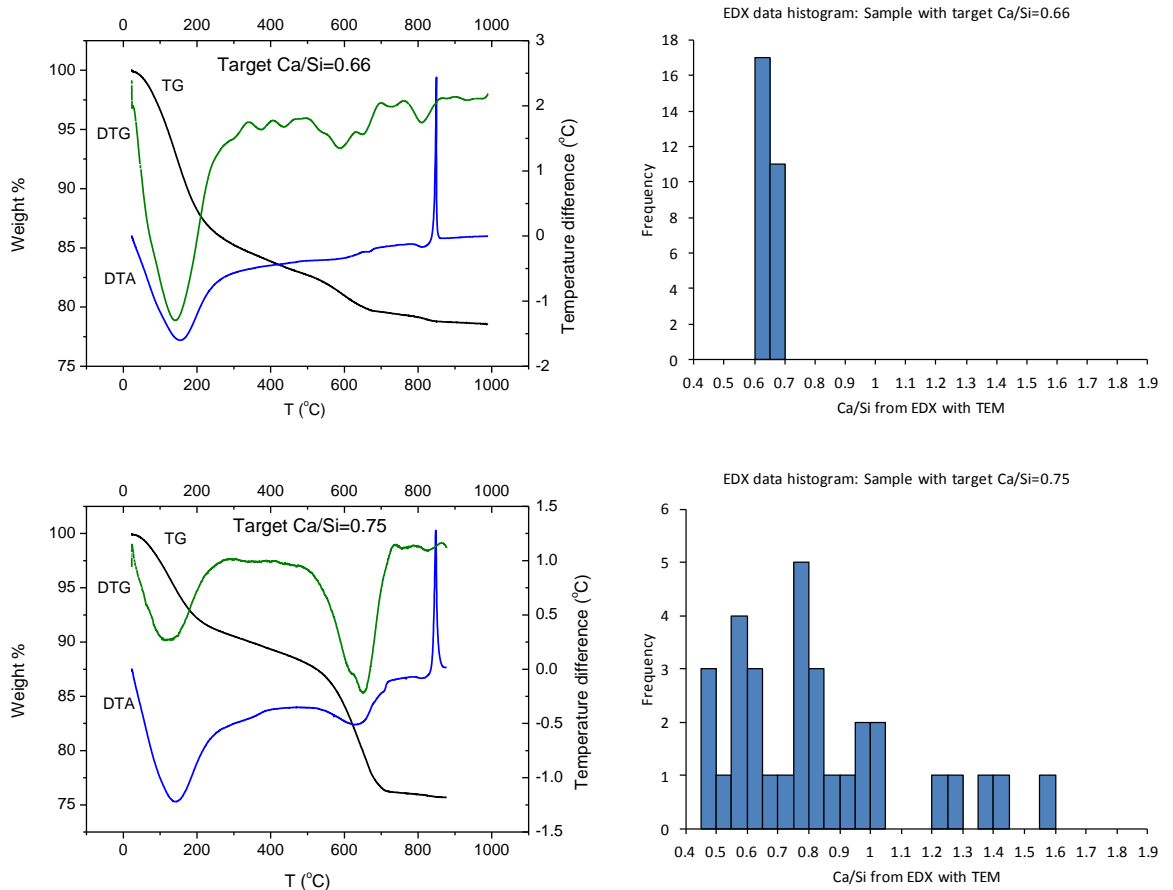


Figure 5.6. TG, DTG and DTA of C-S-H sample with target Ca/Si=0.66 (Upper graphs), and target Ca/Si=0.75 (Lower graphs).

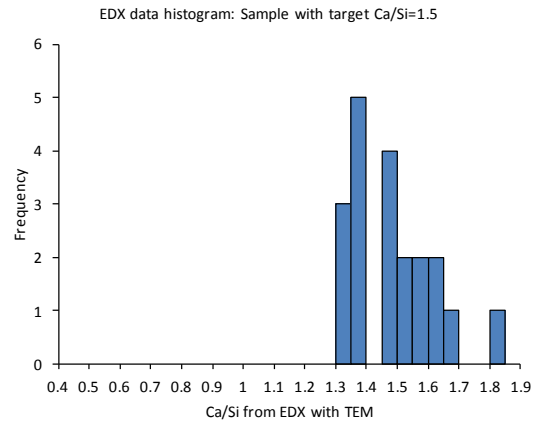
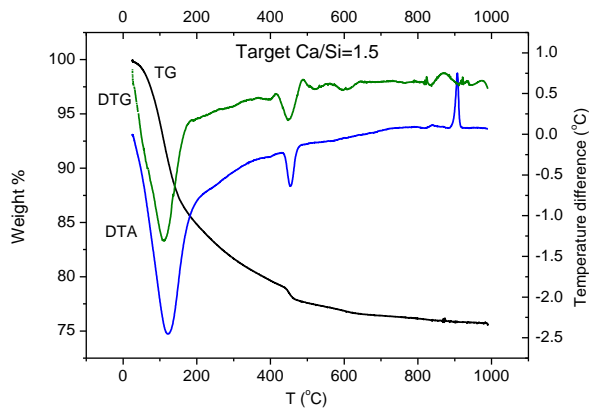
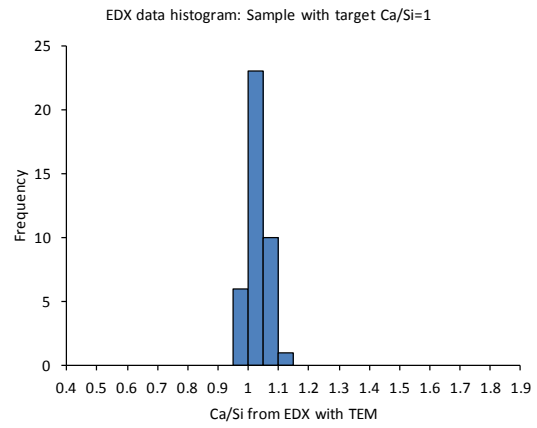
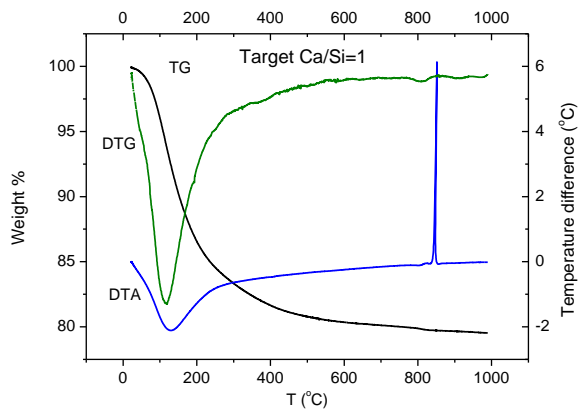


Figure 5.7. TG, DTG and DTA of C-S-H sample with target Ca/Si=1 (Upper graphs), and target Ca/Si=1.5 (Lower graphs).

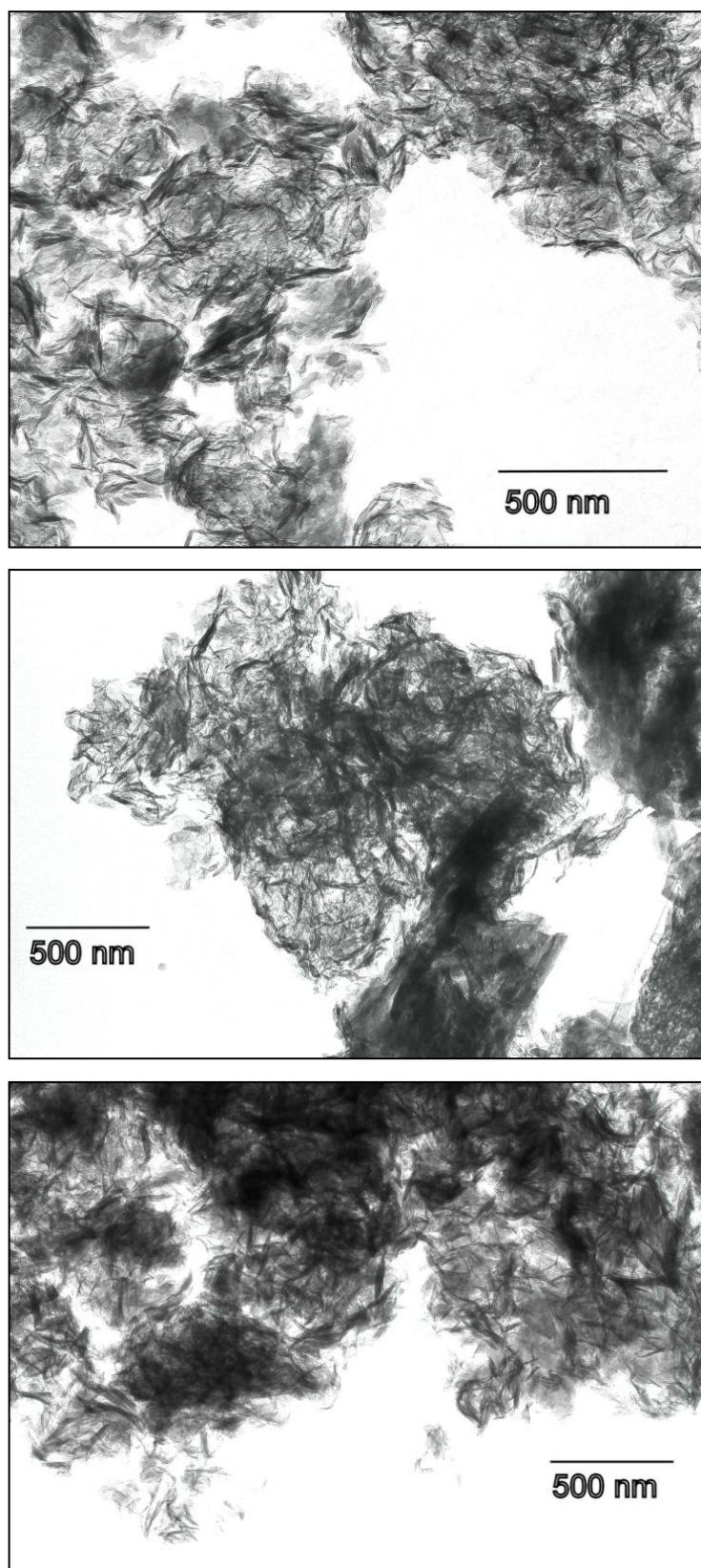


Figure 5.8. TEM micrographs showing the fine crumpled foil-like morphology of mechanochemically synthesized C-S-H with target Ca/Si=0.66 (Upper image), Ca/Si=0.75 (Central image) and Ca/Si=1 (Lower image).

5.3 Fresh mechanochemically synthesized C-S-H

The XRD patterns of the mechanochemical samples along with a reference pattern from portlandite [133] are shown in Figure 5.9. They are consistent with C-S-H(I) [4]. The basal reflection ($2\theta \sim 7^\circ$) is present in all samples. It shifts towards higher 2θ (lower distance in real space) and increases in intensity with increasing Ca/Si. The basal reflection is a sign of 3D ordering in the samples. Thus the structural order in 3D improves with increasing the Ca/Si ratio. Another sign of increasing structural order is the appearance of a shoulder at $2\theta \sim 30^\circ$ with increasing Ca/Si ratio. This was already observed by Garbev et al. [40] in XRD patterns of C-S-H samples fabricated via the same route, opposing Cong and Kirkpatrick [39] who supported the decrease in structural order with increasing Ca/Si due to the decrease in intensity of the reflection at $2\theta \sim 16^\circ$. In the results presented here, this decrease is also present. However, another indication of increasing ordering with higher Ca/Si, that has not been pointed out in literature, is the flattening of the hump that appears in all the patterns at the interval $40^\circ < 2\theta < 48^\circ$; since humps are an indication of amorphous structures. Hence this results support Garbev et al. conclusion about the improvement in structural order while increasing Ca/Si ratio. The patterns show that the samples are single-phase, with respect to crystalline content, when the bulk $\text{Ca/Si} \leq 1.33$. The extra reflections in the sample with $\text{Ca/Si}=1.5$ are due to the presence of portlandite. The only remarkable difference between these samples and the series of Garbev is that for $\text{Ca/Si}=1.33$ their sample contained traces of portlandite.

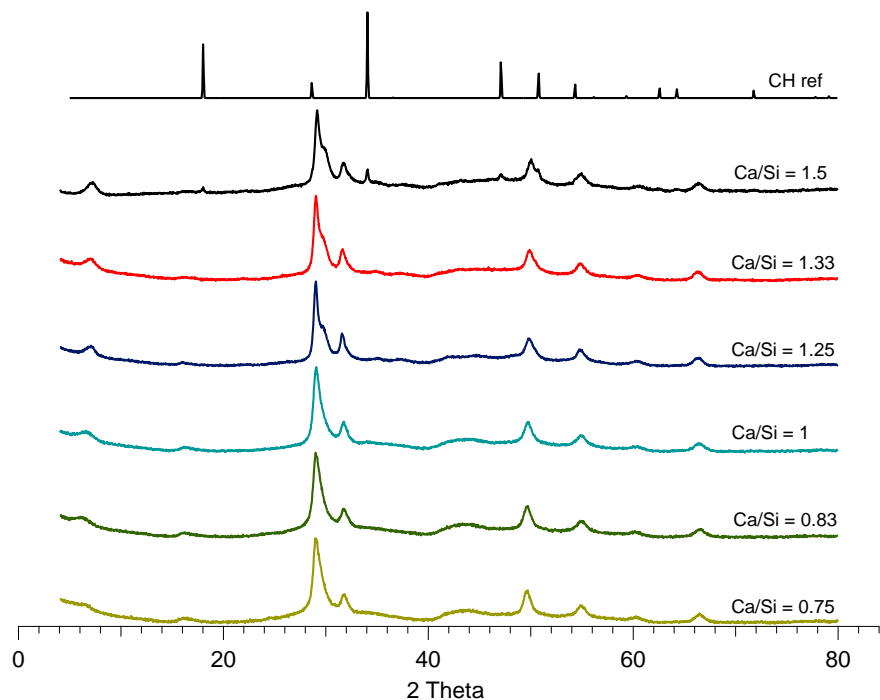


Figure 5.9. XRD patterns of the series of mechanochemical samples fabricated with CaO and Aerosil. The Ca/Si ratios are indicated above the patterns.

The ^{29}Si MAS NMR results of the series of samples are shown in Figure 5.10. The silicate structure of the samples is dominated by middle chain groups (Q^2 at $\sim -85\text{ppm}$) for $\text{Ca}/\text{Si} \leq 1$, while it is dominated by dimers (Q^1 at $\sim -79\text{ppm}$) for $\text{Ca}/\text{Si} \geq 1.25$. The contribution from bridging sites (Q^{2b} at $\sim -82\text{ppm}$) is noticeable in the spectra for $\text{Ca}/\text{Si} \leq 1$. The results were deconvoluted to estimate the percentages of the silicate connectivities and the MCL. The experimental spectra, the simulated spectra and the individual frequencies are shown in Figure 5.11. The percentages of the silicate species and the MCL are shown in Table 5.2. The results are plotted versus TEM-EDX experimental Ca/Si in Figure 5.12 and Figure 5.13. There is an obvious abrupt change of the percentages of Q^1 and Q^2 species at $\text{Ca}/\text{Si}=1$ in Figure 5.12, that can be interpreted as a discontinuity in the solid solution.

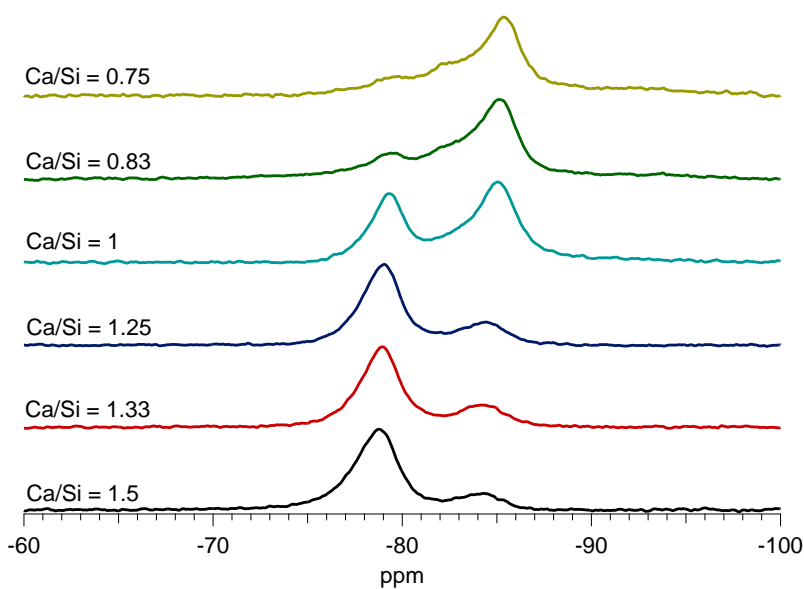


Figure 5.10. ^{29}Si MAS NMR spectra of the mechanochemical C-S-H samples.

Table 5.2. Percentages of the silicate species and MCL for the mechanochemical series. The results have been calculated from the deconvolution of the NMR spectra shown in Figure 5.11.

Bulk Ca/Si	$\text{Q}^1 \pm 2.0$	$\text{Q}^2 \pm 2.0$	$\text{Q}^3 \pm 2.0$	MCL
0.75	9.5 %	79.8 %	10.7 %	21.1 ± 4.0
0.83	19.1 %	77.1 %	3.8 %	10.5 ± 0.9
1.00	35.7 %	62.0 %	2.3 %	5.6 ± 0.2
1.25	74.0 %	26.0 %	0%	2.7 ± 0.2
1.33	79.9 %	20.1 %	0%	2.5 ± 0.2
1.50	87.7 %	12.3 %	0%	2.3 ± 0.3

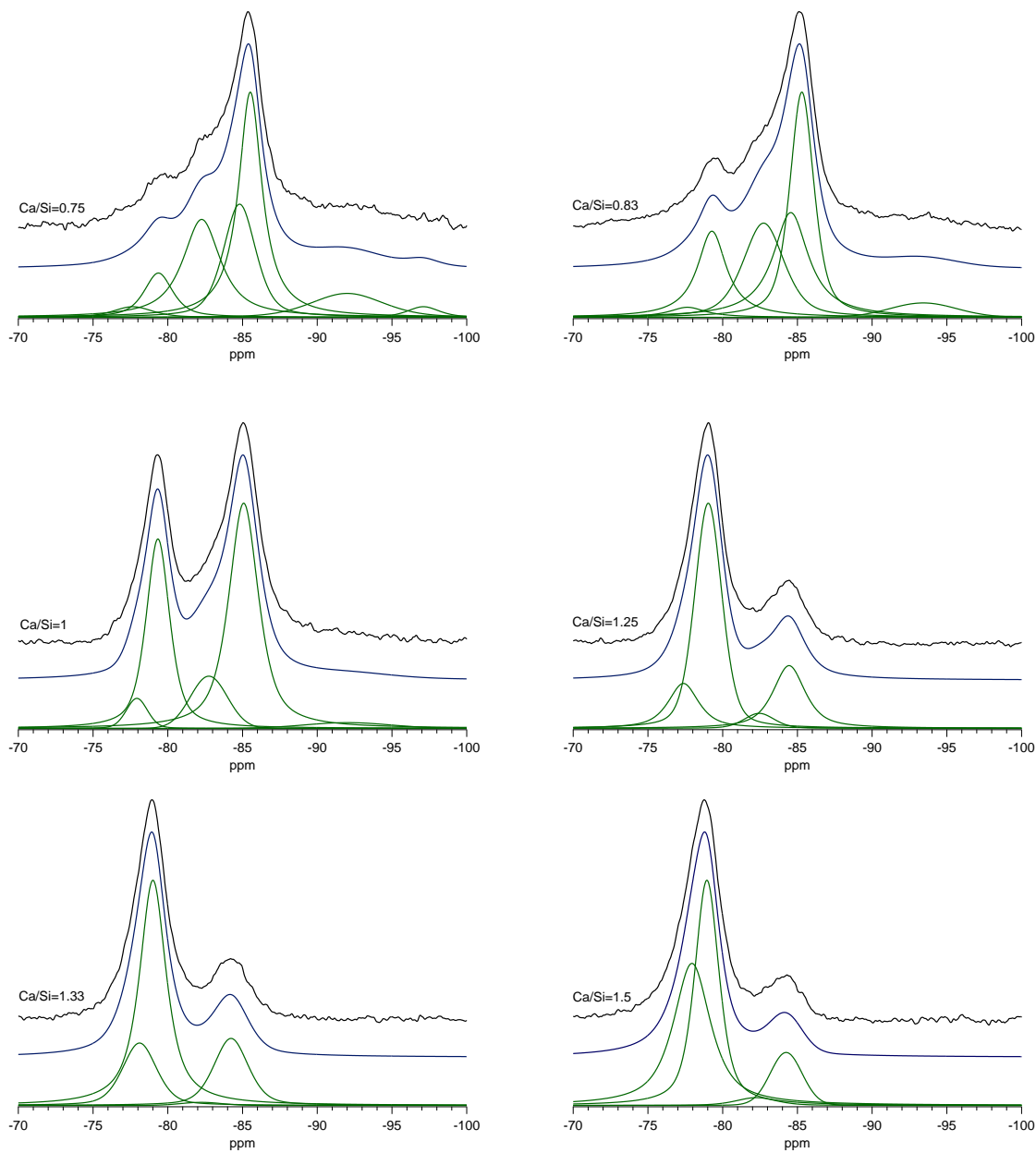


Figure 5.11. Deconvolutions of the ^{29}Si MAS NMR spectra of the mechanochemical samples showing the individual frequencies (green), the simulated spectra as a sum of the individual frequencies (blue) and the experimental spectra (black).

Both intensities for Q^1 and Q^2 arise from groups with slightly different chemical environments, thus giving broader peaks. Two frequencies were used for both Q^1 and Q^2 for the spectra of the samples with $\text{Ca}/\text{Si} \geq 1$. Although Q^1 intensity is originated by dimers and end-chain groups, the frequencies used in the deconvolutions are not a direct representation of these species, but chosen for fitting purposes. Q^2 intensity in C-S-H is known to be originated from middle chain sites (Q^{2p}) at $\sim -85\text{ppm}$ and bridging silicate tetrahedra (Q^{2b}) at $\sim -82\text{ppm}$. Although the frequencies

used for the deconvolutions lie in these ppm, they are not a direct representation of these species either. If a direct representation was required, the line widths and shapes of the chosen frequencies should be constant between samples, and this was not the case in these deconvolutions. These parameters were relaxed during the fitting process and that resulted in variations between samples. For $\text{Ca/Si} < 1$ three frequencies were used for Q^2 , and two for Q^1 , in order to improve the fitting and adjust the simulated spectra as much as possible to the experimental one. The extra frequency chosen for Q^2 is situated at $\sim 84\text{ppm}$. Intensity in this region could have been originated from Q^2 groups in the vicinity of Q^3 groups, or from Q^{2p} situated in the centre of octamers or longer segments. These Q^{2p} will then be connected to identical Q^{2p} , while the Q^{2p} in pentamers are always connected to a bridging site and an end-chain site. From the deconvolution results in Table 5.2, it is clear that the percentage of Q^1 increases with increasing Ca/Si , while the percentage of Q^2 decreases. The presence of less silica in the samples is associated with a tendency to form dimeric silicate units instead of longer silicate chains. This is supported by the decrease of the MCL towards a value of 2 with increasing Ca/Si . For samples with low Ca/Si , thus high silicate content, a percentage of cross linking groups Q^3 is also found. For the sample with $\text{Ca/Si}=1$ the percentage of Q^3 is very low. If Q^3 was not fitted and this intensity was considered to be part of the tail of Q^2 groups, that would change the MCL from 5.5 to 5.6. Thus the MCL is not very sensitive to slight changes in the fitting. The MCL varies from 18.8 to 2.3 while increasing the Ca/Si . In Figure 5.13 it is clear that the decrease in MCL does not depend linearly on the Ca/Si , but exponentially.

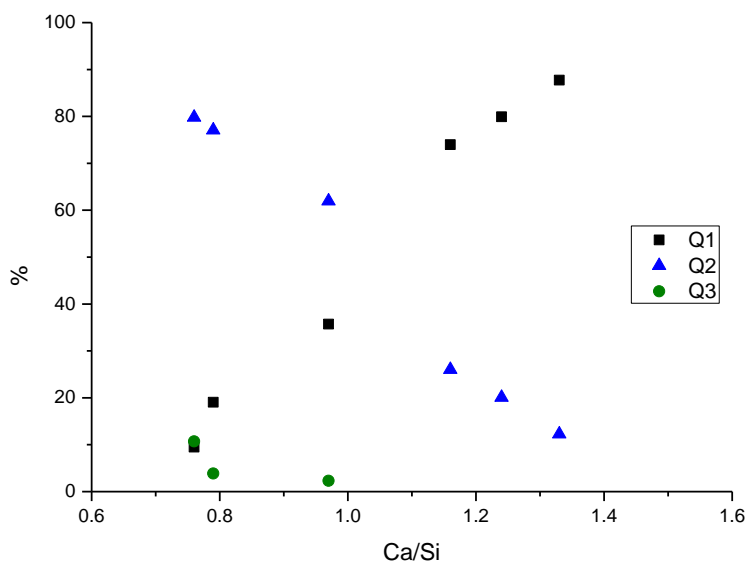


Figure 5.12. Percentage of the silicate species Q^1 , Q^2 and Q^3 obtained from NMR vs. the experimental Ca/Si (TEM-EDX) in the mechanochemical C-S-H.

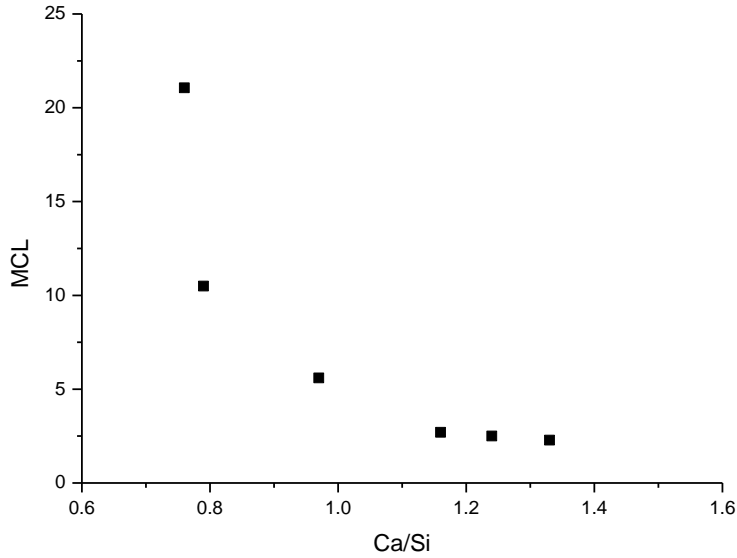


Figure 5.13. Mean silicate chain length vs. Ca/Si (TEM-EDX) in the mechanochemical series.

The TG results of all the samples are shown in Figure 5.14. The results show typical curves for C-S-H phases with the most significant weight loss happening until $\sim 200^\circ\text{C}$. The presence of portlandite in the sample with Ca/Si=1.5 is confirmed by the hump appearing in the TG curve at $\sim 400^\circ\text{C}$, which corresponds to the decomposition of portlandite. The weight loss between $800^\circ\text{C} - 900^\circ\text{C}$ is due to the complete dehydration of the samples to form wollastonite.

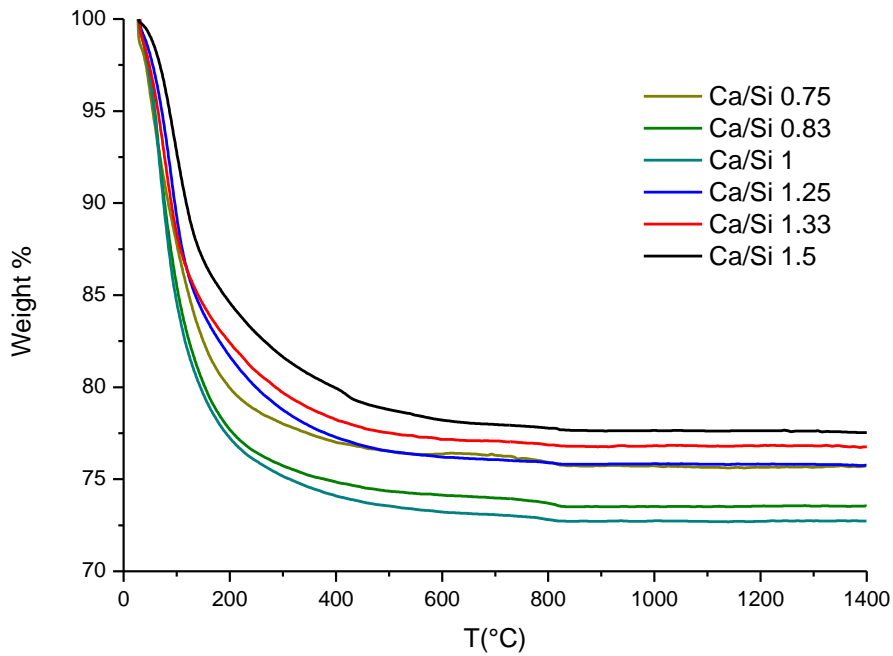


Figure 5.14. TG results from the mechanochemical series of C-S-H samples.

DSC curves were also recorded. The interval between 700°C and 1400°C is shown in Figure 5.15. The curves have been vertically shifted for clarity. They show the transformation from C-S-H into β -wollastonite when C-S-H has completely dehydrated in the approximated interval between 850°C - 950°C, followed by the transformation from β -wollastonite into α -wollastonite at ~1300°C. The temperature for both these transformations depends on the Ca/Si ratio. The temperature at the onset of the transformations is stated in Table 5.3. The transformation into β -wollastonite is accompanied by the presence of SiO₂ for samples with Ca/Si up to 1, and by the formation of C₂S for samples with Ca/Si>1.

Table 5.3. Temperature transformation of C-S-H into β -wollastonite and β -wollastonite into α -wollastonite of the mechanochemical series of C-S-H samples.

Bulk Ca/Si	T (°C)	
	C-S-H → β -wollastonite	β -wollastonite → α -wollastonite
0.75	817.5	1275.8
0.83	826.0	1277.5
1.00	828.1	1247.2
1.25	874.1	1242.7
1.33	891.7	1242.2
1.50	891.3	1225.3

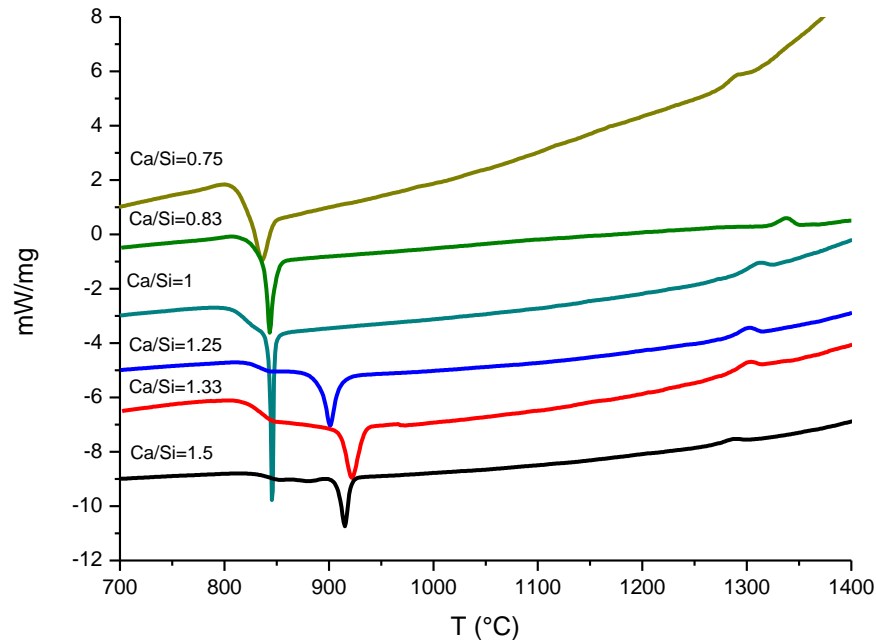


Figure 5.15. DSC data from the mechanochemical C-S-H samples. The curves have been vertically shifted for clarity.

For low Ca/Si ratios the transformation to β -wollastonite happens at lower temperatures than for high Ca/Si ratios. This indicates that water is more chemically bound for samples with high

Ca/Si. The dependence on temperature formation of wollastonite upon Ca/Si has been reported by different authors such as Mitsuda [87], Suzuki [125] and Bornefeld [134]. A comparison of all the data is shown in Figure 5.16. For Ca/Si > 0.6 all the results are in good agreement. Bornefeld showed that the transformation temperature actually depends on the occupancy of the interlayer with Ca or other atoms. Some samples containing potassium with the ratio K/C=0.25 showed a similar temperature transformation than pure C-S-H with Ca/Si=1.25, even when their Ca/Si were lower, proving thus that potassium was bonded in the interlayer [134]. The dependence of the temperature transformation of β -wollastonite into α -wollastonite on the Ca/Si ratio of the C-S-H precursors has never been reported before. The temperature for this transformation decreases with increasing Ca/Si. That implies that an excess of SiO₂ stabilizes the β -polymorph and the excess of CaO stabilizes the α -polymorph. That can be related to the silicate structure of the samples and the silicate structure of both polymorphs. β -wollastonite silicate structure comprises long chains while the silicate structure of α -wollastonite consists of rings of 3 silicate tetrahedra. The silicate structure of the C-S-H with high Ca/Si is mainly dimeric and these samples stabilize the α -polymorph which has the 3 silicate rings, while the silicate structure of the C-S-H with low Ca/Si has longer silicate chains and these samples stabilize the β -polymorph, which has a silicate structure of long chains. This may be the indication of slight differences in the silicate structure of the β -polymorph that forms after heating C-S-H of different Ca/Si ratios, so that it is prone to transform into the α -polymorph at different temperatures. This would need further investigations with a technique such as in-situ Raman spectroscopy.

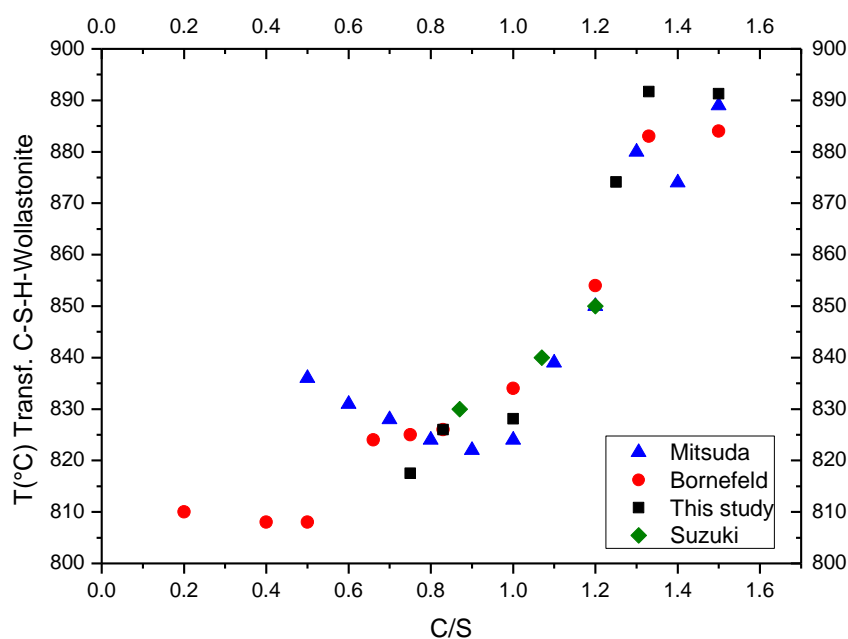


Figure 5.16. Transformation temperature of C-S-H into wollastonite from Mitsuda [87], Bornefeld [134], Suzuki [125] and the mechanochemical samples from this study.

While performing TG and DSC, FTIR was also used to monitor the gases that were expelled from the samples. The water and CO₂ traces are shown together with TG and DSC in Figure 5.17 in order to couple the ejection of the gases from the samples with the TG and DSC events. FTIR makes it possible to quantify the weight loss from each gas and compare the total loss with the one obtained from TG. The results are summarised in Table 5.4 and show that both techniques agree. The real Ca/Si of the samples was calculated by oxide mass balance taking into account the traces of carbonates and portlandite.

Table 5.4. Quantification of the CO₂ and H₂O content and total loss mass percentage of the mechanochemical C-S-H series obtained from FTIR, total loss percentage obtained from TG, and real Ca/Si recalculated taking into account the traces of carbonates and portlandite.

Bulk Ca/Si	CO₂ % content (FTIR)	H₂O% content (FTIR)	Loss % (FTIR)	Loss % (TG)	Real Ca/Si
0.75	1.15	23.33	24.48	24.28	0.72
0.83	1.11	25.32	26.43	26.45	0.80
1.00	1.15	26.36	27.51	27.26	0.96
1.25	0.65	23.61	24.26	24.25	1.23
1.33	1.14	22.03	23.18	23.25	1.29
1.50	1.19	21.30	22.49	22.51	1.34

Figure 5.17 shows that the FTIR water trace is very similar for all samples, showing most of the water being expelled from the samples up to 200°C. This matches a feature in the DSC curve that indicates an endothermal transformation. The sharp feature that appears in the water trace up to 40°C is related to an atmospheric residue due to the opening of the chamber to introduce the sample. This feature is also observed in the CO₂ trace. Wollastonite is a non-hydrated calcium silicate, therefore C-S-H has to lose all its crystal water to transform into wollastonite. The most significant water loss occurs up to 200°C and for samples with Ca/Si=0.75 and 0.83 a small peak in the water trace is appreciated at the onset of the transformation. For the sample with Ca/Si=1.5 the water trace also shows a peak ~ 400°C, which corresponds to the dehydration of portlandite. The CO₂ traces show that most of the gas is expelled at the onset of the transformation to wollastonite. The loss of CO₂ at 400°C - 500°C is associated to the decarbonation of amorphous calcite. For the sample with Ca/Si=1.5 there is a significant CO₂ loss at ~ 600°C that originates from the decomposition of cryptocrystalline calcite. All the water and CO₂ traces are shown together in Figure 5.18. The temperature scales have been chosen so that the significant features of the traces are highlighted. From the water traces it can be appreciated that the maximum release of water shifts towards higher temperatures with increasing Ca/Si. This is an indication of more chemically bound water with increasing Ca/Si.

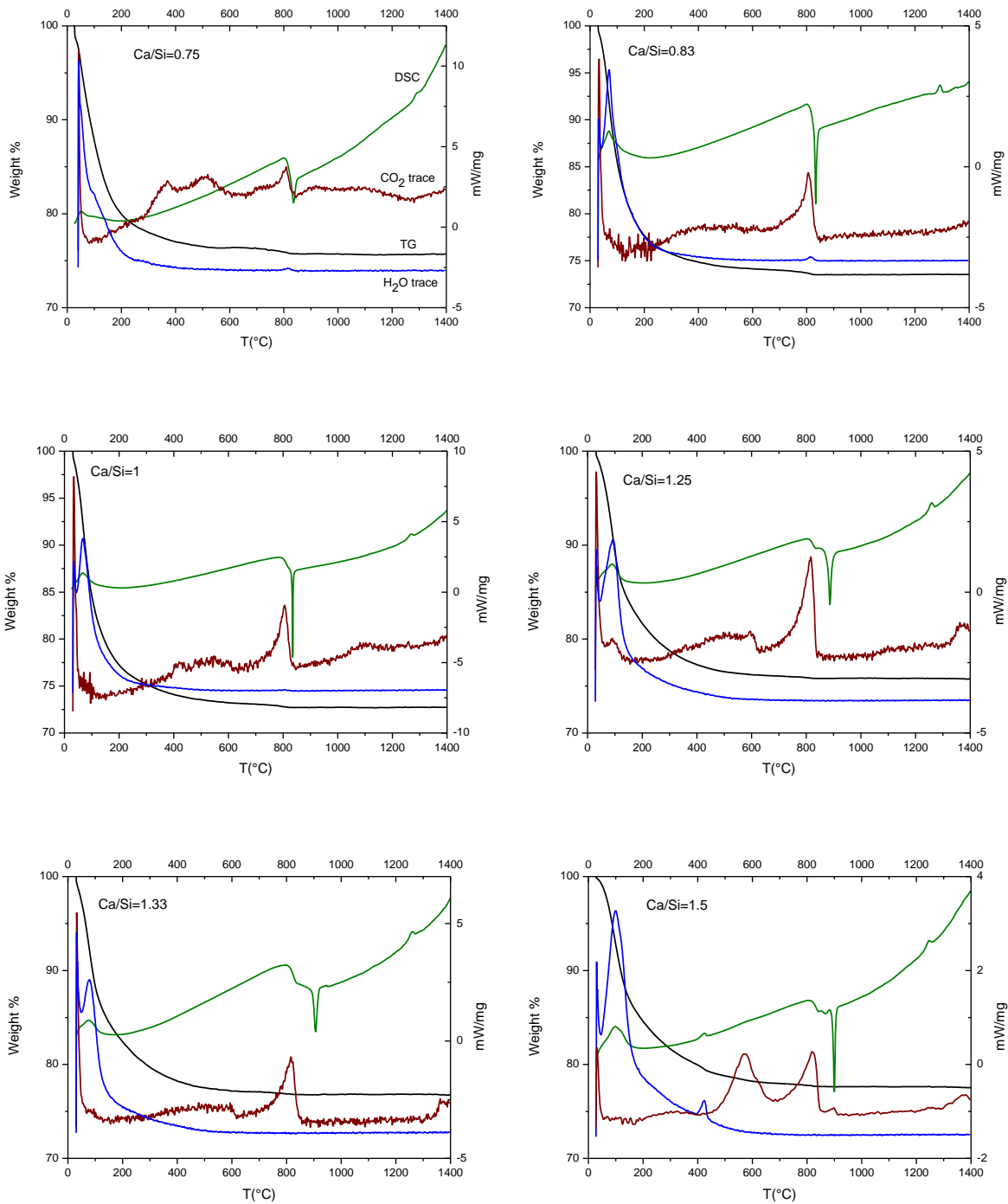


Figure 5.17. Graphs showing TG (black), DSC (green) and the FTIR traces of H₂O (blue) and CO₂ (red) for the mechanochemical series of C-S-H. The FTIR traces have been normalized by sample weight. The vertical scales for the FTIR traces have been chosen arbitrary for clarity, and are not shown in the graphs. For comparison of intensities of the FTIR traces between samples, see Figure 5.18.

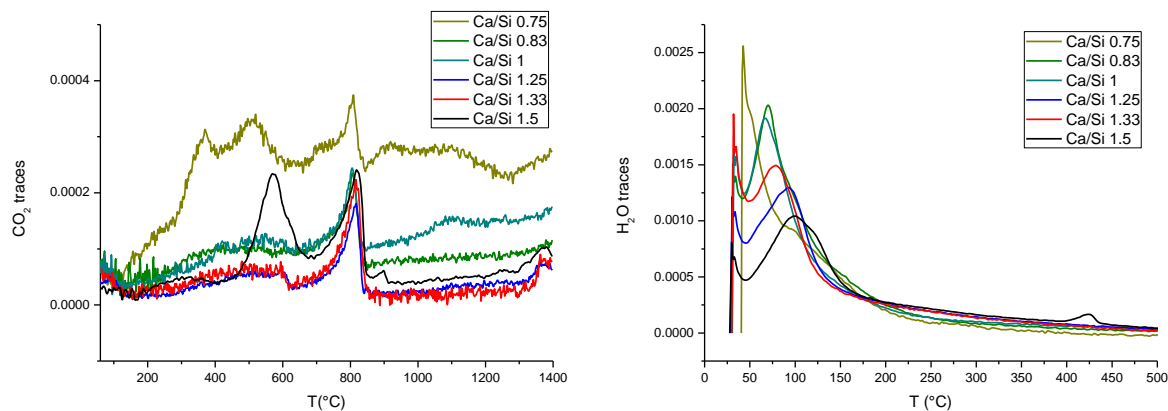


Figure 5.18. Water and CO₂ FTIR traces of the mechanochemical samples recorded while performing TG and DSC.

To complement the thermal stability investigations of the C-S-H samples, morphological analyses were carried out with TEM. Micrographs of all the samples are shown in Figure 5.19. The morphology is crumpled foil-like for all samples regardless of the Ca/Si. The Ca/Si from EDX, XRF and TG are summarised in Table 5.5. The Ca/Si ratios obtained by XRF are not corrected for portlandite nor carbonates, but a direct calculation from oxide masses content. They are however very close to Ca/Si given by TG, in which portlandite and carbonates were taken into account. The Ca/Si given by TEM-EDX are also close to those given by other techniques and the standard deviations are low, which indicates the samples are very homogeneous in composition. The histograms for the Ca/Si obtained by TEM-EDX are shown in Figure 5.20. The histogram that shows more data dispersion is the one that corresponds to the sample with target Ca/Si=1.5. This can be associated to the presence of portlandite in the sample.

Table 5.5. Ca/Si of the mechanochemical samples obtained by TEM-EDX (with standard deviations), XRF and TG.

Ca/Si Bulk	0.75	0.83	1	1.25	1.33	1.5
Ca/Si XRF	0.75	0.81	0.98	1.23	1.29	1.36
Ca/Si TG	0.72	0.80	0.96	1.23	1.29	1.34
Ca/Si EDX	0.76±0.02	0.79±0.03	0.97±0.05	1.16±0.06	1.24±0.04	1.33±0.07
# EDX points	20	30	25	21	20	30

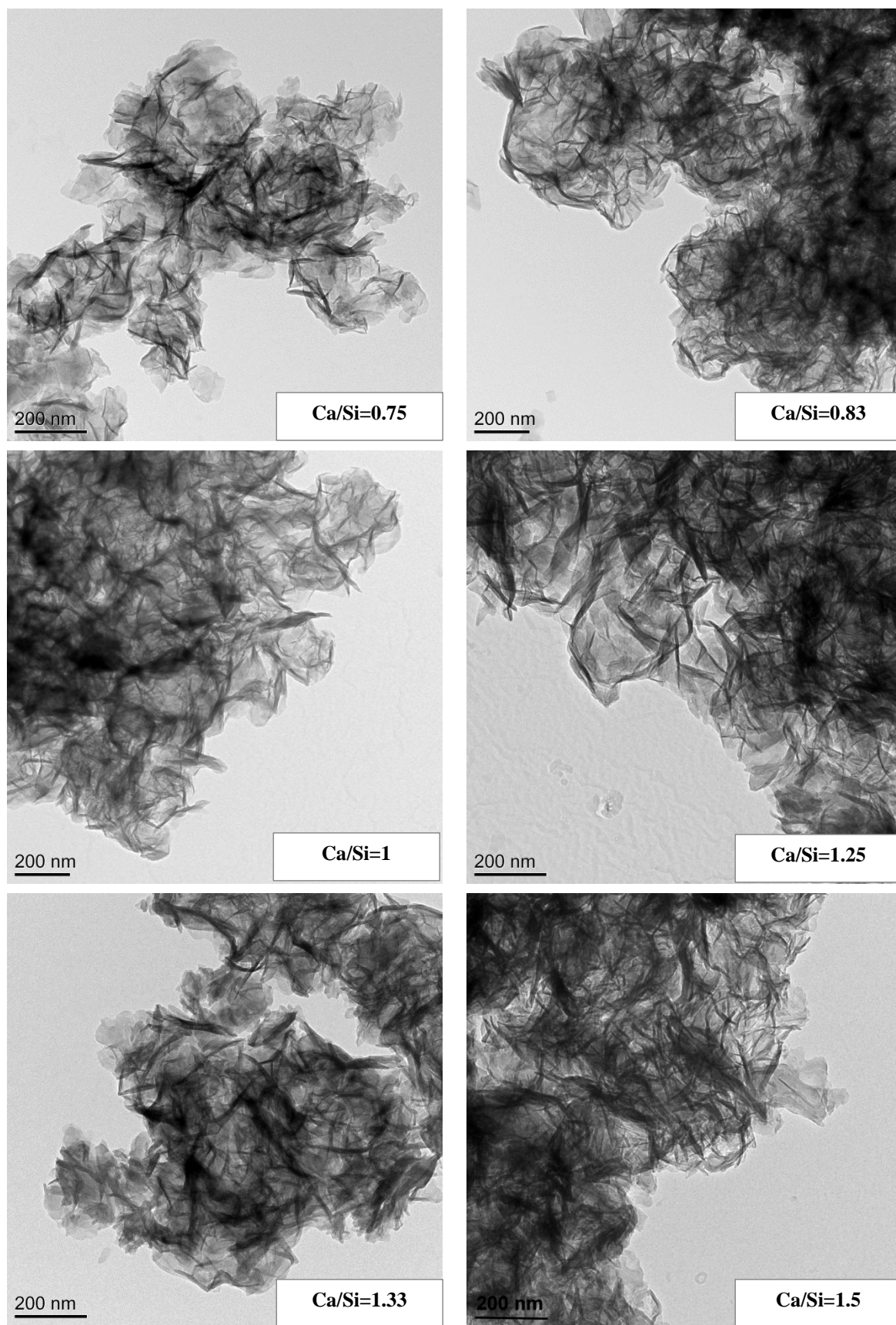


Figure 5.19. TEM micrographs of the mechanochemically synthesized C-S-H. The Ca/Si of the sample is indicated in each micrograph.

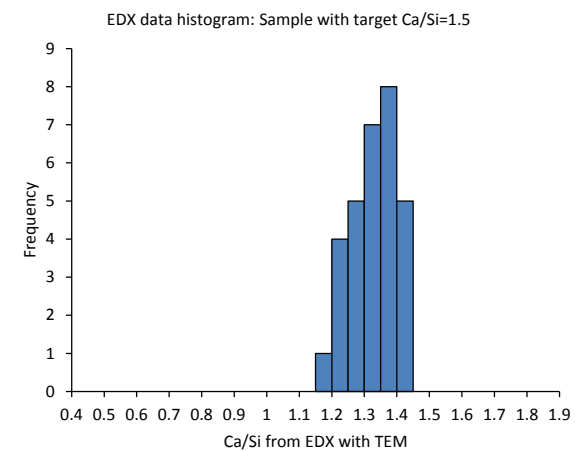
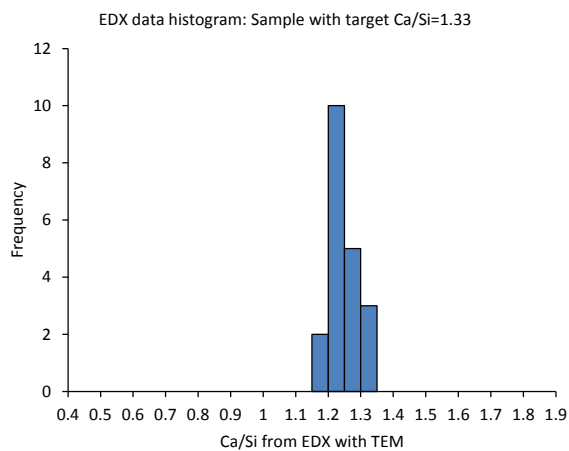
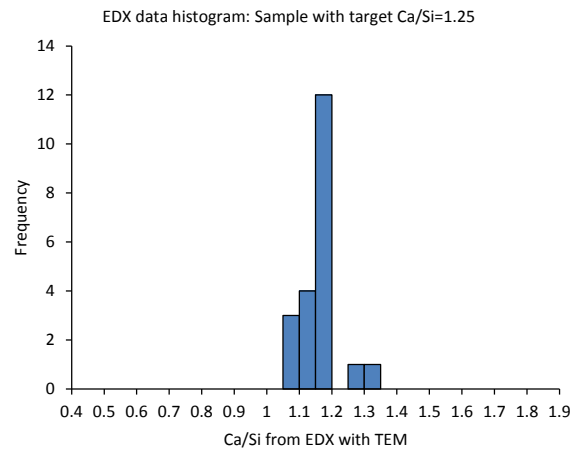
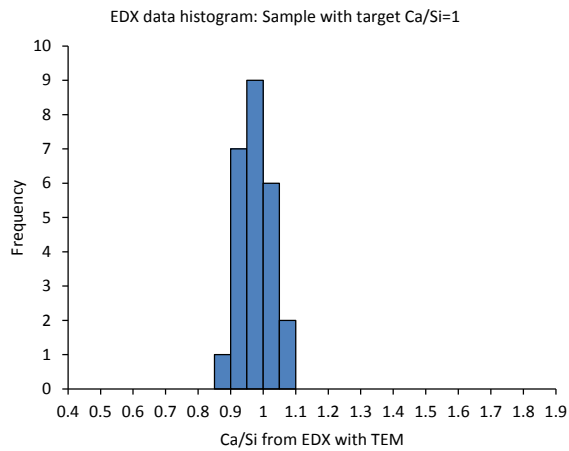
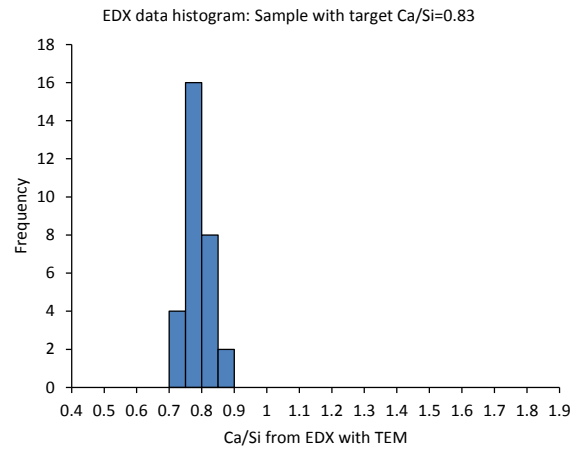
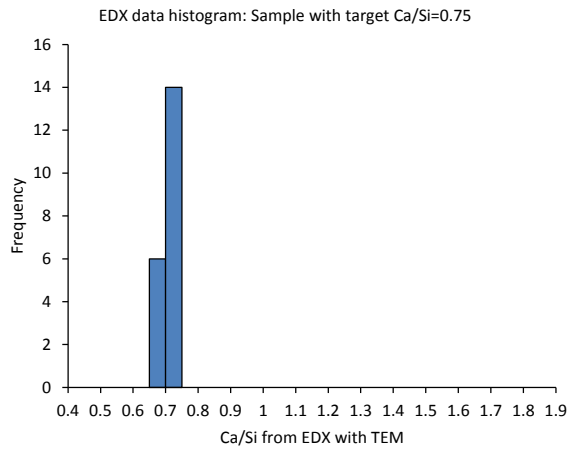


Figure 5.20. Histograms of the Ca/Si obtained with TEM-EDX of the C-S-H mechanochemical samples.

Richardson and Groves' model was applied for charge balance calculations. The height of the histograms for Ca/Si (A bar limited by the minimum and maximum values for the obtained experimental Ca/Si) was plotted against the reciprocal mean chain length for each sample in Figure 5.21. The trends for the tobermorite and jennite structural units with maximum, intermediate and minimum degree of protonation ($w/n=2, 1, 0$) were also plotted. The mean value of Ca/Si obtained by TEM-EDX is indicated with a cross. This is the value used to get the chemical structural formulae. It is evident from the plot that the composition of the samples lays within the tobermorite-like region and no Ca-OH groups are needed in the structures.

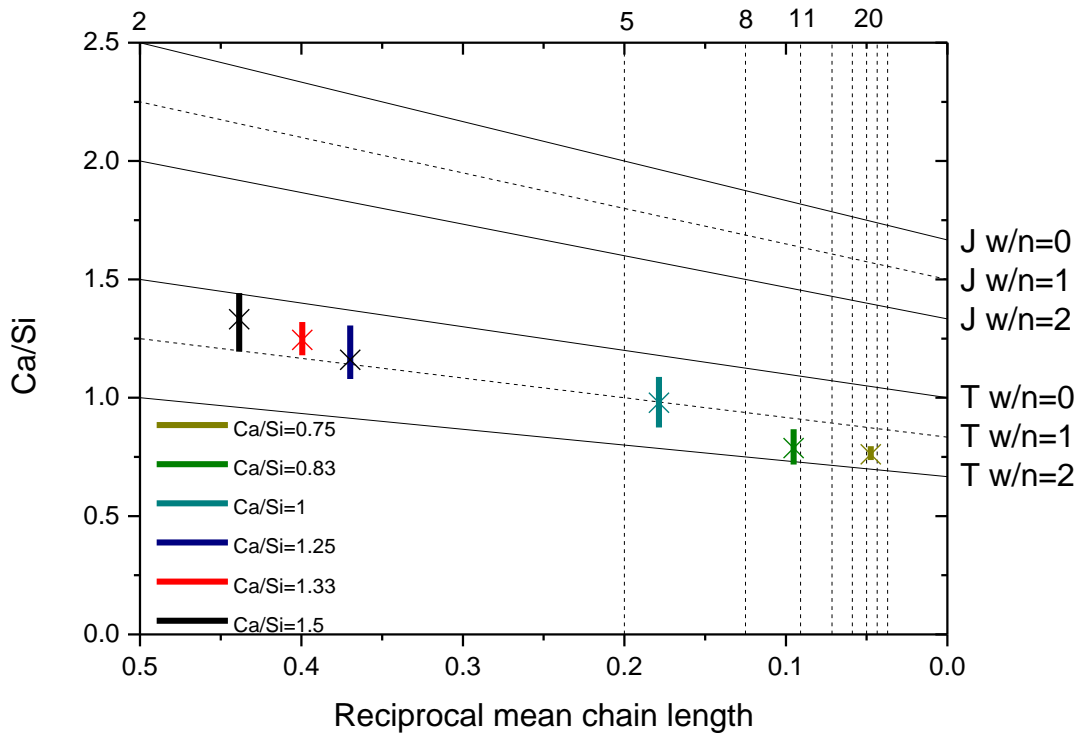
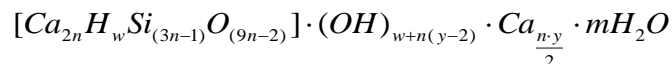


Figure 5.21. Ca/Si vs. reciprocal mean chain length of the mechanochemical C-S-H samples. The length of the bars is limited by the minimum and maximum Ca/Si obtained by TEM-EDX and the mean value is marked with a cross. The structural units for tobermorite and jennite with minimum ($w=0$), intermediate ($w=1$) and maximum ($w=2$) degree of protonation are also marked. The vertical dashed lines represent the $(3n-1)$ structural units: dimer (2), pentamer (5), octamer (8)...

Since no Ca-OH groups are needed, it is irrelevant to use either the T/J view point or T/CH. The T/J formulation was chosen, whose formula is:



In the T/J view of the model $(3n-1)=MCL$ and $Ca/Si=(4n+ny)/(6n-2)$, so that $n=(MCL+1)/3$ and $y=[(Ca/Si)(6n-2)-4n]/n$. The number of silanol groups w depends on the value of y according to:

$$0 \leq y \leq 2 \rightarrow n(2 - y) \leq w \leq 2n$$

$$2 \leq y \leq 4 \rightarrow 0 \leq w \leq 2n$$

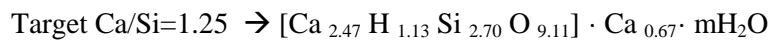
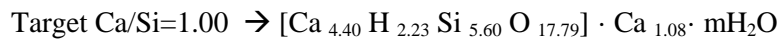
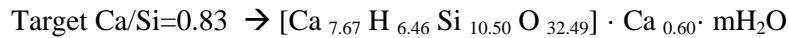
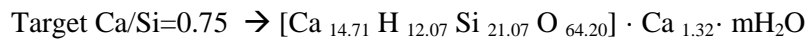
$$4 \leq y \leq 6 \rightarrow 0 \leq w \leq n(6 - y)$$

The calculated values for n , y , w_{\max} (maximum number of silanol groups), w_{\min} (minimum number of silanol groups) and w/n_{\max} (maximum degree of protonation) and w/n_{\min} (minimum degree of protonation) are shown in Table 5.6.

Table 5.6. Calculated values for the parameters of the T/J view point of Richardson and Groves' model for the mechanochemical C-S-H samples.

Target Ca/Si	n	y	w_{\min}	w_{\max}	w/n_{\min}	w/n_{\max}
0.75	7.36	0.36	12.07	14.71	1.64	2
0.83	3.83	0.31	6.46	7.67	1.69	2
1.00	2.20	0.98	2.23	4.40	1.02	2
1.25	1.23	1.08	1.13	2.47	0.92	2
1.33	1.17	1.34	0.78	2.34	0.66	2
1.50	1.09	1.55	0.49	2.19	0.45	2

The minimum degree of protonation was chosen to derive the composition of the samples, since it was the most sensible value according to the position of the mean Ca/Si with respect to the tobermorite trends in Figure 5.21. The resulting structural chemical formulae consist in a tobermorite-like core (within brackets) with no extra Ca either in jennite or solid solution CH:



Since the amount of water is unknown, it is left as m in the structures. Samples with target $\text{Ca/Si} > 1.00$ can be accounted for by a mixture of dimeric and pentameric tobermorite units, T2 and T5 in ref. [1]. The sample with target $\text{Ca/Si}=1$ can be explained with a mixture of T8, T5 and T2 units, the sample with target $\text{Ca/Si}=0.83$ with a mixture of T11, T8, T5 and T2, and the sample with target $\text{Ca/Si}=0.75$ with a mixture of T23 and all the rest of tobermorite units with shorter silicate chains.

5.4 CaO-SiO₂ C-S-H series

The XRD patterns (kindly provided by A. Nonat) of the series of samples fabricated via silica-lime reactions under continuous stirring are shown in Figure 5.22 together with a reference pattern of calcite [135], CH [133], aragonite [136] and vaterite [137]. The basal reflection ($2\theta \sim 7^\circ$) is present in all samples except in sample with target Ca/Si=0.75. It also presents higher intensity with increasing Ca/Si ratio, as in the case of the mechanochemical series, although this is not very clear for the sample with target Ca/Si=1.35. The comparison of the patterns with the reference patterns of calcite and portlandite confirm that the samples do not contain traces of these two phases. Small residual peaks corresponding to aragonite and vaterite are found at 2θ between 25° and 28° for samples with target Ca/Si=0.8, 1.27 and 1.35. The basal spacing of these samples and the mechanochemical samples was calculated with the Bragg condition in Eq. 3.6 taking the position of the maximum in the basal reflection. The results are indicated in Table 5.7. The basal spacing of sample with target Ca/Si=0.75 could not be calculated since the basal reflection is not resolved for this sample.

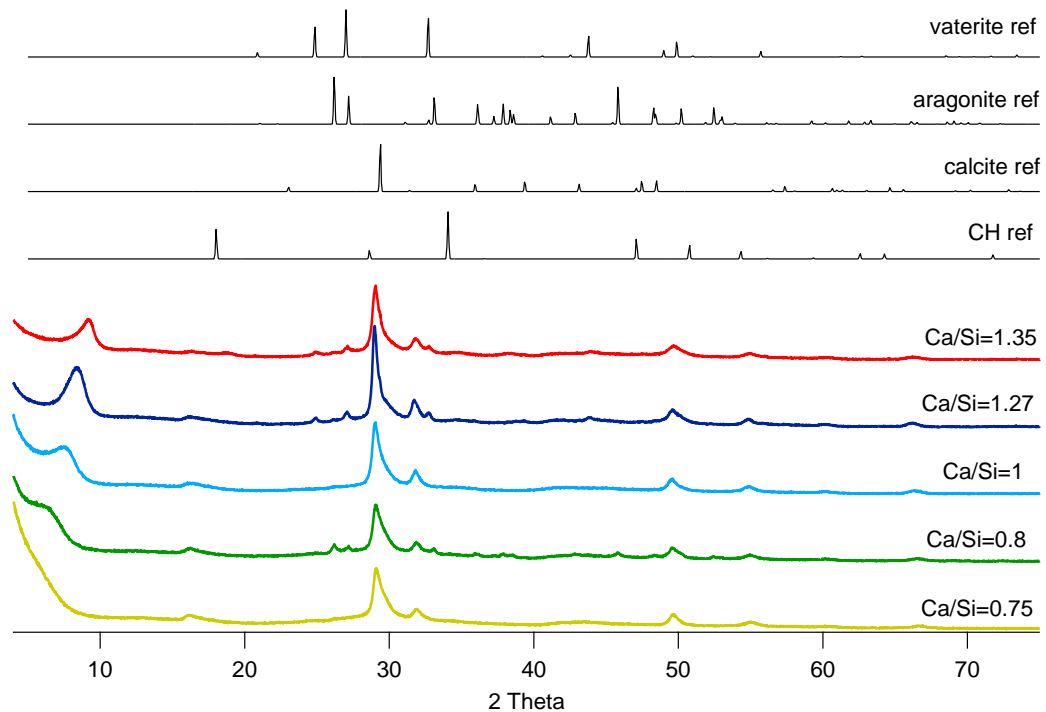


Figure 5.22. XRD patterns of the CaO-SiO₂ C-S-H series with a reference pattern for calcite, portlandite, aragonite and vaterite.

The basal spacing decreases with increasing Ca/Si for both series. This is in agreement with data presented in the literature review in Figure 2.8 taken from ref. [36]. A similar plot including the experimental data measured in this work is shown in Figure 5.23. The basal spacing was plotted

against the mean Ca/Si ratio obtained by TEM-EDX for both series of samples (Ca/Si values for the mechanochemical series indicated in Table 5.5 and in Table 5.9 for the CaO-SiO₂ series).

Table 5.7. Basal spacing in Å for the C-S-H mechanochemical samples and the CaO-SiO₂ C-S-H samples.

Mechanochemical Target Ca/Si	Mechanochemical Basal spacing (Å)	CaO-SiO ₂ Target Ca/Si	CaO-SiO ₂ Basal spacing (Å)
0.75	13.58	0.75	-
0.83	14.31	0.80	13.94
1.00	13.37	1.00	11.75
1.25	12.49	1.27	10.59
1.33	12.55	1.35	9.65
1.50	12.15	1.42	-

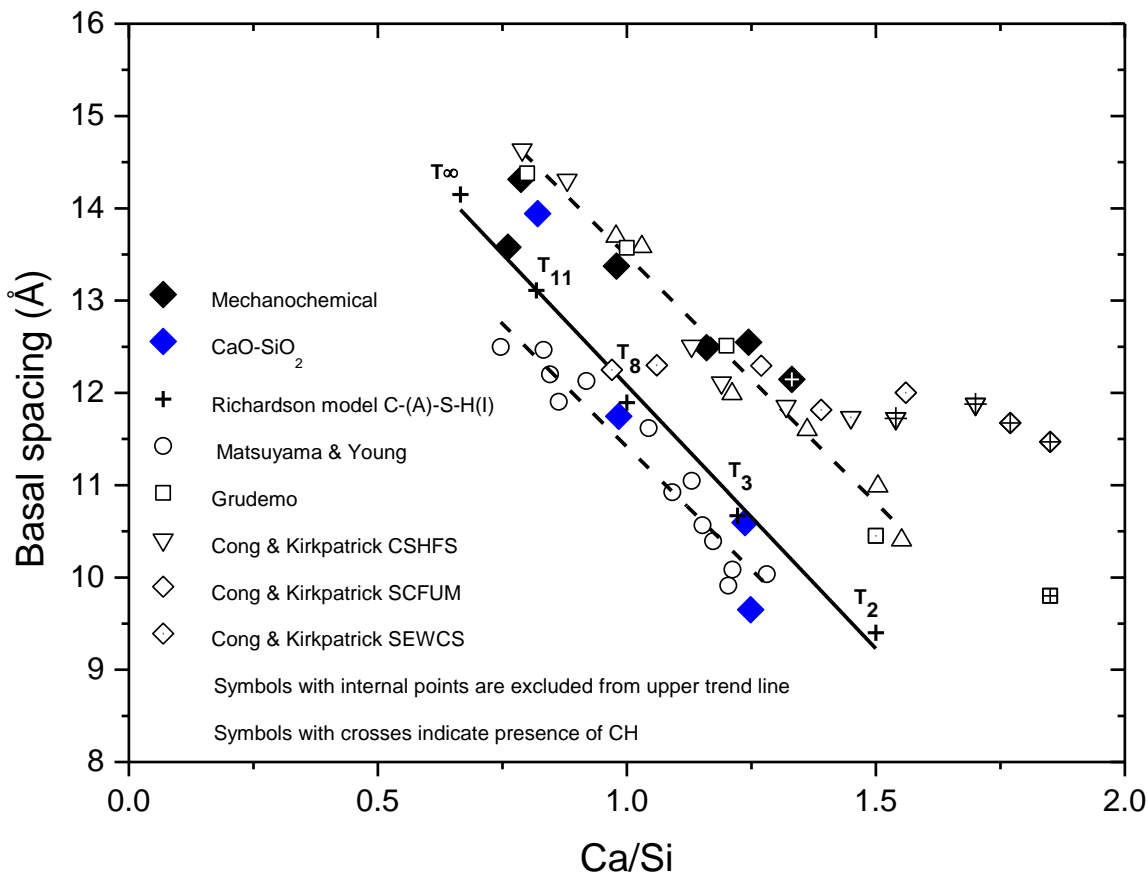


Figure 5.23. Basal spacing against Ca/Si ratio (TEM-EDX) for the C-S-H mechanochemical and the CaO-SiO₂ C-S-H series. Data from Matsuyama and Young [42] was fitted to configure the lower trend line. Data from Richardson’s model structures for C-(A)-S-H(I) [36] configure the middle trend line. Data from Grudemo [42] and Cong and Kirkpatrick [39] configure the upper trend line. Symbols marked with points or crosses belong to the same data groups as the identical

unfilled symbols. They are both not used to fit the upper trend line and the crosses indicate the presence of CH.

Most of the data points that belong to the mechanochemical samples are placed close to the upper trend line, while most of the data points that belong to the CaO-SiO₂ series are placed closer to the lower trend line. As it was discussed in the literature review, the samples that follow the upper trend line present a water molecule more per silicon atom than the samples that follow the lower trend line. This implies the CaO-SiO₂ series is dried to a higher extent than the mechanochemical samples. This agrees with the used drying methods, since the samples fabricated via the mechanochemical method were dried by heating at 60°C and the samples from the CaO-SiO₂ series were dried under vacuum. This last drying method is harsher than heating, so that those samples were expected to present a higher level of drying. Oven drying up to 105°C is considered equivalent to D-drying in terms of the removal of evaporable water [138]. In D-drying, the crushed sample is placed in a sealed container pumped by a rotary pump. The pumping line is connected to a glass container with water ice, which is packed in solid CO₂ (known as dry ice). The drying conditions are then in vacuum at the equilibrium vapour pressure above ice at -79°C (~6.7·10⁻² Pa) [138]. Since D-drying is a more gentle method than vacuum drying and this last method is equivalent to drying at 105°C (only in terms of measuring evaporable water), drying at 60°C must be a less severe method than vacuum dry.

The point for the sample with target Ca/Si=0.8 from the CaO-SiO₂ series is placed closer to the upper trend line than to the lower trend line. This could be due to a shift of the maximum of the basal reflection, associated to the background that appears at low 2θ angles in the XRD patterns in Figure 5.22. The background is present in all samples but it is possible that it affects the position of the basal reflection to a greater extent for the sample with target Ca/Si=0.8, since the basal reflection is less intense and defined than for the rest of the series.

As Richardson discussed [36], data points to the right of the upper trend line are due to intermixture of C-S-H with CH. The sample with higher Ca/Si in the mechanochemical series that contains CH (marked with a white cross in Figure 5.23) is placed slightly to the right of the upper trend line, which agrees with the interpretation by Richardson. The data for the sample with target Ca/Si=1.33 from the same series is also placed slightly to the right of the upper trend line, although this sample is portlandite free.

The ^{29}Si MAS NMR results of the series of samples fabricated via the silica-lime reaction are shown in Figure 5.24. The silicate structure of the samples was dominated by Q^2 groups for $\text{Ca}/\text{Si} \leq 1$, while it was dominated by Q^1 groups for $\text{Ca}/\text{Si} \geq 1.27$. The contribution from bridging sites (Q^{2b} at $\sim -82\text{ppm}$) is shown as a very distinct peak in samples with $\text{Ca}/\text{Si} \geq 1$, as opposing to the mechanochemical series in which the bridging sites contribution was noticed as a hump. The width of the Q^2 frequencies in the high Ca/Si samples is narrower in this series than in the previous one, which implies a much better defined chemical environment for this connectivity. The results were deconvoluted to estimate the percentages of the silicate connectivities and the MCL. Two frequencies were used for both Q^1 and Q^2 for the spectra of the samples with $\text{Ca}/\text{Si} > 1$. For low Ca/Si three frequencies were used for Q^2 , and one for Q^1 . As in the previous series, no structural information was derived from the individual frequencies. For samples with $\text{Ca}/\text{Si} < 1.27$, the Q^2 intensity at $\sim -84\text{ppm}$ could have the origin commented in the previous section, either from Q^2 groups in the vicinity of Q^3 groups, or Q^{2p} attached to identical Q^{2p} in octamers or longer segments. Since no intensity was found for Q^3 groups in the sample with $\text{Ca}/\text{Si}=1$, it is likely that the intensity at $\sim -84\text{ppm}$ is originated from Q^{2p} groups attached to identical Q^{2p} groups. The percentages of the silicate species and the MCL are shown in Table 5.8.

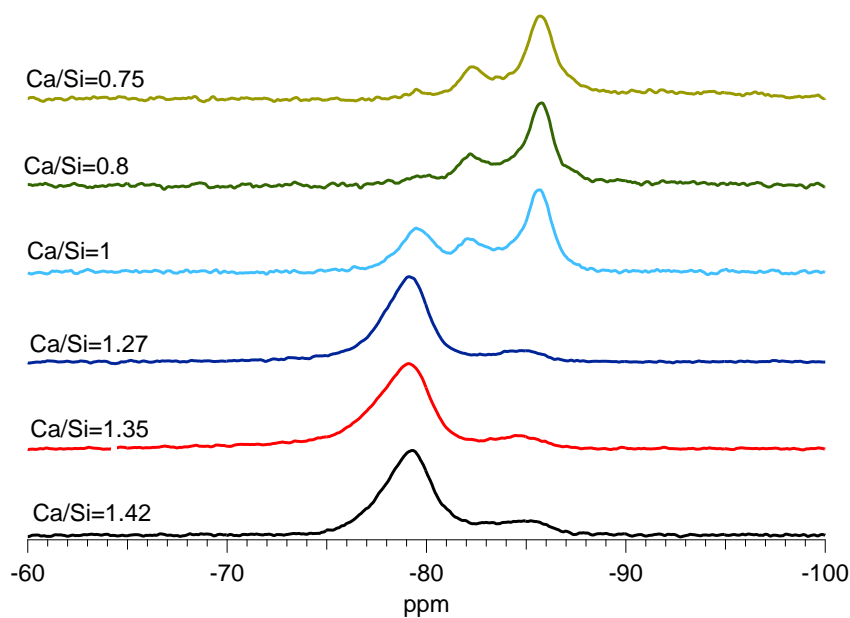


Figure 5.24. ^{29}Si MAS NMR spectra of the CaO-SiO_2 C-S-H samples (Dijon).

Table 5.8. Percentages of the silicate species and MCL for the C-S-H samples fabricated in Dijon by the silica-lime reaction. The results have been calculated from the deconvolution of the NMR spectra shown in Figure 5.25. (The error is not given for the first sample because it results bigger than the measurement, given the atypical low percentage of Q¹).

Bulk Ca/Si	Q¹ ± 2.0	Q² ± 2.0	Q³ ± 2.0	MCL
0.75	1.5 %	83.5 %	15.0 %	137.4 ± -
0.80	4.0 %	90.8 %	5.17 %	49.7 ± 23.7
1.00	34.3 %	65.7 %	0 %	5.8 ± 0.3
1.27	90.6 %	9.4 %	0%	2.2 ± 0.4
1.35	92.5 %	7.5 %	0%	2.2 ± 0.5
1.42	88.0 %	12.0 %	0%	2.3 ± 0.3

The deconvoluted spectra, the simulated spectra and the individual frequencies are shown in Figure 5.25. The results are plotted versus Ca/Si in Figure 5.26 and Figure 5.27, which show that the percentages of the silicate connectivities of these samples are rather constant for samples with Ca/Si>1 and Ca/Si<1. The change in percentage of silicate connectivities with Ca/Si is less gradual than for the mechanochemical series. Given the very low percentage of Q¹ connectivities at low Ca/Si, the MCL is higher in this series than for the mechanochemical samples for Ca/Si<1. For the rest of the samples the MCL is very similar in both series.

The morphology of the samples is crumpled foil-like regardless of the Ca/Si (Figure 5.28), but the foils in this case are finer and appear to be more defined than in the case of the mechanochemical samples. The mechanochemical route is much harsher since the synthesis relies in accelerating the reaction adding mechanical energy by the milling process; therefore it is sensible that the morphology of the samples appears coarser in that case. The Ca/Si ratios given by TEM-EDX are shown in Table 5.9. The values are very close to the bulk composition except in the case of bulk Ca/Si=1.35. The inhomogeneity in this sample could be due to admixture with traces of carbonates, present as indicated by XRD results.

Table 5.9. Mean Ca/Si values (with the standard deviations) obtained by TEM-EDX for the C-S-H samples in the CaO-SiO₂ series.

Ca/Si Bulk	0.75	0.80	1.00	1.27	1.35	1.42
Ca/Si EDX	0.73±0.02	0.82±0.02	0.98±0.03	1.24±0.05	1.25±0.12	1.40±0.04
# EDX points	25	20	31	19	27	20

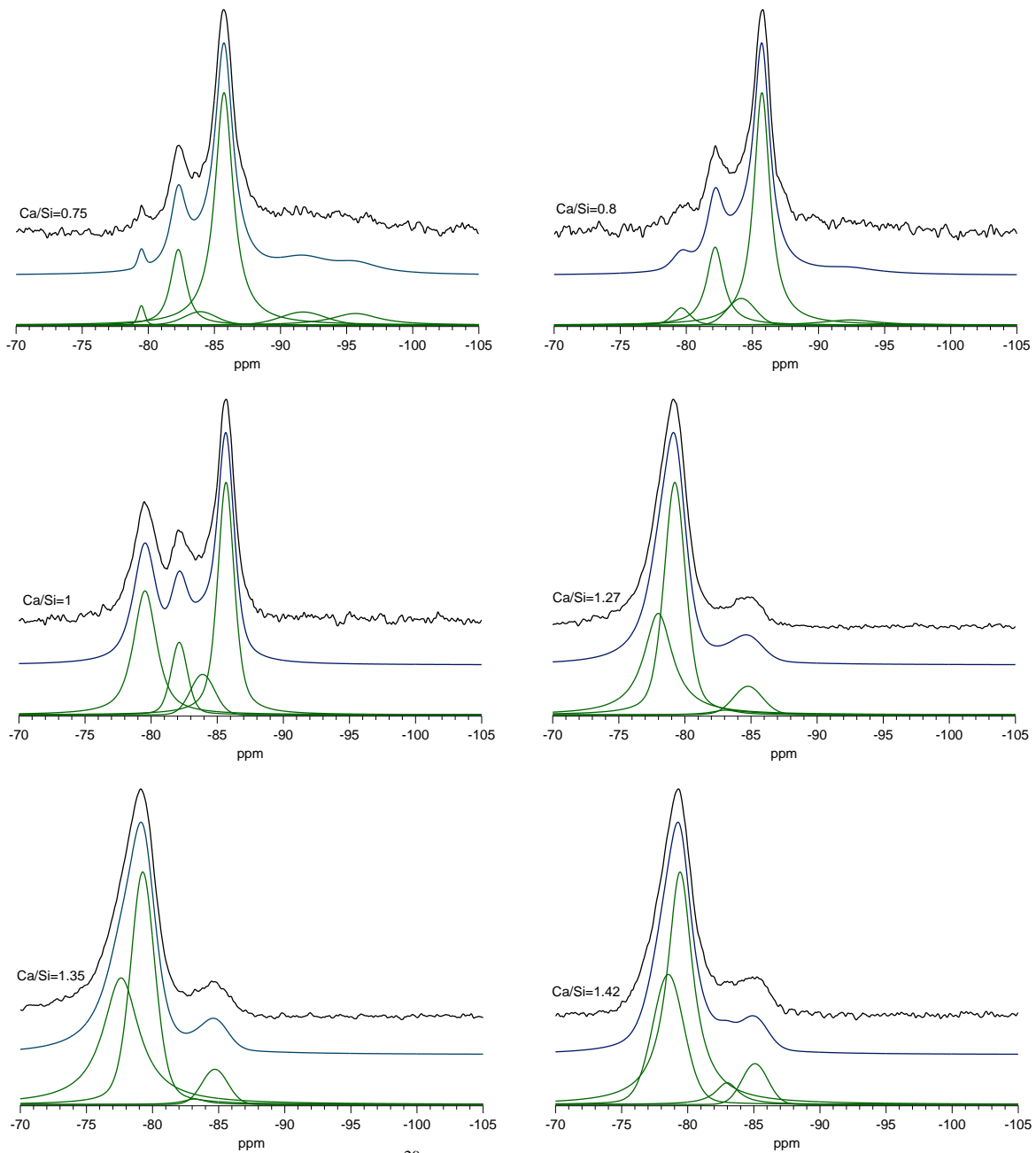


Figure 5.25. Deconvolutions of the ^{29}Si MAS NMR spectra of the CaO-SiO_2 C-S-H samples showing the individual frequencies (green), the simulated spectra as a sum of the individual frequencies (blue) and the experimental spectra (black).

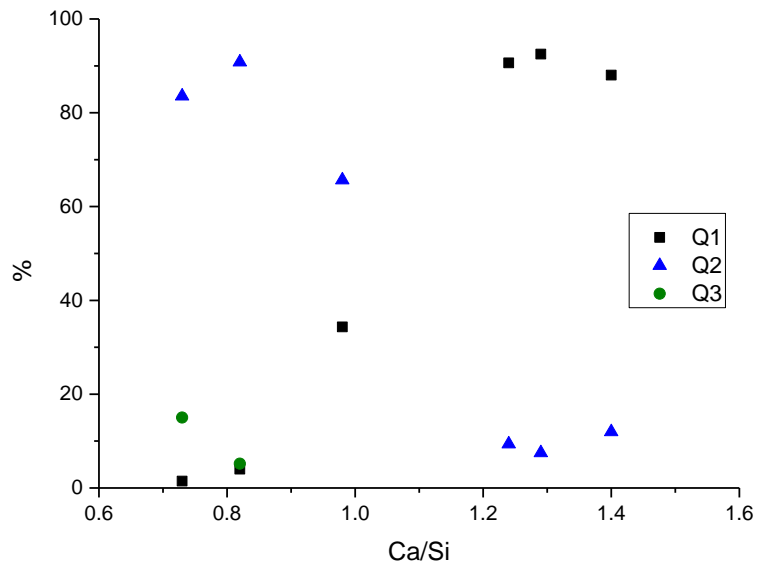


Figure 5.26. Percentage of the silicate species Q^1 , Q^2 and Q^3 obtained from NMR vs. the Ca/Si (TEM-EDX) in the CaO-SiO₂ C-S-H series.

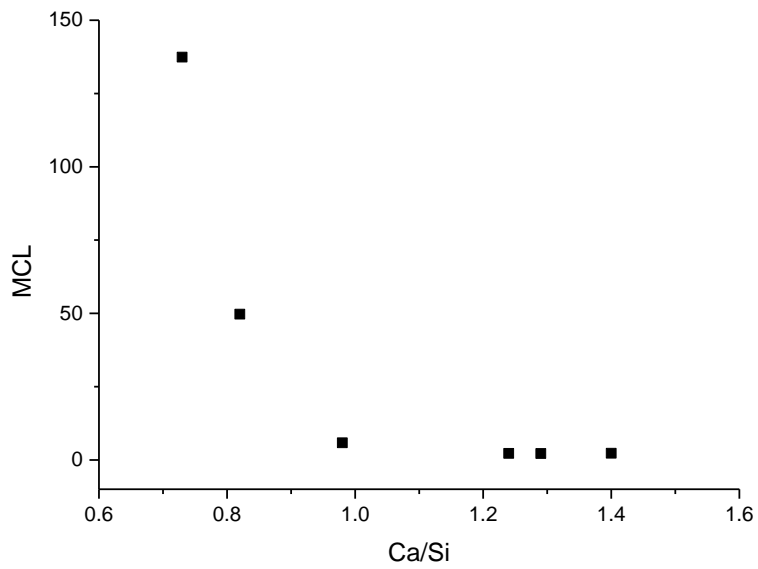


Figure 5.27. Mean silicate chain length vs. Ca/Si (TEM-EDX) in the CaO-SiO₂ C-S-H series.

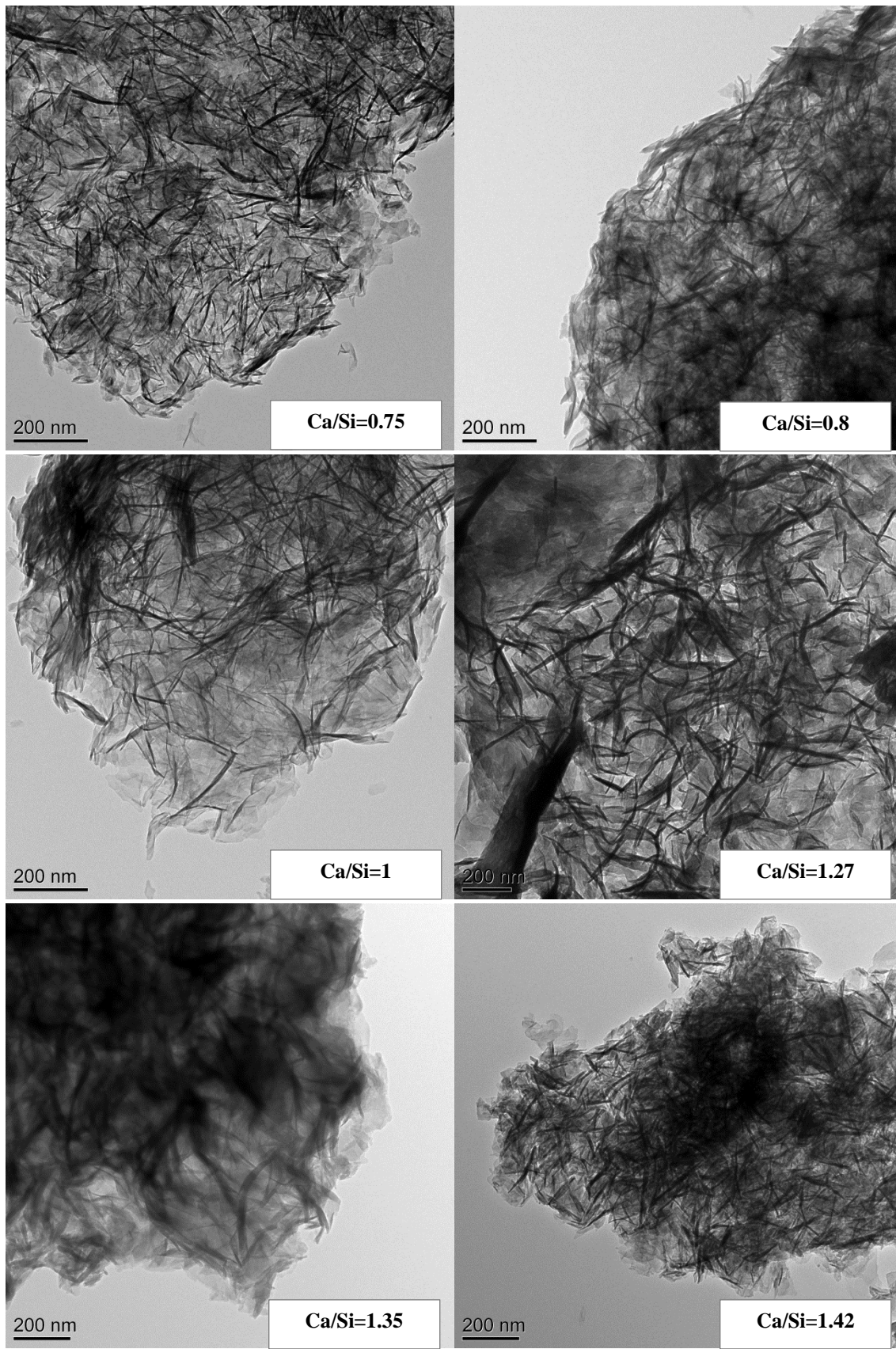


Figure 5.28. TEM micrographs of the CaO-SiO₂ C-S-H series. The Ca/Si of the sample is indicated in each micrograph.

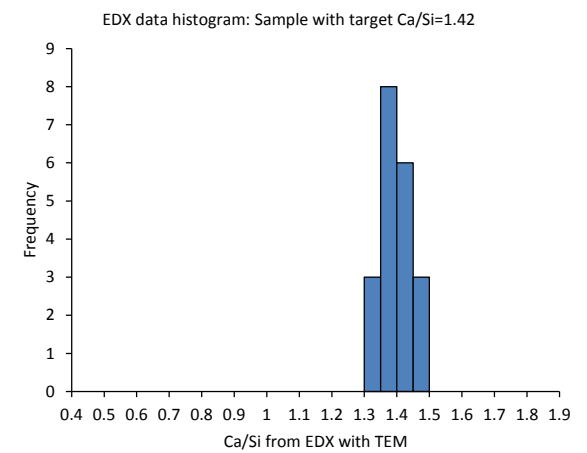
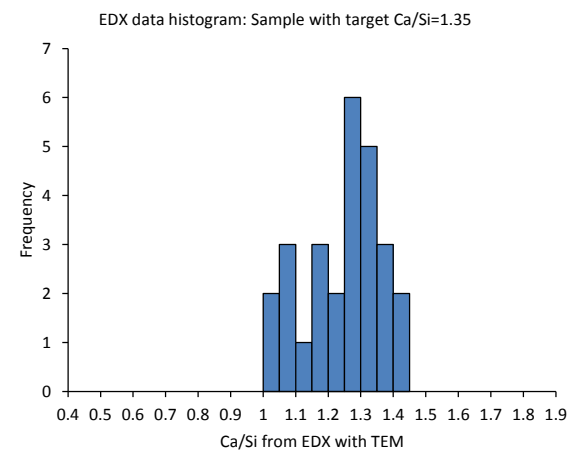
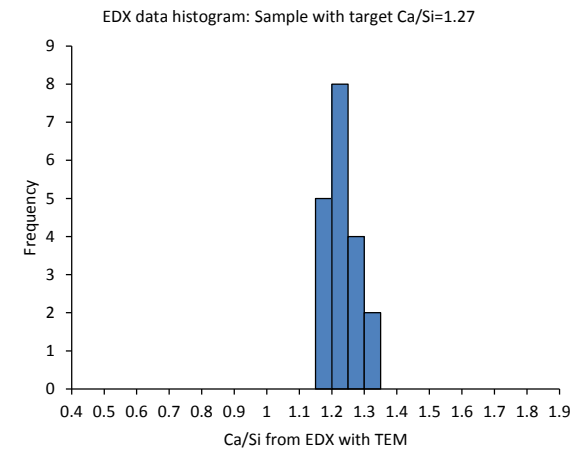
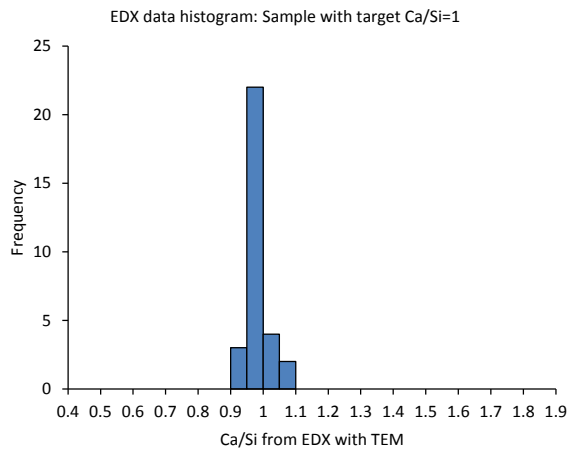
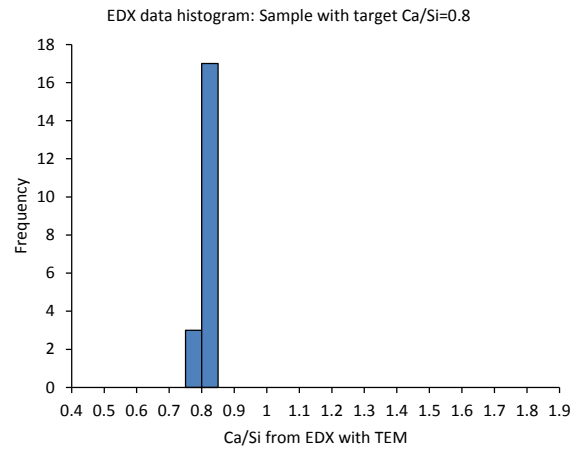
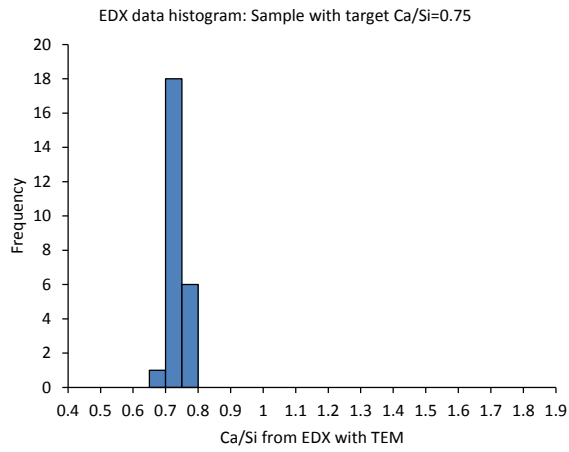


Figure 5.29. Histograms of the Ca/Si obtained with TEM-EDX of the C-S-H CaO-SiO₂ samples.

Richardson and Groves' model was applied for charge balance calculations. The height of the histograms for Ca/Si (A bar limited by the minimum and maximum values for the obtained experimental Ca/Si) was plotted versus the reciprocal mean chain length for each sample in Figure 5.30. The trends for the tobermorite and jennite structural units with maximum, intermediate and minimum degree of protonation ($w/n=2, 1, 0$) were also plotted. The mean value of Ca/Si, obtained by TEM-EDX, was used to get the chemical structural formulae, and it is marked with a cross. As in the case of the mechanochemical samples, the composition of the samples in this series lies within the tobermorite-like region and no Ca-OH groups are needed in the structures either from solid solution CH or jennite units.

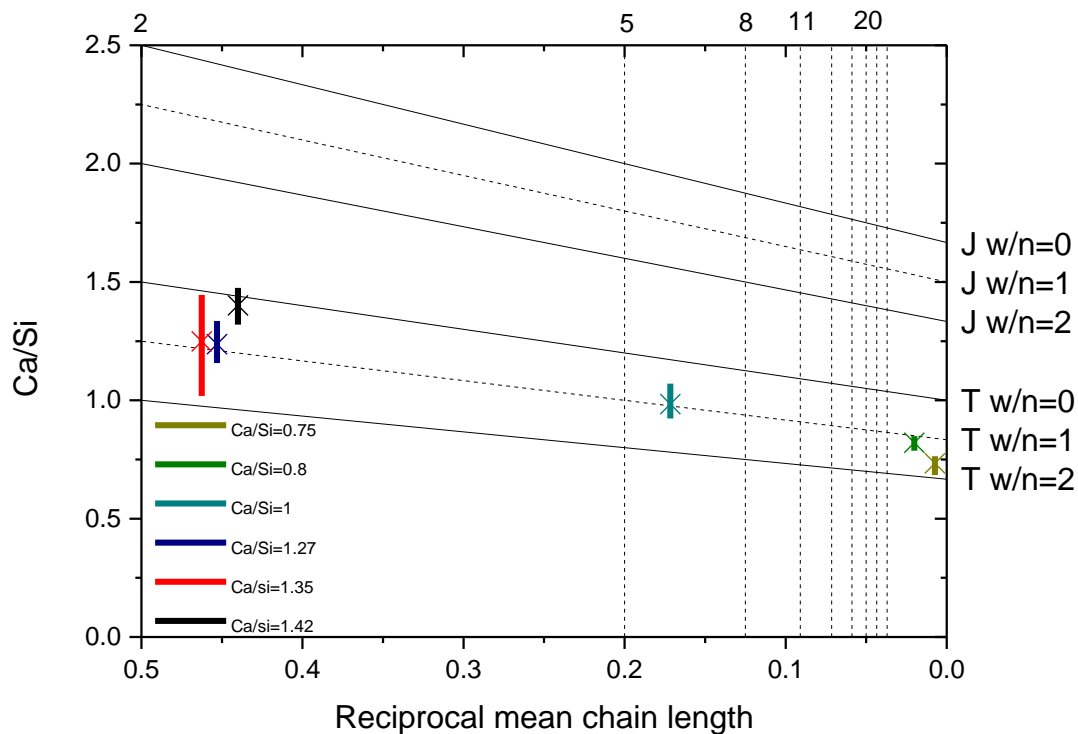
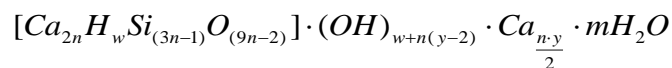


Figure 5.30. Ca/Si vs. reciprocal mean chain length of the CaO-SiO₂ C-S-H samples. The length of the bars is limited by the minimum and maximum Ca/Si obtained by TEM-EDX and the mean value is marked with a cross. The structural units for tobermorite and jennite with minimum ($w=0$), intermediate ($w=1$) and maximum ($w=2$) degree of protonation are also marked. The vertical dashed lines represent the $(3n-1)$ structural units: dimer (2), pentamer (5), octamer (8)...

The T/J formulation was chosen, whose formula is:



In the T/J view of the model $(3n-1)=MCL$ and $Ca/Si=(4n+ny)/(6n-2)$, so that $n=(MCL+1)/3$ and $y= [(Ca/Si)(6n-2)-4n]/n$. The number of silanol groups w depends on the value of y according to:

$$0 \leq y \leq 2 \rightarrow n(2 - y) \leq w \leq 2n$$

$$2 \leq y \leq 4 \rightarrow 0 \leq w \leq 2n$$

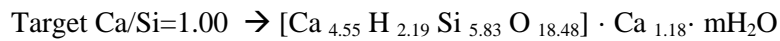
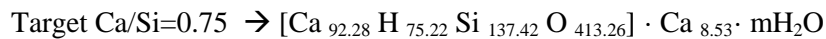
$$4 \leq y \leq 6 \rightarrow 0 \leq w \leq n(6 - y)$$

The calculated values for n , y , w_{\max} (maximum number of silanol groups), w_{\min} (minimum number of silanol groups) and w/n_{\max} (maximum degree of protonation) and w/n_{\min} (minimum degree of protonation) are shown in Table 5.10.

Table 5.10. Calculated values for the parameters of the T/J view point of Richardson and Groves' model for the mechanochemical C-S-H samples.

Target Ca/Si	n	y	w_{\min}	w_{\max}	w/n_{\min}	w/n_{\max}
0.75	46.14	0.37	75.22	92.28	1.63	2
0.80	16.90	0.82	19.82	33.81	1.17	2
1.00	2.28	1.04	2.19	4.55	0.96	2
1.27	1.07	1.11	0.95	2.14	0.89	2
1.35	1.05	1.12	0.93	2.11	0.88	2
1.42	1.09	1.84	0.18	2.18	0.16	2

The minimum degree of protonation was chosen, since it was the most sensible value according to the position of the mean Ca/Si with respect to the tobermorite trends in Figure 5.30. The resulting structural chemical formulae consist in a tobermorite-like core (within brackets) with no extra Ca either in jennite or solid solution CH:



Samples with target Ca/Si >1.00 can be accounted for by a mixture of dimeric and pentameric tobermorite units, T2 and T5 in ref. [1]. The sample with target Ca/Si=1 can be explained with a mixture of T8, T5 and T2 units. The sample with target Ca/Si=0.8 can be explained with a mixture of T50, T47 and all the rest of tobermorite units with shorter silicate chains, and the sample with target Ca/Si=0.75 can be explained with a mixture of T119 and all the rest of tobermorite units with shorter silicate chains.

5.5 Hydration of C₃S at constant lime concentration: Kinetics C-S-H series

The hydration curves of the series of samples of C₃S hydrated until the deceleration period are shown in Figure 5.31. The hydration of the sample at [CaO]=12mmol/l was stopped before the deceleration period due to an error reading the experimental screen. The hydration of samples at [CaO]=25 and 27mmol/l was stopped towards the end of the acceleration period instead of during the deceleration period to avoid the precipitation of portlandite. Experimental tests showed that it was complex to maintain the lime concentration constant at those supersaturated levels since the system is in a metastable state. Towards 800 minutes of hydration the lime concentration decreased indicating the consumption of Ca²⁺ in the solution to precipitate portlandite. Therefore stopping the hydration at the chosen point was a compromise to avoid the precipitation of portlandite and to ensure that the chemical environment in which C-S-H was growing was not perturbed.

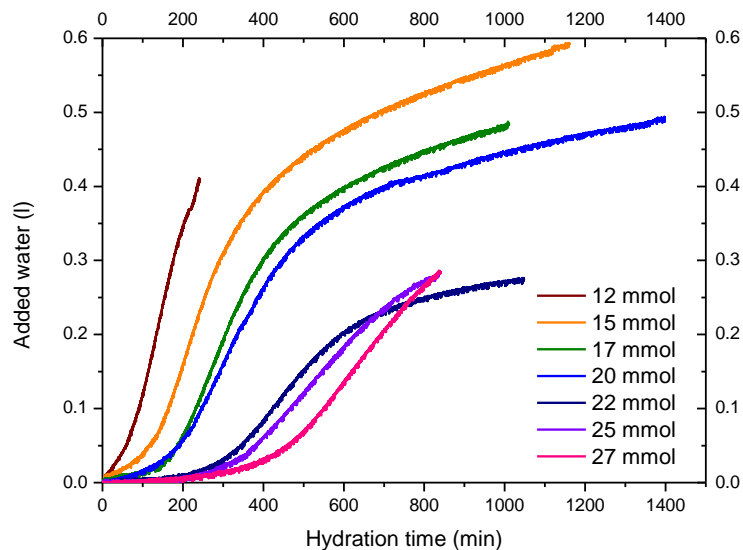


Figure 5.31. Hydration curves (Added water vs. hydration time) of C₃S at fixed lime concentration, from [CaO]=12mmol/l (burgundy curve) to [CaO]=27mmol/l (pink curve), corresponding to hydration times II in Table 4.3.

The XRD patterns of the samples fabricated by the controlled hydration of C₃S are shown in Figure 5.32, Figure 5.33, Figure 5.34 and Figure 5.35 together with the patterns of the anhydrous C₃S and a reference for CH [133]. They show a low degree of hydration, since they are very similar to the anhydrous material pattern. With hydration, a slight decrease in intensity in the reflections at 20~32° and 34° was noticed, due to the consumption of C₃S. The presence of C-S-H is seen as a small hump at ~30°<20<32°, that is more obvious in samples hydrated at lime concentrations of 22 and 27mmol/l (See enlarged area in Figure 5.35). Portlandite is generally not detected in the samples, except for a small trace associated to the incipient reflection at 20~18° for samples hydrated at [CaO]=20mmol/l in Figure 5.32 and Figure 5.33.

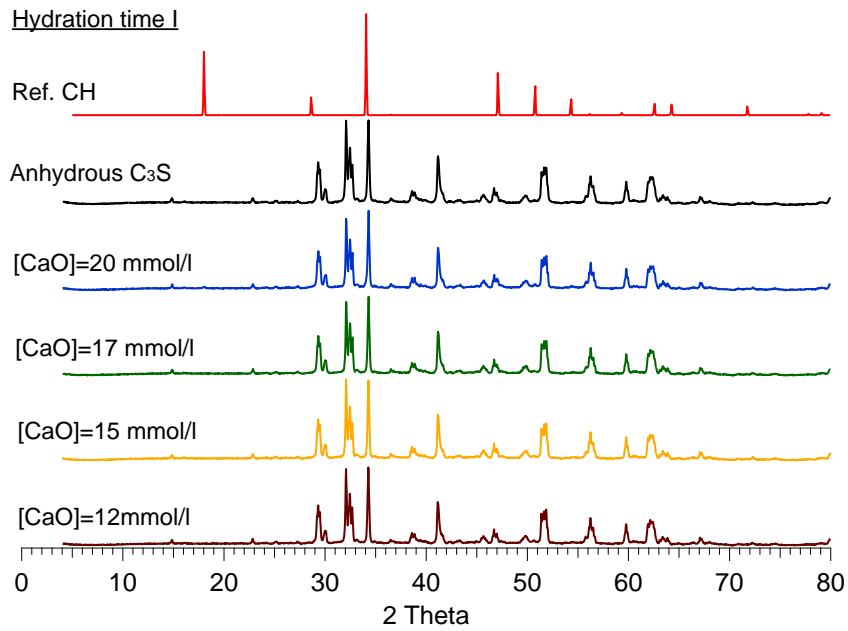


Figure 5.32. XRD patterns of the C_3S hydrated samples at fixed lime concentrations of 12, 15, 17 and 20mmol/l with the hydration stopped at the acceleration period (hydration time I in Table 4.3). The pattern of the anhydrous C_3S is shown for comparison, as well as a reference for CH.

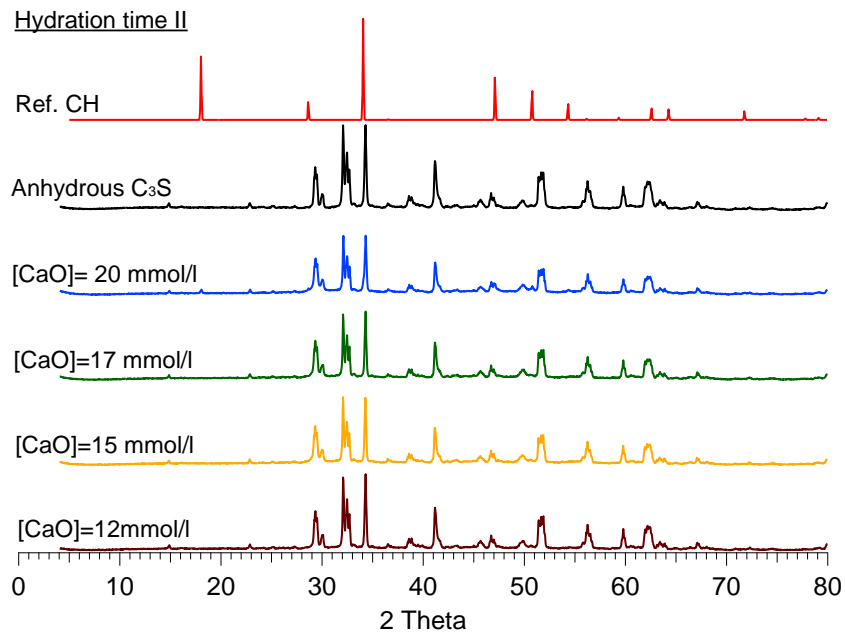


Figure 5.33. XRD patterns of the C_3S hydrated samples at fixed lime concentrations of 12, 15, 17 and 20mmol/l with the hydration stopped at the deceleration period (hydration time II in Table 4.3). The pattern of the anhydrous C_3S is shown for comparison, as well as a reference for CH.

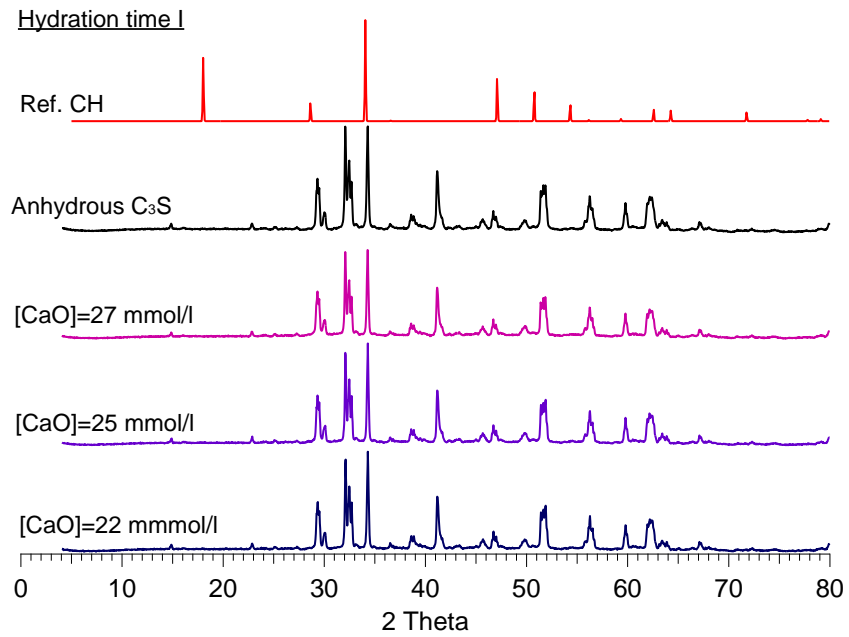


Figure 5.34. XRD patterns of the C_3S hydrated samples at fixed lime concentrations of 22, 25 and 27 mmol/l with the hydration stopped at the acceleration period (hydration time I in Table 4.3). The pattern of the anhydrous C_3S is shown for comparison, as well as a reference for CH.

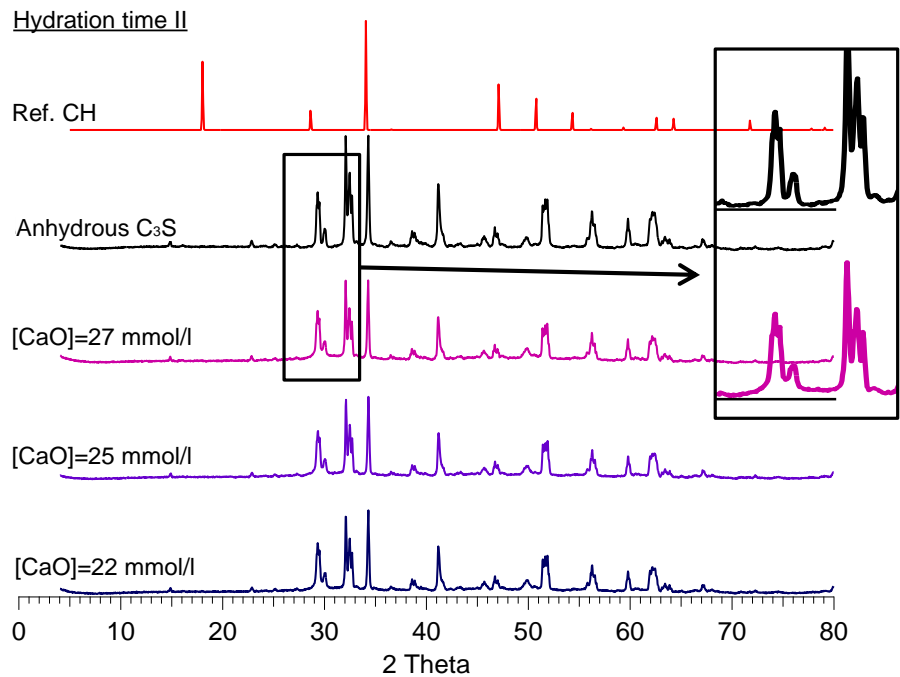


Figure 5.35. XRD patterns of the C_3S hydrated samples at fixed lime concentrations of 22, 25 and 27 mmol/l with the hydration stopped at the deceleration period (hydration time II in Table 4.3). The pattern of the anhydrous C_3S is shown for comparison, as well as a reference for CH. The enlarged area in the figure shows the increase in intensity at $\sim 2\theta=32^\circ$ due to the formation of C-S-H in the pattern for $[CaO]=27\text{mmol/l}$ compared to the pattern of anhydrous C_3S .

The ^{29}Si NMR spectra of the C_3S hydrated samples are shown in Figure 5.36 and Figure 5.37. The spectra show that most of the intensity originated from unreacted C_3S (Q^0 from -67 to -76 ppm), but intensity coming from C-S-H Q^1 (~ -79 ppm) and Q^2 (~ -85 ppm) connectivities is also visible. The intensity of these latter peaks is stronger with hydration time, since more C-S-H is formed for longer hydration periods. For longer hydration times, Q^1 groups dominate the structure of C-S-H. The deconvolution of the spectra was used to quantify the species and calculate the MCL. The results of the quantification are shown in Table 5.11 and Table 5.12.

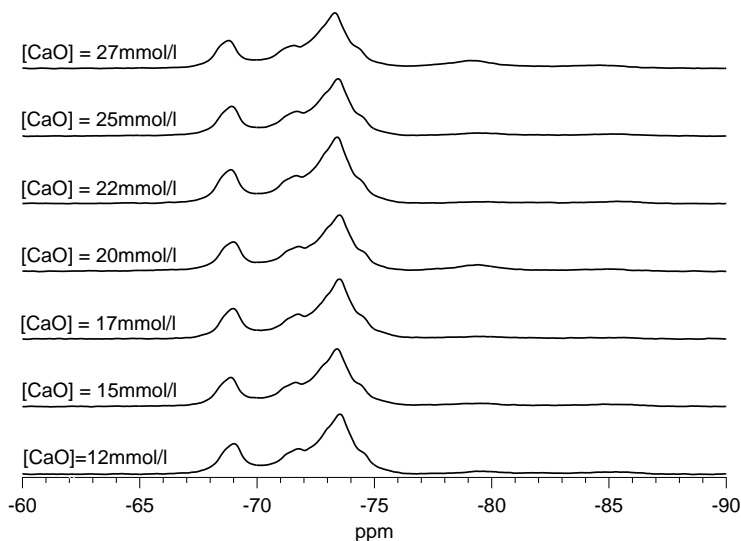


Figure 5.36. ^{29}Si NMR spectra of the C_3S hydrated samples that belong to the short series (Hydration time I). The fixed lime concentration in solution is indicated over each spectrum.

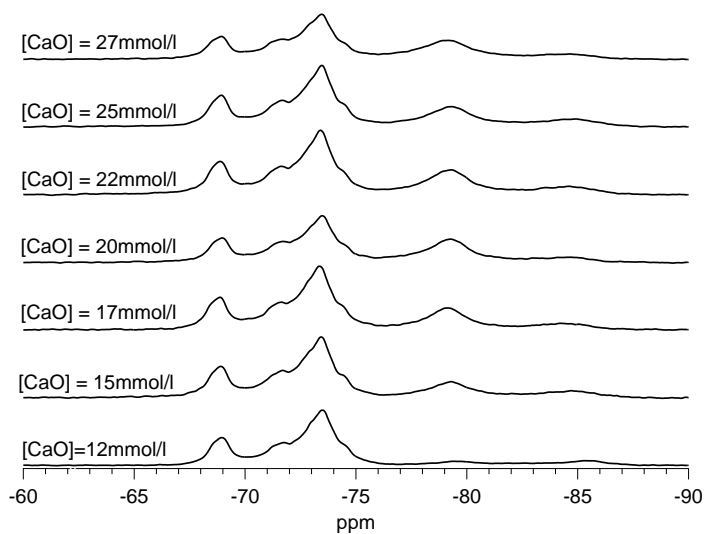


Figure 5.37. ^{29}Si NMR spectra of the C_3S hydrated samples that belong to the long series (Hydration time II). The fixed lime concentration in solution is indicated over each spectrum.

Table 5.11. Percentages of the silicate species, MCL and DR (degree of reaction) for the C-S-H samples fabricated via the controlled hydration of C_3S in the short series (Hydration time I). The results have been calculated from the deconvolution of the NMR spectra shown in Figure 5.36.

[CaO] mmol/l	$Q^0 \pm 2.0$	$Q^1 \pm 2.0$	$Q^2 \pm 2.0$	MCL	DR ± 2.8
12	93.2 %	2.6 %	4.2 %	5.2 ± 3.1	6.8 %
15	90.6 %	4.8 %	4.6 %	3.9 ± 1.4	9.4 %
17	90.5 %	3.2 %	2.3 %	3.5 ± 2.3	5.5 %
20	89.5 %	7.2 %	3.3 %	2.9 ± 1.4	10.5 %
22	94.7 %	1.8 %	3.5 %	6.0 ± 5.3	5.3 %
25	93.8 %	2.4 %	3.8 %	5.2 ± 3.3	6.2 %
27	83.1 %	12.3 %	4.5 %	2.7 ± 0.9	16.9 %

Table 5.12. Percentages of the silicate species, MCL and DR, for the C-S-H samples fabricated via the controlled hydration of C_3S in the long series (Hydration time II). The results have been calculated from the deconvolution of the NMR spectra shown in Figure 5.37.

[CaO] mmol/l	$Q^0 \pm 2.0$	$Q^1 \pm 2.0$	$Q^2 \pm 2.0$	MCL	DR ± 2.8
12	87.0 %	5.8 %	7.2 %	4.5 ± 1.2	13.0 %
15	74.3 %	18.2 %	7.5 %	2.8 ± 0.6	25.7 %
17	71.7 %	20.1 %	8.2 %	2.8 ± 0.5	28.3 %
20	67.6 %	27.2 %	5.2 %	2.4 ± 0.8	32.4 %
22	67.8 %	24.7 %	7.5 %	2.6 ± 0.6	32.2 %
25	68.2 %	22.5 %	9.3 %	2.8 ± 0.5	31.8 %
27	63.0 %	30.8 %	6.2 %	2.4 ± 0.7	37.0 %

The MCL calculated in Table 5.11 does not follow any trend. Although dimeric chains are expected at the first stages of C_3S hydration, most of the samples at short hydration times show higher MCL. This can be associated to errors in the quantification of the spectra, since the signal of C-S-H is very low. The samples hydrated for longer periods of time show dimeric silicate chains, according to the results shown in Table 5.12, except the sample hydrated at [CaO]=12mmol/l, that shows a higher MCL. This agrees with the expected silicate structure at low degrees of reaction and hydration times below 24h [15-17]. The fact that the sample hydrated at [CaO]=12mmol/l shows a much lower degree of reaction may have affected the quantification of the spectra. Since the kinetics of the reaction depends on the lime concentration in solution, the degree of reaction varies from sample to sample, given also the different hydration times for all of them. As the aim of these experiments was not comparing similar hydration times, nor degrees of reaction, but to compare the morphology of hydrated samples at two different stages of the hydration curve, the fact that the degrees of reaction and hydration times differ is not relevant. All the ^{29}Si NMR spectra and the deconvolutions, showing the simulated spectra and individual lines are shown in Figure 5.38 and Figure 5.39. Seven frequencies were used to deconvolute the signal of C_3S and two frequencies

were used for each of the C-S-H connectivities. Structural information is derived from the total integral of Q^0 , Q^1 and Q^2 , but not from the individual frequencies used in the deconvolutions.

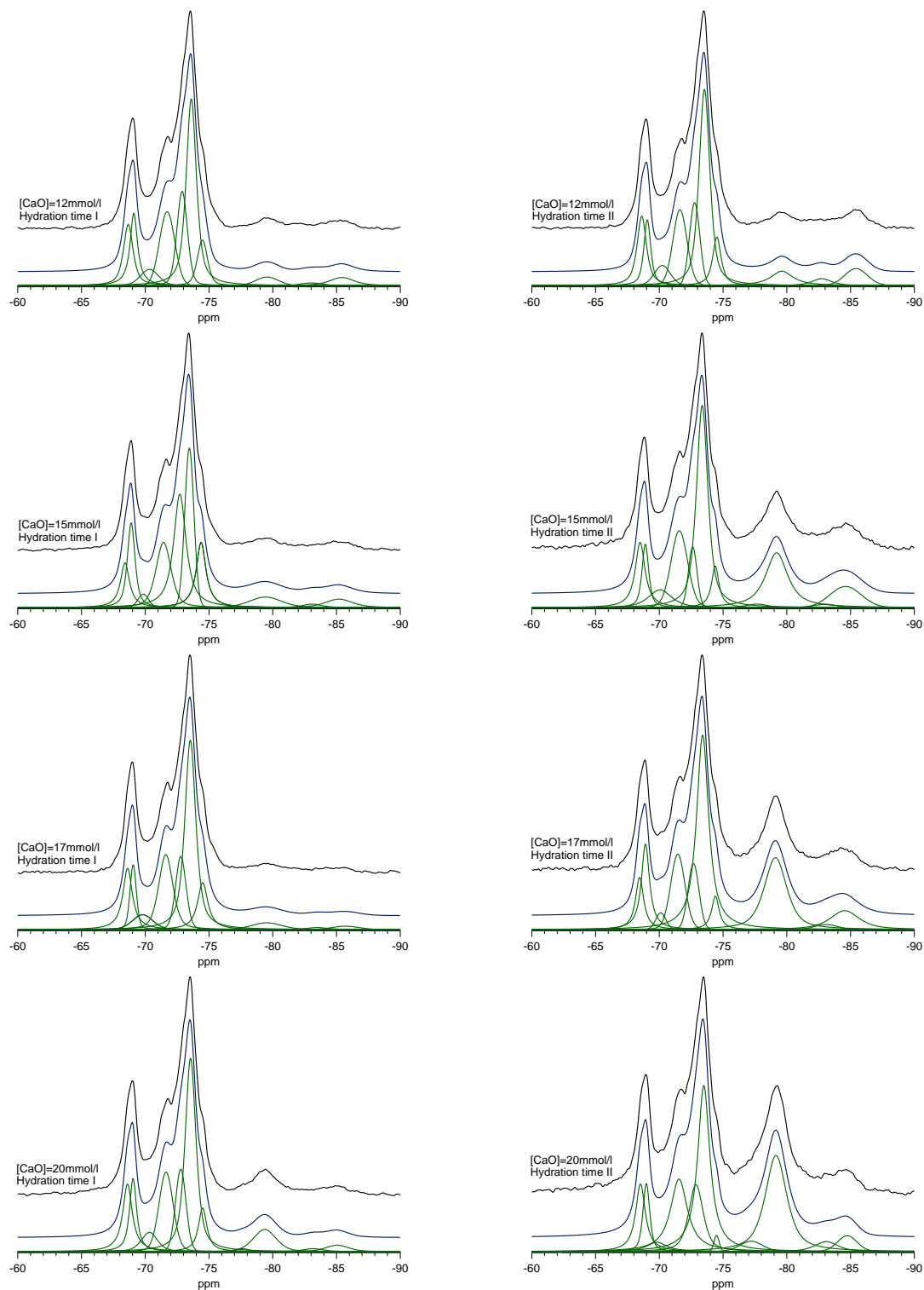


Figure 5.38. ^{29}Si NMR experimental spectra (black), simulated spectra (blue), and individual frequencies (green), of the C_3S samples hydrated for hydration times I and II at fixed lime concentrations of 12, 15, 17 and 20mmol/l.

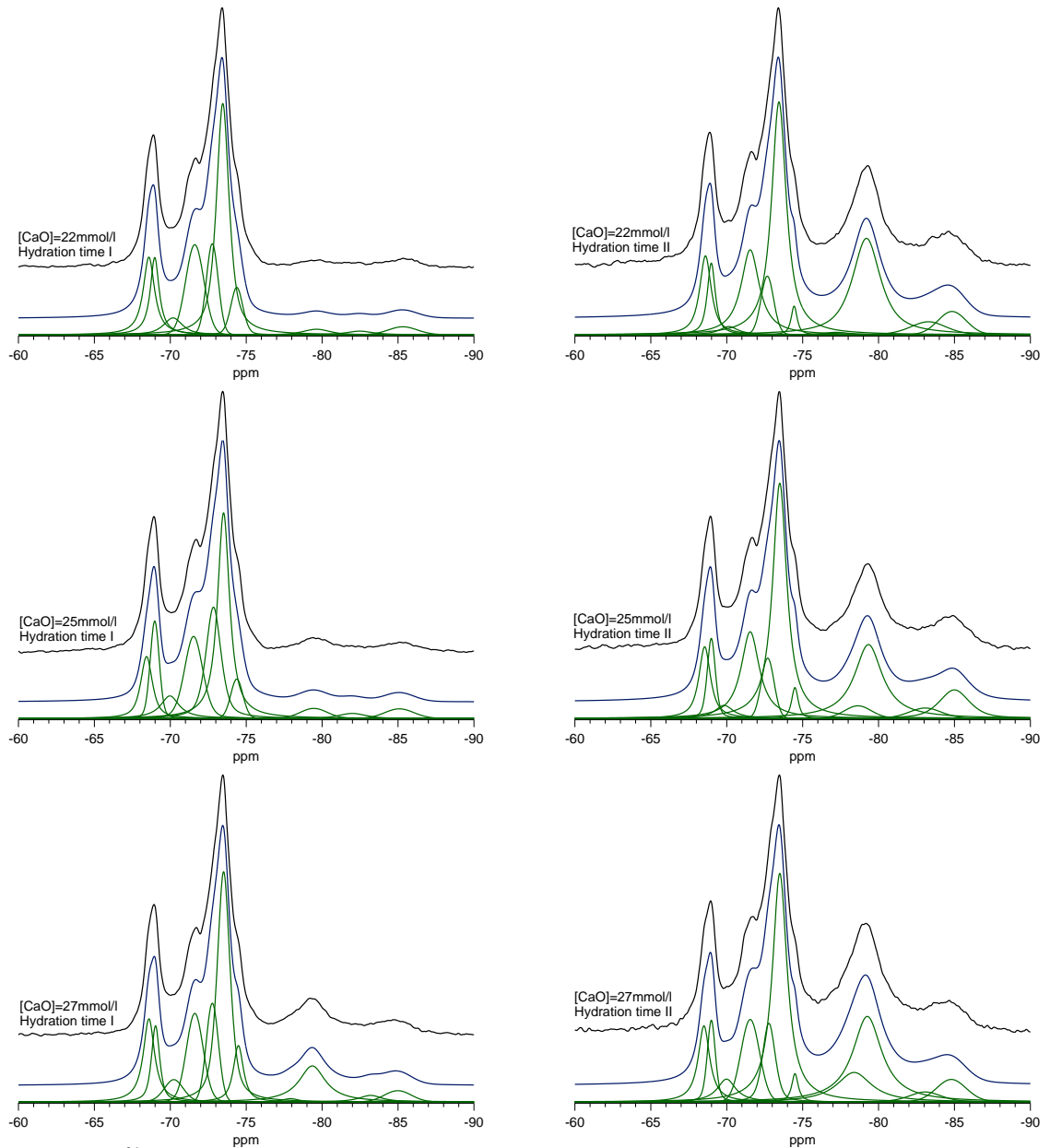


Figure 5.39. ^{29}Si NMR experimental spectra (black), simulated spectra (blue), and individual frequencies (green), of the C_3S samples hydrated for hydration times I and II at fixed lime concentrations of 22, 25 and 27mmol/l.

The TEM micrographs of the samples are shown in Figure 5.40, Figure 5.41 and Figure 5.42. C-S-H can be seen on the surface of the C_3S particles. The darker areas correspond to a superposition of the C-S-H layer on the C_3S grain. At lime concentration of 12 and 15mmol/l (Figure 5.40 and Figure 5.41) C-S-H presents a foil-like morphology that resembles the morphology found in blends of Portland cement and glass ground granulated blast furnace slag or neat slag pastes (See Fig. 16-17 in ref. [1]).

At $[\text{CaO}] = 17 \text{ mmol/l}$ and 20 mmol/l (Figure 5.41) the morphology of C-S-H is also foil-like; however, the product appears denser. At $[\text{CaO}] = 22 \text{ mmol/l}$ (Figure 5.42), the growth of C-S-H is more directional and the morphology is a mixture of fibrils and foils. At $[\text{CaO}] = 25 \text{ mmol/l}$ (Figure 5.42) C-S-H is completely fibrillar and denser than for lower $[\text{CaO}]$. At 27 mmol/l (Figure 5.42) some fibrils of C-S-H can be clearly seen sticking out on the surface of the C_3S grain. The micrographs clearly show that the hydration time does not affect the morphology for a given $[\text{CaO}]$. The morphology of the product that develops at an early stage of the hydration curve, in the acceleration period, is the same than the morphology that develops at a later stage of the hydration curve for a fixed $[\text{CaO}]$. This suggests the morphology of C-S-H is determined by the $[\text{CaO}]$ in solution and does not depend on growth kinetics. Local variations of the lime concentration while pastes hydrate can explain the development of different morphologies in blends with supplementary cementitious materials. Often C-S-H presents different morphologies when growing outside the supplementary particles or from them [65]. Foil-like C-S-H can grow from fully reacted PFA particles (See Fig.13 in ref. [65]), which are SiO_2 rich, and in turn contain a small percentage of CaO, while fibrillar C-S-H develops in other regions of OPC-PFA pastes that may have been subjected to chemical environments richer in Ca^{2+} (See Fig. 11-12 in ref. [65]). Interestingly this can be reversed in presence of alkalis, finding fibrillar product inside the reacted particles and foil-like product outside (See Fig.15 in ref.[65]).

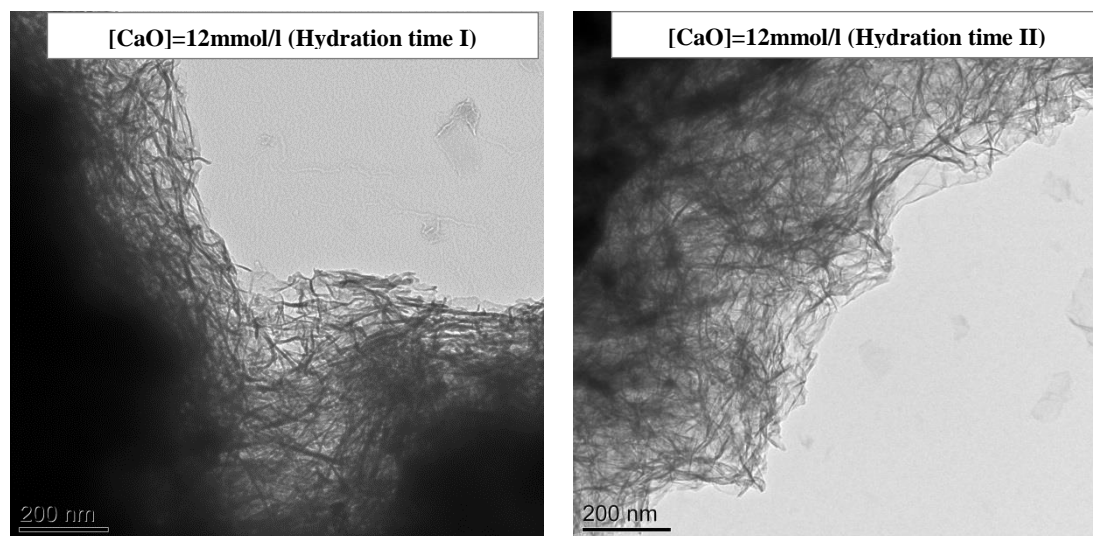


Figure 5.40. TEM micrographs of C_3S samples hydrated at $[\text{CaO}] = 12 \text{ mmol/l}$ for 170 min (left) and 240 min (right), showing foil-like C-S-H.

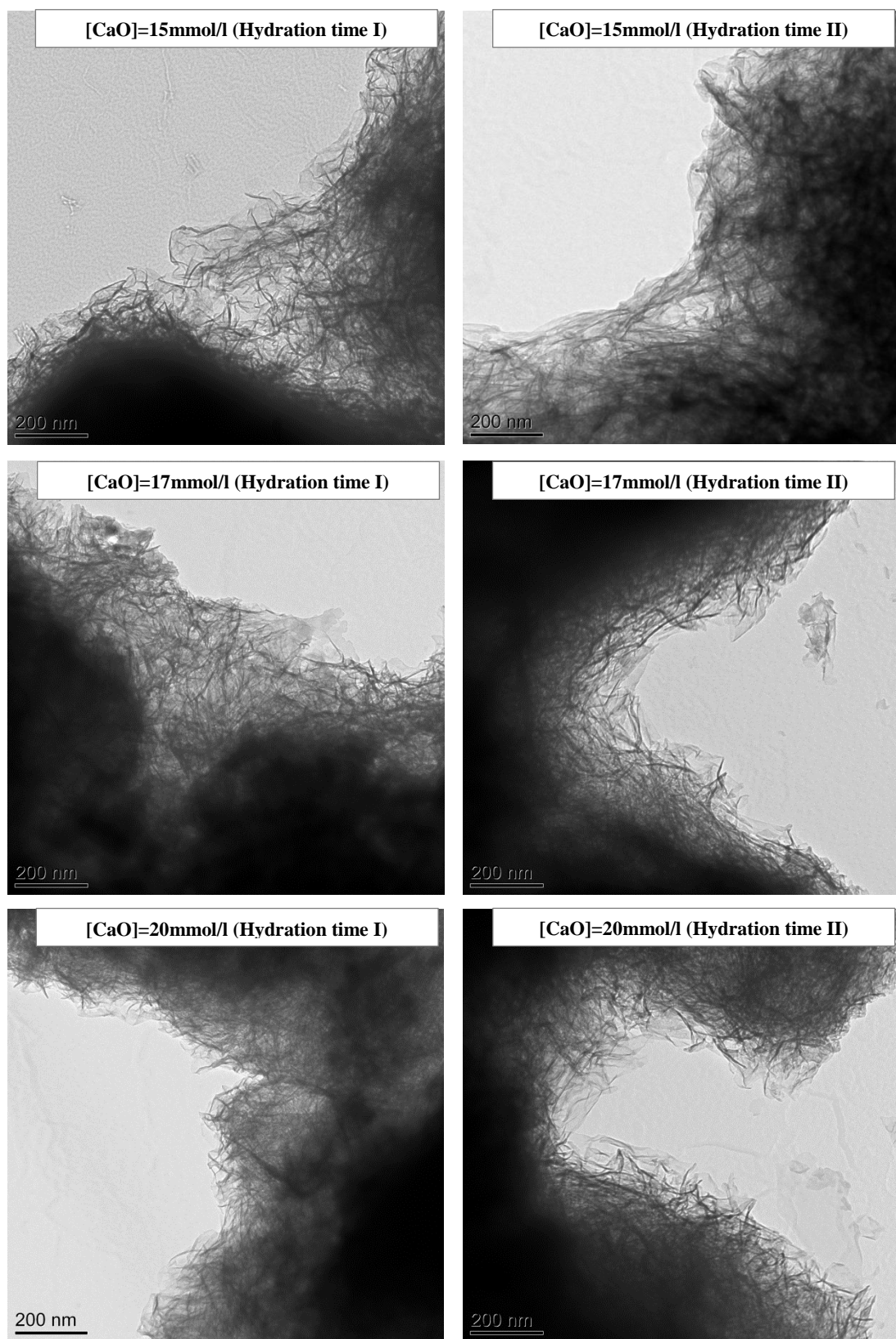


Figure 5.41. TEM micrographs of C_3S samples hydrated at $[CaO]=15\text{mmol/l}$ for 260 min and 1161 min (upper left and right respectively), at $[CaO]=17\text{mmol/l}$ hydrated for 255 min and 1011 min (middle left and right respectively), and $[CaO]=20\text{mmol/l}$ hydrated for 375 min and 1398 min (lower left and right respectively) showing foil-like C-S-H.

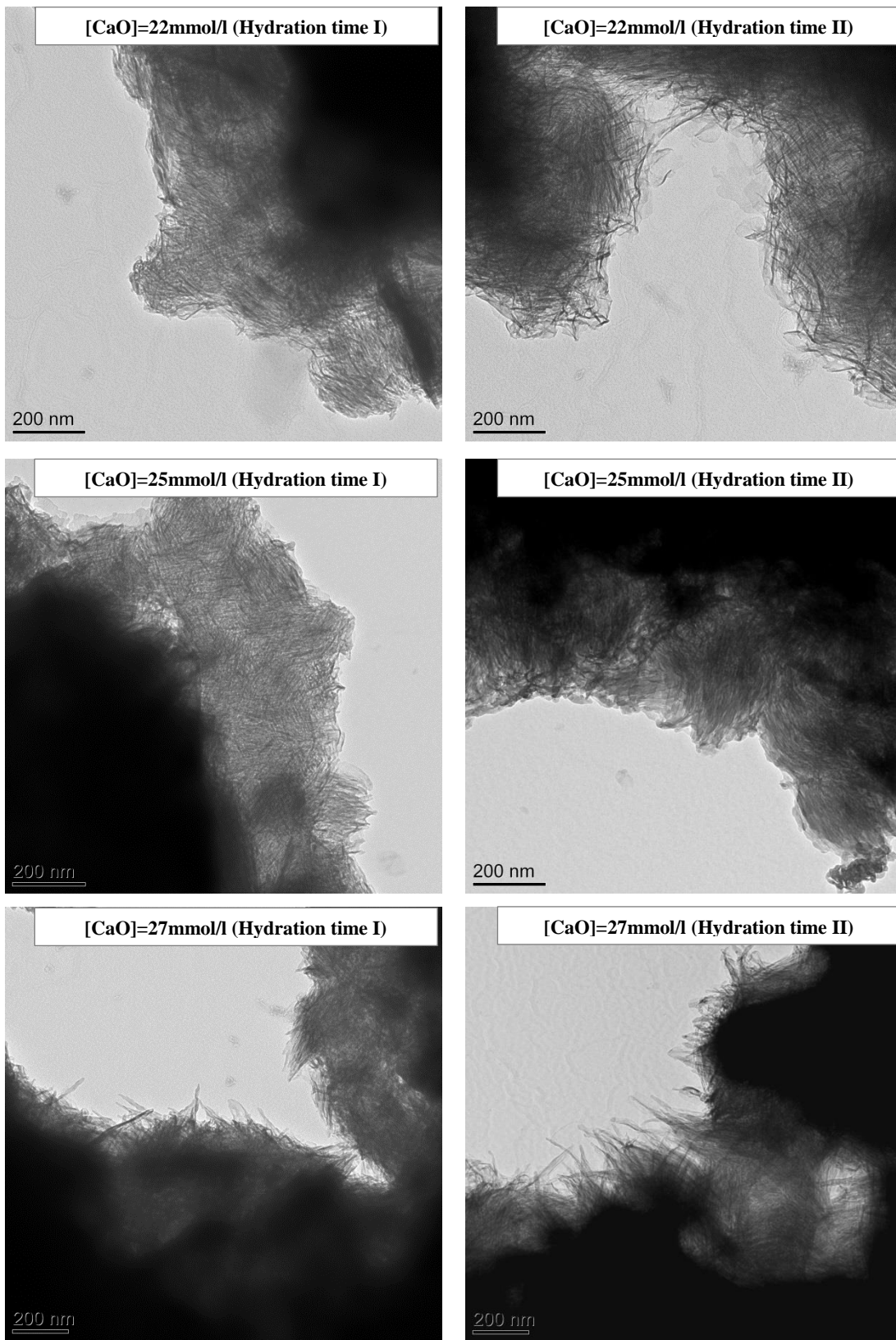


Figure 5.42. TEM micrographs of C₃S samples hydrated at [CaO]=22mmol/l for 401 min and 1048 min (upper left and right respectively), showing a mixture of foil-like and fibrillar C-S-H, at [CaO]=25mmol/l for 492 min and 835 min (middle left and right respectively) and [CaO]=27mmol/l for 600 min and 840 min (lower left and right respectively), showing fibrillar C-S-H.

The Ca/Si of the samples hydrated until the deceleration period (Hydration time II) was obtained by TEM-EDX analyses. The results are summarised in Table 5.13 and the histograms of the data are shown in Figure 5.47 and Figure 5.48. The histograms show that the samples are not as homogeneous in composition as the samples in the previous sections. As expected, the Ca/Si increased with the lime concentration in solution, since more Ca^{2+} was available to react when the lime concentration was higher. However; the Ca/Si values were unusually high. Even though the EDX points were carefully chosen in areas where the diffraction patterns were free from diffraction spots, the obtained high values suggest certain degree of admixture with C_3S . Moreover the values are higher than the reported ones for similar lime concentrations in ref. [49, 94]. The experimental values of the Ca/Si given by TEM-EDX were used as an input in Eq. 4.5 to calculate the degree of reaction for samples hydrated at Hydration times II. The obtained degrees of reaction are much higher than those obtained by NMR (See Figure 5.43 and Table 5.14). Using Ca/Si expected in equilibrium (Ca/Si ** in Table 5.14) according to Haas thermodynamic model [93] in Figure 2.23, the obtained degrees of reaction are closer to the ones calculated from the NMR data. This indicates the real Ca/Si of C-S-H in these samples is lower than the experimental mean value given by TEM-EDX, and confirms the admixture.

Table 5.13. Summary of the calculated Ca/Si (with the standard deviations) from TEM-EDX for the C-S-H present in the C_3S samples hydrated at fixed lime concentrations (left column) in the long series (Hydration time II). The number of EDX point analyses used to calculate the average Ca/Si is indicated in the right column.

[CaO] (mmol/l)	Ca/Si	# EDX analyses
12	1.69 ± 0.16	20
15	1.99 ± 0.08	33
17	2.09 ± 0.18	25
20	2.21 ± 0.10	21
22	2.25 ± 0.05	20
25	2.28 ± 0.13	24
27	2.35 ± 0.08	22

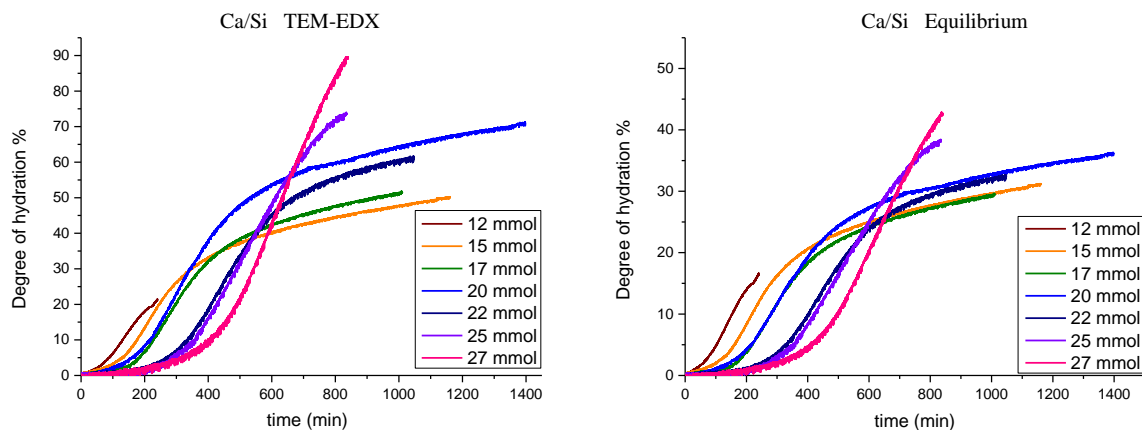


Figure 5.43. Degree of hydration (%) vs. hydration time for the C-S-H samples fabricated via the controlled hydration of C_3S at fixed lime concentration up to the deceleration period (Hydration times II in Table 4.3). The degree of hydration was calculated using Eq. 4.5 taking the experimental Ca/Si ratios from TEM-EDX in Table 5.13 (Left) and expected Ca/Si ratios at equilibrium in Table 5.14 (Right).

Table 5.14. Degree of reaction of the C-S-H samples synthesized by the controlled hydration of C_3S at fixed lime concentrations indicated in the left column given by the results in the left graph of Figure 5.43, marked with * and the right graph in Figure 5.43, marked with **. The degree of reaction given by ^{29}Si NMR is also listed in the last column for comparison.

[CaO] mmol/l	Ca/Si *	DR *	Ca/Si **	DR **	DR NMR
12	1.69	21.5	1.31	16.6	13.0
15	1.99	50.1	1.37	31.1	25.7
17	2.09	51.4	1.41	29.4	28.3
20	2.21	71.0	1.45	36.2	32.4
22	2.25	61.4	1.58	32.5	32.2
25	2.28	73.7	1.61	38.3	31.8
27	2.35	90.0	1.63	42.8	37.0

The surface of some of the samples was also studied with SEM. The hollow features created by crumpled foil-like C-S-H in the sample hydrated at $[CaO]=12\text{mmol/l}$ for 240 min (Hydration time II) are visible in Figure 5.44. The surface of the C_3S grain appears partly covered by C-S-H, which grows in a very disordered manner creating a sponge-like open surface. The surface of the samples hydrated at $[CaO]=27\text{mmol/l}$ for 600 min and 840 min is shown in Figure 5.45. C-S-H appears very different in this case, showing a more directional growth, forming sticky fibrillar elements pointing out of the C_3S grain. The length of these segments increases with hydration time. Several thin platelets of portlandite are also seen. Although the control hydration of C_3S should dissolve portlandite, it is possible that some crystals were formed, since the system was in a metastable state. A comparison of both types of structures (foils and fibrils) seen with TEM and SEM, is shown in Figure 5.46, which illustrates the change in C-S-H morphology from foils to fibrils while increasing the lime concentration in solution (increasing Ca/Si) during C_3S hydration.

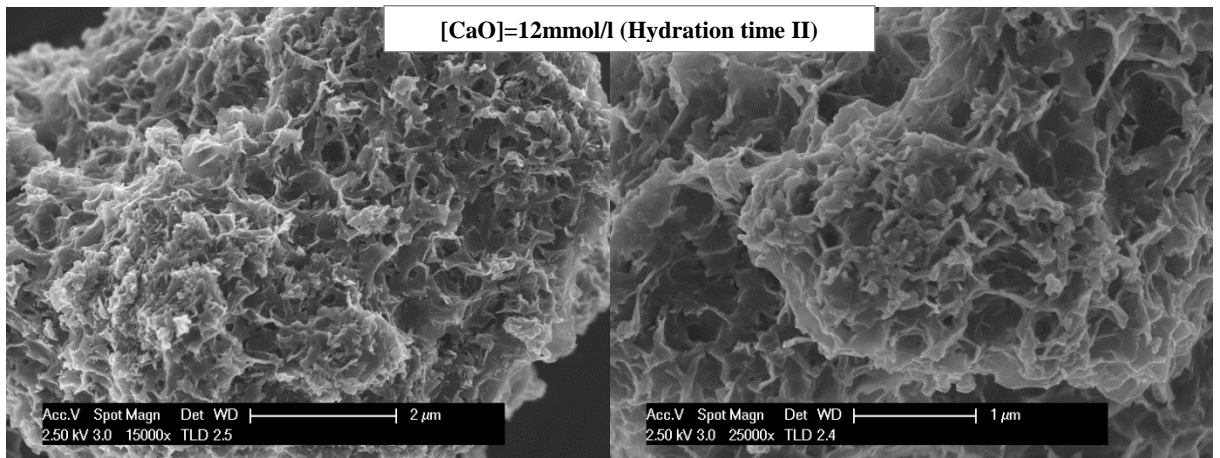


Figure 5.44. SEM micrographs of the sample hydrated at $[\text{CaO}]=12\text{mmol/l}$ for 240 min (Hydration time II). The surface of the samples appears to be crumpled foil-like presenting hollow features (Images taken by Emmanuel Boehm-Courjault at EPFL).

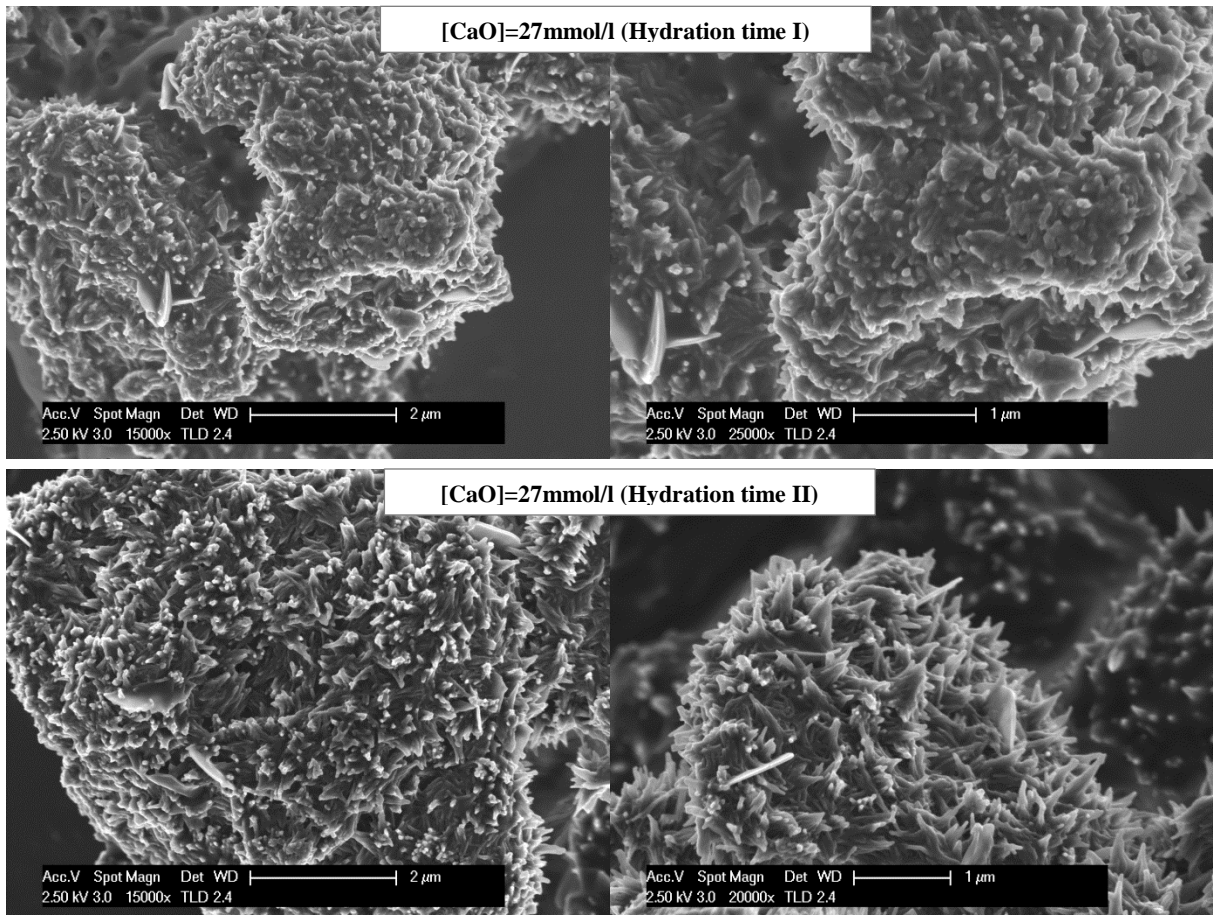


Figure 5.45. SEM micrographs of the samples hydrated at $[\text{CaO}]=27\text{mmol/l}$ for 600 min (Upper micrographs) and 840 min (lower micrographs), showing fibrillar C-S-H. The development of the fibrils with hydration time is appreciated, since the lower micrographs show longer fibrils (Images taken by Emmanuelle Boehm-Courjault at EPFL).

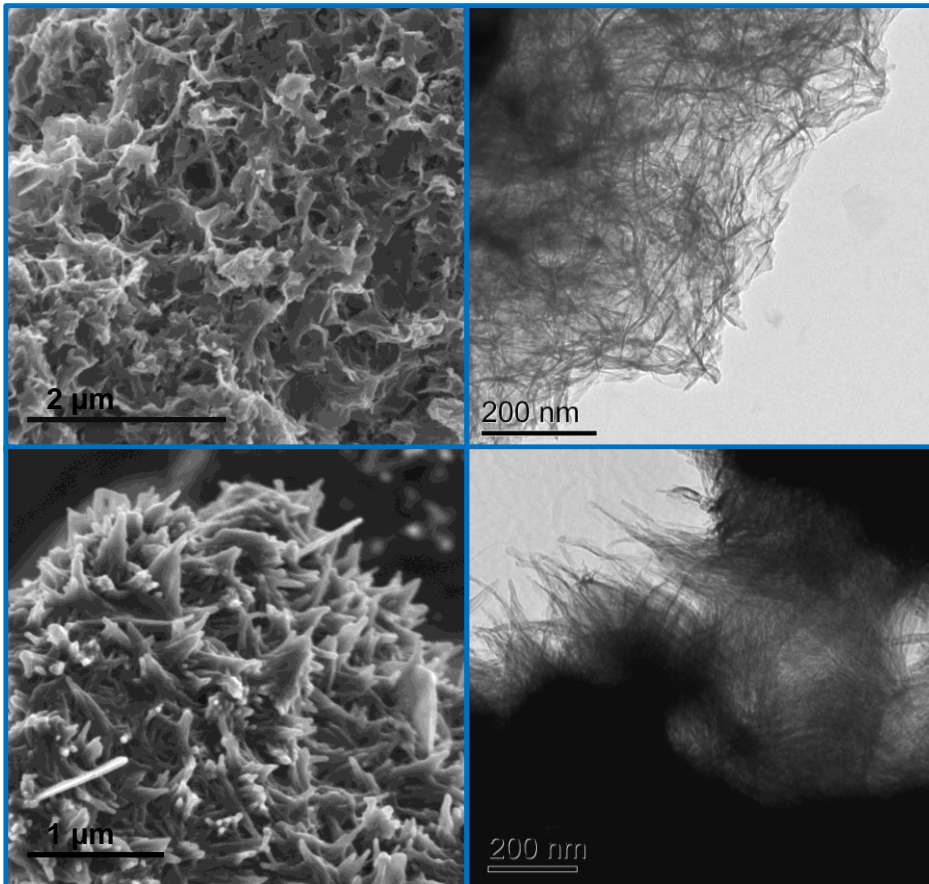


Figure 5.46. SEM and TEM micrographs of the C_3S samples hydrated at $[CaO]=12\text{mmol/l}$ for 240 min (Hydration time II) showing foil-like C-S-H (upper images) and at $[CaO]=27\text{mmol/l}$ for 600 min (Hydration time II) showing fibrillar C-S-H (lower images).

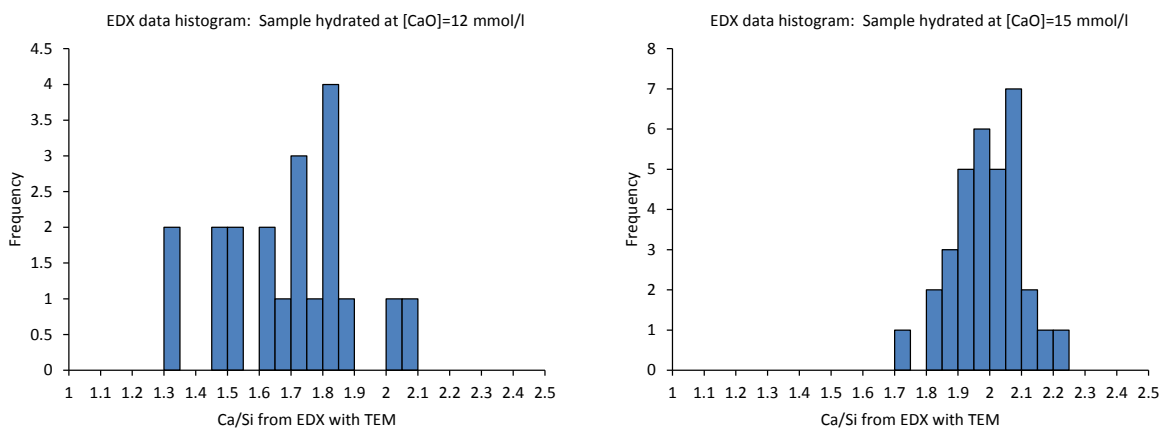


Figure 5.47. Histograms of the Ca/Si obtained by TEM-EDX for the samples hydrated at $[CaO]=12$ and 15mmol/l at Hydration times II.

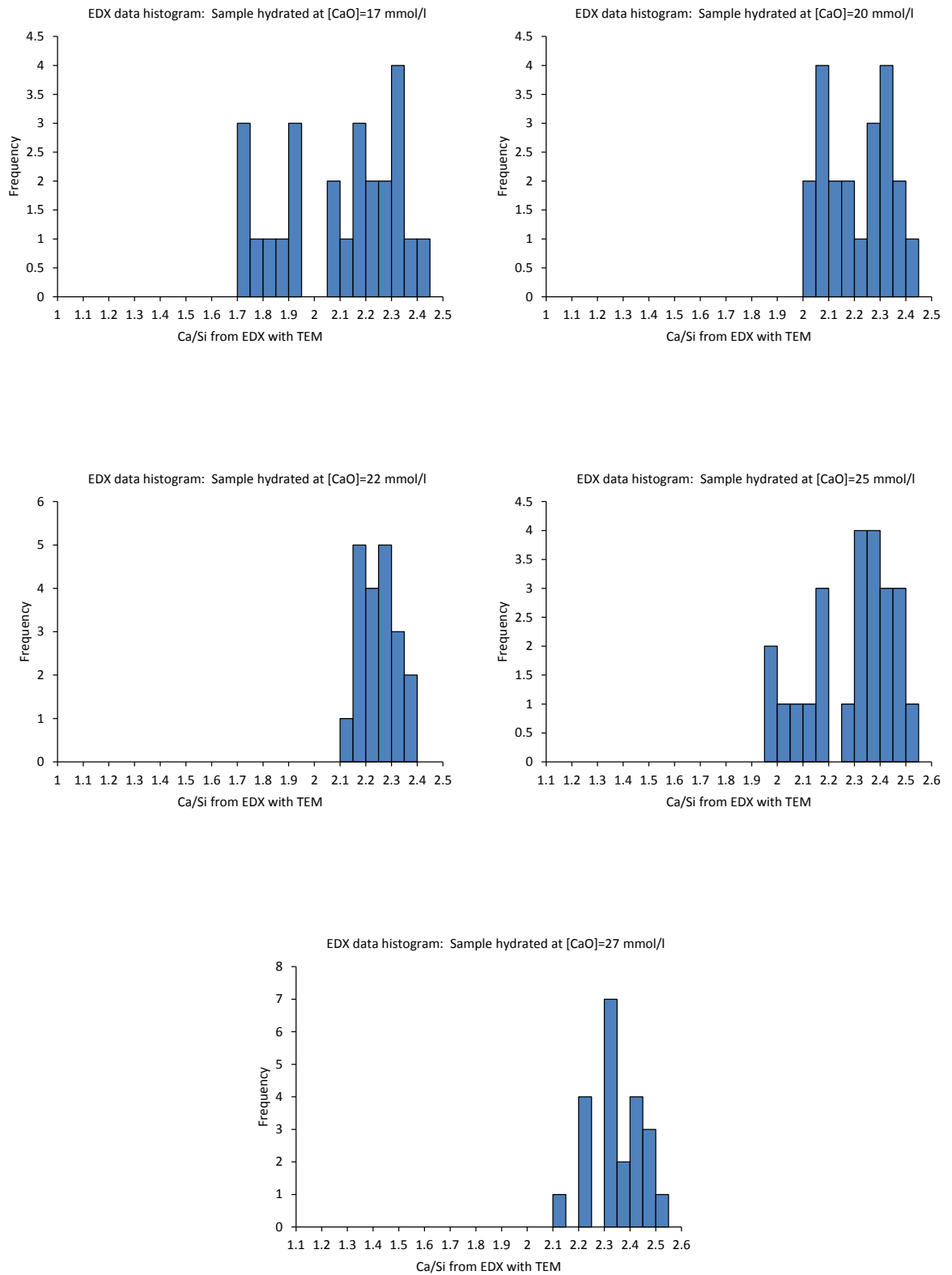


Figure 5.48. Histograms of the Ca/Si obtained with TEM-EDX of the samples hydrated at [CaO]= 17, 20, 22, 25 and 27 mmol/l for Hydration times II.

Richardson and Groves' model was applied for charge balance calculations. The height of the histograms for Ca/Si (A bar limited by the minimum and maximum values for the obtained experimental Ca/Si) is plotted versus the reciprocal mean chain length for each sample in Figure 5.49. The trends for the tobermorite and jennite structural units with maximum, intermediate and minimum degree of protonation ($w/n=2, 1, 0$) were also plotted. The values of Ca/Si given by Haas model [93] were used to get the chemical structural formulae. As discussed before, these values are closer to the real Ca/Si of the samples than those given by TEM-EDX. The data predicted thermodynamically for the samples hydrated at $[CaO] < 22\text{mmol/l}$ are very close to the tobermorite trend line with minimum degree of protonation, so that these samples are mainly tobermorite-like. The data for the samples hydrated at $[CaO] > 20\text{mmol/l}$ are placed between the tobermorite and jennite trend lines. This implies that a certain amount of Ca-OH groups is needed in the structure.

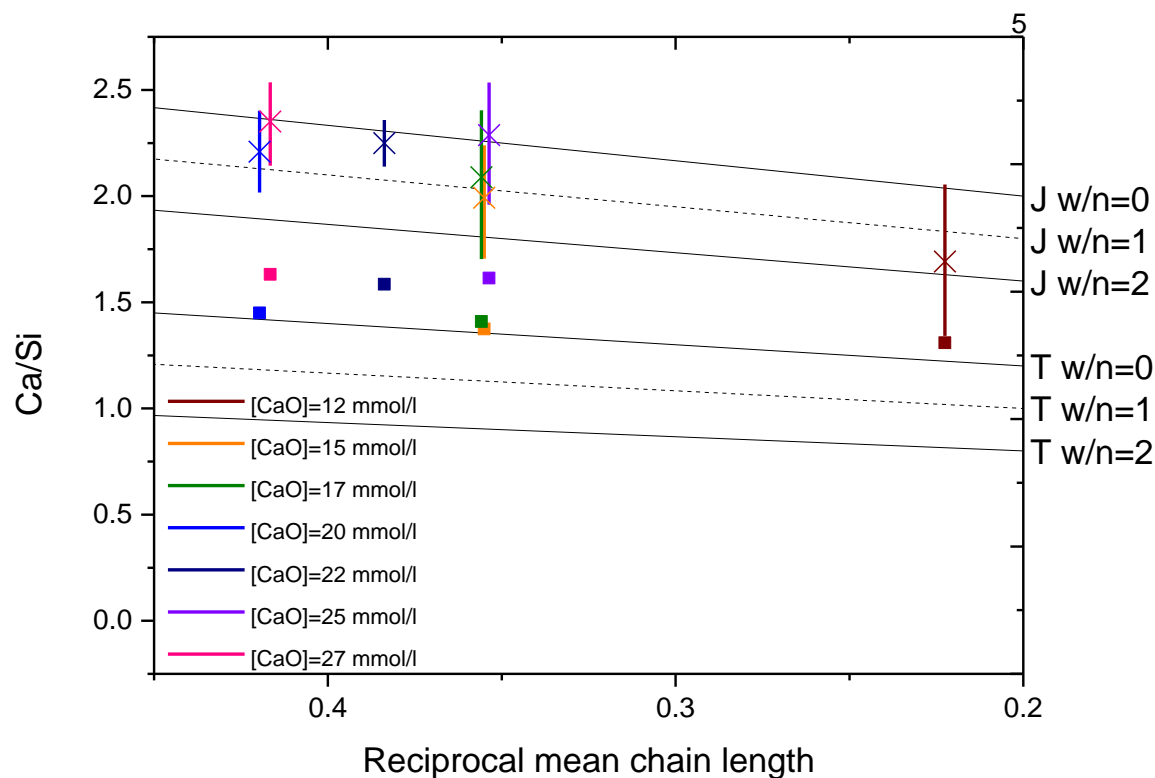


Figure 5.49. Ca/Si (obtained by TEM-EDX) vs. reciprocal mean chain length (obtained by NMR) of the C-S-H series fabricated via the controlled hydration of C_3S at Hydration times II. The length of the bars is limited by the minimum and maximum Ca/Si and the mean value is marked with a cross. The values indicated with squares are those given by Haas model [93] (Ca/Si ** in Table 5.14). The structural units for tobermorite and jennite with minimum ($w=0$), intermediate ($w=1$) and maximum ($w=2$) degree of protonation are also marked. The pentamer is marked over the top axis. The dimer is out of the scale of the plot and would be situated at reciprocal mean chain length 0.5.

Both T/J and T/CH view points are used to get the structural chemical formulae in this case. When Si is partly substituted by Al in C-S-H, an Al/Ca vs. Si/Ca plot (See Figure 2.6) can serve to identify which view point is more suitable. In this case Al is not present, so that both views could explain the data. Since the hydration of C₃S at controlled lime concentration should generate portlandite free samples and XRD showed no crystalline CH or an insignificant amount, the T/J view point seems more suitable in this case. However, microcrystalline CH was found in an area of the sample hydrated at [CaO]=25mmol/l (Figure 5.50 c)). The presence of microcrystalline CH throughout extensive areas in the samples is not evident judging by the TEM micrographs. Microcrystalline CH creates a characteristic contrast in TEM images (See ref. [11] and Fig. 13 in ref.[1]) that is not evident in these samples. Although due to the different reasons discussed, the T/J view point seems more adequate, the T/CH is also used as an equally valid explanation for the structures.

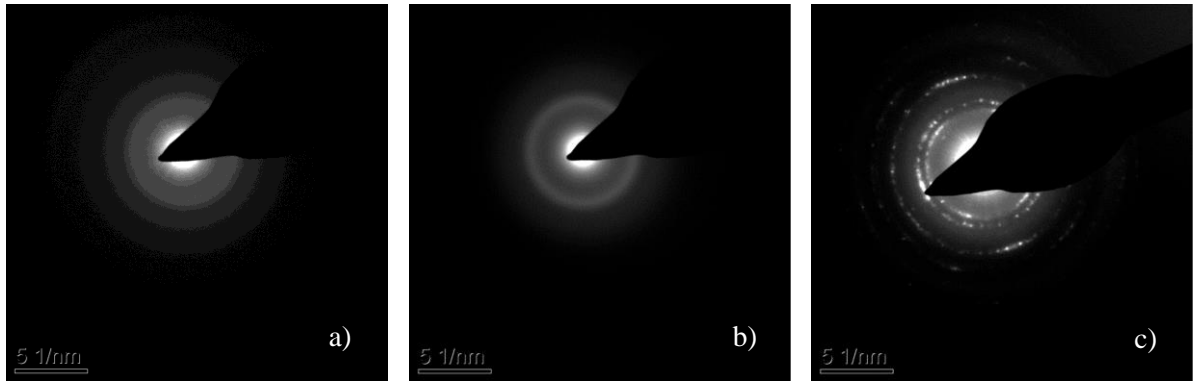
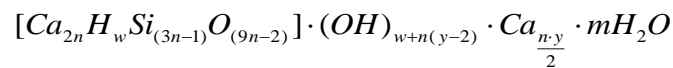


Figure 5.50. Selected area electron diffraction patterns of the C-S-H samples hydrated at: a) [CaO]=15mmol/l, c) and d) [CaO]=25mmol/l. The halos in the patterns shown in a) and b) are consistent with C-S-H, while the reflections seen in pattern c) are characteristic of microcrystalline CH.

The T/J formulation is:



In the T/J view of the model $(3n-1)=MCL$ and $Ca/Si=(4n+ny)/(6n-2)$, so that $n=(MCL+1)/3$ and $y= [(Ca/Si)(6n-2)-4n]/n$. The number of silanol groups w depends on the value of y according to:

$$0 \leq y \leq 2 \rightarrow n(2 - y) \leq w \leq 2n$$

$$2 \leq y \leq 4 \rightarrow 0 \leq w \leq 2n$$

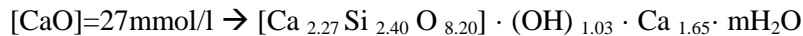
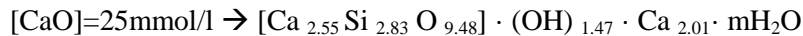
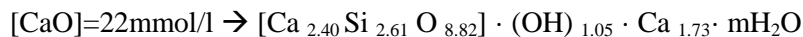
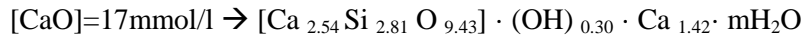
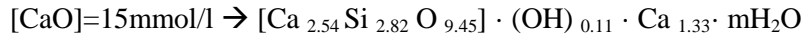
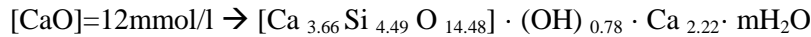
$$4 \leq y \leq 6 \rightarrow 0 \leq w \leq n(6 - y)$$

The calculated values for n , y , w_{\max} (maximum number of silanol groups), w_{\min} (minimum number of silanol groups) and w/n_{\max} (maximum degree of protonation) and w/n_{\min} (minimum degree of protonation) are shown in Table 5.15.

Table 5.15. Calculated values for the parameters of the T/J view point of Richardson and Groves' model for the C-S-H samples fabricated via the controlled hydration of C_3S at Hydration times II.

[CaO] (mmol/l)	n	y	w_{\min}	w_{\max}	w/n_{\min}	w/n_{\max}
12	1.83	2.42	0	3.66	0	2
15	1.27	2.09	0	2.54	0	2
17	1.27	2.24	0	2.54	0	2
20	1.13	2.13	0	2.26	0	2
22	1.20	2.87	0	2.40	0	2
25	1.28	3.15	0	2.55	0	2
27	1.13	2.91	0	2.26	0	2

The minimum degree of protonation was chosen, since it was the most sensible value according to the position of the predicted Ca/Si with respect to the tobermorite trends in Figure 5.49. The resulting structural chemical formulae are:

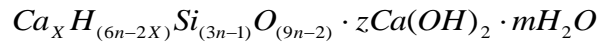


All the samples can be explained as a combination of T2, T5, J2 and J5 structural units. The structural chemical formulae for samples hydrated at $[\text{CaO}]=15$, 17 and 20mmol/l contain a small amount of OH groups and are mainly tobermorite-like. The amount of OH groups increases in the case of the sample hydrated at $[\text{CaO}]=12$ mmol/l since the data point for this sample is situated further from the tobermorite trend line with minimum degree of protonation. The MCL of this

sample was higher than those of the rest of the samples (See Table 5.12). As discussed previously, the lower degree of reaction of this sample with respect to the rest, may have affected the quantification of the spectra, since the signal coming from connectivities in C-S-H was lower in this case. If the real MCL was lower, the data point would be situated closer to the tobermorite trend line since it would be shifted towards the left in Figure 5.49.

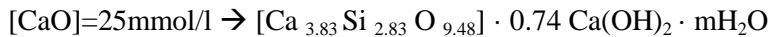
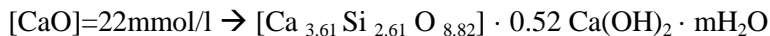
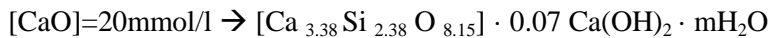
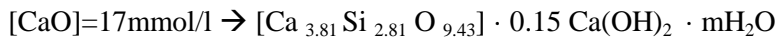
The structural chemical formulae of samples hydrated at $[\text{CaO}] > 20 \text{ mmol/l}$ present a higher content of OH groups. The inclusion of more OH groups coincides with the fact that the morphology of the samples changes from foil-like to fibrillar.

Alternatively, the T/CH formulation is:



$$\text{Where } X = (6n - w) / 2 \quad z = (w + n(y - 2)) / 2$$

X and Z were calculated using the values of n, y and w_{\min} in Table 5.15. The structural chemical formulae of the samples according to the T/CH view point are:



5.6 Hydration of C_3S at constant lime concentration: Ultrasound C-S-H series

The XRD patterns of the samples fabricated via C_3S hydration at high lime concentrations with the aid of an ultrasound gun are shown in Figure 5.51 together with a reference pattern of CH [133]. The patterns show that the degree of reaction is higher for these samples than for all the series from the previous section, since the intensity of the peaks that correspond to anhydrous C_3S is much less in this case than in Figure 5.32, Figure 5.33, Figure 5.34 and Figure 5.35. The features associated with C-S-H are also more evident in this case. The two peaks at $2\theta \sim 30^\circ$ present more similarities with the patterns of synthetic C-S-H samples in Figure 5.9 than with the patterns in the previous section. There is an incipient hump in the patterns at $2\theta \sim 45^\circ$ that resembles the hump in the synthetic phases at $2\theta \sim 44^\circ$. In the samples hydrated at $[CaO]=27$ and 28mmol/l a trace of portlandite is found, which corresponds to the incipient reflection at $2\theta \sim 18^\circ$.

The ^{29}Si NMR spectra of the samples are shown in Figure 5.52. The intensity from the Q^1 ($\sim -79\text{ppm}$) and Q^2 ($\sim -85\text{ppm}$) silicate groups that are part of the C-S-H structure is much higher in these spectra than for the samples of the previous series, indicating a higher degree of reaction. The sample hydrated at $[CaO]=27\text{mmol/l}$ shows less intensity for the C-S-H connectivities compared to the intensity coming from C_3S , than the other two samples, which indicates a lower degree of reaction. This couples very well with the XRD patterns in Figure 5.51, since for the samples hydrated at lime concentrations of 28 and 29mmol/l the main reflections originating from C_3S at $2\theta \sim 32^\circ$ and 34° have less intensity than the main reflections associated with C-S-H at $2\theta \sim 30^\circ$, but it is the opposite for the sample hydrated at $[CaO]=27\text{mmol/l}$.

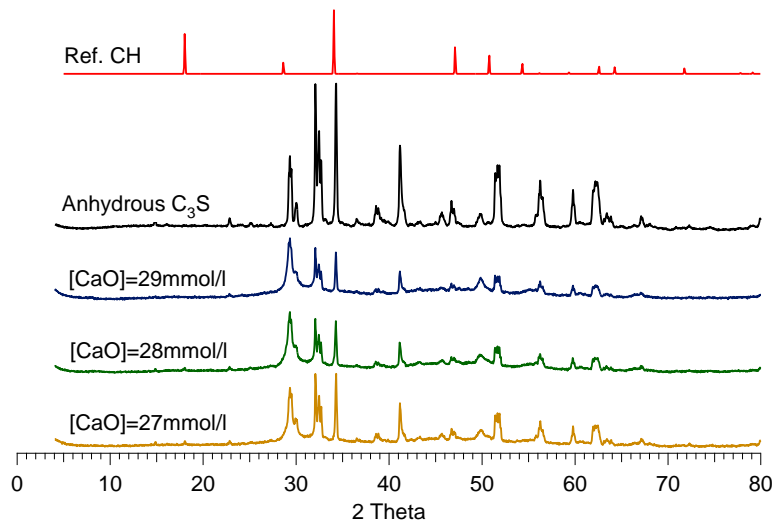


Figure 5.51. XRD patterns of C-S-H samples fabricated by the controlled hydration of C_3S at lime concentrations of 27, 28 and 29mmol/l with the use of an ultrasound gun. The pattern of anhydrous C_3S and a reference for portlandite are also included.

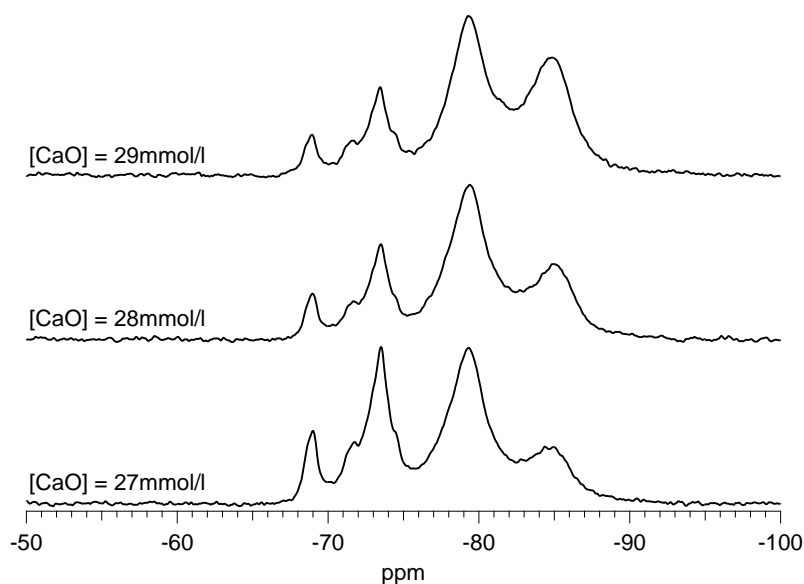


Figure 5.52. ^{29}Si MAS NMR spectra of the C-S-H samples synthesized via the controlled hydration of C_3S with the use of an ultrasound gun at fixed lime concentrations of 27, 28 and 29mmol/l.

The degree of reaction, together with the MCL and the percentages of the silicate connectivities, calculated from the deconvolutions shown in Figure 5.53 are summarised in Table 5.16. Seven frequencies were used to deconvolute the signal from C_3S and two frequencies for each of the silicate connectivities in C-S-H. Structural information was derived from the total integral of Q^0 , Q^1 and Q^2 , rather than from individual frequencies used for deconvolutions. The degrees of reaction are higher for the samples hydrated at lime concentrations of 28 and 29mmol/l. The percentage of unreacted C_3S (Q^0) is lower in these two samples than for the sample hydrated at $[\text{CaO}]=27\text{mmol/l}$. The MCL is increasing with the degree of reaction.

Table 5.16. Percentages of the silicate species, mean silicate chain length and degree of reaction of the C-S-H samples prepared by controlled hydration of C_3S with the use of an ultrasound gun. The results are obtained from the deconvolutions of the ^{29}Si NMR spectra shown in Figure 5.53.

$[\text{CaO}]$ mmol/l	$\text{Q}^0 \pm 2.0$	$\text{Q}^1 \pm 2.0$	$\text{Q}^2 \pm 2.0$	MCL	DR ± 2.8
27	34.7 %	49.9 %	15.4 %	2.6 ± 0.3	65.3 %
28	23.8 %	46.9 %	29.3 %	3.3 ± 0.2	76.2 %
29	17.3 %	44.7 %	38.0 %	3.7 ± 0.2	82.7 %

The morphology of the samples is shown in Figure 5.54 and appears to be mainly foil-like and similar to the morphology of samples synthesized via lime-silica reactions (mechanochemical and CaO-SiO_2 series), although it appears denser. Some fibrils can also be appreciated in some areas of the samples. These are clearly seen in the enlarged area of the sample hydrated at lime concentration of 27mmol/l at the upper right corner in Figure 5.54. Some fibrils can also be appreciated at the surface in the particle at the bottom right corner of the image, which corresponds

to the sample hydrated at $[\text{CaO}]=29\text{mmol/l}$. The surface of the samples was investigated with SEM and some micrographs of the sample hydrated at $[\text{CaO}]=27\text{mmol/l}$ are shown in Figure 5.55. The surface is much more flattened compared to the samples in the previous section in Figure 5.44 and Figure 5.45. A hexagonal crystal of portlandite can be seen at the lower left corner on the left image in Figure 5.55. The use of the ultrasound gun is clearly the cause of the surface flattening. Some spiky features can be seen on the right image, which shows a similar morphology to the sample shown in the upper part of Figure 5.45, which was hydrated at the same lime concentration. However, the spiky features appear more rounded as a consequence of the ultrasound gun. Two of these samples showed a range of compositions, counting on average Ca/Si and standard deviations (Table 5.17), that falls in the region of Ca/Si in which both fibrils and foils are expected, according to the range found for the kinetics series (mixture of foils and fibrils found at $\text{Ca/Si}\sim 1.58$). The use of the ultrasound gun may have disrupted the growth of the fibrils that were expected at these high lime concentrations, given the fact that fibrils are not clearly seen in all the samples.

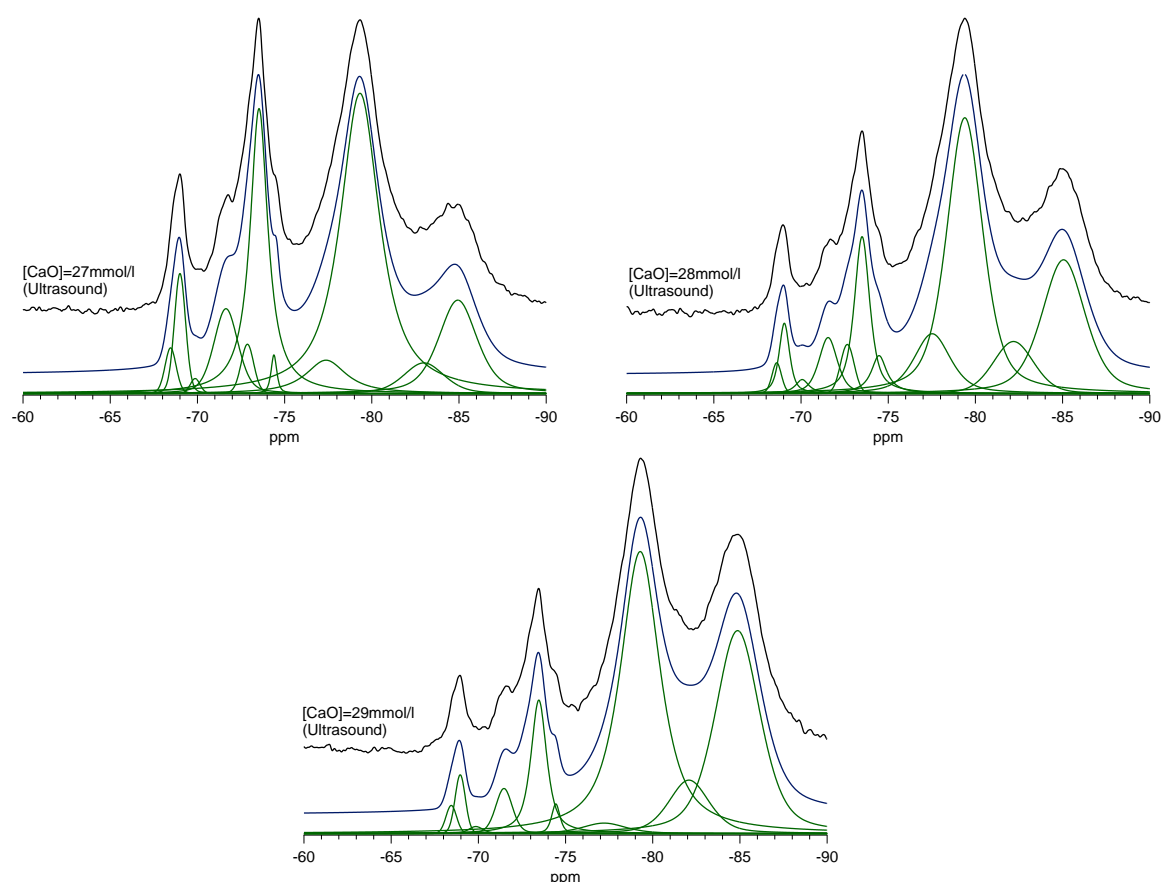


Figure 5.53. Deconvolutions of the ^{29}Si MAS NMR spectra of the C-S-H samples fabricated via the controlled hydration of C_3S with an ultrasound gun at fixed lime concentrations of 27mmol/l (upper left), 28mmol/l (upper right) and 29mmol/l (low). The individual frequencies are shown in green, the simulated spectra in blue and the experimental spectra in black.

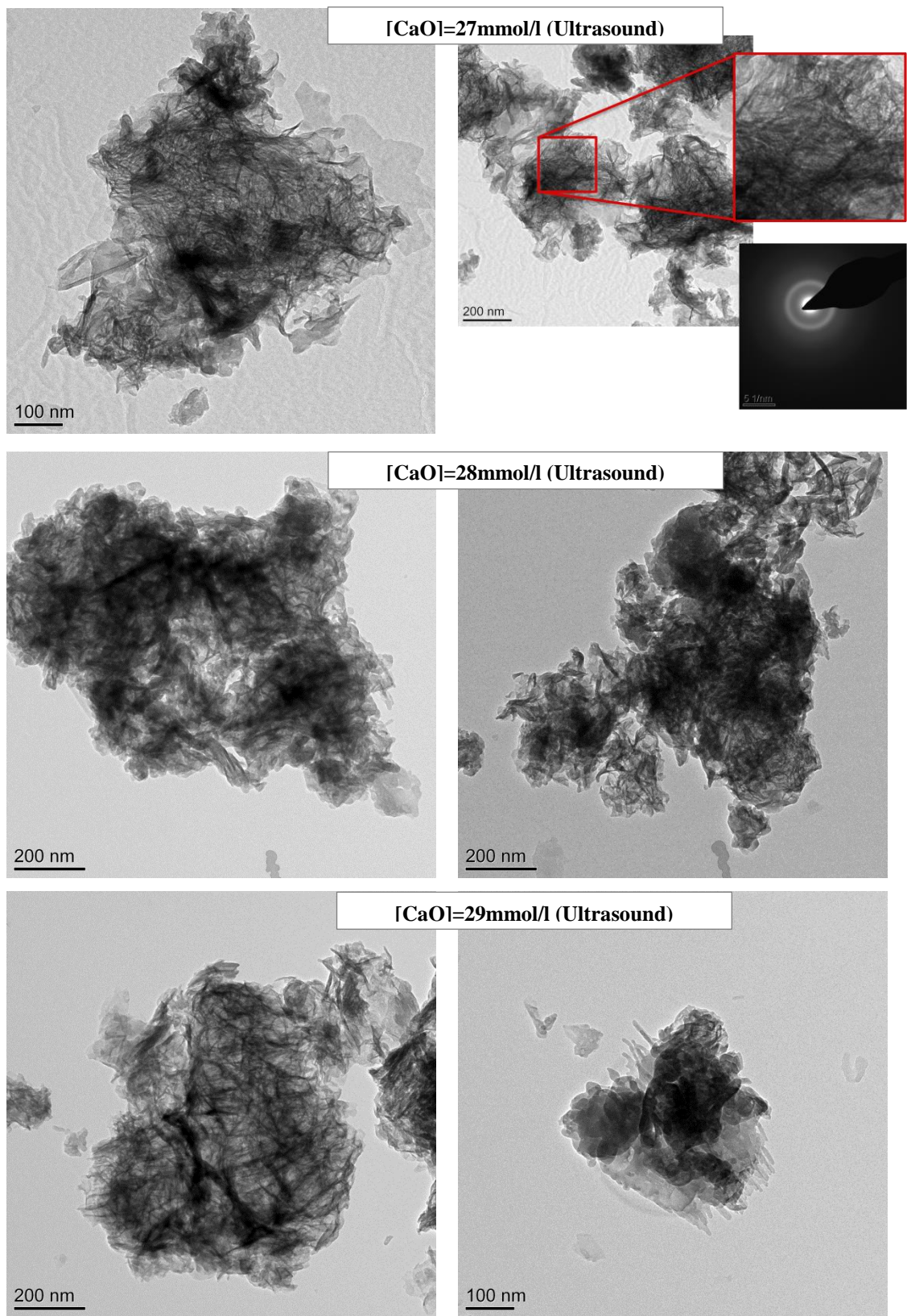


Figure 5.54. TEM micrographs of the C-S-H samples synthesized via the controlled hydration of C_3S with the use of an ultrasound gun at fixed lime concentrations of 27mmol/l (Upper images with a SAED pattern), 28mmol/l (middle images) and 29mmol/l (lower images). The enlargement in the upper right corner shows a fibrillar area of the sample hydrated at 27mmol/l.

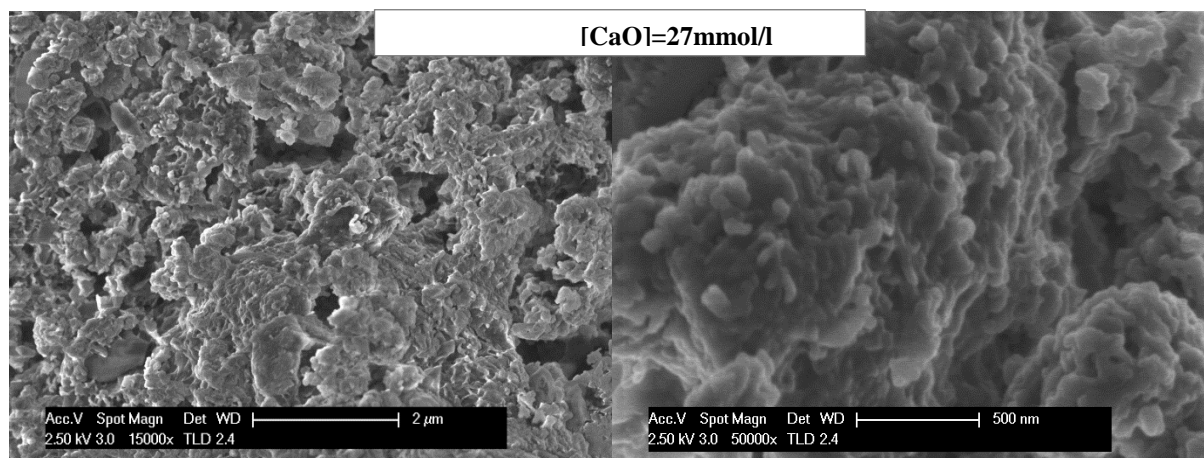


Figure 5.55. SEM micrographs of the C-S-H sample fabricated via the controlled hydration of C_3S with an ultrasound gun at lime concentration of 27mmol/l. The left image shows a considerably flattened surface, however, an area with sticky features is shown on the right image (Micrographs taken by Emmanuelle Boehm-Courjault at EPFL).

The mean Ca/Si values obtained by TEM-EDX are shown in Table 5.17. The Ca/Si ratio is ~1.5-1.6, as expected for high lime in solution. It increases with the lime concentration in solution as expected. The histograms for the TEM-EDX data are shown in Figure 5.56. The dispersion of the Ca/Si data in these samples is high, presenting intervals with no data points. In the case of $[CaO]=28mmol/l$ the distribution of Ca/Si seems to be bimodal, but this is not as clear in the case of the other two samples.

Table 5.17. Mean Ca/Si values (with the standard deviations) of C-S-H fabricated via the controlled hydration of C_3S with the use of an ultrasound gun.

[CaO] (mmol/l)	Ca/Si (TEM-EDX)	# EDX analyses
27	1.45 ± 0.17	37
28	1.55 ± 0.32	26
29	1.59 ± 0.31	28

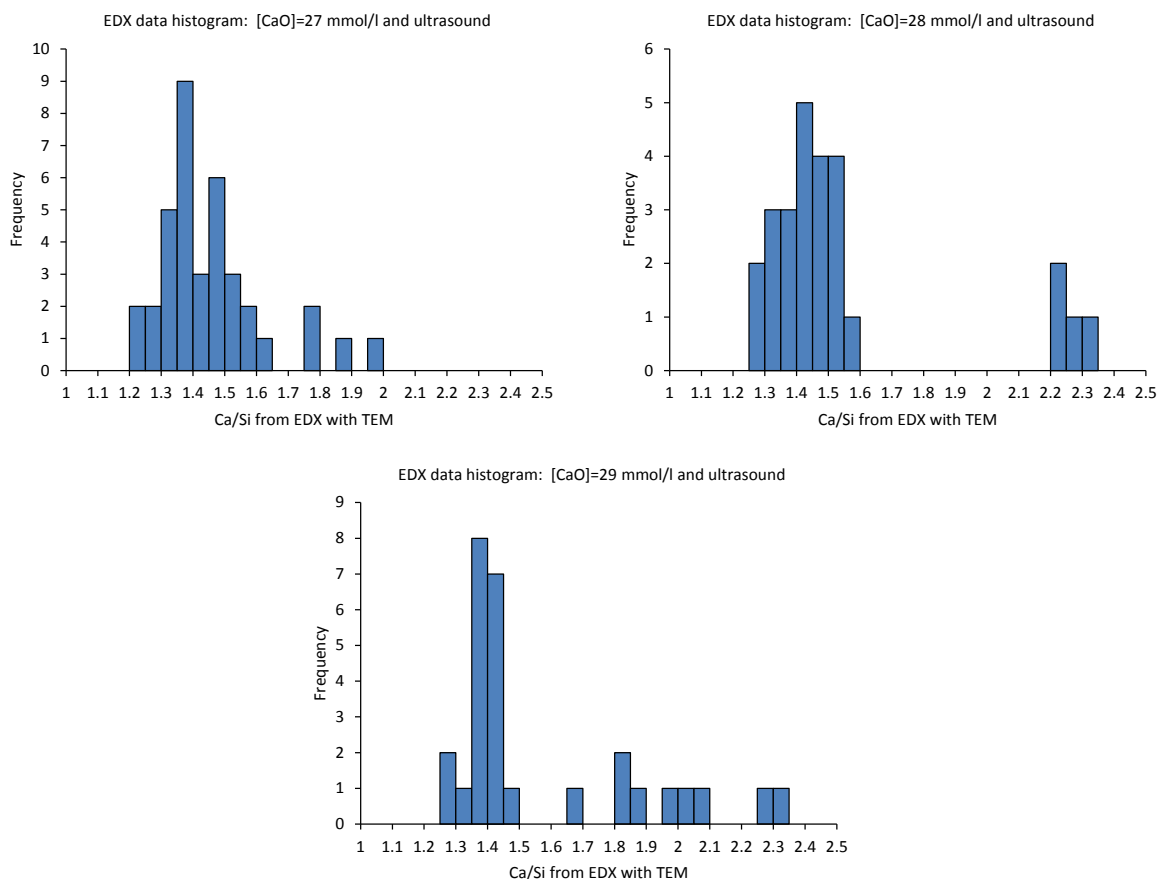


Figure 5.56. Histograms of the Ca/Si obtained with TEM-EDX of the samples hydrated at [CaO]= 27, 28 and 29mmol/l with the use of an ultrasound gun.

Richardson and Groves' model was applied for charge balance calculations. The height of the histograms for Ca/Si (A bar limited by the minimum and maximum values for the obtained experimental Ca/Si) is plotted versus the reciprocal mean chain length for each sample in Figure 5.57. The trends for the tobermorite and jennite structural units with maximum, intermediate and minimum degree of protonation ($w/n=2, 1, 0$) are also plotted. The mean Ca/Si value is indicated with a cross and it is the value used to derive the structural chemical formulae. These mean values are situated between the tobermorite-like and jennite-like region of the plot. This implies Ca-OH groups are needed in the structures.

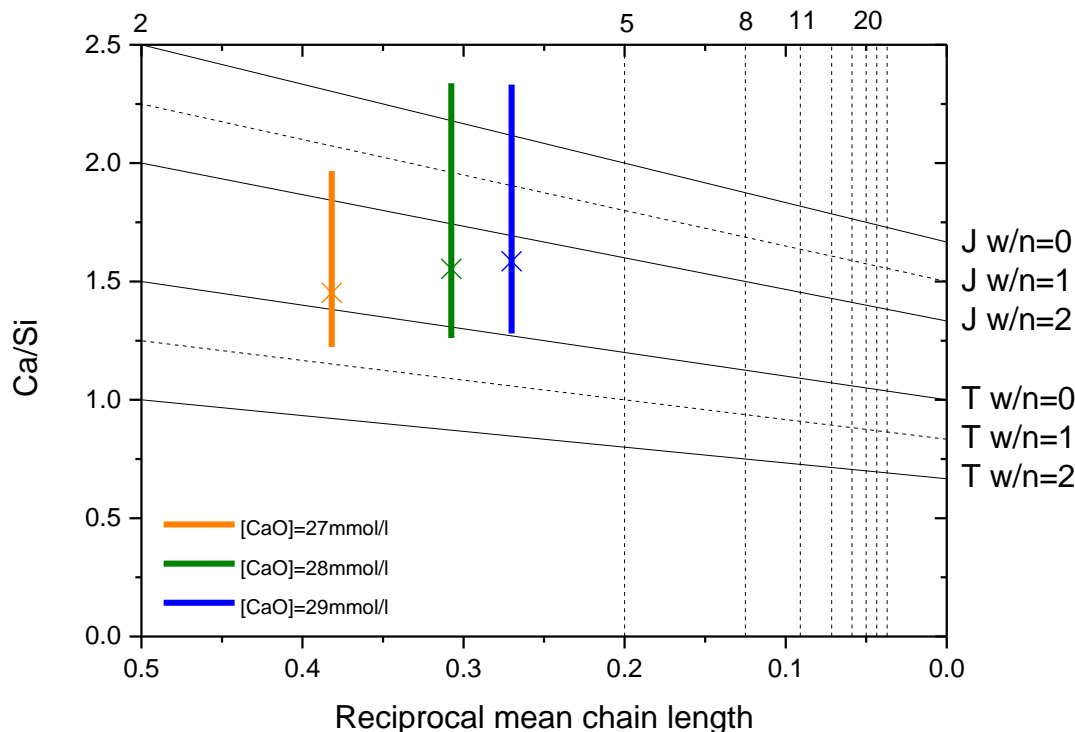
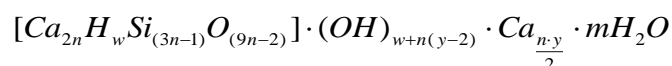


Figure 5.57. Ca/Si (obtained by TEM-EDX) vs. reciprocal mean chain length (obtained by NMR) of the C-S-H series fabricated via the controlled hydration of C_3S with the use of an ultrasound gun. The length of the bars is limited by the minimum and maximum Ca/Si and the mean value is marked with a cross. The structural units for tobermorite and jennite with minimum ($w=0$), intermediate ($w=1$) and maximum ($w=2$) degree of protonation are also marked. The vertical dashed lines represent the $(3n-1)$ structural units: dimer (2), pentamer (5), octamer (8)...

Both the T/J and T/CH view points can be used to get the structural chemical formulae, since without Al substitution, they can equally explain the data. As in the case of the kinetics series, the T/J view point should be more suitable since the controlled hydration of C_3S should avoid the precipitation of portlandite. An electron diffraction pattern of a selected area of the sample hydrated at $[CaO]=27\text{mmol/l}$ shows the typical halo associated to C-S-H (Figure 5.54). Although microcrystalline CH was not found by inspection of other areas of the sample, this does not exclude its presence. Both view points of the model are thus used as equally valid explanations for the structure of the samples.

The formulation for the T/J is:



In the T/J view of the model $(3n-1)=MCL$ and $Ca/Si=(4n+ny)/(6n-2)$, so that $n=(MCL+1)/3$ and $y= [(Ca/Si)(6n-2)-4n]/n$. The number of silanol groups w depends on the value of y according to:

$$0 \leq y \leq 2 \rightarrow n(2 - y) \leq w \leq 2n$$

$$2 \leq y \leq 4 \rightarrow 0 \leq w \leq 2n$$

$$4 \leq y \leq 6 \rightarrow 0 \leq w \leq n(6 - y)$$

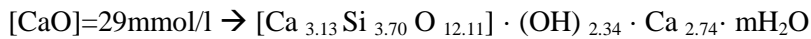
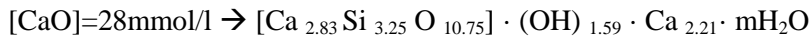
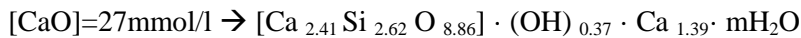
The calculated values for n , y , w_{\max} (maximum number of silanol groups), w_{\min} (minimum number of silanol groups) and w/n_{\max} (maximum degree of protonation) and w/n_{\min} (minimum degree of protonation) are shown in Table 5.18.

Table 5.18. Calculated values for the parameters of the T/J view point of Richardson and Groves' model for the C-S-H samples fabricated via the controlled hydration of C_3S with the use of an ultrasound gun.

[CaO] (mmol/l)	n	y	w_{\min}	w_{\max}	w/n_{\min}	w/n_{\max}
27	1.21	2.31	0	2.41	0	2
28	1.42	3.13	0	2.83	0	2
29	1.57	3.49	0	3.13	0	2

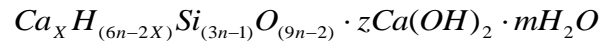
The minimum degree of protonation was chosen, since it was the most sensible value according to the position of the mean Ca/Si with respect to the tobermorite trends in Figure 5.57.

The resulting structural chemical formulae are:



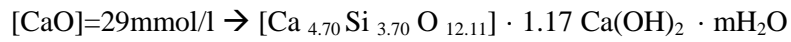
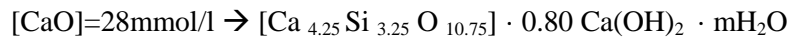
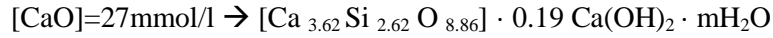
The samples can be explained by a combination of T2, T5, J2 and J5 structural units. The amount of necessary OH groups in the structures increases with lime concentration in solution.

Alternatively, the T/CH formulation is:



$$\text{Where } X = (6n - w)/2 \quad z = (w + n(y - 2))/2$$

X and Z were calculated using the values of n, y and w_{\min} in Table 5.18. The structural chemical formulae of the samples according to the T/CH view point are:



5.7 Hydration of C_3S at constant lime concentration: Xseed C-S-H series

The XRD patterns of the samples fabricated via C_3S hydration at high lime concentrations with the addition of Xseed are shown in Figure 5.58 together with a reference pattern of CH [133]. These patterns are very similar to the ones in Figure 5.51, showing also a higher degree of reaction than samples hydrated via the controlled hydration of C_3S without the addition of any accelerators. No traces of portlandite are detected in these samples.

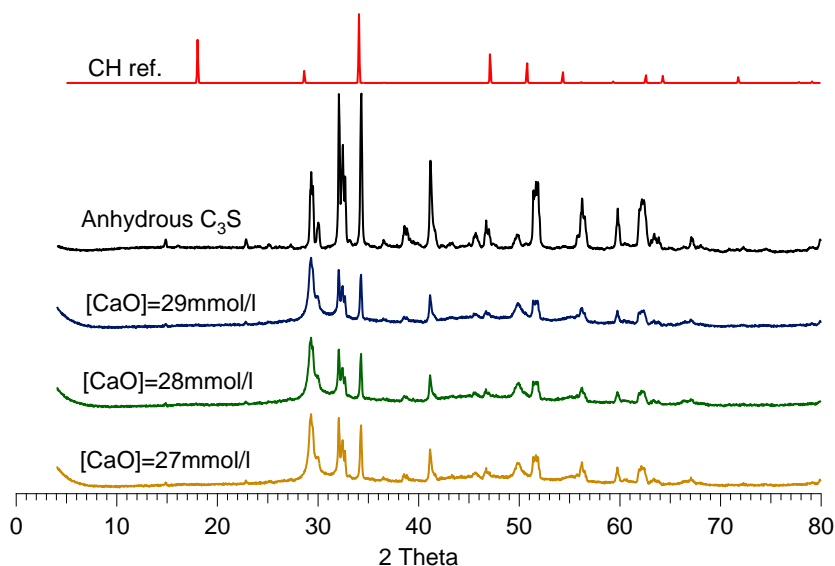


Figure 5.58. XRD patterns of C-S-H samples fabricated by the controlled hydration of C_3S at lime concentrations of 27, 28 and 29mmol/l with the use of C-S-H platelets (X-seed). The pattern of anhydrous C_3S and a reference for portlandite are also included.

The ^{29}Si NMR spectra of the samples are shown in Figure 5.59. These spectra show that the degree of reaction of the samples is also much higher than for the samples in section 5.5, since the intensity originating from unreacted C_3S is much less than the intensity coming from the C-S-H connectivities. The samples present a typical spectrum of C-S-H with high Ca/Si, with much more intensity originating from Q^1 groups than from Q^2 groups. The quantification of the different silicate connectivities, obtained through the deconvolutions of the spectra shown in Figure 5.60, the mean silicate chain length and the degree of reaction are shown in Table 5.19. Seven frequencies were used to deconvolute the signal of C_3S and two frequencies to deconvolute each of the Q^1 and Q^2 contributions from C-S-H. In the case of [CaO]=27mmol/l, the frequency used at -85ppm was split into two frequencies to adjust the rounded appearance of the Q^2 peak. Structural information was derived from the total integral of Q^0 , Q^1 and Q^2 , rather than from individual frequencies used for deconvolutions. The MCL increases with the degree of reaction, as it was the case for the samples fabricated with the ultrasound gun.

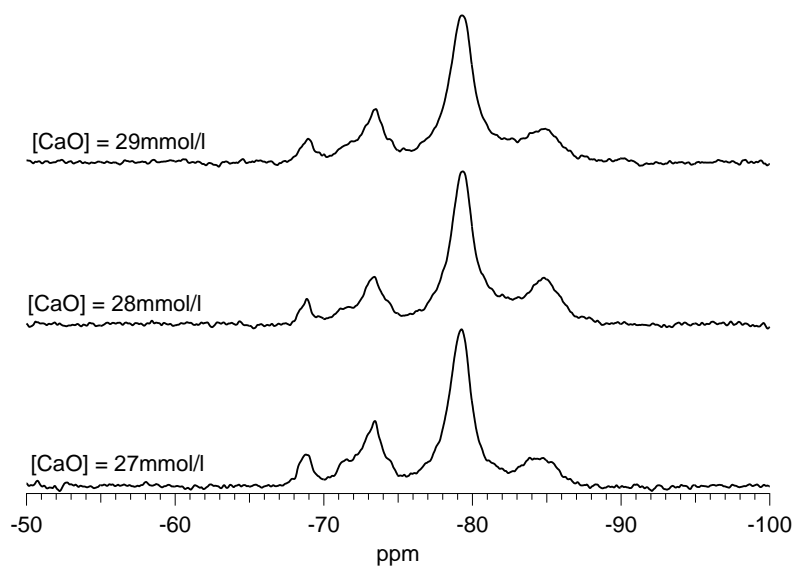


Figure 5.59. ^{29}Si MAS NMR spectra of the C-S-H samples synthesized via the controlled hydration of C_3S with the use of C-S-H platelets (Xseed) at fixed lime concentrations of 27, 28 and 29mmol/l.

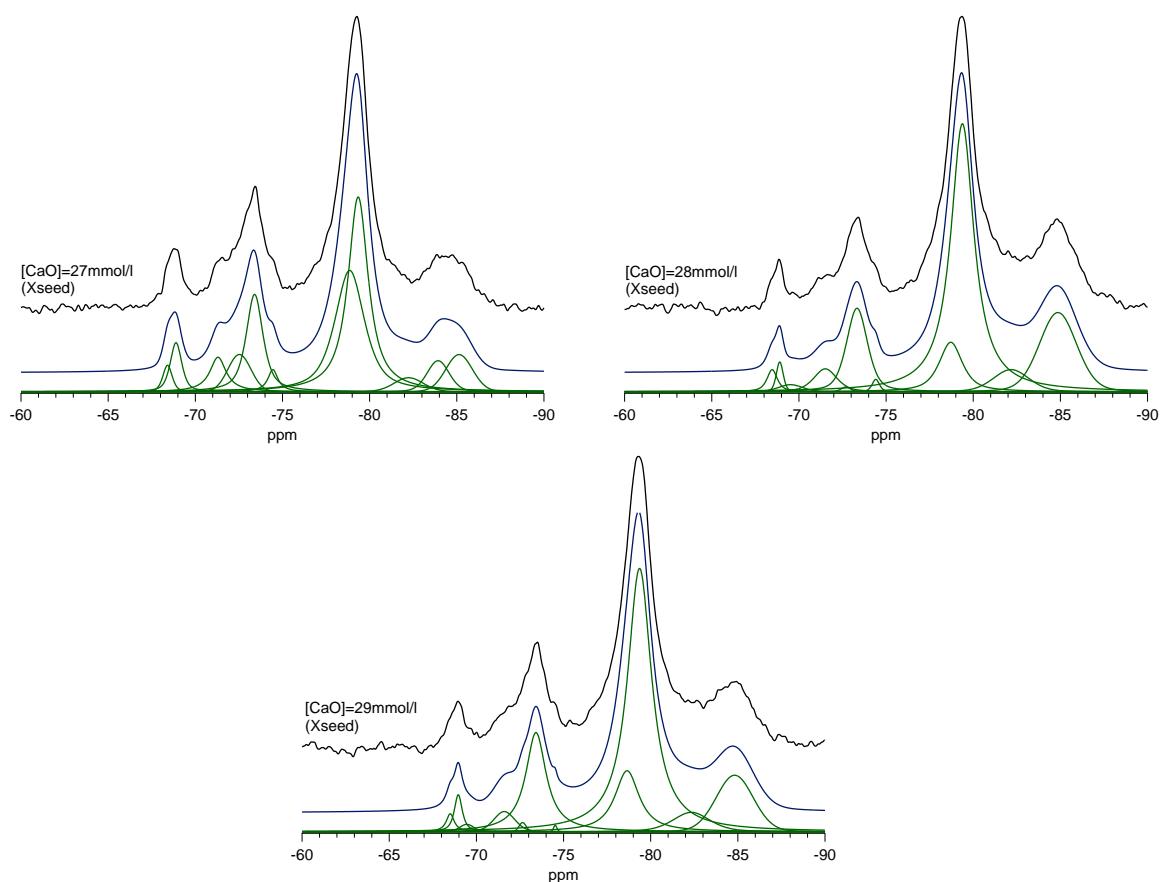


Figure 5.60. Deconvolutions of the ^{29}Si MAS NMR spectra of the C-S-H samples fabricated via the controlled hydration of C_3S with C-S-H platelets (Xseed) at fixed lime concentrations of 27mmol/l (upper left), 28mmol/l (upper right) and 29mmol/l (low). The individual frequencies are shown in green, the simulated spectra in blue and the experimental spectra in black.

Table 5.19. Percentage of the silicate connectivities calculated from the deconvolutions in Figure 5.60, mean silicate chain length and the degree of reaction of the C-S-H samples synthesized via the controlled hydration of C₃S with the use of Xseed.

[CaO] mmol/l	Q ⁰ ± 2.0	Q ¹ ± 2.0	Q ² ± 2.0	MCL	DR ± 2.8
27	29.0 %	58.8 %	12.2 %	2.4 ± 0.3	71.0 %
28	19.4 %	58.8 %	21.8 %	2.7 ± 0.2	80.6 %
29	22.6 %	61.6 %	15.8 %	2.5 ± 0.3	77.4 %

The morphology of these samples is shown in the TEM and SEM micrographs in Figure 5.61 and Figure 5.62. In the TEM images the samples appear as a mixture of foils and fibrils. As for the ultrasound samples, the composition of these samples (Table 5.20) also falls in the range of Ca/Si in which a mixture of foils and fibrils was present in the kinetics series. The image in the upper left corner ([CaO]=27mmol/l) in Figure 5.61 shows certain similarities with the fully hydrated C₃S sample shown in the upper and lower images in Figure 5.4. The rest of the images in Figure 5.61 show a very fine fibrillar product mixed with foils, similar to the morphology found for the samples hydrated at [CaO]=22mmol/l in the kinetics series (Figure 5.42). Interestingly, the surface of the sample hydrated at [CaO]=27mmol/l, shown in the left image in Figure 5.62, has some similarities with the foil-like samples in Figure 5.44, but the structure is less opened and the growth is more directional. It should be noted that not only spiky features growing out from the surface give a fibrillar appearance on TEM images, but also surfaces like the one seen in the left image of Figure 5.62, which is defined by very packed foil-like features. However, at higher magnification the foil-like features seem to be not continuous presenting some holes. Some thin and round platelets are also observed. They could be portlandite crystals or platelets of the Xseed product. Since they are round (portlandite in normal conditions should be hexagonal [139]) they must be platelets of the Xseed product. Some areas, such as the one shown in the right image in Figure 5.62, are found to have some spiky features, such as the ones seen on the right image in Figure 5.55 from the sample hydrated also at [CaO]=27mmol/l with the use of the ultrasound gun. Since these samples with Xseed were fabricated without controlling the w/s ratio, this could have affected the morphology. As Richardson stated, it is possible that fibrils grow in systems where the availability of space is lower than when foils grow [1]. However, the results from the C-S-H samples of the kinetics series in section 5.5 point towards the fact that the space may not be relevant. Both morphologies were found in those systems synthesized in very diluted solutions (w/s=50). Fibrils grew in systems with a high availability of space compared to real systems with typical w/s=0.4.

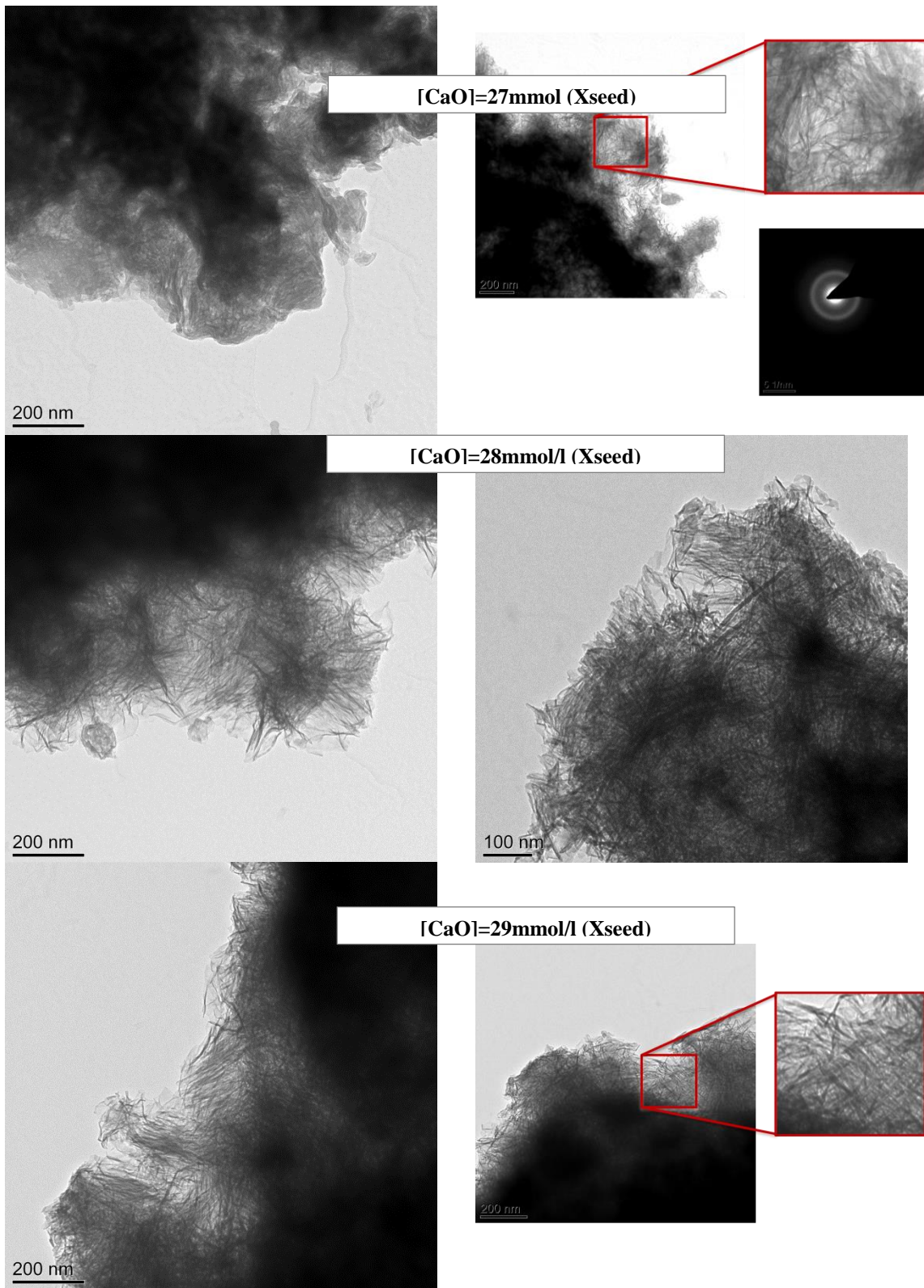


Figure 5.61. TEM micrographs of the C-S-H samples synthesized via the controlled hydration of C_3S with C-S-H platelets (Xseed) at fixed lime concentrations of 27mmol/l (Upper images with a SAED pattern), 28mmol/l (middle images) and 29mmol/l (lower images). The enlargements in the upper/lower right corners show a mixed foil-fibrillar area of the sample hydrated at $[CaO]=27mmol/l$ and a fibrillar area of the sample hydrated at $[CaO]=29mmol/l$.

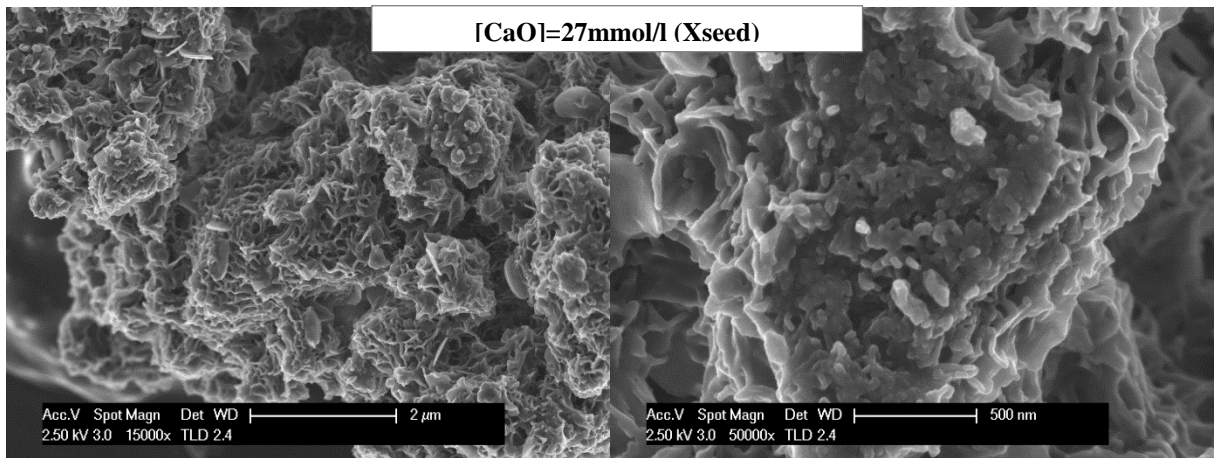


Figure 5.62. SEM micrographs of the C-S-H sample fabricated via the controlled hydration of C_3S with Xseed at $[CaO]=27\text{mmol/l}$. The left image shows a flowery surface. Some sticky fibrillar elements are seen on the right image (Micrographs taken by Emmanuelle Boehm-Courjault at EPFL).

The mean Ca/Si values of the samples are shown in Table 5.20. The Ca/Si increases with the lime concentration in solution. The mean Ca/Si values are higher than in the case of the use of the ultrasound gun. This agrees with the silicate structure of the samples shown by ^{29}Si NMR, since the samples fabricated with the ultrasound gun showed more intensity coming from Q^2 groups, and higher percentage of Q^2 groups is associated with lower Ca/Si ratios. The histograms of the Ca/Si EDX data are shown in Figure 5.63. They show less dispersion than those from the samples fabricated with the ultrasound gun, although they also present occasional gaps.

Table 5.20. Mean Ca/Si values (with standard deviations) of C-S-H fabricated via the controlled hydration of C_3S with the use of Xseed.

[CaO] (mmol/l)	Ca/Si	# EDX analyses
27	1.53 ± 0.12	20
28	1.62 ± 0.12	14
29	1.62 ± 0.16	29

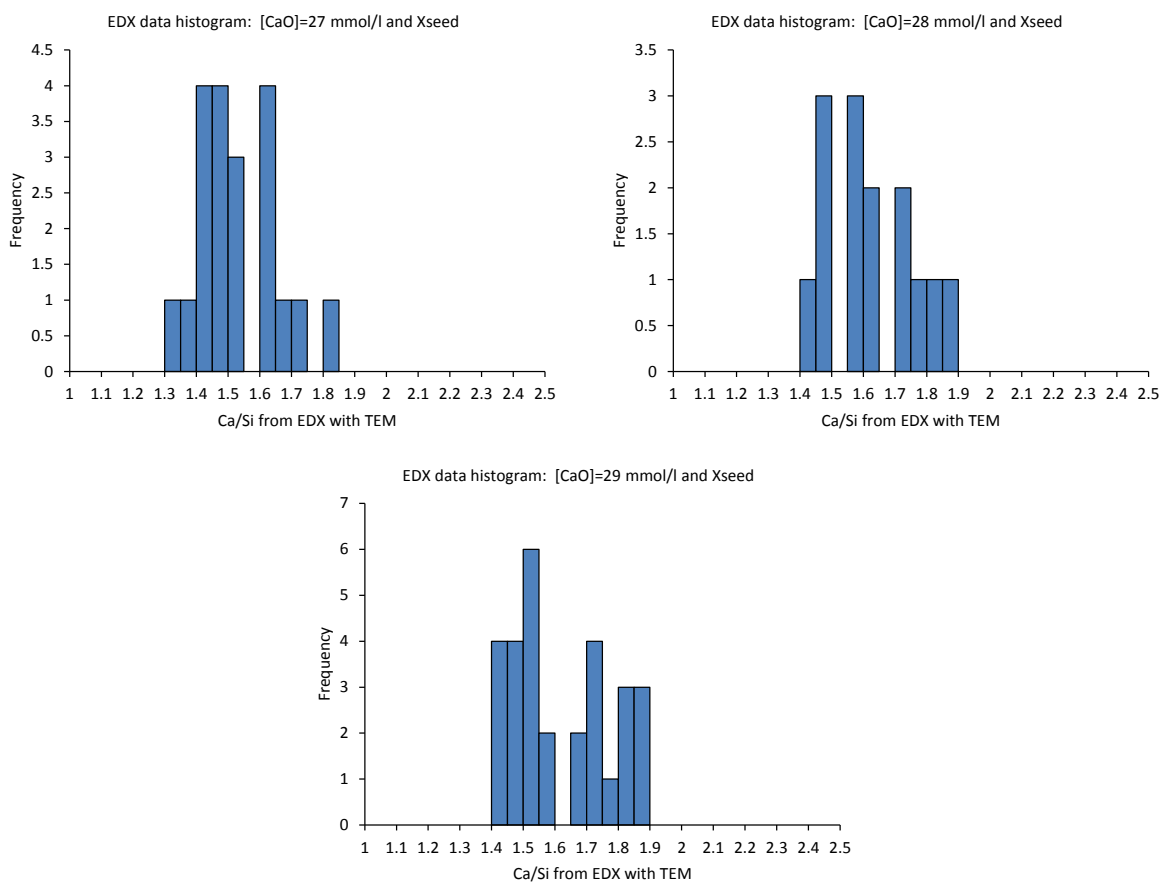


Figure 5.63. Histograms of the Ca/Si obtained with TEM-EDX of the samples hydrated at [CaO]= 27, 28 and 29mmol/l with the use of an ultrasound gun.

Richardson and Groves' model was used for charge balance calculations. The height of the histograms for Ca/Si (A bar limited by the minimum and maximum values for the obtained experimental Ca/Si) is plotted versus the reciprocal mean chain length in Figure 5.64. The trends for the tobermorite and jennite structural units with maximum, intermediate and minimum degree of protonation ($w/n=2, 1, 0$) are also plotted. The mean Ca/Si value is indicated with a cross and it is used to derive the structural chemical formulae. These mean values are situated between the tobermorite-like and jennite-like region of the plot, as it was the case for the previous batch of samples. Thus Ca-OH groups are needed in the structures.

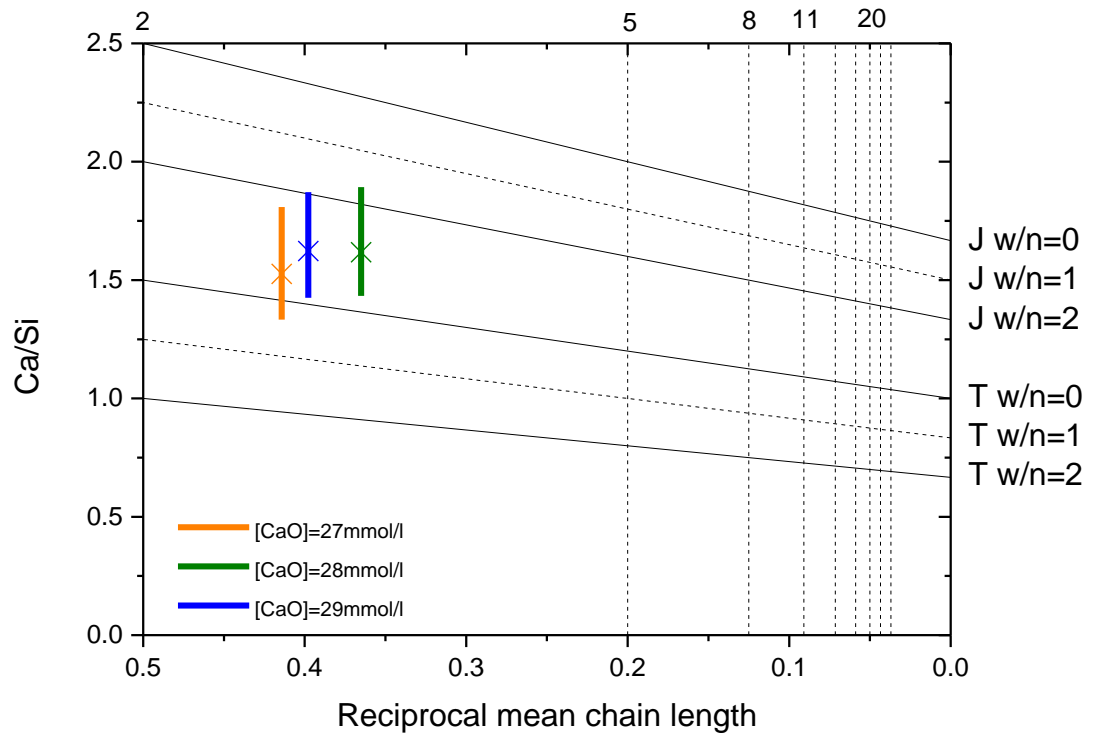
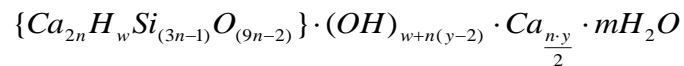


Figure 5.64. Ca/Si (obtained by TEM-EDX) vs. reciprocal mean chain length (obtained by NMR) of the C-S-H series fabricated via the controlled hydration of C_3S with the use of Xseed. The length of the bars is limited by the minimum and maximum Ca/Si and the mean value is marked with a cross. The structural units for tobermorite and jennite with minimum ($w=0$), intermediate ($w=1$) and maximum ($w=2$) degree of protonation are also marked. The vertical dashed lines represent the $(3n-1)$ structural units: dimer (2), pentamer (5), octamer (8)...

Both the T/J and T/CH view points can be used to get the structural chemical formulae, since for pure C-S-H without Al, they can equally explain the data. As in the case of the ultrasound series, the T/J view point should be more suitable since the controlled hydration of C_3S should avoid the precipitation of portlandite. An electron diffraction pattern of a selected area of the sample hydrated at $[CaO]=27\text{mmol/l}$ shows the typical halo originated by C-S-H (Figure 5.61). Although microcrystalline CH was not found by inspection of other areas of the sample, this does not exclude its presence. Both view points of the model are thus used as equally valid explanations for the structure of the samples.

The formulation for the T/J is:



In the T/J view of the model $(3n-1)=MCL$ and $Ca/Si=(4n+ny)/(6n-2)$, so that $n=(MCL+1)/3$ and $y= [(Ca/Si)(6n-2)-4n]/n$. The number of silanol groups w depends on the value of y according to:

$$0 \leq y \leq 2 \rightarrow n(2 - y) \leq w \leq 2n$$

$$2 \leq y \leq 4 \rightarrow 0 \leq w \leq 2n$$

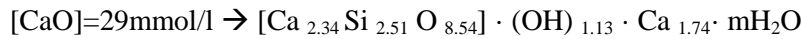
$$4 \leq y \leq 6 \rightarrow 0 \leq w \leq n(6 - y)$$

The calculated values for n , y , w_{\max} (maximum number of silanol groups), w_{\min} (minimum number of silanol groups) and w/n_{\max} (maximum degree of protonation) and w/n_{\min} (minimum degree of protonation) are shown in Table 5.21.

Table 5.21. Calculated values for the parameters of the T/J view point of Richardson and Groves' model for the C-S-H samples fabricated via the controlled hydration of C_3S with the use of Xseed.

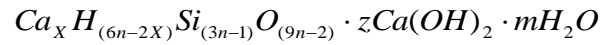
[CaO] (mmol/l)	n	y	w_{\min}	w_{\max}	w/n_{\min}	w/n_{\max}
27	1.14	2.48	0	2.28	0	2
28	1.27	3.11	0	2.49	0	2
29	1.17	2.97	0	2.34	0	2

The minimum degree of protonation was chosen, since it was the most sensible value according to the position of the mean Ca/Si with respect to the tobermorite trends in Figure 5.64. The resulting structural chemical formulae are:



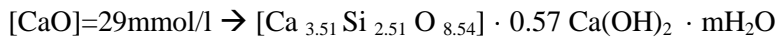
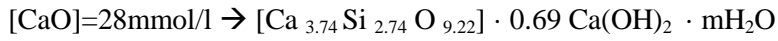
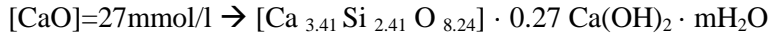
The samples can be explained by a combination of T2, T5, J2 and J5 structural units.

Alternatively, the T/CH formulation is:



$$\text{Where } X = (6n - w) / 2 \quad z = (w + n(y - 2)) / 2$$

X and Z were calculated using the values of n, y and w_{\min} in Table 5.21. The structural chemical formulae of the samples according to the T/CH view point are:



5.8 Comparison of morphology and chemical structure of C-S-H samples of the ultrasound and Xseed series

The ratio Q^2/Q^1 vs. the degree of reaction for the samples fabricated via the controlled hydration of C_3S with the use of an ultrasound gun and the Xseed is shown in Figure 5.65. As these samples have no Q^3 , their MCL is proportional to the ratio Q^2/Q^1 , so this ratio gives an indication of the extent of the reaction in terms of the MCL of the C-S-H. For similar degrees of reaction calculated through NMR, the samples synthesized with the ultrasound gun have higher Q^2/Q^1 ratios. This indicates they show a higher apparent degree of reaction than the ones fabricated with the Xseed, since they are more polymerized. The higher percentage of Q^2 silicate groups in the samples synthesized with the ultrasound gun can be due to a temperature effect. Even though the temperature was controlled with a water flow through the reaction vessel, the ultrasound pulses may have increased the temperature locally in the solution. The studies of the surface of the samples fabricated at $[CaO]=27\text{mmol/l}$ by both synthesis routes showed that the sample fabricated with the ultrasound gun had a flattened surface, while the sample fabricated with the Xseed had a very flower-like surface with more edgy features. The silicate chains must be accommodated in space; therefore it is reasonable that more end-chain silicate groups are found in a structure with edgy features than in a flattened surface, where longer chains would be accommodated. This responds to the higher MCL and Q^2 percentages found in the ultrasound samples. This could explain the differences in chemical structures that samples with similar Ca/Si can show and would mean there is a link between the chemical structure and the morphology of C-S-H.

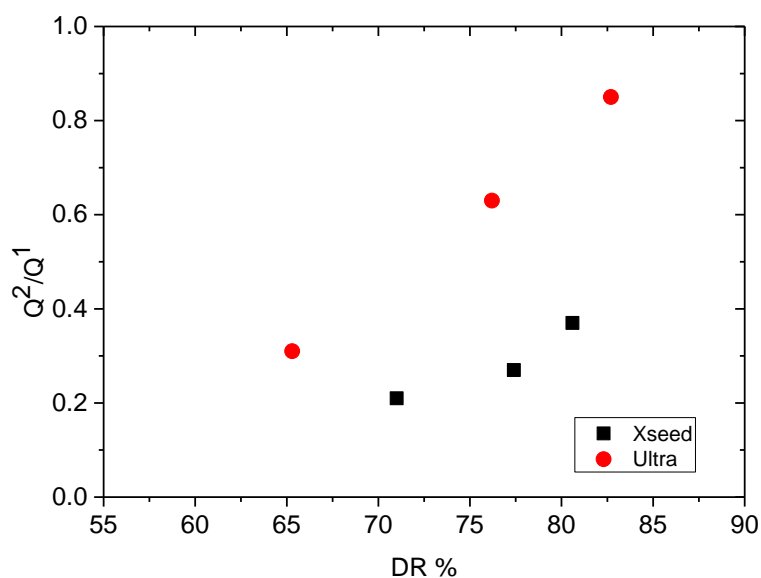


Figure 5.65. Graph showing the ratio of silicate connectivities Q^2/Q^1 vs. the degree of reaction for the C-S-H samples synthesized via the controlled hydration of C_3S with the use of an ultrasound gun (circles) and Xseed (squares).

5.9 Comparison of MCL vs. Ca/Si and Ca/Si vs. [CaO] with reported data

The MCL of all the samples discussed previously is plotted against the experimental Ca/Si ratio obtained by TEM-EDX in Figure 5.66. For the kinetics series, only the predicted values (shown in Table 5.14) are plotted. The dotted line (Also shown as a dotted line in Figure 2.9) corresponds to Eq. 2.15, which was used as a constraint to develop Richardson's C-(A)-S-H(I) model structures. The dashed lines are the tobermorite lines with minimum (right), intermediate (middle) and maximum (left) degree of protonation in Richardson and Groves' model. The inset shows the same figure at a different scale to include data from samples with higher MCL.

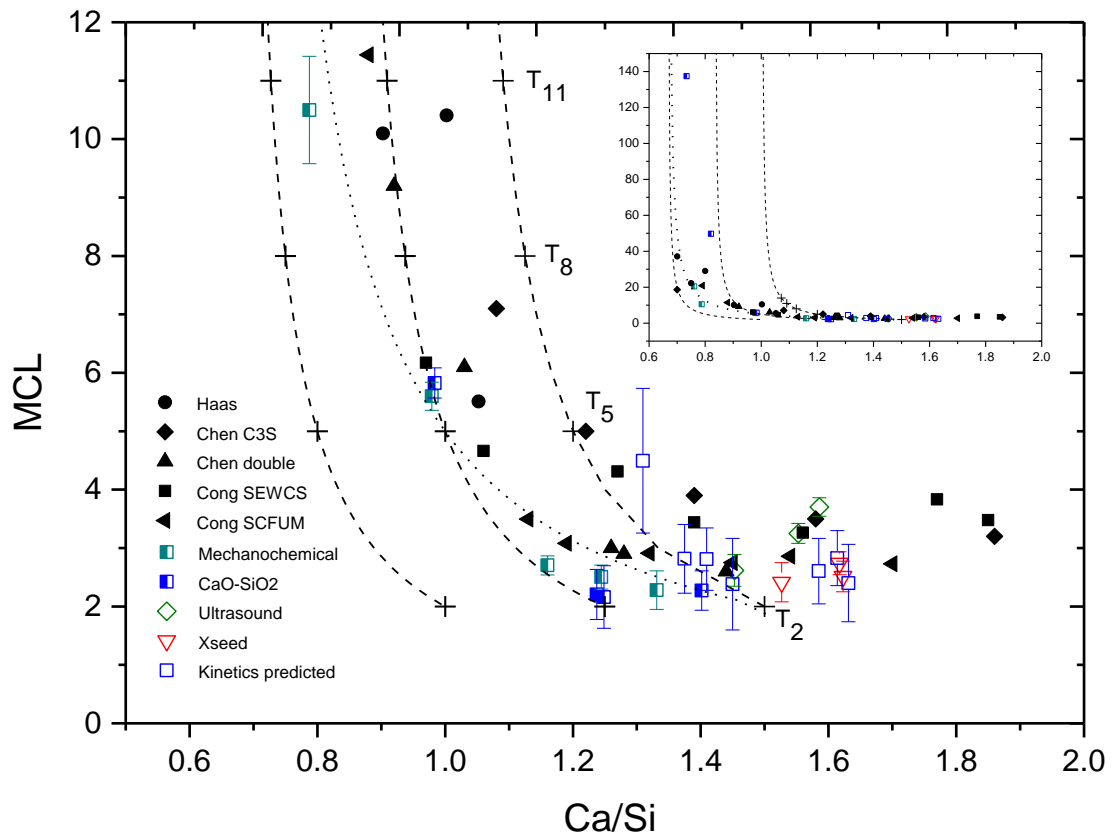


Figure 5.66. MCL vs. Ca/Si for all the C-S-H series of samples. Reported data is marked with black filled symbols and it is taken from ref. [39, 46, 93]. The dotted line represents the constraint for Richardson's C-(A)-S-H(I) model structures [36] and the dashed lines are equivalent to the tobermorite lines with minimum, intermediate and maximum degree of protonation from Richardson and Groves' model [1]. The inset shows the same plot with the y axis expanded to MCL=150.

The experimental data of MCL vs. Ca/Si ratio presented in this work are comparable to other reported data. The data for the mechanochemical samples are placed considerably close to the dotted line, suggesting the C-(A)-S-H(I) model structures by Richardson are a good representation for these samples. The data from all the samples fabricated by the controlled hydration of C₃S (kinetics, ultrasound and Xseed series) are placed to the right of the dashed line, what indicates the presence of Ca-OH groups is needed in their structures. For the kinetics series, the predicted values place the data points close to the right dashed line in the case of the samples fabricated at [CaO]<22mmol/l (4 data points at lower Ca/Si). The point for the sample at lower Ca/Si, hydrated at [CaO]=12mmol/l, may be subjected to more errors in the quantification of the MCL, as discussed previously, and the real MCL could be lower. Considering the experimental errors in the MCL, marked with vertical bars, the real data points could be placed on or below the dashed line. This would mean there is no need for Ca-OH groups in the structure of these samples that are foil-like, so that the inclusion of Ca-OH groups would coincide with the change to fibrillar morphology.

Examining both the reported and the experimental data, it can be noticed that there is a dramatic decrease of the MCL up to Ca/Si~1, followed by a slow decrease up to Ca/Si~1.3, where the MCL remains constant to a value of ~3 upon increasing Ca/Si. The reason why no further change in MCL is possible from Ca/Si~1.3 is because a dimeric silicate structure has almost been reached at this point. Variations in the structure, when the Ca/Si increases, come from the removal of bridging tetrahedra and the addition of positive ions to balance the charge (Ca and protons or either one of them). Starting from infinite silicate chains, a removal of up to half of the bridging sites will have a slight effect on the Ca/Si ratio, but change the MCL considerably. If the fraction of bridging sites removed is between half and the unity, the change in the MCL will not be significant, while the Ca/Si ratio will vary more than with the loss of up to half the bridging sites. This is clear from the values in Table 5.22 where the Ca/Si and MCL have been calculated with Eq. 2.12 and Eq. 2.14 for the case of minimum degree of protonation (i=0), intermediate degree of protonation (i=1) and maximum degree of protonation (i=2).

Table 5.22. Fraction of vacant bridging tetrahedra f_{vBT} , fraction of vacant tetrahedral sites v , and the corresponding MCL and Ca/Si ratios for minimum (i=0), intermediate (i=1) and maximum (i=2) degrees of protonation in a tobermorite-like chain.

f_{vBT}	v	MCL	$(Ca/Si)_{max} (i=0)$	$Ca/Si (i=1)$	$(Ca/Si)_{min} (i=2)$
1/5	1/15	14	1.07	0.89	0.71
1/4	1/12	11	1.09	0.91	0.73
1/3	1/9	8	1.13	0.94	0.75
1/2	1/6	5	1.20	1.00	0.80
1	1/3	2	1.50	1.25	1.00

The Ca/Si ratios of the samples fabricated via the controlled hydration of C_3S are plotted against the lime concentration in solution in Figure 5.67. The points for the ultrasound and Xseed series are close to the trend marked by the experimental data reported by Haas [93]. The predicted Ca/Si values for the kinetics series, given by Haas' thermodynamic model [93], must be a good approximation to the real values, since they are close to other experimental reported values by Nonat and Lecoq [49], Haas [93] and Taylor [4], up to lime concentrations of 22mmol/l. The sudden increase of the Ca/Si at lime concentration of 22mmol/l reported by Taylor is only evident in the data from Lecoq. The rest of the data in the plot, including the experimental data from the Xseed and ultrasound series and the calculated data from Haas' thermodynamic model, do not present this sudden change of Ca/Si at high lime concentration. The discrepancy of the data in this region suggests further investigations are needed to elucidate whether there are several equilibrium curves for Ca/Si of C-S-H at high lime concentrations.

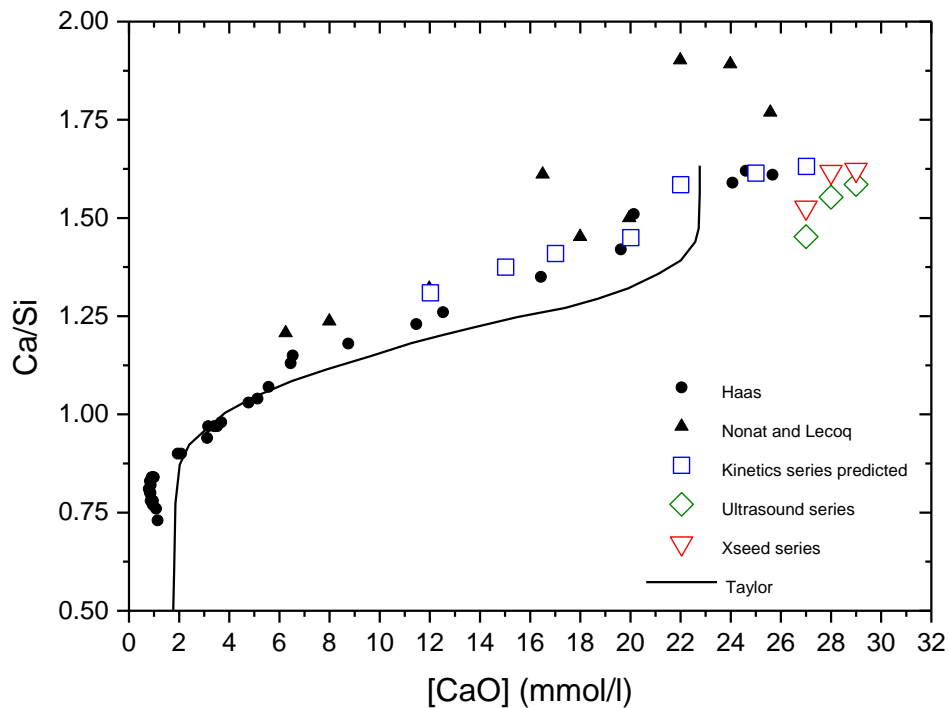


Figure 5.67. Ca/Si ratio vs. lime concentration in solution for the kinetics, ultrasound and Xseed C-S-H series (predicted Ca/Si ratios calculated with the thermodynamic model by Haas [93] for the kinetics series, and Ca/Si ratios obtained with TEM-EDX for the ultrasound and Xseed series). Other reported data by Haas [93], Nonat and Lecoq [49] and Taylor [4] are also plotted.

5.10 C-A-S-H series

The series of C-A-S-H samples with Ca/Si=1 and Al/Si from 0.01 to 0.05 was analysed by TEM. XRD and TG results of these samples were reported elsewhere and showed the samples were single-phased, and the concentration of Ca in solution in equilibrium was in between 2 and 4 mmol/l [140, 141]. The mean Ca/Si, Al/Si and Ca/(Si+Al) values obtained by TEM-EDX for these samples are shown in Table 5.23. The results match very well the bulk composition of the samples, confirming the composition of the samples is as expected. The histograms of the Ca/(Si+Al) data are shown in Figure 5.69. The histograms show that samples with target Al/Si=0.03 and 0.05 present more dispersion in the Ca/(Si+Al) ratio, as it is also indicated by the standard deviations in Table 5.23.

The morphology of the samples, shown in Figure 5.68, is crumpled foil-like for all Al/Si ratios. The fact that the samples are foil-like and the concentration of calcium in solution at equilibrium is very low, agrees with the results presented in section 5.5, where samples synthesized at lime concentrations below 22mmol/l were foil like. Hence, this level of Al substitution does not seem to markedly affect properties relative to Al-free C-S-H, although only morphology was examined here.

Table 5.23. Al/Si, Ca/Si and Ca/(Si+Al) ratios from TEM-EDX of the series of C-A-S-H samples

Bulk Al/Si	TEM-EDX Al/Si	TEM-EDX Ca/Si	TEM-EDX Ca/(Si+Al)	# EDX analyses
0	-	0.95 ± 0.05	0.95 ± 0.05	29
0.01	0.011 ± 0.002	0.96 ± 0.05	0.95 ± 0.05	30
0.02	0.021 ± 0.002	0.96 ± 0.05	0.94 ± 0.05	35
0.03	0.030 ± 0.003	1.03 ± 0.18	1.00 ± 0.05	29
0.04	0.042 ± 0.004	1.00 ± 0.06	0.96 ± 0.05	30
0.05	0.050 ± 0.005	0.95 ± 0.14	0.91 ± 0.05	28

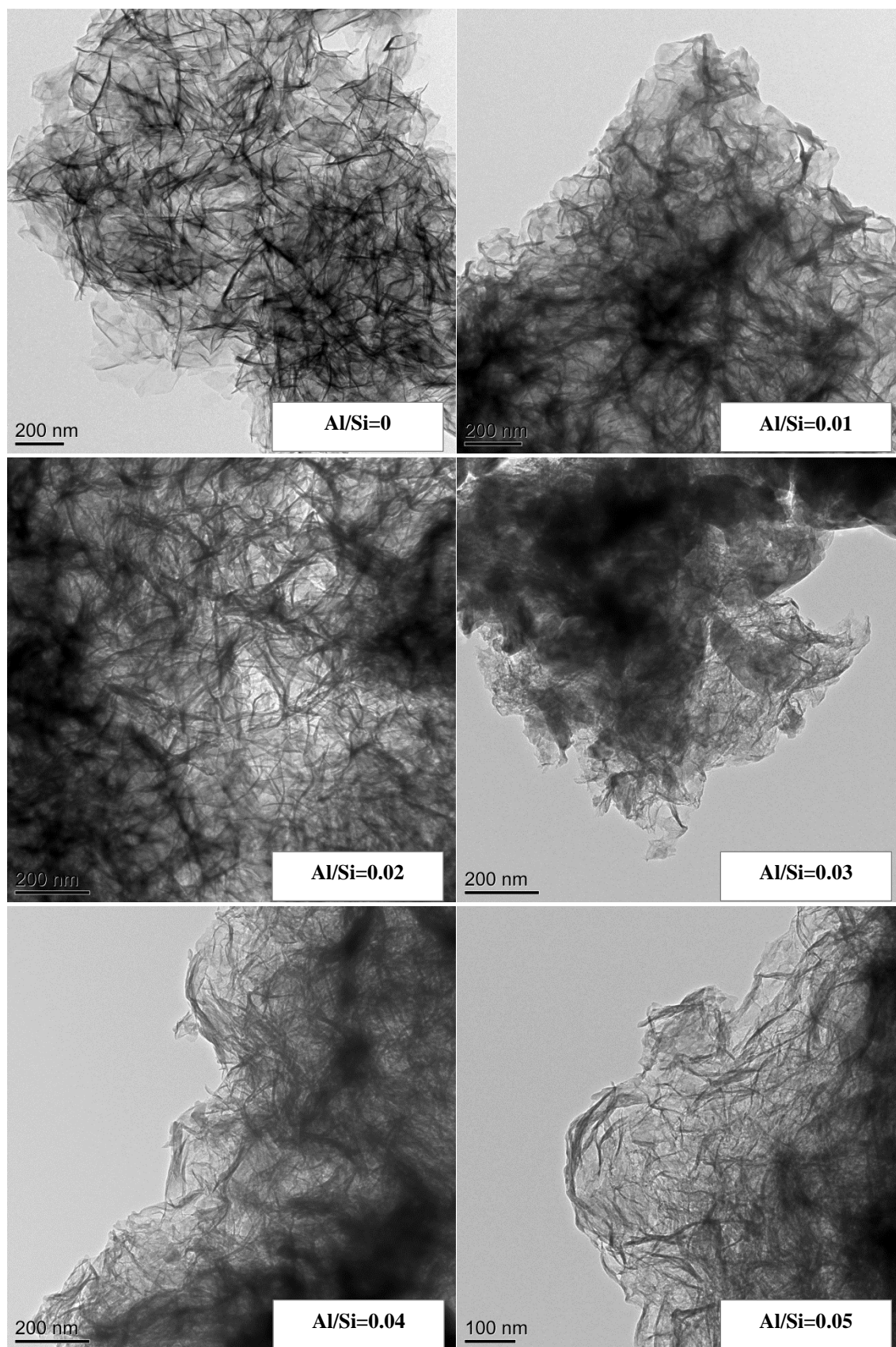


Figure 5.68. TEM micrographs of the C-A-S-H series. The Al/Si of the sample is indicated in each micrograph.

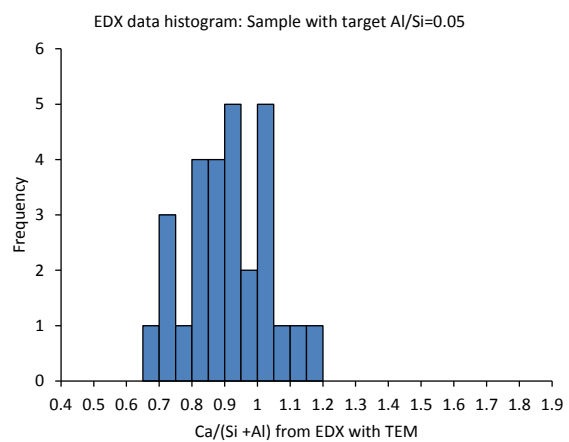
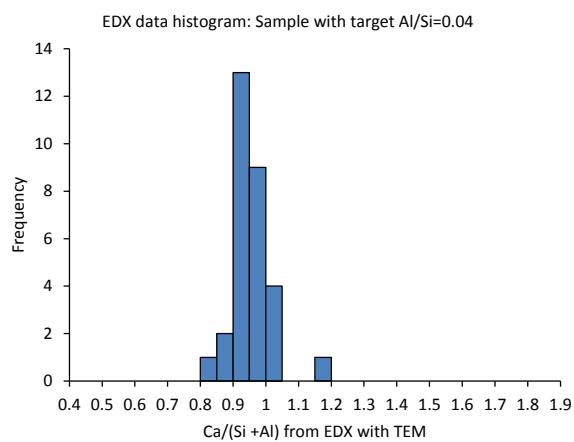
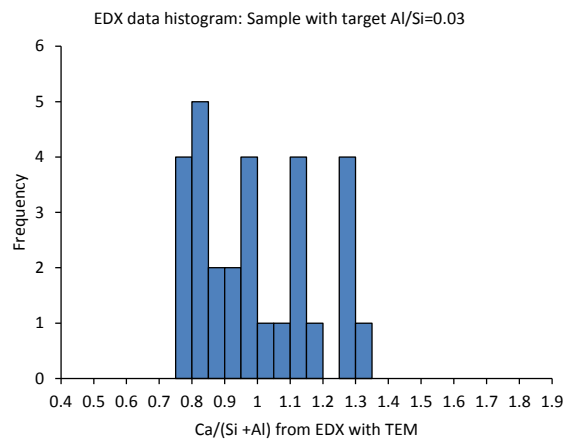
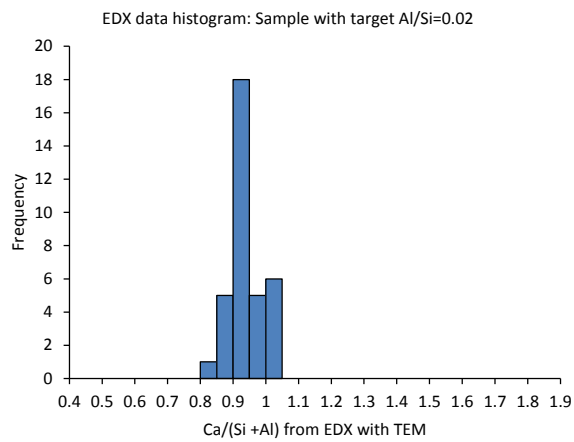
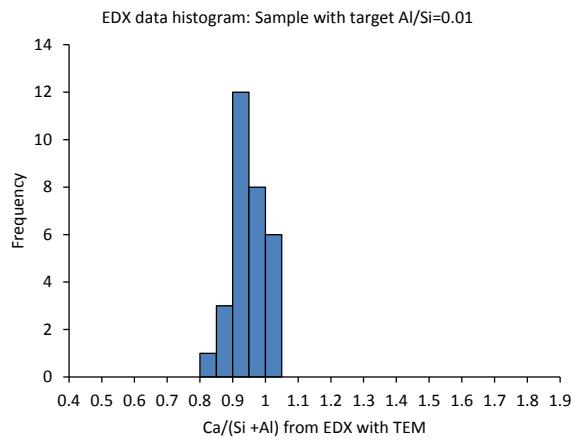
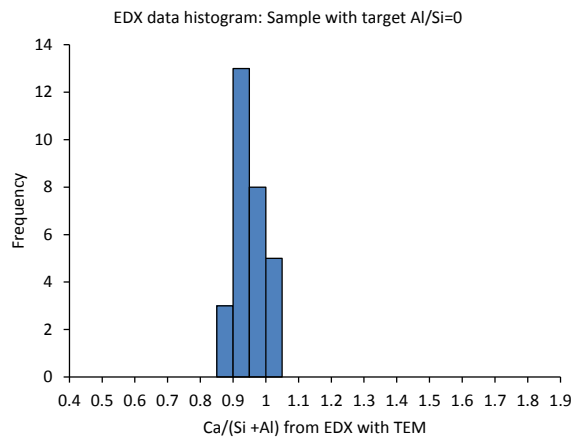


Figure 5.69. Histograms of the Ca/(Si+Al) obtained with TEM-EDX of the C-A-S-H samples.

Richardson and Groves' model was used for charge balance calculations. The height of the histograms for $\text{Ca}/(\text{Si}+\text{Al})$ (A bar limited by the minimum and maximum values for the obtained experimental $\text{Ca}/(\text{Si}+\text{Al})$ is plotted versus the reciprocal mean chain length (MCL taken from ref. [140]) in Figure 5.70. The trends for the tobermorite and jennite structural units with maximum, intermediate and minimum degree of protonation ($w/n=2, 1, 0$) are also plotted. The mean $\text{Ca}/(\text{Si}+\text{Al})$ value is indicated with a cross and it is used to derive the structural chemical formulae. These mean values are situated in the tobermorite-like region of the plot, so that the samples can be explained by a complete tobermorite-like structure without the need of Ca-OH groups coming from either jennite or CH.

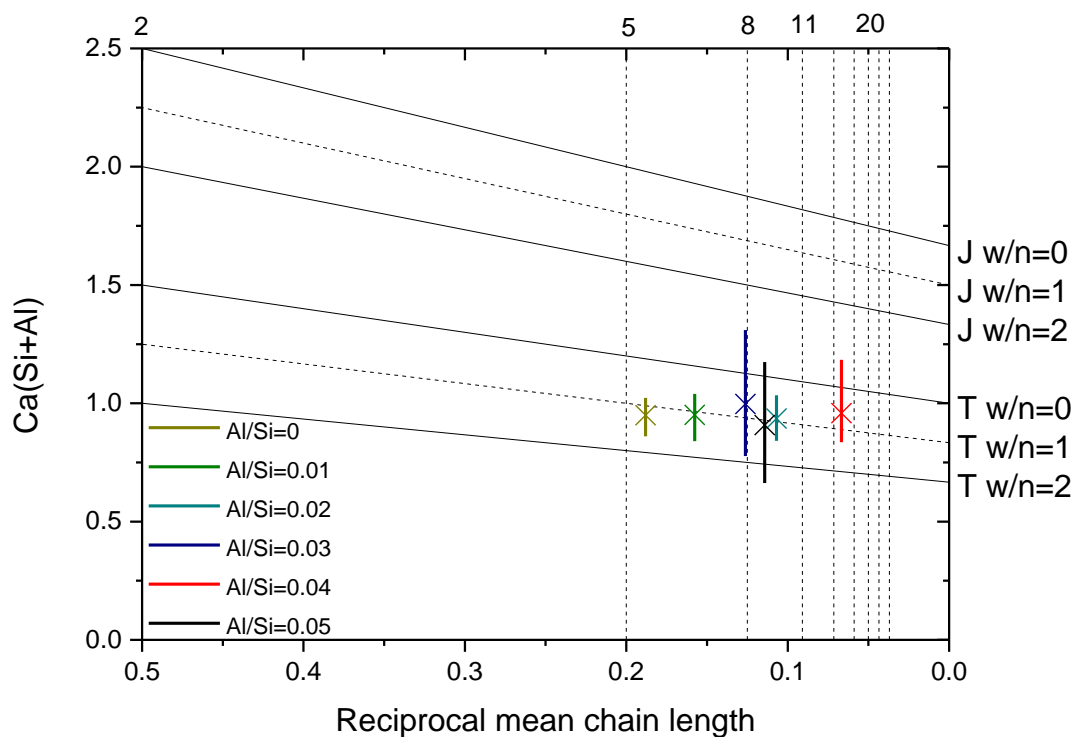
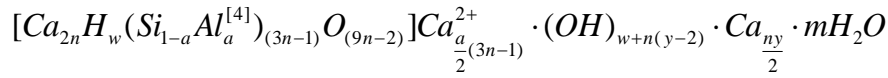


Figure 5.70. $\text{Ca}/(\text{Si}+\text{Al})$ (obtained by TEM-EDX) vs. reciprocal mean chain length (taken from ref.[140]) of the C-A-S-H series. The length of the bars is limited by the minimum and maximum $\text{Ca}/(\text{Si}+\text{Al})$ and the mean value is marked with a cross. The structural units for tobermorite and jennite with minimum ($w=0$), intermediate ($w=1$) and maximum ($w=2$) degree of protonation are also marked. The vertical dashed lines represent the $(3n-1)$ structural units: dimer (2), pentamer (5), octamer (8)...

Both T/J or T/CH view points could be used to get the structural chemical formulae. Since only tobermorite units are needed, the T/J view point is used, since it is the formulation used for all the

rest of the samples in the particular case of no Ca-OH presence. The formulation for the T/J with the incorporation of Al assuming Ca charge balancing the incorporation of Al is:



In the T/J view of the model with incorporation of trace elements $(3n-1)=MCL$, $Al/Si=a/(1-a)$ and $Ca/Si=[4n+ny+a(3n-1)]/[2(1-a)(3n-1)]$ so that $n=(MCL+1)/3$, $a=(Al/Si)/[1+(Al/Si)]$ and $y=[2Ca/Si(1-a)-4n-a(3n-1)]/n$. The number of silanol groups w depends on the value of y according to:

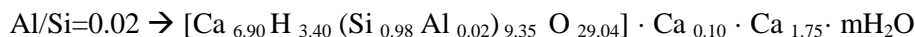
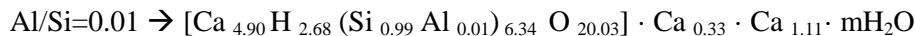
$$\begin{aligned} 0 \leq y \leq 2 &\rightarrow n(2-y) \leq w \leq 2n \\ 2 \leq y \leq 4 &\rightarrow 0 \leq w \leq 2n \\ 4 \leq y \leq 6 &\rightarrow 0 \leq w \leq n(6-y) \end{aligned}$$

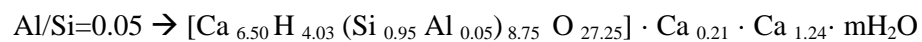
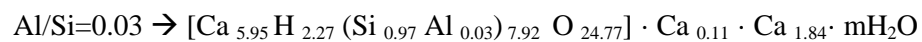
The calculated values for n , a , y , w_{\max} (maximum number of silanol groups), w_{\min} (minimum number of silanol groups) and w/n_{\max} (maximum degree of protonation) and w/n_{\min} (minimum degree of protonation) are shown in Table 5.24.

Table 5.24. Calculated values for the parameters of the T/J view point of Richardson and Groves' model for the C-A-S-H samples.

Bulk Al/Si	n	a	y	w _{min}	w _{max}	w/n _{min}	w/n _{max}
0	2.11	0	0.79	2.54	4.21	1.21	2
0.01	2.45	0.01	0.90	2.68	4.90	1.10	2
0.02	3.45	0.02	1.01	3.40	6.90	0.99	2
0.03	2.97	0.03	1.24	2.27	5.95	0.76	2
0.04	5.33	0.04	1.28	3.86	10.67	0.72	2
0.05	3.25	0.05	0.76	4.03	6.50	1.24	2

The minimum degree of protonation was chosen, since it was the most sensible value according to the position of the mean Ca/Si with respect to the tobermorite trends in Figure 5.70. The resulting structural chemical formulae are completely tobermorite-like with the tobermorite core between brackets:





The samples with Al/Si=0.01 and 0.03 can be explained as a combination of T8, T5 and T2 units. The samples with Al/Si=0.02 and 0.05 can be explained with a mixture of T11, T8, T5 and T2 units and the sample with Al/Si=0.04 can be accounted for by a combination of T17, T14, T11, T8, T5 and T2 structural units.

6 Conclusions and further work

The results presented in this thesis suggest that C-S-H morphology depends on its chemical composition and chemical silicate structure, rather than on growth kinetics.

The Ca/Si ratio of C-S-H fabricated via silica-lime reactions is limited by the precipitation of portlandite. At room temperature, the lime concentration in solution at the final equilibrium for the synthesis of these samples would not exceed the saturation value for portlandite precipitation (~22mmol/l). All samples fabricated via these reactions with bulk Ca/Si ratios from 0.75 to 1.5 were shown to be foil-like. C-A-S-H samples with Ca/Si=1 and Al/Si=0-0.05 that show concentrations of Ca in solution in equilibrium between 2 and 4mmol/l were found to be foil-like.

The morphology of C-S-H which forms during the controlled hydration of C_3S at fixed lime concentration was found to be dependent on the lime concentration in solution. Samples fabricated at lime concentrations between 12 and 20mmol/l (Ca/Si from ~1.25 to ~1.4) were foil-like, samples at lime concentrations of 22mmol/l (Ca/Si ~1.58) showed more directional growth and a mixture of foil and fibrillar morphology, and samples at lime concentrations of 25 and 27mmol/l (Ca/Si ~1.6-1.65) were found to be fibrillar, with fibrils sticking out of the C_3S grain. The morphology of the samples was found to be the same for a fixed value of lime concentration at two different stages of the hydration curve; at the acceleration period of C_3S hydration, when the C-S-H growth is fast, and at the deceleration period of C_3S hydration when the growth is slow. This suggests kinetics do not alter the C-S-H morphology, but the morphology is determined by the chemical environment in which C-S-H grows. Further work could be done in this direction introducing samples grown at low and high lime concentrations in solutions with controlled high and low lime concentrations respectively, allowing them to react further to observe if the morphology reverses. If the morphology reversed, this would be a final proof of C-S-H morphology being uniquely composition dependent. The role of kinetics could also be studied further, if accelerators and decelerators for the hydration of C_3S were used for each fixed lime concentration.

The silicate structure of the synthetic samples in this study was shown to be dependent on the Ca/Si ratio as expected. This dependence is very clear in the mechanochemical and the CaO-SiO₂ series, both fabricated via lime-silica reactions. The samples of these two series with Ca/Si<1.2 had a silicate structure with a high percentage of Q² species while the samples with Ca/Si>1.2 had a silicate structure with a high percentage of Q¹ species. When the NMR signal corresponding to C-S-H in samples fabricated via the controlled hydration of C_3S , was intense enough to be properly quantified, all samples fabricated with and without accelerators, showed

silicate structures with a high percentage of Q^1 species. Since the samples had $Ca/Si > 1.2$, the silicate structures were as expected.

Differences in the morphology of fracture surfaces and the silicate structure of C-S-H samples fabricated via the controlled hydration of C_3S at high lime concentrations of 27, 28 and 29 mmol/l with the use of different reaction accelerators were found. Samples synthesized with the use of an ultrasound gun were found to contain a higher percentage of Q^2 species, and more flattened surfaces, than samples fabricated with Xseed (a solution containing C-S-H seeds). A relationship between the silicate structure and the morphology at the surfaces of the samples was found. Samples with flattened surfaces could accommodate longer silicate chains than samples with rougher surfaces, with more features and edges, which could accommodate shorter silicate chains and show a higher percentage of Q^1 end-chain groups. Although the percentages of silicate species in C-S-H depend on the Ca/Si ratio (low Ca/Si ratio implies high percentage of Q^2 and high Ca/Si ratio implies high percentage of Q^1), inferring Ca/Si ratios from NMR spectra is a challenging work that would need a model which combined crystal-chemical structural information and morphology, since a relationship between the morphology and silicate structure was found in this study.

Although lime concentration in solution is an important parameter that determines the morphology of C-S-H, the output of this study clearly shows that every synthesis route gives a unique C-S-H product. This is due to the fact that other factors such as drying methods, the use of accelerators for the hydration of C_3S , and the addition of mechanical energy by milling, also play a role in determining the final properties of the product. Silica-lime reactions yield foil-like C-S-H with a maximum Ca/Si ratio of 1.5. The foils were coarser when the samples were fabricated via the mechanochemical method than when fabricated via continuous stirring, due to the addition of mechanical energy. The basal spacing of samples synthesized by silica-lime reactions was also proved to be dependent on the drying method, since samples that were dried by heating at 60°C showed longer basal spacings than samples that were dried under vacuum. The controlled hydration of C_3S is a better synthesis method to reproduce C-S-H in real cementitious systems than the silica-lime reaction, both in terms of C-S-H composition and morphology. Tailoring the lime concentration in solution it is possible to obtain a wider range of Ca/Si ratios that approximate better the range found in real cementitious systems. Moreover, systems grown under the controlled reaction of C_3S presented a change in morphology from foils to fibrils when the lime concentration in solution increases, and thus the Ca/Si ratio increases too. This represents very well the previously found morphological change of C-S-H in OPC-slag systems, since for higher replacement of cement with slag, the morphology changes from fibrillar to foil-like. Since slag has a higher content of SiO_2 than cement, its use must lower the calcium concentration in solution when cement hydrates, thus

promoting the formation of foils. A similar morphology can be found in fly ash blends, in which foil-like C-S-H grows from fully reacted fly ash particles that are also SiO₂ rich. Including reaction accelerators, such as an ultrasound gun and Xseed (a solution containing C-S-H seeds), during the controlled hydration C₃S at high lime concentrations of 27-29mmol/l, also produced distinct C-S-H morphologies. A mixture of foils and fibrils was found in both kinds of samples under TEM examination, with average Ca/Si ratios from ~1.45 to ~1.62. The Ca/Si ratio at which samples synthesized without accelerators showed a mixture of both kinds of morphology (Ca/Si~1.58) was included in the range of compositions of most of these samples, taking into account the standard deviations of the Ca/Si. Although both kinds of samples showed a mixture of foils and fibrils, the surfaces of the samples were much more flattened with the use of the ultrasound. This was attributed to the power of the gun that may have distorted the fibrils that should have grown at such lime concentrations. The surface of the samples fabricated with the Xseed showed a dense packing of foil-like features, which under closer examination, seemed to be not continuous. The edges of these foil-like features created the fibrillar manner in the TEM images. Thus fibrillar features in TEM do not necessarily correspond to fibrils sticking out of a grain or particle.

The application of Richardson and Groves' model to derive structural chemical formulae showed that C-S-H samples fabricated via silica-lime reactions with bulk Ca/Si from 0.7 to 1.5 and C-A-S-H samples with Ca/Si=1 and Al/Si from 0 to 0.05 can be explained entirely by tobermorite units. Since these samples are foil-like, it is reasonable to associate foil-like morphology with tobermorite-like structures. This agrees with the applicability of the model to pastes reported by Richardson [1]. The results for the samples hydrated via the controlled hydration of C₃S, with and without the use of accelerators, have shown the structures require Ca-OH groups for all the samples, regardless of their morphology. However, the samples hydrated at [CaO]<22mmol/l present data of Ca/Si against mean silicate chain length considerably close to the limit of maximum Ca/Si without the addition of Ca-OH groups. Considering the experimental errors in the mean silicate chain length, it is plausible that the real structure of these samples do not require Ca-OH groups. This would be in agreement with the fact that the samples are foil-like and would fall in the group of those that can be explained entirely by tobermorite units. The inclusion of Ca-OH groups coming from either jennite or CH units would therefore coincide with the change to fibrillar morphology.

In addition to the morphological and structural studies, the thermal analysis of C-S-H phases synthesized via silica-lime reactions, by the mechanochemical route, showed that the temperature for the transformation from β-wollastonite into α-wollastonite depended on the Ca/Si ratio of the samples. The transformation temperature was decreasing with increasing Ca/Si. Therefore an excess of SiO₂ stabilized the β-polymorph and an excess of CaO stabilized the α-

polymorph. β -wollastonite silicate structure comprises long chains while the silicate structure of α -wollastonite consists of rings of 3 silicate tetrahedra. The silicate structure of the C-S-H with high Ca/Si is mainly dimeric and these samples stabilize the α -polymorph, which has 3 silicate rings, while the silicate structure of the C-S-H with low Ca/Si has longer silicate chains and these samples stabilize the β -polymorph, which has a silicate structure of long chains. A hypothesis was made suggesting slight differences in the silicate structure of the β -polymorph that formed after heating C-S-H of different Ca/Si ratios, so that it was prone to transform into the α -polymorph at different temperatures. This would need to be further validated with a technique such as in-situ Raman spectroscopy.

The overall findings of the project are linked to the purpose of its joint collaboration TRANSCEND; which is to describe the water transport in cement and concrete. Since C-S-H defines the capillary porosity in a cementitious matrix, predicting the morphology of C-S-H should be important to model the transport of water in cementitious materials. However, up to date, there is no established link between C-S-H morphology and capillary porosity. This knowledge gap should be filled in order to further understand and model how the morphology of C-S-H may affect mechanical properties, such as strength. A combination of microscopy and relaxation ^1H NMR may be the tool to achieve such goal, since the last technique can distinguish interlayer, gel pore and capillary water populations in cement. Relaxation ^1H NMR was applied successfully to white cements with and without silica fume in the joint collaboration, and the standardization of this technique is being developed as a follow up project by one of the Fellows.

In terms of aiding simulations of water dynamics in cementitious materials, the findings of this project can serve to modify the tendency to use the well-known tobermorite 11Å and 14Å structures to simulate water dynamics in C-S-H. The project has shown feasible crystal chemical formulae for C-S-H of various compositions. For simplicity reasons, the structures of tobermorite minerals are those employed as a starting point in most simulations that deal with C-S-H, but the cement community has other structures available, such as the structures given by the model of Richardson and Groves, that should be further explored. The morphological studies performed in this project served also as a reference for simulations of the growth of C-S-H in spherical confinements that was commented in the literature review, and were central for a project within the joint collaboration.

References

1. Richardson, I.G., *Tobermorite/jennite- and tobermorite/calcium hydroxide-based models for the structure of C-S-H: applicability to hardened pastes of tricalcium silicate, beta-dicalcium silicate, Portland cement, and blends of Portland cement with blast-fumace slag, metakaolin, or silica fume*. Cement and Concrete Research, 2004. **34**(9): p. 1733-1777.
2. *TRANSCEND Marie Curie Training Course 1: Introduction and Initiation to cementitious materials*, Maastricht, February 2011.
3. Bye, G.C., *Portland cement : composition, production and properties*. 2nd ed. 1999, London: Thomas Telford.
4. Taylor, H.F.W., *Cement chemistry*. 2nd ed. 1997, London: Thomas Telford.
5. Bigare, M., et al., *Polimorphism of tricalcium silicate and its solid solutions*. Journal of the American Ceramic Society, 1967. **50**(11): p. 609-619.
6. Maki, I. and S. Chromy, *Microscopic study on polymorphism of Ca_3SiO_5* . Cement and Concrete Research, 1978. **8**(4): p. 407-414.
7. Bensted, J., *Gamma-dicalcium silicate and its hydraulicity*. Cement and Concrete Research, 1978. **8**(1): p. 73-76.
8. Nurse, R.W., *The effect of phosphate on the constitution and hardening of Portland cement*. Journal of Applied Chemistry, 1952. **2**(12): p. 708-716.
9. Takeuchi, Y., F. Nishi, and I. Maki, *Crystal-chemical characterization of the $3CaO.Al_2O_3-Na_2O$ solid-solution series*. Zeitschrift Fur Kristallographie, 1980. **152**(3-4): p. 259-307.
10. Aggarwal, P.S., et al., *Synthesis and properties of dicalcium aluminate $2CaO.Al_2O_3$* . Cement and Concrete Research. **2**(3): p. 291-297.
11. Groves, G.W., *Microcrystalline calcium hydroxide in Portland-cement pastes of low water-cement ratio*. Cement and Concrete Research, 1981. **11**(5-6): p. 713-718.
12. Groves, G.W., P.J. Lesueur, and W. Sinclair, *Transmission electron-microscopy and microanalytical studies of ion-beam-thinned sections of tricalcium silicate paste*. Journal of the American Ceramic Society, 1986. **69**(4): p. 353-356.
13. Richardson, I.G. and G.W. Groves, *Microstructure and microanalysis of hardened ordinary Portland-cement pastes*. Journal of Materials Science, 1993. **28**(1): p. 265-277.
14. Mohan, K. and H.F.W. Taylor, *A trimethylsilylation study of tricalcium silicate pastes*. Cement and Concrete Research, 1982. **12**(1): p. 25-31.
15. Lippmaa, E., et al., *A high-resolution Si-29 NMR-study of the hydration of tricalcium-silicate*. Cement and Concrete Research, 1982. **12**(5): p. 597-602.
16. Brough, A.R., et al., *In-situ solid-state NMR-studies of Ca_3SiO_5 -hydration at room-temperature and at elevated-temperatures using Si-29 enrichment*. Journal of Materials Science, 1994. **29**(15): p. 3926-3940.
17. Rodger, S.A., et al. *A study of tricalcium silicate hydration from very early to very late stages*. in *Mat. Res. Soc. Symp. Proc.* 85. 1987.
18. Chen, J.J., *PhD Thesis*, 2003, Northwestern University.
19. Scrivener, K.L. and P.L. Pratt, *Microstructural studies of the hydration of C_3S and C_4AF independently and in cement paste*. Proc. Br. Ceram. Soc, 1984. **35**: p. 207.
20. Rashid, S., X. Turrillas, and P. Barnes. *Dynamic studies on the reactions of calcium aluminate cements with sulphate solutions monitored by synchrotron radiation energy-dispersive diffraction in 4th European Powder Diffraction Conference (EPDIC IV)*. 1996. Chester, England.
21. Scrivener, K.L., *The microstructure of concrete*, in *Materials Science of concrete*, J.P. Skalny, Editor. 1989, American Ceramic Society. p. 127-161.
22. Scrivener, K.L., *PhD thesis*, 1984, University of London.
23. *PCA Manual, Chapter 3: Fly ash, Slag, Silica Fume and Natural Pozzolans*. Available from: http://www.ce.memphis.edu/1101/notes/concrete/PCA_manual/Chap03.pdf.

24. Thomas, J.J., H.M. Jennings, and A.J. Allen, *Relationships between Composition and Density of Tobermorite, Jennite, and Nanoscale CaO-SiO₂-H₂O*. Journal of Physical Chemistry C, 2010. **114**(17): p. 7594-7601.
25. Bonaccorsi, E., S. Merlino, and A.R. Kampf, *The crystal structure of tobermorite 14 Å (Plombierite), a C-S-H phase*. Journal of the American Ceramic Society, 2005. **88**(3): p. 505-512.
26. Bonaccorsi, E., S. Merlino, and H.F.W. Taylor, *The crystal structure of jennite, Ca₉Si₆O₁₈(OH)₆•8H₂O*. Cement and Concrete Research, 2004. **34**(9): p. 1481-1488.
27. Taylor, H.F.W., *Hydrated Calcium Silicates. Part I. Compound Formation at Ordinary Temperatures*. Journal of the Chemical Society, 1950: p. 3682-3690.
28. Gard, J.A. and H.F.W. Taylor, *Calcium silicate hydrate II ("C-S-H (II))"*. Cement and Concrete Research, 1976. **6**(5): p. 667-677.
29. Seryotkin, Y.V., E.V. Sokol, and S.N. Kokh, *Natural pseudowollastonite: Crystal structure, associated minerals, and geological context*. Lithos, 2012. **134-135**(0): p. 75-90.
30. Henmi, C., et al., *The 3T-polytype, 4T-polytype and 5T-Polytype of wollastonite from Kushiro, Hiroshima prefecture, Japan*. American Mineralogist, 1983. **68**(1-2): p. 156-163.
31. Mazzucato, E. and A.F. Gualtieri, *Wollastonite polytypes in the CaO-SiO₂ system. Part I. Crystallisation kinetics*. Physics and Chemistry of Minerals, 2000. **27**(8): p. 565-574.
32. Richardson, I.G., *The nature of C-S-H in hardened cements*. Cement and Concrete Research, 1999. **29**(8): p. 1131-1147.
33. Taylor, H.F.W., *Proposed structure for calcium silicate hydrate gel*. Journal of the American Ceramic Society, 1986. **69**(6): p. 464-467.
34. Richardson, I.G. and G.W. Groves, *Models for the composition and structure of calcium silicate hydrate (C-S-H) gel in hardened tricalcium silicate pastes*. Cement and Concrete Research, 1992. **22**(6): p. 1001-1010.
35. Richardson, I.G. and G.W. Groves, *The incorporation of minor and trace-elements into calcium silicate hydrate (C-S-H) gel in hardened cement pastes*. Cement and Concrete Research, 1993. **23**(1): p. 131-138.
36. Richardson, I.G., *Model Structures for C-(A)-S-H(I)*. Acta Crystallographica Section B-Structural Science, 2014. **70**: p. 903-923.
37. Matsuyama, H. and J.F. Young, *Intercalation of polymers in calcium silicate hydrate: A new synthetic approach to biocomposites?* Chemistry of Materials, 1999. **11**(1): p. 16-19.
38. Matsuyama, H. and J.F. Young, *Effects of pH on precipitation of quasi-crystalline calcium silicate hydrate in aqueous solution*. Advances in Cement Research, 2000. **12**(1): p. 29-33.
39. Cong, X. and R.J. Kirkpatrick, *²⁹Si NMR study of the structure of calcium silicate hydrate*. Advanced Cement Based Materials, 1996. **3**(3:4): p. 144-156.
40. Garbev, K., et al., *Cell dimensions and composition of nanocrystalline calcium silicate hydrate solid solutions. Part I: Synchrotron-based x-ray diffraction*. Journal of the American Ceramic Society, 2008. **91**(9): p. 3005-3014.
41. Black, L., K. Garbev, and I. Gee, *Surface carbonation of synthetic C-S-H samples: A comparison between fresh and aged C-S-H using X-ray photoelectron spectroscopy*. Cement and Concrete Research, 2008. **38**(6): p. 745-750.
42. Grudemo, A., *An electronographic study of the morphology and crystallization properties of calcium silicate hydrates*. Proc.– Swedish Cem. Conc. Res. Inst. Royal Inst. Technol., Stockholm, (Handlinger–Svenska Forskningsinstitutet för Cement Och Betong vid Kungliga Tekniska Högskolan i Stockholm), 1955. **26**: p. 1-103.
43. Renaudin, G., et al., *Structural characterization of C-S-H and C-A-S-H samples-Part I: Long-range order investigated by Rietveld analyses*. Journal of Solid State Chemistry, 2009. **182**(12): p. 3312-3319.
44. Taylor, H.F.W. and J.W. Howison, *Relationships between calcium silicates and clay minerals*. Clay Mineral Bulletin, 1956. **3**: p. 98-111.
45. Taylor, H.F.W., *Hydrated Calcium Silicates .5. The water content of calcium silicate hydrate(I)*. Journal of the Chemical Society, 1953(JAN): p. 163-171.

46. Chen, J.J., et al., *Solubility and structure of calcium silicate hydrate*. Cement and Concrete Research, 2004. **34**(9): p. 1499-1519.
47. Damidot, D., et al., *C₃S hydration in diluted and stirred suspensions: (III) NMR study of C-S-H precipitated during the two kinetic steps*. Advances in Cement Research, 1995. **7**(1): p. 1-8.
48. Grutzeck, M., A. Benesi, and B. Fanning, *Silicon-29 magic spinning nuclear magnetic resonance study of calcium silicate hydrates*. Journal of the American Ceramic Society, 1989. **72**(4): p. 665-668.
49. Nonat, A. and X. Lecoq, *The Structure, Stoichiometry and Properties of C-S-H Prepared by C₃S Hydration Under Controlled Conditions*, in *NMR Spectroscopy of Cement Based Materials*, Springer-Verlag, Editor. 1998. p. 197-207.
50. Brunet, F., et al., *Application of Si-29 homonuclear and H-1-Si-29 heteronuclear NMR correlation to structural studies of calcium silicate hydrates*. Journal of Physical Chemistry B, 2004. **108**(40): p. 15494-15502.
51. García-Lodeiro, I., et al., *C-S-H Gels: Interpretation of 29Si MAS-NMR Spectra*. Journal of the American Ceramic Society, 2012. **95**(4): p. 1440-1446.
52. Pellenq, R.J.M., et al., *A realistic molecular model of cement hydrates*. Proceedings of the National Academy of Sciences of the United States of America, 2009. **106**(38): p. 16102-16107.
53. Allen, A.J., J.J. Thomas, and H.M. Jennings, *Composition and density of nanoscale calcium-silicate-hydrate in cement*. Nature Materials, 2007. **6**(4): p. 311-316.
54. Richardson, I.G., *The importance of proper crystal-chemical and geometrical reasoning demonstrated using layered single and double hydroxides*. Acta Crystallographica Section B-Structural Science, 2013. **69**: p. 150-162.
55. Powers, T.C., *Structure and physical properties of hardened Portland cement paste*. Journal of the American Ceramic Society, 1958. **41**(1): p. 1-6.
56. Feldman, R.F. and P.J. Sereda, *A new model for hydrated portland cement and its practical implications*. Engineering Journal, 1970. **53**: p. 53-59.
57. Jennings, H.M., *Colloid model of C-S-H and implications to the problem of creep and shrinkage*. Materials and Structures, 2004. **37**(265): p. 59-70.
58. Jennings, H.M., *Refinements to colloid model of C-S-H in cement: CM-II*. Cement and Concrete Research, 2008. **38**(3): p. 275-289.
59. Etzold, M.A., P.J. McDonald, and A.F. Routh, *Growth of sheets in 3D confinements - a model for the C-S-H meso structure*. Cement and Concrete Research, 2014. **63**: p. 137-142.
60. Muller, A.C.A., et al., *Densification of C-S-H Measured by H-1 NMR Relaxometry*. Journal of Physical Chemistry C, 2013. **117**(1): p. 403-412.
61. Kalousek, G.L. and A.F. Prebus, *Crystal chemistry of hydrous calcium silicates: III, Morphology and other properties of tobermorite and related phases*. Journal of the American Ceramic Society, 1958. **41**(4): p. 124-132.
62. Collepardi, M. and B. Marchese, *Morphology and surface properties of hydrated tricalcium silicate pastes*. Cement and Concrete Research, 1972. **2**(1): p. 57-65.
63. Berger, R.L., J.F. Young, and F.V. Lawrence, *Discussion of the paper "Morphology and surface properties of hydrated tricalcium silicate paste" by M. Collepardi and B. Marchese*. Cement and Concrete Research, 1972. **2**(5): p. 633-636.
64. Jennings, H.M., B.J. Dalglish, and P.L. Pratt, *Morphological development of hydrating tricalcium silicate as examined by electron-microscopy techniques*. Journal of the American Ceramic Society, 1981. **64**(10): p. 567-572.
65. Girao, A.V., et al., *Composition, morphology and nanostructure of C-S-H in 70% white Portland cement-30% fly ash blends hydrated at 55 degrees C*. Cement and Concrete Research, 2010. **40**(9): p. 1350-1359.
66. Taylor, R., I.G. Richardson, and R.M.D. Brydson, *Nature of C-S-H in 20 year old neat ordinary Portland cement and 10% Portland cement-90% ground granulated blast furnace slag pastes*. Advances in Applied Ceramics, 2007. **106**(6): p. 294-301.

67. Richardson, I.G. and G.W. Groves, *The structure of the calcium silicate hydrate phases present in hardened pastes of white Portland cement blast-furnace slag blends*. Journal of Materials Science, 1997. **32**(18): p. 4793-4802.
68. Garbev, K., et al., *Structural features of C-S-H(I) and its carbonation in air - A Raman spectroscopic study. Part I: Fresh phases*. Journal of the American Ceramic Society, 2007. **90**(3): p. 900-907.
69. Allen, A.J., et al., *Development of the fine porosity and gel structure of hydrating cement systems*. Philosophical Magazine B-Physics of Condensed Matter, Statistical Mechanics, Electronic, Optical and Magnetic Properties, 1987. **56**(3): p. 263-288.
70. Thomas, J.J., H.M. Jennings, and A.J. Allen, *Determination of the neutron scattering contrast of hydrated Portland cement paste using H₂O/D₂O exchange*. Advanced Cement Based Materials, 1998. **7**(3-4): p. 119-122.
71. Thomas, J.J., H.M. Jennings, and A.J. Allen, *The surface area of cement paste as measured by neutron scattering: Evidence for two C-S-H morphologies*. Cement and Concrete Research, 1998. **28**(6): p. 897-905.
72. Thomas, J.J. and H.M. Jennings, *Effects of D₂O and mixing on the early hydration kinetics of tricalcium silicate*. Chemistry of Materials, 1999. **11**(7): p. 1907-1914.
73. Thomas, J.J., H.M. Jennings, and A.J. Allen, *The surface area of hardened cement paste as measured by various techniques*. Concrete Science and Engineering, 1999. **1**: p. 45-64.
74. Allen, A.J., *Time-resolved phenomena in cements, clays and porous rocks*. Journal of Applied Crystallography, 1991. **24**: p. 624-634.
75. Thomas, J.J., et al., *Effects of decalcification on the microstructure and surface area of cement and tricalcium silicate pastes*. Cement and Concrete Research, 2004. **34**(12): p. 2297-2307.
76. Allen, A.J. and J.J. Thomas, *Analysis of C-S-H gel and cement paste by small-angle neutron scattering*. Cement and Concrete Research, 2007. **37**(3): p. 319-324.
77. Allen, A.J. and R.A. Livingston, *Relationship between differences in silica fume additives and fine-scale microstructural evolution in cement based materials*. Advanced Cement Based Materials, 1998. **8**(3-4): p. 118-131.
78. Sen, D., S. Mazumder, and S. Tarafdar, *Pore morphology and pore surface roughening in rocks: a small-angle neutron scattering investigation*. Journal of Materials Science, 2002. **37**(5): p. 941-947.
79. Häussler, F., S. Palzer, and A. Eckart, *Nondestructive microstructural investigations on hydrating cement paste and tricalcium silicate by small angle neutron scattering*, in *F. Leipzig Annual Civil Engineering Report*1999. p. 47-64.
80. Häussler, F., S. Palzer, and A. Eckart, *Nanostructural investigations on carbonation of hydrating tricalcium silicate by small angle neutron scattering*, in *F. Leipzig Annual Civil Engineering Report*2000. p. 181-194.
81. Tritthart, J. and F. Haussler, *Pore solution analysis of cement pastes and nanostructural investigations of hydrated C₃S*. Cement and Concrete Research, 2003. **33**(7): p. 1063-1070.
82. Thomas, J.J., A.J. Allen, and H.M. Jennings, *Structural Changes to the Calcium-Silicate-Hydrate Gel Phase of Hydrated Cement with Age, Drying, and Resaturation*. Journal of the American Ceramic Society, 2008. **91**(10): p. 3362-3369.
83. Fratini, E., et al., *Hydration water and microstructure in calcium silicate and aluminate hydrates*. Journal of Physics-Condensed Matter, 2006. **18**(36): p. S2467-S2483.
84. Chiang, W.S., et al., *Microstructure Determination of Calcium-Silicate-Hydrate Globules by Small-Angle Neutron Scattering*. Journal of Physical Chemistry C, 2012. **116**(8): p. 5055-5061.
85. Chiang, W.S., et al., *Microstructural changes of globules in calcium-silicate-hydrate gels with and without additives determined by small-angle neutron and X-ray scattering*. Journal of Colloid and Interface Science, 2013. **398**: p. 67-73.

86. Cong, X.D. and R.J. Kirkpatrick, *O-17 and Si-29 MAS NMR study of beta-C₂S hydration and the structure of calcium-silicate hydrates*. Cement and Concrete Research, 1993. **23**(5): p. 1065-1077.
87. Mitsuda, T., S. Kobayakawa, and H. Toraya. *Characterization of hydrothermally formed C-S-H*. in *Proc. Int. Symp. Chem. Cem.*, 8th, 3. 1986.
88. Shaw, S., S.M. Clark, and C.M.B. Henderson, *Hydrothermal formation of the calcium silicate hydrates, tobermorite (Ca₅Si₆O₁₆(OH)₂•4H₂O) and xonotlite (Ca₆Si₆O₁₇(OH)₂): an in situ synchrotron study*. Chemical Geology, 2000. **167**(1-2): p. 129-140.
89. Garbev, K., *PhD Thesis*, 2004, Forschungszentrum Karlsruhe.
90. Saito, F., G.M. Mi, and M. Hanada, *Mechanochemical synthesis of hydrated calcium silicates by room temperature grinding*. Solid State Ionics, 1997. **101**: p. 37-43.
91. Garrault, S., T. Behr, and A. Nonat, *Formation of the C-S-H layer during early hydration of tricalcium silicate grains with different sizes*. Journal of Physical Chemistry B, 2006. **110**(1): p. 270-275.
92. Steinoor, H.H. *C-S-H stability and pore solution chemistry*. in *3rd ISCC*. 1954.
93. Haas, J. and A. Nonat, *From C-S-H to C-A-S-H: Experimental study and thermodynamic modelling*. Cement and Concrete Research, 2015. **68**(0): p. 124-138.
94. Haas, J., *Etude expérimentale et modélisation thermodynamique du système CaO-SiO₂-(Al₂O₃)-H₂O (Thesis)*, 2012, University of Bourgogne, Dijon.
95. Black, L., et al., *X-ray photoelectron spectroscopy of aluminium-substituted tobermorite*. Cement and Concrete Research, 2005. **35**(1): p. 51-55.
96. Pardal, X., I. Pochard, and A. Nonat, *Experimental study of Si-Al substitution in calcium-silicate-hydrate (C-S-H) prepared under equilibrium conditions*. Cement and Concrete Research, 2009. **39**(8): p. 637-643.
97. Ramachandran, V.S. and J.J. Beaudoin, *Handbook of Analytical Techniques in Concrete Science and Technology. Principles, Techniques and Applications*. 2001, Park Ridge, New Jersey, U.S.A.: Noyes Publications.
98. Girao, A.V., *PhD Thesis*, 2007, University of Leeds.
99. Rietveld, H.M., *The Rietveld method*. Physica Scripta, 2014. **89**(9).
100. Cullity, B.D. and S.R. Stock, *Elements of X-ray diffraction*. 3rd ed. 2001, London: Prentice-Hall International.
101. Jenkins, R., *X-Ray fluorescence spectrometry*. Vol. 99. 1988, Chichester; New York: Wiley.
102. Lachance, G.R. and F. Claisse, *Quantitative X-ray fluorescence analysis: theory and application*. 1995, Chichester: Wiley.
103. Richardson, I.G., *Electron microscopy of cements*, in *Structure and Performance of Cements*, P.a.B. Barnes, J., Editor. 2002, Spon Press: London. p. 500-556.
104. Tajuelo, E., *Master's Thesis: Growth at cryogenic temperatures and structural characterization of Cr/Sc multilayer X-ray mirrors.*, in *Department of Physics, Chemistry and Biology*. 2010, Linköpings University.
105. Williams, D.B. and C.B. Carter, *Transmission Electron Microscopy. A text book for Materials Science*. 1996, New York: London: Plenum Press.
106. Lippmaa, E., et al., *Structural studies of silicates by solid-state high-resolution Si-29 NMR*. Journal of the American Chemical Society, 1980. **102**(15): p. 4889-4893.
107. Rodger, S.A., et al., *Hydration of tricalcium silicate followed by Si-29 NMR with cross-polarization*. Journal of the American Ceramic Society, 1988. **71**(2): p. 91-96.
108. Bellmann, F., et al., *Improved evidence for the existence of an intermediate phase during hydration of tricalcium silicate*. Cement and Concrete Research, 2010. **40**(6): p. 875-884.
109. Magi, M., et al., *Solid-State High-Resolution Silicon-29 chemical shifts in silicates*. journal of Physical Chemistry 1984. **88**: p. 1518-1522.
110. Love, C.A., I.G. Richardson, and A.R. Brough, *Composition and structure of C-S-H in white Portland cement-20% metakaolin pastes hydrated at 25 degrees C*. Cement and Concrete Research, 2007. **37**(2): p. 109-117.

111. Thomas, S., et al., *MAS NMR-studies of partially carbonated Portland-cement and tricalcium pastes*. Journal of the American Ceramic Society, 1993. **76**(8): p. 1998-2004.
112. Tong, Y., H. Du, and L. Fei, *Comparison between the hydration processes of tricalcium silicate and beta-dicalcium silicate*. Cement and Concrete Research, 1991. **21**(4): p. 509-514.
113. Cong, X.K., R. J., *¹H-²⁹Si CPMAS NMR study of the structure of calcium silicate hydrate*. Advances in Cement Research, 1995. **7**(27): p. 103-111.
114. Skibsted, J., H.J. Jakobsen, and C. Hall, *Direct observation of aluminium guest ions in the silicate phases of cement minerals by Al-27 MAS NMR-Spectroscopy*. Journal of the Chemical Society-Faraday Transactions, 1994. **90**(14): p. 2095-2098.
115. Cong, X. and R.J. Kirkpatrick, *¹⁷O MAS NMR Investigation of the structure of calcium silicate hydrate gel*. Journal of the American Ceramic Society, 1996. **79**: p. 1585-1592.
116. Greener, J., et al., *Monitoring of Hydration of White Cement Paste with Proton NMR Spin-Spin Relaxation*. Journal of the American Ceramic Society, 2000. **83**: p. 623-627.
117. McDonald, P.J., et al., *Surface relaxation and chemical exchange in hydrating cement pastes: A two-dimensional NMR relaxation study*. Physical Review E, 2005. **72**((1)): p. 011409.
118. Dorazio, F., et al., *Molecular-diffusion and NMR relaxation of water in unsaturated porous silica glass*. Physical Review B, 1990. **42**(16): p. 9810-9818.
119. Halperin, W.P., J.-Y. Jehng, and Y.-Q. Song, *Application of spin-spin relaxation to measurement of surface area and pore size distributions in a hydrating cement paste*. Magnetic Resonance Imaging, 1994. **12**(2): p. 169-173.
120. Muller, A.C.A., et al., *Use of bench-top NMR to measure the density, composition and desorption isotherm of C-S-H in cement paste*. Microporous and Mesoporous Materials, 2013. **178**: p. 99-103.
121. Sevelsted, T.F., et al., *¹³C MAS NMR spectroscopy in cement science: Characterization of limestone-Portland cements and carbonated C-S-H phases by ¹³C, ²⁷Al and ²⁹Si MAS NMR, in 31st Cement and Concrete Science Conference.2011: Imperial College, London*.
122. Garbev, K., et al., *Cell dimensions and composition of nanocrystalline calcium silicate hydrate solid solutions. Part 2: X-ray and thermogravimetry study*. Journal of the American Ceramic Society, 2008. **91**(9): p. 3015-3023.
123. Black, L., et al., *Characterisation of crystalline C-S-H phases by X-ray photoelectron spectroscopy*. Cement and Concrete Research, 2003. **33**(6): p. 899-911.
124. Black, L., et al., *Structural features of C-S-H(I) and its carbonation in air - A Raman spectroscopic study. Part II: Carbonated phases*. Journal of the American Ceramic Society, 2007. **90**(3): p. 908-917.
125. Suzuki, K., et al., *Effect of NaCl or NaOH on the formation of C-S-H*. Cement and Concrete Research, 1986. **16**: p. 333-340.
126. Lecoq, X., *Etude de l'hydratation à concentration contrôlée du silicate tricalcique Ca₃SiO₅ et des caractéristiques de ses produits de réaction (Thesis)* 1993, University of Bourgogne, Dijon.
127. Garrault, S., *PhD Thesis*, 1998, University of Bourgogne, Dijon.
128. Merz, D., et al. *Ammonia release in the thermal treatment of high-protein waste fractions. in Hyphenated Techniques in Thermal Analysis : Proc. of the 3rd SKT*. 2000. Bad Orb.
129. Yang, H.X. and C.T. Prewitt, *On the crystal structure of pseudowollastonite (CaSiO₃)*. American Mineralogist, 1999. **84**(5-6): p. 929-932.
130. Richardson, I.G., et al., *The characterization of hardened alkali-activated blast-furnace slag pastes and the nature of the calcium silicate hydrate (C-S-H) phase*. Cement and Concrete Research, 1994. **24**(5): p. 813-829.
131. Li, Q., *PhD Thesis*, 2008, University of Leeds.
132. Black, L., et al., *X-ray photoelectron spectroscopic investigation of nanocrystalline calcium silicate hydrates synthesised by reactive milling*. Cement and Concrete Research, 2006. **36**(6): p. 1023-1031.

133. Petch, H.E., *Hydrogen positions in portlandite, Ca(OH)₂, as indicated by electron distribution*. Acta Crystallographica, 1961. **14**(9): p. 950-957.
134. Bornefeld, M.J., *PhD Thesis*, 2013, Ruprecht-Karls-University of Heidelberg.
135. Sass, R.L., R. Vidale, and J. Donohue, *Interatomic distances and thermal anisotropy in sodium nitrate and calcite*. Acta Crystallographica, 1957. **10**(9): p. 567-570.
136. Dalnegro, A. and Ungarett.L, *Refinement of crystal structure of aragonite*. American Mineralogist, 1971. **56**(5-6): p. 768.
137. Kamhi, S.R., *On structure of vaterite, CaCO₃*. Acta Crystallographica, 1963. **16**(8): p. 770-772.
138. *Cement monograph*. Available from:
http://iti.northwestern.edu/cement/monograph/Monograph7_3_2.html
http://iti.northwestern.edu/cement/monograph/Monograph7_3_2.html.
139. Galmarini, S., et al., *Changes in portlandite morphology with solvent composition: Atomistic simulations and experiment*. Cement and Concrete Research, 2011. **41**(12): p. 1330-1338.
140. L'Hopital, E., *PhD Thesis*, 2014, Ecole Polytechnique Federale de Lausanne.
141. L'Hopital, E., et al., *Incorporation of aluminium in calcium-silicate-hydrate*. Submitted to Cement and Concrete Research, 2014.